Title
Lens-Free Computational Microscopy for Disease Diagnosis

Author
Zhang, Yibo

Publication Date
2018

Peer reviewed|Thesis/dissertation

UNIVERSITY OF CALIFORNIA

Los Angeles

Lens-Free Computational Microscopy for Disease Diagnosis

A dissertation submitted in partial satisfaction of the

requirements for the degree Doctor of Philosophy

in Electrical and Computer Engineering

by

Yibo Zhang

2018

ABSTRACT OF THE DISSERTATION

Lens-Free Computational Microscopy for Disease Diagnosis

by

Yibo Zhang

Doctor of Philosophy in Electrical and Computer Engineering

University of California, Los Angeles, 2018

Professor Aydogan Ozcan, Chair

The optical microscope has served as a workhorse for the medical community for hundreds of years and has been one of the gold-standards for the diagnosis of numerous diseases. However, the high cost and bulkiness of lens-based microscopes largely restrict them to advanced imaging labs in centralized clinics; whereas the limited throughput increases the time and labor for the diagnostician to reach a diagnosis, which in turn increases the cost of diagnosis.

In this dissertation, a novel imaging modality, namely *lens-free computational microscopy*, and the techniques and methods that enable its applications to medical diagnostic tasks will be introduced. With no lenses in the optical setup, the lens-free microscope directly captures defocused holographic patterns of the sample using an optoelectronic image sensor, and computationally recovers the sample's image with image reconstruction algorithms. This unique design makes the lens-free microscope extremely cost-effective, wide-field, robust and compact. Centered around lens-free microscopy, three application domains are covered in this dissertation:

bright-field pathology slide imaging for cancer diagnosis (pathology), polarized microscopy for gout/pseudogout diagnosis (rheumatology), and rapid screening of parasite infection in bodily fluids (microbiology). First, a multi-height-based phase retrieval method was developed for lens-free microscopy, which enabled imaging of pathology slides of tissue sections and cell smears for diagnosis of various diseases such as cancers. In addition, an absorbance spectrum estimation-based colorization method was developed to provide accurate colorization of lens-free microscopy images of stained tissues and cells, and an edge sparsity-based autofocusing algorithm improved the automation and robustness of the image processing pipeline. Furthermore, using chemical tissue clearing, i.e., the simplified CLARITY method, wide-field three-dimensional imaging of thick tissues was demonstrated, which could potentially be used for cell phenotyping and clinical diagnosis. Next, on the basis of some of these techniques, a polarization-sensitive lens-free microscopy platform was created, which could image birefringent crystals in the synovial fluid for high-throughput diagnosis of gout and pseudogout. Lastly, a novel optical technique for sensitive and high-throughput detection of parasitic infections is developed, named *lensless time-resolved holographic speckle imaging*, which analyses the motility patterns of parasites in the bloodstream or other bodily fluids using deep learning.

The dissertation of Yibo Zhang is approved.

Pei-Yu Chiou

Asad Mohamed Madni

Oscar M. Stafsudd

Chee Wei Wong

Aydogan Ozcan, Committee Chair

University of California, Los Angeles

2018

Table of Contents

List of Figures

List of Tables

Acknowledgements

Foremost, I would like to thank my PhD advisor, Prof. Aydogan Ozcan, to the greatest extent for supporting me throughout my PhD study and research. Prof. Ozcan is one of the smartest and most knowledgeable people I have ever known, and I have been constantly inspired by his extraordinary scholarship, absolute dedication, and inexhaustible creativity. The unique privilege to work with and learn from Prof. Ozcan has helped me grow rapidly as a researcher and an engineer and is extremely important to my professional development. I would like to also thank my doctoral committee members, Prof. Pei-Yu Chiou, Prof. Asad Mohamed Madni, Prof. Oscar M. Stafsudd and Prof. Chee Wei Wong, for their invaluable scientific advice and career suggestions.

I feel extremely lucky to have the chance to work with my great colleagues, who have helped me through the journey and inspired me with their exceptional intelligence. A special thanks to Alon Greenbaum, Wei Luo, Zoltan Gorocs, Yair Rivenson, Yichen Wu, Hongda Wang, Hatice Ceylan Koydemir, Michelle Shimogawa, Steve Feng, Tairan Liu, Yi Luo, Pengbin Yin, Sam Yang, Bijie Bai, Yilin Luo, Sener Yalcin, Yujia Huang, Ilker Oguz, Da Teng, Miu Tamamitsu, Qingshan Wei, Euan McLeod, Yoonjung Shin, Kevin Sung, Harrison Chen, Seung Yoon Celine Lee, Michael Alexander, Mustafa Daloglu, Aniruddha Ray, Vittorio Bianco, Yinxu Bian, Alborz Feizi, Zhensong Wei, Zach Ballard, Calvin Brown, Derek Tseng, Muhammed Veli, Kevin De Haan, Daniel Shir, Hyouarm Joung, Yingnan Wang, Harun Gunaydin, Yun Zhang, Bohan Zhang, Quanjie Geng, Rohan Nadkarni, Zhuoran Duan, Xuewei Liu, Chloe Cheung, Raymond Chan, Ping-Luen Chung, Henry Zhu, Eunso Shin, Ruilin Jiang, Chuangwei Yue.

I also would like to express my utmost gratitude to my family for their unconditional love and support: to my wife, Yingyuan, for her selfless support, love, understanding, and encouragement; and to my loving parents.

Lastly, I would like to acknowledge the American Association for the Advancement of Science (AAAS) and the Optical Society of America (OSA) for permitting me to reuse my co-authored papers published in their journals in this dissertation.

Vita

Yibo Zhang received his BS degree from Electrical Engineering (EE) Department, Tsinghua University in Beijing, China in 2013. In the same year, he joined Prof. Aydogan Ozcan's Bio- and Nano-Photonics Group at Electrical and Computer Engineering Department, UCLA to pursue a PhD degree. Yibo's research focuses on computational microscopy and sensing for biomedical applications and disease diagnosis.

During his education at UCLA, Yibo received the 2015 SPIE Photonics West BiOS Translational Reseach Best Paper Award, 2nd place in the 2015 UCLA Grad Slam, Best Poster Presentation in the 2018 UC Systemwide Bioengineering Symposium, and Dissertation Year Fellowship in 2018. Yibo has also co-authored 26 publications in renowned journals and international conferences.

Selected publications

1. Y. Rivenson†, Y. Zhang†, H. Günaydın, D. Teng, and A. Ozcan, "Phase recovery and holographic image reconstruction using deep learning in neural networks," Light: Science & Applications **7**, 17141 (2018) (†Equally contributing authors)
2. Y. Zhang, *et al.*, "3D imaging of optically cleared tissue using a simplified CLARITY method and on-chip microscopy," Science Advances **3**, e1700553 (2017)
3. A. Greenbaum, Y. Zhang, A. Feizi, P.-L. Chung, W. Luo, S. R. Kandukuri, and A. Ozcan, "Wide-field computational imaging of pathology slides using lens-free on-chip microscopy," Science Translational Medicine **6**, 267ra175-267ra175 (2014)
4. Y. Zhang, S. Y. C. Lee, Y. Zhang, D. Furst, J. Fitzgerald, and A. Ozcan, "Wide-field imaging of birefringent synovial fluid crystals using lens-free polarized microscopy for gout diagnosis," Scientific Reports **6**, 28793 (2016)
5. Y. Zhang, H. Wang, Y. Wu, M. Tamamitsu, and A. Ozcan, "Edge sparsity criterion for robust holographic autofocusing," Optics Letters **42**, 3824 (2017)

Chapter 1. Introduction to lens-free computational microscopy

The optical microscope has assisted the science, engineering and medical communities to observe the microscopic world for hundreds of years, leading to continuous advances and discoveries. In medical diagnosis, thanks to its capability to directly observe what cannot be normally seen, e.g., a lesion in a histological tissue section, or a pathogen within the bodily fluid of a patient, etc., the medical professional is provided with invaluable information that may lead to a diagnosis and guide treatment. However, owing to the use of lens-based optics, the traditional optical microscope is limited by a number of drawbacks, including high cost, bulkiness, limited field of view (FOV), limited depth of field, and sensitivity to alignment. These drawbacks limit the application of optical microscopy, making them less suitable for areas such as point-of-care diagnostics, lab-on-a-chip applications, global health applications, telemedicine, etc. Therefore, it is imperative to develop an alternative to the traditional optical microscope that is cost-effective, compact, robust and high-throughput.

In this dissertation, I will focus on a novel imaging technique that satisfies the above requirements, namely *lens-free computational microscopy*, and its numerous applications to disease diagnosis in pathology, rheumatology and microbiology. The dissertation is structured as follows:

In Chapter 1, I will introduce the background, optical setup and hologram formation, and the basic image reconstruction techniques of lens-free microcopy.

Next, Chapters 2-4 will be focused on several important building blocks of lens-free image reconstruction. These algorithms and methods were tailored for high-throughput imaging of pathology slides for the diagnosis of various diseases (e.g., cancers), but can also be used for various other applications. In Chapter 2, I will discuss a central challenge in holography, i.e., phase

retrieval, and demonstrate a multi-height-based phase retrieval method, which enabled the lens-free imaging of histological tissue sections. In Chapter 3, I will demonstrate an absorbance spectrum estimation-based color correction method for accurate-color lens-free microscopy of stained tissues and cells. In Chapter 4, I will present a robust autofocusing method for holographic microscopy of tissues and cells, which is essential to the automation of lens-free microscopy and other holographic imaging systems.

Then, in Chapters 5-7, I will cover three other biomedical applications of lens-free microscopy and the related techniques, which include imaging of optical cleared thick tissues for cell phenotyping, polarized microscopy of birefringent crystals for gout/pseudogout diagnosis, and rapid screening of bodily fluids for sensitive detection of parasite infection. Some of the methods/techniques in these chapters were newly created for these important applications, while some were adapted from Chapters 2-4.

Finally, I will summarize the dissertation in Chapter 8,

Part of Chapter 1 has been previously published in A. Greenbaum, Y. Zhang, A. Feizi, P.-L. Chung, W. Luo, S. R. Kandukuri, and A. Ozcan, "Wide-field computational imaging of pathology slides using lens-free on-chip microscopy," Science Translational Medicine **6**, 267ra175-267ra175 (2014) (reused with permission from AAAS).

1.1 Background

Recent developments in optics and electronics technologies, mainly image sensor chips with larger numbers of pixels and smaller pixel-sizes, together with the constantly reducing cost of high-performance computation, prompted the field of computational microscopy, which endeavors to overcome the limitations of traditional light microscopes using novel imaging designs and reconstruction algorithms [1–18]. For example, recent advances in incoherent holography methods

and spatial light modulators fostered new computational microscopy techniques that permit 3D imaging of fluorescent samples in a single shot [5,19–21]. As another important example, compressive sampling techniques [22] enabled 3D reconstruction of objects from a relatively small number of image frames or pixels [1,2]. All of these emerging computational imaging approaches and various others [6,8,10,23–28] utilize reconstruction algorithms for significantly improving the performances of lens-based imaging designs.

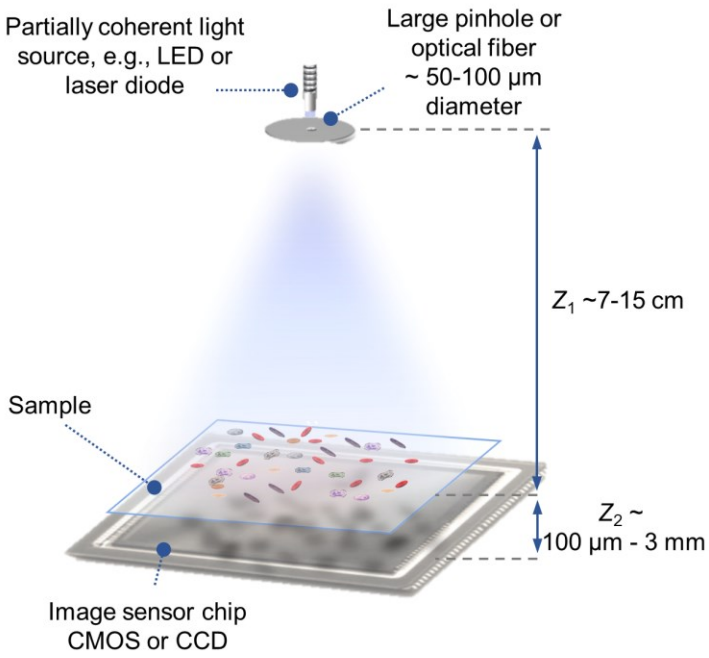

Figure 1. 1. Basic optical setup of the lens-free on-chip holographic microscope.

Lens-free on-chip imaging, on the other hand, takes an alternative approach and uses an opto-electronic sensor-array to directly sample an object's diffraction pattern to digitally reconstruct its image [13,15,29,30]. Based on the principles of digital in-line holography, this recently emerging computational imaging approach does not require objectives or other lenses to form an image, enabling its set-up to be simple, compact, and cost-effective [13,31]. Owing to its unique imaging geometry, in which the light-source to object distance (z_1) is much larger than the sample to sensor distance (z_2), the lens-free holograms of the objects are captured with unit magnification (Fig. 1.1).

As a result of this, the FOV of a lens-free microscope is equal to the image sensor's active area (e.g., 20-30 mm^2) and can be hundreds of times larger than a lens-based microscope, which typically has a FOV of less than 0.1-0.2 mm^2 for high-resolution imaging [13]. This imaging configuration is also referred to as "on-chip microscopy", since the sample literally sits on the sensor chip (with a small gap that is typically <1 mm, or a few millimeters at most).

Unlike other on-chip microscopes which are based on contact imaging [17,32], the 3D spatial information of the objects can be reconstructed or digitally refocused through holographic processing, without the need for a perfectly planar and tilt-free object. This makes lens-free microscopy highly suitable for imaging of volumetric samples (e.g., fluid samples) [30,33,34], samples with natural tilting/warping [35,36], or samples on curved surfaces [37]. Combined with advantages of wide FOV, low cost and compact footprint, lens-free microscopy has found numerous applications in biofluid analysis [34,38–41], cytometry [40,42,43], digital pathology [35,44–50], dynamic imaging of microswimmers [30,34,51], etc.

1.2 Optical setup and hologram formation

Overview of the optical setup

As shown in Fig. 1.1, the optical setup of a lens-free microscope consists of a partially coherent light source and an optoelectronic image sensor. The sample is placed in close proximity to the image sensor, such that the distance from the sample to the image sensor (z_2) is typically less than 3 mm. The distance from the light source to the sample, i.e., z_1, is typically around 7-15 cm. The image sensor records the diffraction pattern, i.e., in-line hologram, of the sample. Because $z_1 >> z_2$, the imaging system has a unit fringe magnification. As a result, the FOV, i.e., the sample area that can be imaged at once, is equal to the image sensor's active area, which ranges between several

tens of mm^2 to tens of cm^2. In the following subsections, I will discuss the image formation in lens-free microscopy as well as each key component of the lens-free microscope in further depths.

Hologram formation

When the light that is emitted by the light source hits the sample, part of the light is scattered by the sample. The in-line hologram is formed as a result of interference between the light wave scattered by the sample and the light wave that is directly transmitted. If the illumination can be approximated as a plane wave, the light wave that impinges on the image sensor can be written as

$$U(x,y) = A + a(x,y) \tag{1.1}$$

where A is the reference wave, and $a(x, y)$ is the scattered wave that propagates to the sampling plane.

As optoelectronic image sensors are only sensitive to the intensity of the light wave but not the phase, the light intensity measured by an ideal image sensor (with infinitely small and noiseless pixels) can be written as [52]

$$I(x,y) = \left|A + a(x,y)\right|^2 = |A|^2 + \left|a(x,y)\right|^2 + A^* a(x,y) + A a^*(x,y). \tag{1.2}$$

In Eq. (1.2), $A^* a(x, y)$ is a term proportional to the scattered wave and $|A|^2$ is a constant that is independent of spatial positions. These two terms are proportional to the right-hand side of Eq. (1.1), thus can be considered as "desired" terms. The other two terms, $A a^*(x, y)$ and $|a(x, y)|^2$, are artifact terms as a result of the loss of phase information. Specifically, the artifact related to $A a^*(x, y)$ is called the "twin image", because it is equal to the complex conjugate of the scattered wave term, $A^* a(x, y)$; the second-order artifact, $|a(x, y)|^2$, is usually negligible for weakly-scattering objects, but is non-negligible for strongly scattering samples such as connected tissue sections.

Another equivalent way to look at the image formation model, i.e., the "forward model", is through the sample's complex transmission function. When a plane wave hits an object, assuming the object's thickness can be ignored, the process can be modeled as a multiplication of the incident wave field with the complex transmission function of the object. The complex transmission function, denoted by

$$O(x,y) = \left|O(x,y)\right| \exp\left(j\varphi(x,y)\right), \tag{1.3}$$

models the interaction between light and the object. The amplitude, $|O(x, y)|$, is equal to the square-root of the transmission of the light intensity, thus is related to absorption or reflectance of the sample. The additional phase delay, $\varphi(x, y)$, is related to the refractive index difference between the object and the surrounding medium.

The propagation (or diffraction) of coherent light inside homogenous medium can be modeled with the angular spectrum formulation in Fourier optics theory [52]. Denote a given complex optical wave field on the plane $z = 0$ as $U(x, y; 0)$. The angular spectrum of $U(x, y; 0)$ is given by its Fourier transform

$$A\left(f_x, f_y; 0\right) = \iint U\left(x, y, 0\right) \exp\left[-j2\pi\left(f_x x + f_y y\right)\right] \mathrm{d}x\mathrm{d}y \ . \tag{1.4}$$

The angular spectrum of the optical field on an arbitrary parallel plane $z = z_0$ can be calculated by

$$A\left(f_x, f_y; z_0\right) = A\left(f_x, f_y; 0\right) \cdot H\left(f_x, f_y; z_0\right). \tag{1.5}$$

The free-space transfer function, $H(f_x, f_y; z_0)$, is given by

$$H\left(f_x, f_y; z_0\right) = \begin{cases} \exp\left[j2\pi \dfrac{n}{\lambda_0} z_0 \sqrt{1 - \left(\dfrac{\lambda_0 f_x}{n}\right)^2 - \left(\dfrac{\lambda_0 f_y}{n}\right)^2} \right], & \sqrt{f_x^2 + f_y^2} \le f_{\text{cut-off}} \\ 0, \quad \text{others} \end{cases} \tag{1.6}$$

where λ_0 is the optical wavelength in vacuum, n is the refractive index of the medium, and $f_{\text{cut-off}}$ is the cut-off frequency for free-space propagation.

The optical wave field on the plane $z = z_0$ is obtained by the inverse Fourier transform,

$$U(x, y; z_0) = \iint A(f_x, f_y; z_0) \exp\left[j2\pi \left(f_x x + f_y y \right) \right] \mathrm{d}f_x \mathrm{d}f_y \ . \tag{1.7}$$

1.3 Key components in a lens-free microscope

Light source

The selection of the light source is important to ensuring a high imaging resolution and quality. As a holographic imaging method, narrow-band and partially coherent illumination sources should be used to preserve the interference fringes, such as light-emitting diodes (LEDs) and lasers. The temporal and spatial coherence of the light source should be considered when choosing the light source [13].

The temporal coherence of the light source is quantified by the spectral bandwidth. Depending on the distance between the sample and the image sensor, as well as the resolution requirement of the imaging system, the spectral bandwidth of the light source may vary between under 1 nm to tens of nanometers. When using LEDs as the light source, single-color LEDs should be selected, which typically have a spectral bandwidth of 15-40 nm. Narrower bandwidths are preferred, which will lead to a better resolution. An additional spectral filter may be added to reduce the spectral bandwidth, which can typically improve the spatial resolution, but at the same time, reduce the optical power that can be used for imaging. Lasers typically have high brightness and high temporal coherence. But the high temporal coherence can lead to interference fringes caused by multiple reflections at the various interfaces in the system as well as speckle noise.

Besides temporal coherence, the spatial coherence is an additional concern when choosing the light source. Because lens-free imaging has the geometrical relationship $z_1 >> z_2$, the requirement for the spatial coherence of the light source is loosened. When LEDs are used, it can be simply butt-coupled (glued) to an optical fiber section (e.g., 50 μm – 200 μm core diameter) or a large pinhole. When a laser diode is used, typically an uncollimated laser diode can be directly used as the light source without other complication. This greatly simplifies the construction of the light source of the lens-free microscope.

Image sensor

Owing to the unit magnification geometry, the FOV of the lens-free microscope is typically equal to the active area of the optoelectronic image sensor that is used for image acquisition. Therefore, using state-of-the-art CCD or CMOS chips, the FOV per single-shot can be ~20 mm^2 to ~20 cm^2, depending on the pixel number and the pixel size.

The pixel size of the image sensor is of key importance to the resolution of the lens-free imaging system. Because no optical magnification is used, the resolution of a lens-free microscope is influenced by the pixel size, which determines the spatial sampling period. Therefore, choosing an image sensor with a small pixel size can in general improve the resolution of the imager. However, some image sensors are designed to correct for the chief ray angle, which has different amounts of shifting between the microlens and the pixel at different parts of the FOV. This causes aberrated angular response, thus is not ideal for lens-free microscopy.

Thanks to the consumer electronics market, there has been a continual trend in the semiconductor industry to develop image sensors with higher pixel count, smaller pixel size, lower noise as well as higher quantum efficiency. Various image sensors nowadays have sub-micron

pixel sizes and/or >40 megapixels. Lens-free microscope can greatly benefit from the advances of image sensor technologies to achieve better resolution and wider FOV.

1.4 Reconstruction techniques

Following the acquisition of a hologram (or multiple holograms), a computational post-processing pipeline is performed to (1) improve the resolution of the hologram, (2) perform autofocusing to estimate the z_2 distance, (3) perform phase retrieval to remove the "twin image" and second-order artifacts, (4) back-propagate the hologram to the sample plane, and (5) perform colorization. Depending on the application, sometimes only a subset of the steps is taken,. While (2), (3) and (5) will be covered in Chapters 2-4 of the dissertation, this section will briefly discuss (1) and (4).

Pixel super-resolution (PSR) to mitigate resolution loss due to spatial under-sampling

The resolution of lens-free microcopy is mainly limited by a few factors. First, the resolution of a microscope is fundamentally limited by the optical diffraction limit. Second, the pixel size of the image sensor limits the spatial sampling frequency, which, according to the Nyquist sampling theorem, limits the spatial resolution. Third, the limited angular response of the image sensor pixels further adds additional attenuation to the high-spatial-frequency component of the optical field. Over the past decade, various techniques have been developed to address each of these limits [13,47,49,50,53], pushing the resolution limit of lens-free microscope to ~225 nm (Fig. 1.2) [53] and an equivalent numerical aperture (NA) of 1.4 (Fig. 1.3) [49].

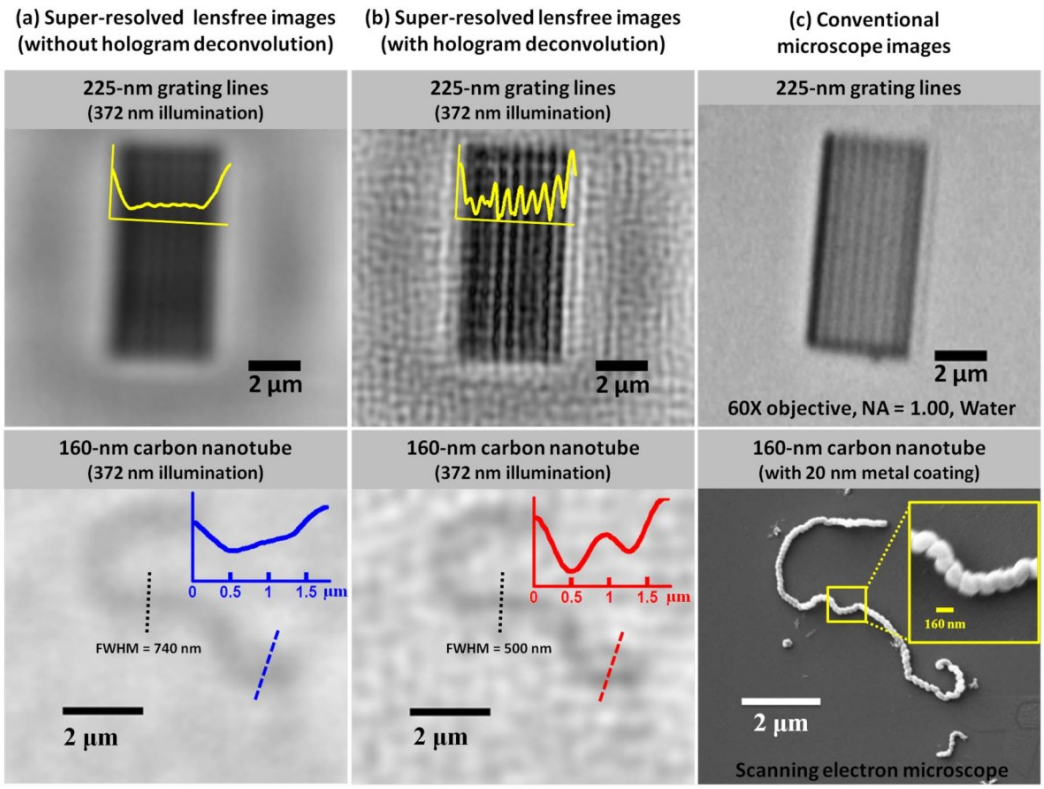

Figure 1. 2. The resolution of lens-free on-chip imaging using a 1.12 µm CMOS image sensor was pushed to 225 nm (linewidth), corresponding to an effective NA of ~0.83, using the PSR technique with experimentally characterized pixel function. Image source: Ref. [53]; reused under the Creative Commons Attribution-NonCommercial-NoDerivs 3.0 Unported Licence (CC BY-NC-ND 3.0; https://creativecommons.org/licenses/by-nc-nd/3.0/).

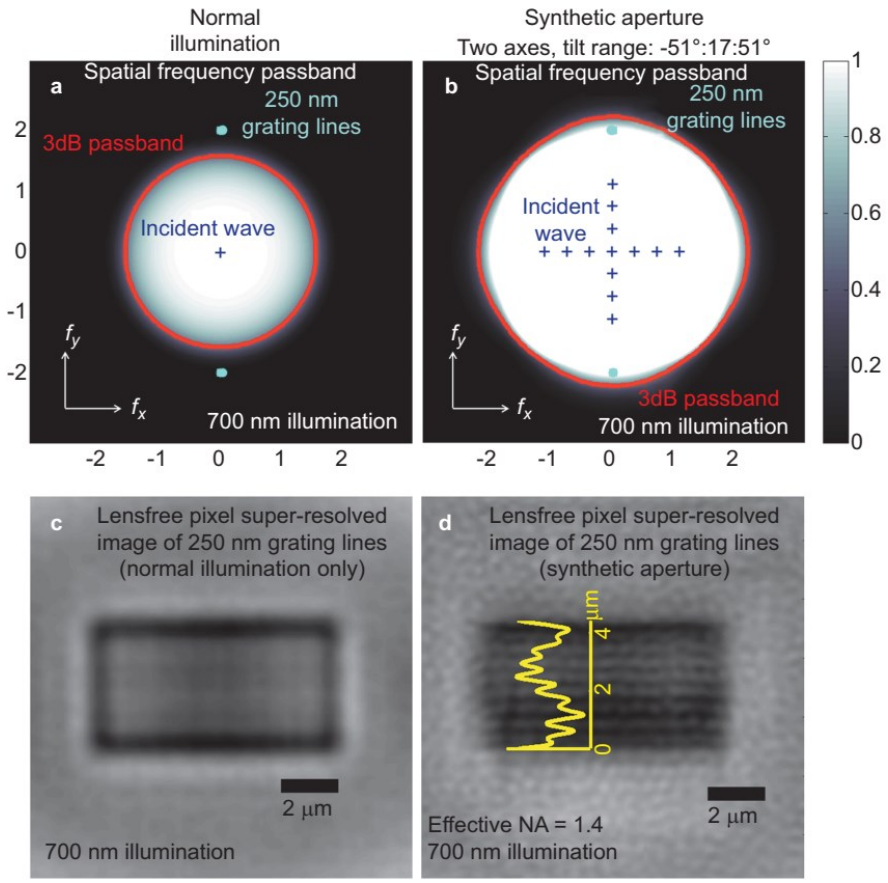

Figure 1. 3. Using the synthetic aperture-based on-chip microscopy technique, the effective NA of the lens-free microscope was increased to ~1.4, with a resolution of 250 nm at a wavelength of 700 nm. Image source: Ref. [49]; reused under the Creative Commons Attribution-NonCommercial-NoDerivs 3.0 Unported Licence (CC BY-NC-ND 3.0; https://creativecommons.org/licenses/by-nc-nd/3.0/).

The PSR technique has been developed to address the resolution limit related to the spatial under-sampling by the finite pixel size [48,54–56]. PSR's working principle is by computationally combining multiple low-resolution holograms that are sub-pixel-shifted from each other into a high-resolution hologram. To create sub-pixel shifting, either an array of light sources (e.g., a fiber-coupled LED array) that is turned on sequentially [31,56], mechanical shifting of the light source [53], mechanical shifting of the sample [36], or mechanical shifting of the image sensor can be used. The amount of shifting between holograms may be random, or it may be on a regular

grid corresponding to $1/N$ ($N = 2, 3, 4, \ldots$) of the pixel size. Because of the demagnification factor z_2/z_1, creating a light source array or mechanical shifting of the light source have a looser tolerance than shifting the sample or the image sensor. However, if the sample cannot be considered as two-dimensional, i.e., it has a three-dimensional structure, creating a light source array or shifting the light source will introduce different shifting of the hologram corresponding to different depths within the sample volume, making it challenging to fuse the multiple low-resolution hologram into a high-resolution one.

Typically, two algorithmic steps are taken to achieve PSR. First, the exact amount of shifting between images needs to be first calculated, i.e., the *shift-estimation* step. Second, the multiple low-resolution holograms are computationally combined into a single high-resolution hologram based on the calculated shifts. The second step is also called *fusion*.

A shift-estimation algorithm is used to automatically estimate the sub-pixel shift among holograms, which does not need any feedback from the mechanical translation stage, or, in the case of a light source array, its spacings. A robust and accurate shift-estimation algorithm is adapted based on the method proposed by Hardie *et al.* [57], which iteratively minimizes the squared difference between the translated version of each given hologram and a reference hologram, with the x and y shifts as the arguments. The reference hologram is typically selected as the first (or last) hologram that is captured.

After estimation of the shifts, different algorithms can be used to fuse the multiple low-resolution holograms together. In one approach, the fusion problem can be formulated as a least-square optimization problem with a regularized cost function, where the loss is defined as the squared difference between the high-resolution hologram and the low-resolution raw measurements plus a L2 regularizer [57]. This optimization can be solved reliably using the

conjugate gradient method [15,48,57]. Although this method can deal with random shifts among holograms, it is relatively slow and computation-intensive. Alternatively, when the shifts approximately lie on a regular grid, a "shift-and-add" method can be adopted [35,58]. The raw pixels of the low-resolution holograms are used to fill a high-resolution grid, followed by a deconvolution step to boost the high-frequency components that are attenuated by the pixel function in the end. This method is computationally very efficient but may suffer from high-frequency noise, because typically the shifts are not distributed precisely on a regular grid, depending on the accuracy of the hologram shifting mechanism.

Numerical back-propagation of a hologram

As formulated in Eqs. (1.4)-(1.6), numerical back-propagation of a hologram can also utilize the angular spectrum method, which digitally reverses light diffraction. Using this approach, an in-focus image can be obtained for any given sample depth. For a hologram, whether or not it is phase-retrieved, it is transformed to the spatial frequency domain using a two-dimensional fast Fourier transform (FFT) (Eq. (1.4)), obtaining its angular spectrum. Then, the angular spectrum is multiplied with a phase function (Eq. (1.5)), parameterized by the z distance, the wavelength and the refractive index of the medium (Eq. (1.6)). A frequency cutoff representing the diffraction limit is applied, which removes all evanescent waves that may result in numerical instability when the propagation direction is backwards. Finally, an inverse FFT is used to transform the angular spectrum back to the space domain to obtain the complex optical wave at the destination plane (Eq. (1.7)).

An example of numerical back-propagation if shown in Fig. 1.4. The phase-retrieved images in Fig. 1.4(d, e) are obtained using the multi-height-based phase retrieval method detailed in Chapter 2.

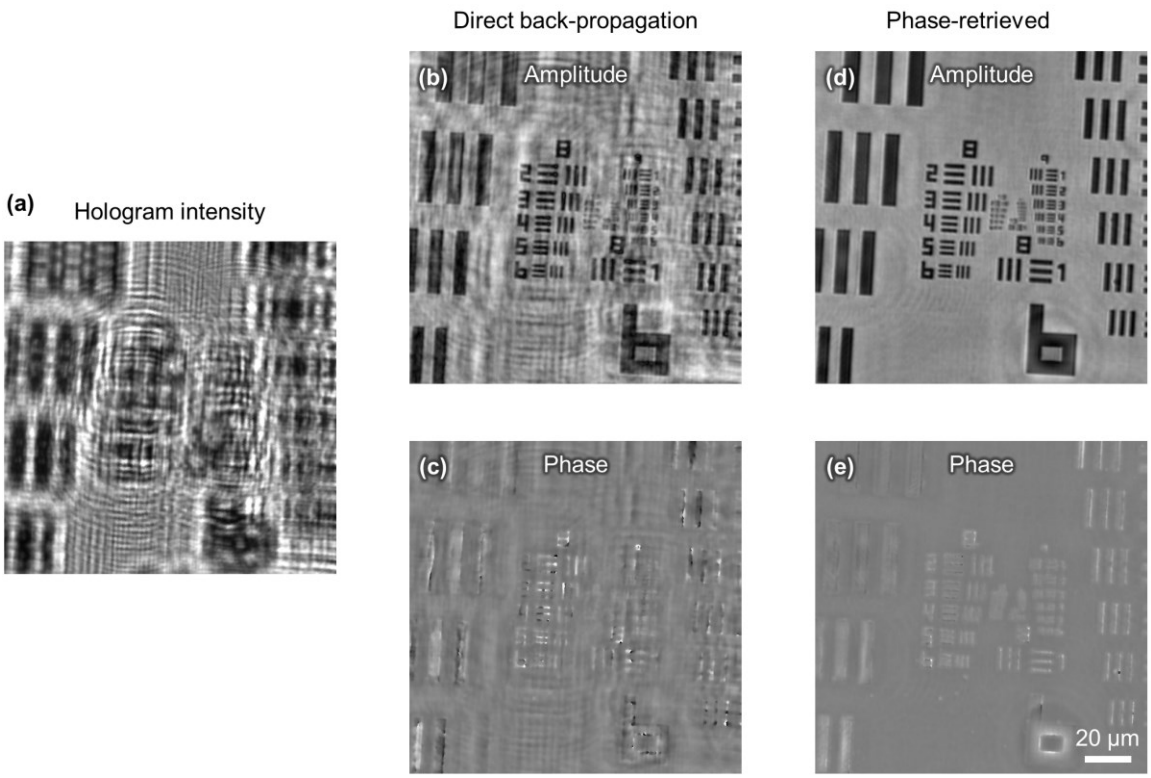

Figure 1. 4. Numerical back-propagation of a hologram. (a) Intensity of a hologram of the USAF-1951 resolution test target at a wavelength of 532 nm and a z_2 distance of ~189.6 μm. **(b, c)** Direct back-propagation of the hologram intensity. Because the loss of phase information when the hologram is recorded by the image sensor, the twin image and second-order artifacts are visible in the amplitude and phase, as compared to **(d, e)**, which are the phase-retrieved amplitude and phase images of the sample.

Chapter 2. Multi-height-based phase retrieval technique for lens-free imaging of pathology slides

Phase retrieval is a central challenge in in-line holography; it is especially important to lens-free imaging of histological tissue sections and dense cells, owing to the high density and strong light scattering of these samples. The previously demonstrated multi-height iterative phase retrieval technique suffers from the phase stagnation problem and artifacts from uncontrolled sample tilting [54–56,59]. In this chapter, a novel hybrid phase retrieval method is demonstrated. This method generates an initial phase guess using the transport-of-intensity equation (TIE) [60], and this initial guess is passed on to the iterative phase retrieval algorithm for further refinement. A computational tilt correction algorithm is incorporated into the iterative phase retrieval algorithm to automatically correct for sample tilting. With these technical advances, lens-free imaging of dense specimens is achieved with a leapfrog improvement in the imaging performance. Moreover, pathology slides of tissue sections are imaged using the lens-free microscope for the first time, opening up new possibilities in the cost-effective and high-throughput diagnosis of cancers and other chronic diseases. We successfully imaged invasive carcinoma cells within human breast sections, Papanicolaou smears revealing a high-grade squamous intraepithelial lesion, and sickle cell anemia blood smears over a FOV of 20.5 mm^2. The resulting wide-field lens-free images had sufficient image resolution and contrast for clinical evaluation and diagnosis after examination by an expert pathologist. By providing high-resolution images of large-area pathology samples with 3D digital focus adjustment, lens-free on-chip microscopy can be useful in resource-limited and point-of-care settings.

Part of this chapter has been previously published in A. Greenbaum, Y. Zhang, A. Feizi, P.-L. Chung, W. Luo, S. R. Kandukuri, and A. Ozcan, "Wide-field computational imaging of pathology

slides using lens-free on-chip microscopy," Science Translational Medicine **6**, 267ra175-267ra175 (2014) (reused with permission from Ref. [35], AAAS).

2.1 Introduction

Large human populations especially in developing countries still suffer from limited access to medical services, as a result of either poor access to medical infrastructure or the lack of trained medical personnel. Recent advances in communication technologies and telemedicine offer unique opportunities to bridge some of these gaps by enabling rapid and secure sharing of medical data and patient health records with remote physicians, helping to improve the standard of care in many branches of medicine. However, pathology is still by and large constrained to advanced clinical laboratory settings, since it is partially bottlenecked by the requirements of high-throughput image acquisition devices that can reliably scan and digitize large sample areas, ideally automatically. The current gold-standard for pathologists to observe micro-scale objects within a tissue section or a smear is the bright-field optical transmission microscopy. Although high-resolution imaging capabilities have contributed to the optical microscope's widespread use in clinical settings, it has several limitations. First, a high-quality pathology microscope and its carefully crafted objective lenses are costly. Additionally, the microscope's field-of-view (FOV: the area of the specimen that can be imaged) is inversely proportional to the square of its total magnification factor, thus limiting its ability to observe large samples, such as whole histology slides, without mechanical scanning. Lateral scanning can expand the FOV of a microscope image; however, its usefulness is partially compromised owing to the potential sample tilt and out-of-plane regions that naturally occur in large pathology samples, which necessitate dynamic focus adjustment through additional depth scanning and digital signal processing [61].

Recent advances in optoelectronic image sensor technologies, together with high-performance computation platforms, has led to the rapid development of computational microscopy, which aims to empower or even replace traditional microscopy paradigms through innovative imaging designs and novel algorithms [1–18]. Among computational microscopy modalities, lens-free on-chip microscopy has the advantages of low cost, high throughput, compactness and portability, making it a promising candidate to replace traditional microscopes and to be used in resource-limited settings [30,40,62–64]. However, because current optoelectronic image sensors cannot respond to the phase of the optical wave, only the intensity of the diffracted optical wave (i.e., hologram) can be recorded and the phase is lost. Reconstruction of an in-line hologram without phase information results in the so-called "twin image" artifact in addition to a second-order noise term. To address this problem, phase retrieval methods are developed, which computationally recover the phase information and can help to remove the twin image and the second-order noise terms. Over the past decades, various phase retrieval techniques have been proposed, such as phase retrieval using the object support [65,66], using multiple defocused images [13,35,54–56,59,67–69], using multiple angles and/or wavelengths [47,49,50], etc. Recently, data-driven phase retrieval methods using the convolutional neural network (CNN) has also been demonstrated [70].

Phase retrieval is especially central to the lens-free microscopy of histological tissue sections and dense cells. Owing to the high density and strong light scattering of these samples, the twin image cannot be easily separately from the original image of the object using object support, and the second-order noise term is also non-negligible. In 2012 and 2013, Greenbaum *et al.* started to adopt the multi-height phase retrieval method in lens-free microscopy and demonstrated promising reconstruction results of densely distributed cells [54–56,59]. However, the iterative multi-height phase retrieval algorithm suffers from the phase stagnation problem, manifested by slow

convergence and unsatisfactory phase reconstruction, especially for low spatial frequency components of the phase. Moreover, the uncontrolled tilting between the sample and the image sensor introduces additional out-of-focus artifacts, which deteriorates quality of image.

In this chapter, a multi-height-based phase retrieval technique is presented, which uses multiple defocused images for phase retrieval and enables lens-free microscopy to image connected tissue sections and dense cell smears. In this method, multiple holograms corresponding to different diffraction distances are captured. Then, the transport-of-intensity equation (TIE) is used to generate an initial guess of the phase, and an iterative algorithm utilizing the constraints of the measured hologram intensities is used to refine the initial guess, reaching convergence over tens of iterations. A digital tilt correction method using the rotational field transformation is incorporated into the iterative algorithm to correct for potential tilting between the sample and the image sensor chip.

2.2 Materials and methods

Lens-free imaging set-up

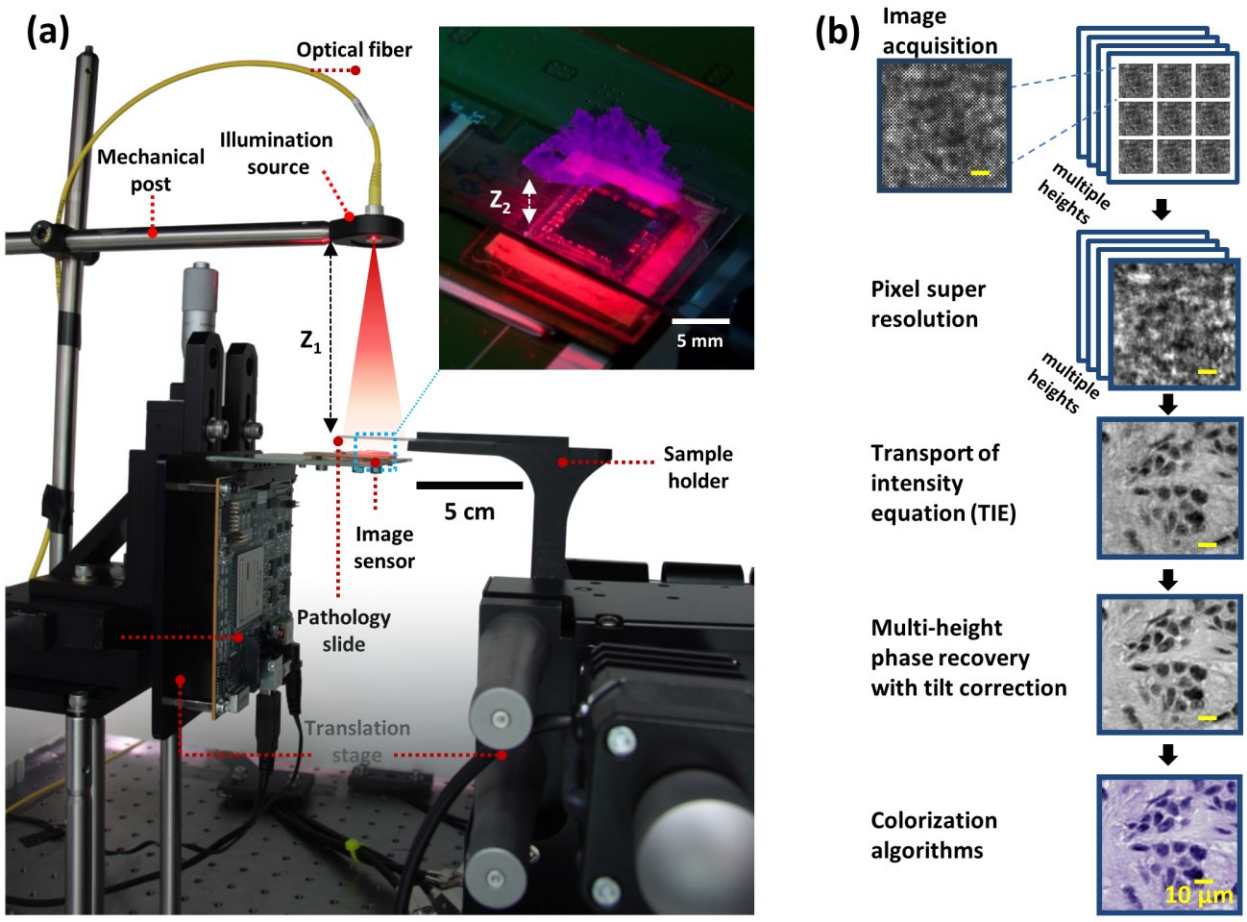

Figure 2. 1. Lens-free imaging experimental set-up and image reconstruction. (a) The set-up contained a partially coherent illumination source, a sample (a pathology slide), and an image sensor chip. **(b)** Block diagram of the image reconstruction steps.

The set-up of a lens-free on-chip microscope based on multi-height phase retrieval is shown in Fig. 2.1(a). The microscope was composed of a partially coherent illumination source (Fianium, 2 nm bandwidth), a scanning stage (Thorlabs, NanoMax 606), a CMOS image sensor chip (Sony, IMX081, with 1.12 µm pixel size), and a computer that controlled the set-up (Dell, Optiplex 9010). The pathology slide of interest was mounted on the stage through a 3D-printed sample holder, and

was illuminated to project an in-line hologram onto the sensor chip, whose intensity was recorded and saved to the computer for digital processing. The distance from the light source to the sample (z_1) was 7-20 cm, while the distance from the sample to the image sensor (z_2) was 100-800 μm. Owing to the fact that $z_1 >> z_2$, the magnification of the hologram plane with respect to the object plane is unit [62], enabling a sample FOV as large as the active area of the image sensor chip, which is 20.5 mm^2 for the CMOS sensor used in this work, but can be as large as ~18 cm^2 for a CCD image sensor [13]. As a result of this unit magnification and the finite pixel-size of the image sensor, spatial under-sampling imposed a major limitation on the smallest resolvable feature and our image quality. This finite pixel-size not only limited the highest spatial frequency that was recorded, but also introduced errors due to spatial frequency aliasing. To mitigate this problem, a pixel super-resolution technique was implemented to reduce the effective pixel-size of the image sensor and prevent sampling errors [56–58,71,72]. By capturing a number of low-resolution holograms at sub-pixel shifts with respect to each other, the number of sample points is increased and the pixel-size is equivalently reduced.

Instead of using a highly coherent source (e.g. a laser with very narrow bandwidth) that is typically used in holographic imaging, a partially coherent illumination source is adopted in our case to reduce noise due to speckle and multiple-reflection interference. Note also that because of the small distance between the sample and sensor planes, this limited (i.e., partial) temporal coherence of our illumination does not pose a resolution limit for our reconstructed images. The stage was programmed to first apply sub-pixel lateral shifts to the specimen on a 6×6 or 8×8 orthogonal grid, and then moved incrementally in the z-direction to reach the next height. This process was repeated for multiple heights (typically eight) generating a 3D stack of lens-free

images, which were fed to the image-processing algorithm for pixel super-resolution synthesis and multi-height phase reconstruction (Fig. 2.1(b)).

Analytical phase retrieval using the TIE

TIE (Eq. (2.1)) is an elliptic partial differential equation derived based on the wave equation, which relates the phase of the optical wave to its intensity and the intensity derivative long the propagation direction [60]:

$$\frac{\partial I(x,y)}{\partial z} = -\frac{\lambda}{2\pi}\nabla_{\perp}\cdot\left(I(x,y)\nabla_{\perp}\varphi(x,y)\right) \tag{2.1}$$

where $\nabla_{\perp} = \left[\frac{\partial}{\partial x}, \frac{\partial}{\partial y}\right]$, I is the intensity of light, and φ is the phase of light. Therefore, if I and $\partial I/\partial z$ can be obtained, the phase can be solved for.

In our work, the intensity derivative along the axial direction is approximated by the differentiation of intensity measurements at two different heights divided by the distance between them. The first height is picked as the lowest one, and the second height is picked among the other heights so that they are separated by approximately 100 μm with respect to each other. TIE is solved using a finite element method based elliptic equation solver [73,74]. Owing to the fact that the phase at the boundary is difficult to measure in practice, we tapered the intensity derivative gradually to zero at the edges using a Tukey window and assumed a zero Dirichlet boundary condition at the edges of the aperture. The output of the equation solver was fed to the multi-height phase retrieval algorithm as the initial guess for the optical phase. To increase the speed of the TIE solver, a faster solution to the TIE can also be generated using a fast Fourier transform (FFT) based approach, but it is in theory less accurate than the elliptic equation solver owing to its periodic assumption of the boundary conditions [67,75]. Note, however, that this FFT-based method does

not introduce any visible degradation of the reconstructed image quality compared to elliptic equation solver.

Multi-height phase recovery using the initial phase guess generated by TIE

The "conventional" iterative multi-height phase retrieval algorithm works by assuming an initial phase guess for the complex optical field and propagating it back and forth among different heights, where at each plane the amplitude of the current guess is averaged with the amplitude of the super-resolved hologram (i.e., the measurement), while keeping the current status of the phase. In each iteration, the algorithm started from the lowest plane to the highest one, processing all the heights in between, and then went backwards. As the iterations proceeded, the twin image artifact that was inconsistent from one height to another was gradually removed and the estimate of the true complex field persisted (in other words, convergence was achieved). Typically eight heights, with vertical separations of ~15 μm between adjacent heights, and 10-20 iterations were used to achieve convergence; nevertheless, as few as 3-4 heights can also generate satisfactory results.

In this iterative algorithm, which can also be broadly referred to as "error-reduction algorithm", the initial phase guess of the complex field is important, and it would affect the processing time required for convergence. A simple initial guess can be taken using the amplitude of the super-resolved hologram at the lowest height with zero-phase; however, a better guess can be generated using TIE. The TIE performance is typically limited by the low-numerical-aperture assumption, imperfect knowledge of axial derivative of intensity, relatively high susceptibility to noise, and the need for the knowledge of the phase at the perimeter of the aperture, which is usually not available [60,76]. Note, however, that we only used the TIE solution for the initial phase guess to our iterative multi-height phase retrieval algorithm, and therefore our images were not affected by the low-resolution Fresnel approximation that is inherent to TIE. Although for relatively sparse

and less connected objects, TIE solution might not always be needed; for dense and connected objects, such as histopathology slides, it provides convergence advantages.

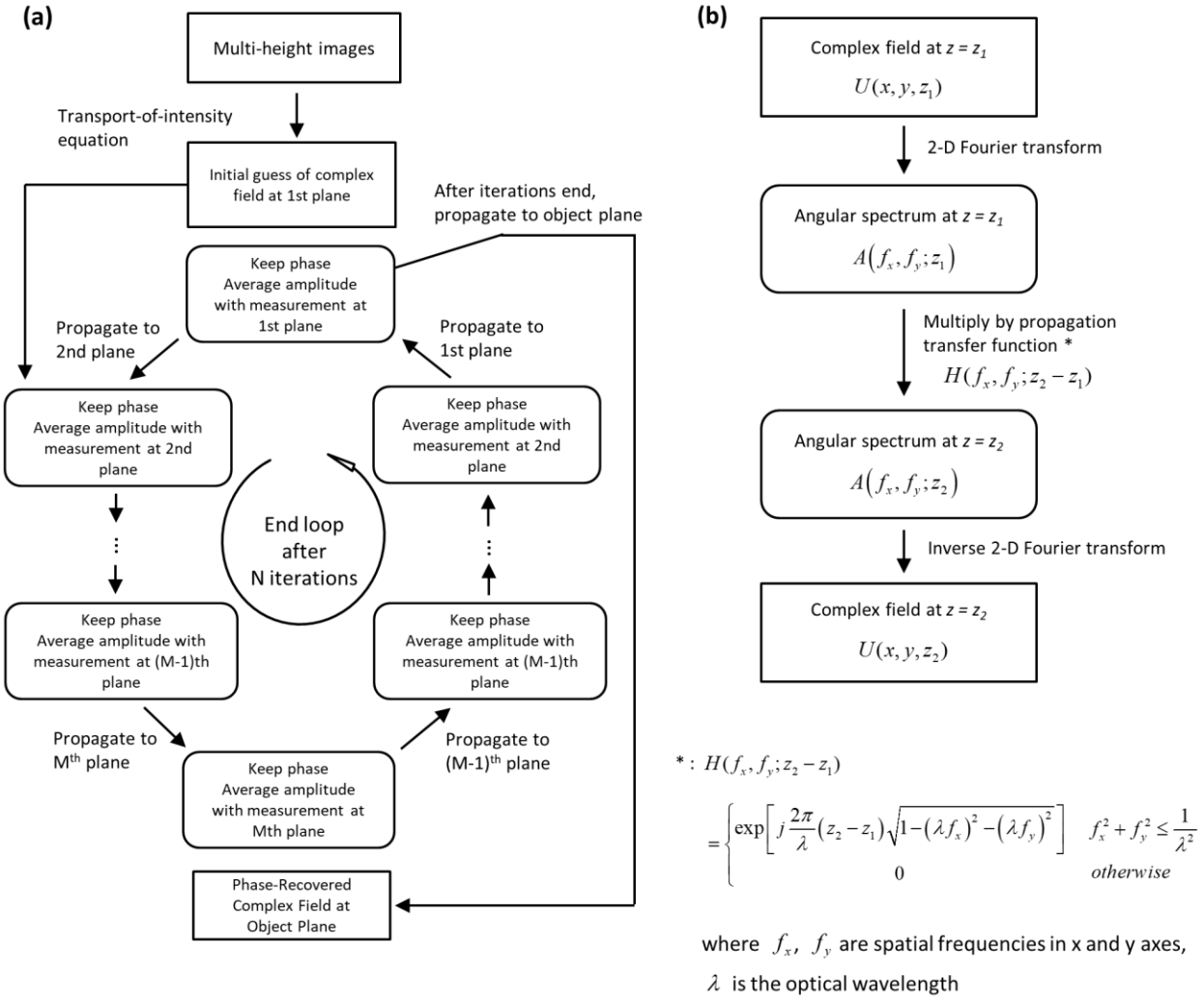

Figure 2. 2. Block diagrams of multi-height phase retrieval and wave propagation algorithms. (a) Block diagram of multi-height iterative phase retrieval algorithm. The pixel super-resolved multi-height image stack is fed to the algorithm as input. TIE is used to generate an initial guess of the complex field. Then the current guess of the complex field is iteratively propagated (using the algorithm outlined in (b)) from plane to plane, where in each plane, the resulting phase is retained while partially updating the amplitude according to the measurement acquired in the corresponding plane. After N iterations (usually $N = 10$), the loop ends, and the complex field is propagated to the object plane to yield the complex image of the specimen. **(b)** Block diagram of the wave propagation algorithm between parallel planes.

The flow chart of the phase recovery algorithm that combines TIE and the iterative phase retrieval method is illustrated in Fig. 2.2.

Field transformations among tilted planes

Rotational transformation of a complex optical field is a computational method that enables the reconstruction of an image on arbitrary tilted planes using the phase information of an optical wave [77–80]. For example, when trying to image a tilted surface using a bright-field microscope, the microscope user has to constantly refocus the microscope at different locations within the FOV. However, if one has access to the complex field information, the entire sample can be digitally focused all at once using rotational transformations. This method is computationally inexpensive as it involves two FFT operations and a single interpolation step in the Fourier domain [80,81]. To implement it, and to digitally focus the entire FOV of our lens-free on-chip microscope, the local tilt angles between the image sensor and the sample need to be determined. We automatically estimate these local tilt angles by utilizing the autofocus algorithm at different spatial locations on the sample FOV and finding their absolute heights. We can then fit a plane to match these heights (see, e.g., Fig. 2.3(c)), using which the tilt angles can readily be found and a 3D rotation transformation matrix can be built for implementing the needed local field transformation. This interpolation method in the frequency domain was implemented in C language to minimize the processing time.

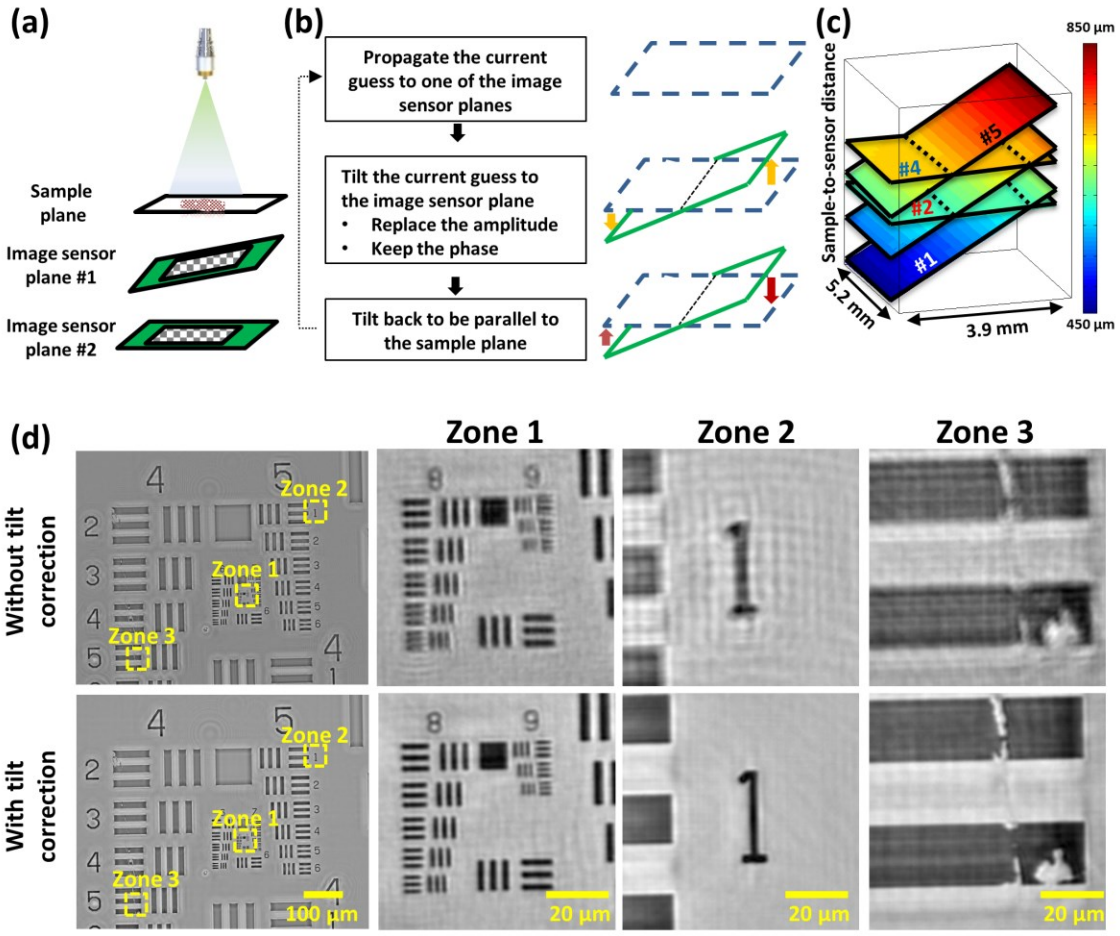

Figure 2. 3. Computational tilt correction in multi-height phase-recovery algorithm. (a) When using a low-end stage to mechanically modulate the sample-to-sensor distance, mechanical tilts between the sample and the image sensor planes might occur as illustrated in the schematic drawing. **(b)** A modification of the multi-height phase-recovery algorithm, which corrects for mechanical tilts between the sample and the image sensor planes. **(c)** Sample-to-sensor distances at five different heights, when the tilt angle between the planes alternated between 3.5˚ to 0.2˚. This experiment represents a poorly aligned lens-free imaging set-up and these tilted measurements are used to reconstruct images shown in (d). **(d)** Lens-free amplitude images reconstructed with or without tilt correction. Zoomed-in images of zones 1-3 are shown to the right.

Multi-height phase recovery with tilt correction

To take into account the tilts between the image sensor and the sample planes we modified the multi-height phase recovery algorithm. First, the tilt angles between different planes are evaluated

using our autofocus algorithm. Second, the multi-height phase recovery process is evoked without tilt correction for ten iterations. The result of this previous step serves as an initial guess for the modified multi-height algorithm. In this modified algorithm (Fig. 2.3(b)), the current guess is still propagated among different measured planes, however, after the propagation step the current guess (blue dashed rectangle) is projected to the tilted image-sensor plane (green solid rectangle) using the rotational transformation discussed earlier. The tilted current guess is then registered to the measured hologram. After the registration step, the tilted current guess amplitude is averaged with the measured amplitude, while the phase of the current guess is maintained for the next cycle of iterations. After this step, the current guess is rotated back to a parallel plane (blue dashed rectangle) and it is digitally propagated to the next measured plane/height until convergence is achieved, which usually takes 10-20 iterations.

Sample preparation and acquisition

All the pathology slides that were imaged in this paper were anonymous and provided by a vendor or a third party without any patient related information. The human adenocarcinoma of breast sample (H&E stained, Fig. 2.4), the normal human blood smear (Wright's stain, Fig. 2.7) and the human sickle cell anemia smear (Fig. 2.7) were acquired from Carolina® (Item # 318766, #313158 and #317374 respectively). The human carcinoma of the breast slides (H&E stained, Fig. 2.5 and Table 2.1) were acquired from the Translational Pathology Core Laboratory (TPCL) at UCLA, with de-identified surgical pathology reports. The Pap smears slides (SurePath™ and ThinPrep® preparations, Figs. 2.6 and 2.8(a)) were de-identified and provided by UCLA Department of Pathology (IRB #11-003335). The extreme USAF resolution test target (Fig. 2.8(b)) was purchased from Ready Optics (Item# 2012B).

2.3 Results and discussion

Imaging human invasive ductal carcinoma cells

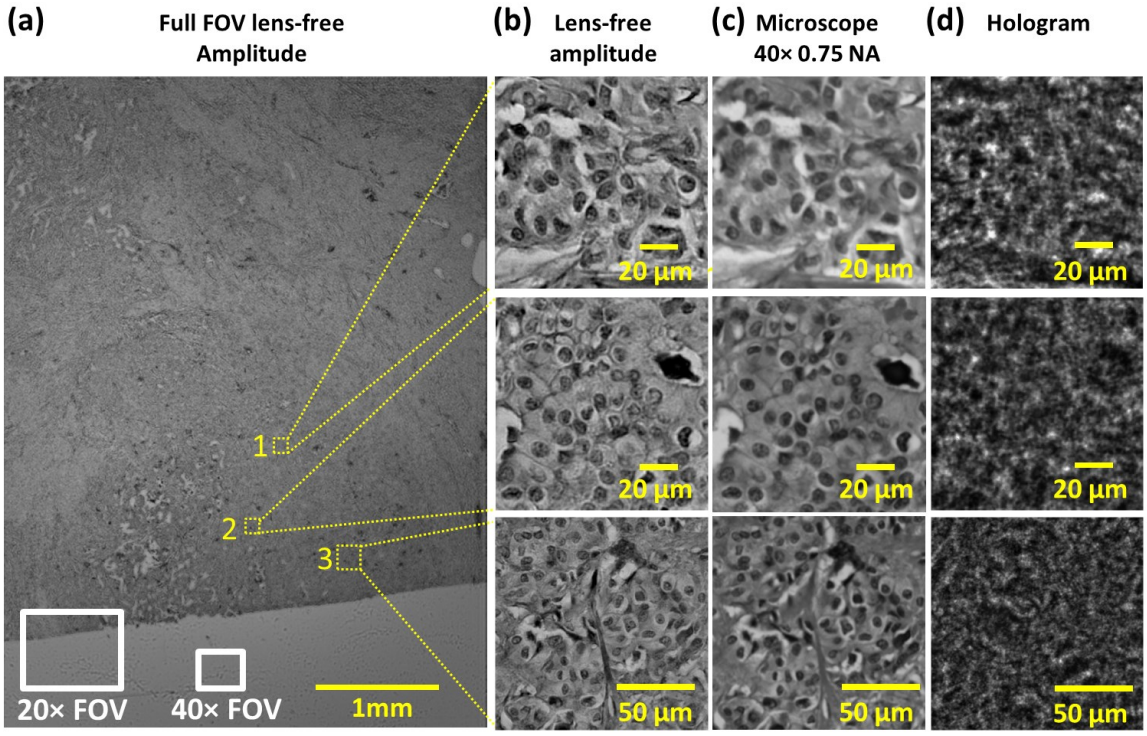

Figure 2. 4. Lens-free imaging of invasive ductal carcinoma of the human breast. (a) A full FOV (20.5 mm^2) lens-free amplitude image of the specimen (~7 µm thick). For comparison, the FOVs of 40× and 20× microscope objectives are shown using white solid rectangles. **(b)** Zoomed-in regions outlined by dotted yellow squares in the lens-free image in (a), which show atypical disordered epithelium. The cells exhibited nuclear enlargement, irregular nuclear contours, open chromatin, and moderate delicate cytoplasm. **(c)** Microscope comparison images of (b) taken with a 40× objective lens (0.75 NA). **(d)** The super-resolved lens-free holograms before digitally reconstructed to yield the images shown in (b).

To demonstrate that our lens-free, holographic, on-chip technology can properly image histology slides, we chose to image a tissue slice 7-µm thick from a patient with breast adenocarcinoma. Fig. 2.4(a) shows a full FOV reconstruction (FOV = 20.5 mm^2) of the slide, where the lens-free holograms that lead to this reconstruction are highlighted in Fig. 2.4(d). To

emphasize the wide FOV of lens-free imaging compared to traditional lens-based microscopy, the digital fields-of-view of 40× and 20× microscope objectives are also shown in Fig. 2.4(a) (note that these rectangular FOVs for lens-based digital microscopes are estimated as the upper bounds, assuming a camera adapter with unit magnification). Using the lens-free reconstructed images (Fig. 2.4(b)) a pathologist confirmed atypical disordered epithelium. The cells exhibited nuclear enlargement, irregular nuclear contours, open chromatin, and moderate delicate cytoplasm. All of these observations made by the pathologist were also in agreement with the 40 × microscope objective images (NA=0.75) taken to validate the pathologist diagnosis (Fig. 2.4(c)).

Note that the lens-free image shown in Fig. 2.4 was acquired using a single illumination wavelength (λ = 532 nm), and that is why it is mono-color. However, as will be detailed next, a pseudo-color mapping can digitally generate lens-free color images.

Pseudo-colored lens-free images of invasive human carcinoma cells

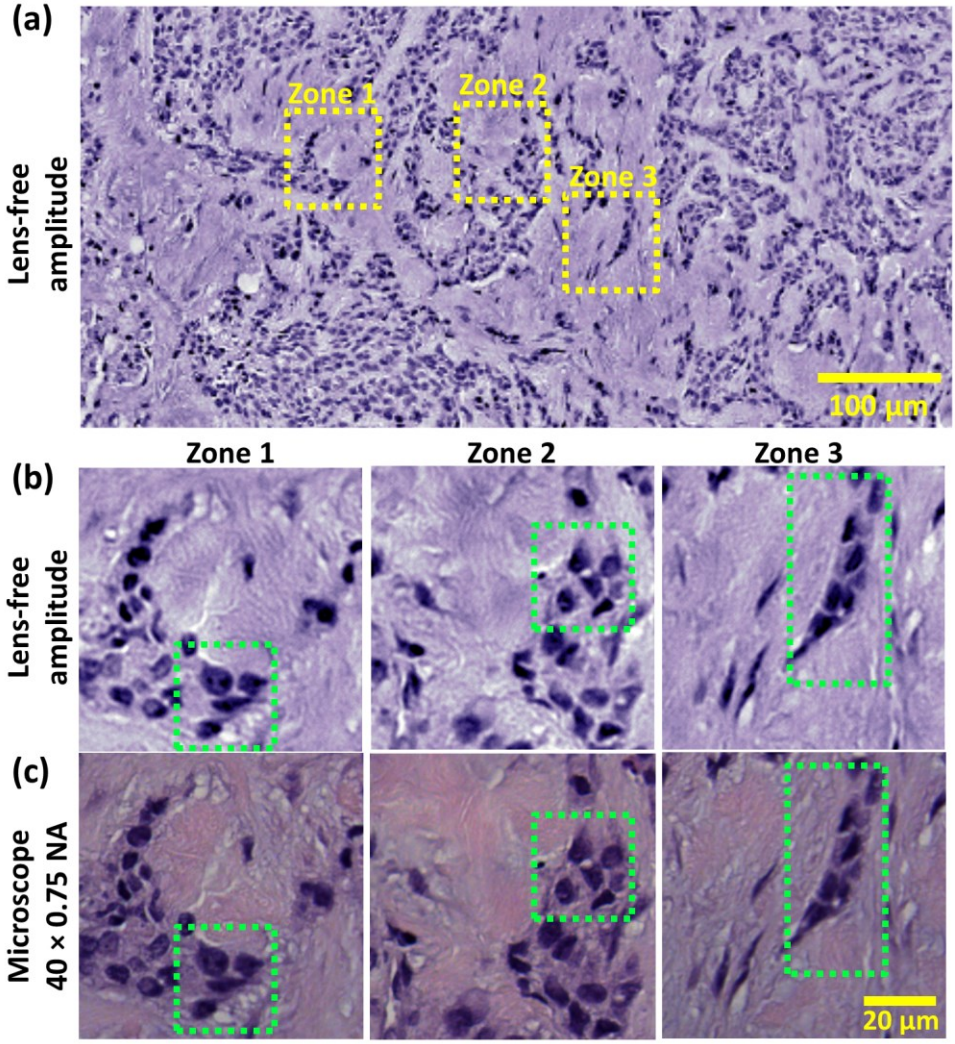

Figure 2. 5. **Lens-free pseudo-color image of human carcinoma of the breast. (a)** Lens-free amplitude image that shows invasive carcinoma cells arranged in irregular nests within the connective tissue. The image was captured using a single illumination wavelength (λ = 550 nm) and automatically colored using a transformation that maps intensity to color. **(b)** Zoomed-in lens-free amplitude images of zones 1-3 outlined in (a). The cells within the dashed green boxes are invasive carcinoma cells with increased nuclear to cytoplasmic ratios, hyperchromasia, irregular nuclear contours, and scant cytoplasm. **(c)** Microscope comparison images of (b) taken with a 40 × objective lens (0.75 NA). Scale bars in (b and c), 20 µm.

After establishing that lens-free, on-chip microscopy provides high-quality images of connected tissue samples over a large FOV, we next imaged a 4-μm thick tissue section from a patient with breast carcinoma (Fig. 2.5). Although the raw lens-free image was captured using only one illumination wavelength, we digitally colorized the reconstructed image using a transformation that maps intensity to color through prior learning statistics. This color transformation is built once by finding the average color for each intensity value in a set of microscope images, then by matching the histograms of the lens-free images to the learning set and having each gray-scale value mapped to a unique color. In this method, because all holograms were captured at a single wavelength, the image acquisition time was equal to the mono-color case and there is no need for a multi-wavelength experiment. The initial learning step needs to be carried out *only once* for a specific stain-tissue combination, and therefore new samples of the same type can be rapidly colored using the same mapping function. Fig. 2.5 illustrates a pseudo-colored lens-free image of carcinoma cells invading a connective tissue region. A pathologist examining the lens-free reconstructed color image noted that the cells were arranged in irregular nests within the connective tissue (green dashed rectangles in Fig. 2.5(b)). Each nest contained cells that exhibited increased nuclear-to-cytoplasmic ratios, hyperchromasia, irregular nuclear contours, and scant cytoplasm. After examining our lens-free reconstructed color images shown in Figs. 2.5(a, b), the same pathologist later verified her diagnosis by examining the same FOVs using 40× microscope images shown in Fig. 2.5(c).

Blinded test with a board-certified pathologist to quantify the diagnostic accuracy using the images from a lens-free microscope

To quantitatively evaluate the ability of a pathologist to diagnose cancerous breast tissue based on our lens-free colored images we have also performed a blind test. The tissue slides that we

Table 2. 1. Quantitative comparison of diagnosis accuracy of breast tissue using conventional and lens-free on-chip microscopy. A board-certified pathologist reviewed and diagnosed 150 images of breast tissue taken by a conventional and lens-free microscope. Three clinical conditions were selected: benign, atypical/DCIS and invasive carcinoma.

Diagnosis		Board-certified pathologist		Accuracy (%)
		Correct	Incorrect	
Benign	Conventional microscope	25	0	100
	Lens-free microscope	24	1	96
Atypical/DCIS	Conventional microscope	25	0	100
	Lens-free microscope	25	0	100
Invasive carcinoma	Conventional microscope	25	0	100
	Lens-free microscope	25	0	100
Total		149	1	99.3

used in this study were separated into three groups: (i) benign, (ii) atypical with ductal carcinoma in situ (DCIS) and (iii) invasive carcinoma. From these slides 25 different FOVs for each clinical condition were imaged and digitized by a conventional bright field microscope as well as our lens-free microscope, creating a total of 150 images. To quantify the correlation in breast tissue diagnosis between conventional and lens-free microscopy two blind tests (one for each imaging platform) were administered to a board-certified pathologist. The results of this comparison, as summarized in Table 2.1, revealed that the pathologist had only one false positive diagnosis using our lens-free images, and all the rest of her decisions matched the anonymous pathology surgical reports provided by the vendor of the slides, yielding an overall accuracy of ~ 99%.

Lens-free color images of a Papanicolaou (Pap) smear

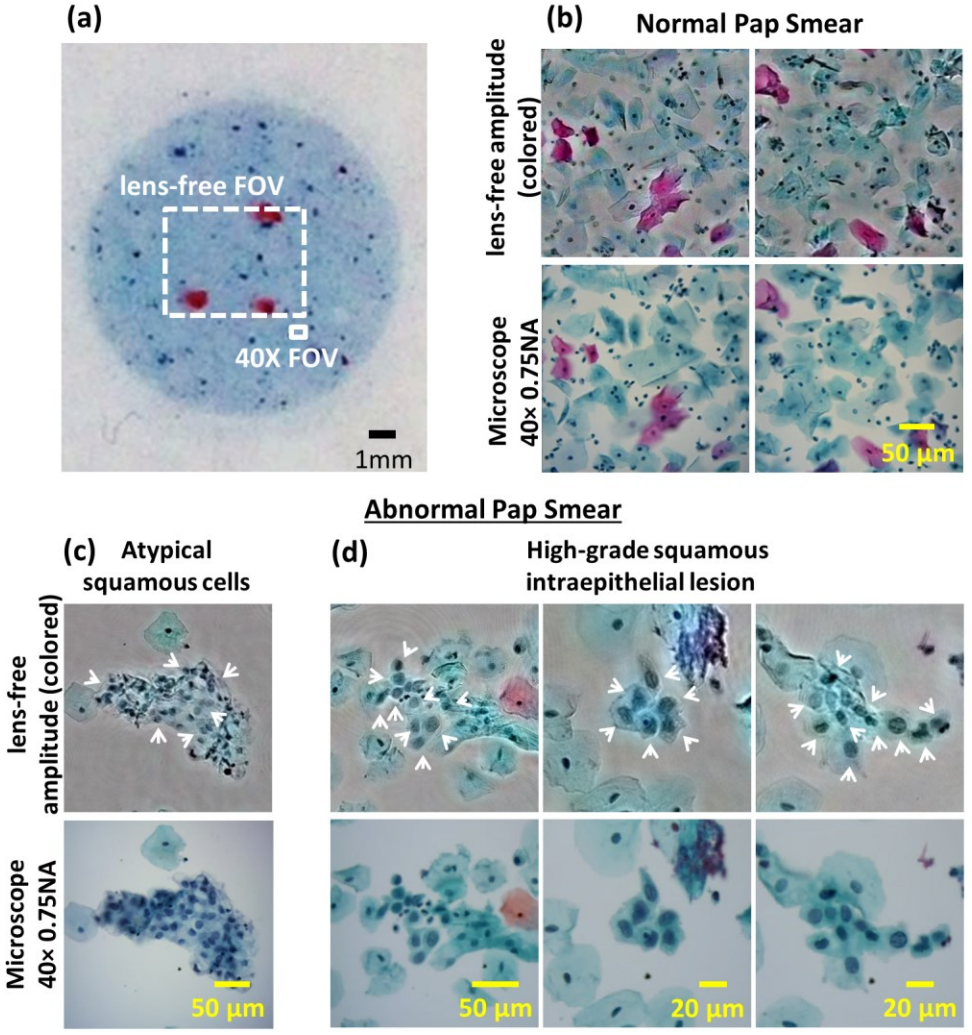

Figure 2. 6. **Lens-free color imaging of normal and abnormal Papanicolaou (Pap) smears. (a)** A photograph of a normal Pap smear slide (SurePath™ preparation). For comparison, the FOV of our lens-free microscope and of a bright field microscope equipped with a 40× objective lens were marked by a dashed and a solid rectangle, respectively. **(b)** Lens-free images of a normal Pap smear taken from the smear in (a), and their microscope comparison images taken with a 40× (0.75 NA) objective lens. **(c, d)** Abnormal Pap smears. **(c)** A lens-free color image of atypical squamous cells. The white arrows mark a cluster of squamous epithelial cells with nuclear crowding, increased nuclear to cytoplasmic ratios, and slightly irregular nuclear contours. **(d)** Lens-free color images that show cells with high nuclear-to-cytoplasmic ratios, markedly irregular nuclear contours, hyperchromasia, and scant cytoplasm (white

arrows). These findings are consistent with a high-grade squamous intraepithelial lesion. Microscope comparison images of (c, d) taken with a 40× objective lens (0.75 NA) are shown directly below the holographic images.

Cervical cancer screening would benefit from high-throughput and cost-effective imaging solutions, especially in resource-limited clinics. The pathologist or cytotechnologist is required to mechanically scan, using a light microscope, large-area (at least 0.8 cm^2, depending on the sample preparation technique) Pap smear samples in search for pre-cancerous cells. The large 20.5 mm^2 FOV of our lens-free imaging technology could assist the pathologist to minimize the mechanical scanning (Fig. 2.6(a)). Moreover, when a suspicious cell is detected, the pathologist typically refocuses the objective lens to different depth slices within the suspicious cell, to better assess the cell's morphology before classifying the cell. Lens-free holographic imaging can address this need because it possesses the ability to digitally focus the sample image to different depths after the image capture using the reconstructed complex wave of the specimen, which includes both phase and amplitude information of the object.

Lens-free images of a normal Pap smear and their conventional microscope comparison images are shown side by side in Fig. 2.6(b). Two different abnormality types of Pap smears imaged from two different pathology slides were confirmed by a pathologist using lens-free holographic imaging (Fig. 2.6(c, d)) (ThinPrep® preparation). In Fig. 2.6(c), white arrows mark a cluster of squamous epithelial cells with nuclear crowding, increased nuclear-to-cytoplasmic ratios, and slightly irregular nuclear contours. In Fig. 2.6(d), the white arrows mark the cells that show high nuclear-to-cytoplasmic ratios, irregular nuclear contours, hyperchromasia, and scant cytoplasm. These cellular features were consistent with a high-grade squamous intraepithelial lesion, as noted by the pathologist who first diagnosed the sample using our lens-free amplitude images and then verified this conclusion by inspecting the 40× microscope images of the same FOV.

In addition to using a mathematical transformation to digitally color lens-free holographic images as described for Fig. 2.5, the colorization technique that we used here was based on YUV color space averaging [54]. In the YUV color space, the color information is separated from brightness, therefore allowing color manipulation without compromising the spatial resolution of the brightness channel. Consequently YUV color space enables averaging out spatial color artifacts that are common in some holographic imaging approaches [82,83]. For unknown specimens that the color map transformation approach presented in Fig. 2.5 could not be immediately applied due to lack of prior statistics, this YUV color space averaging approach can be used as a viable digital colorization approach in lens-free imaging.

Lens-free imaging of whole blood smears

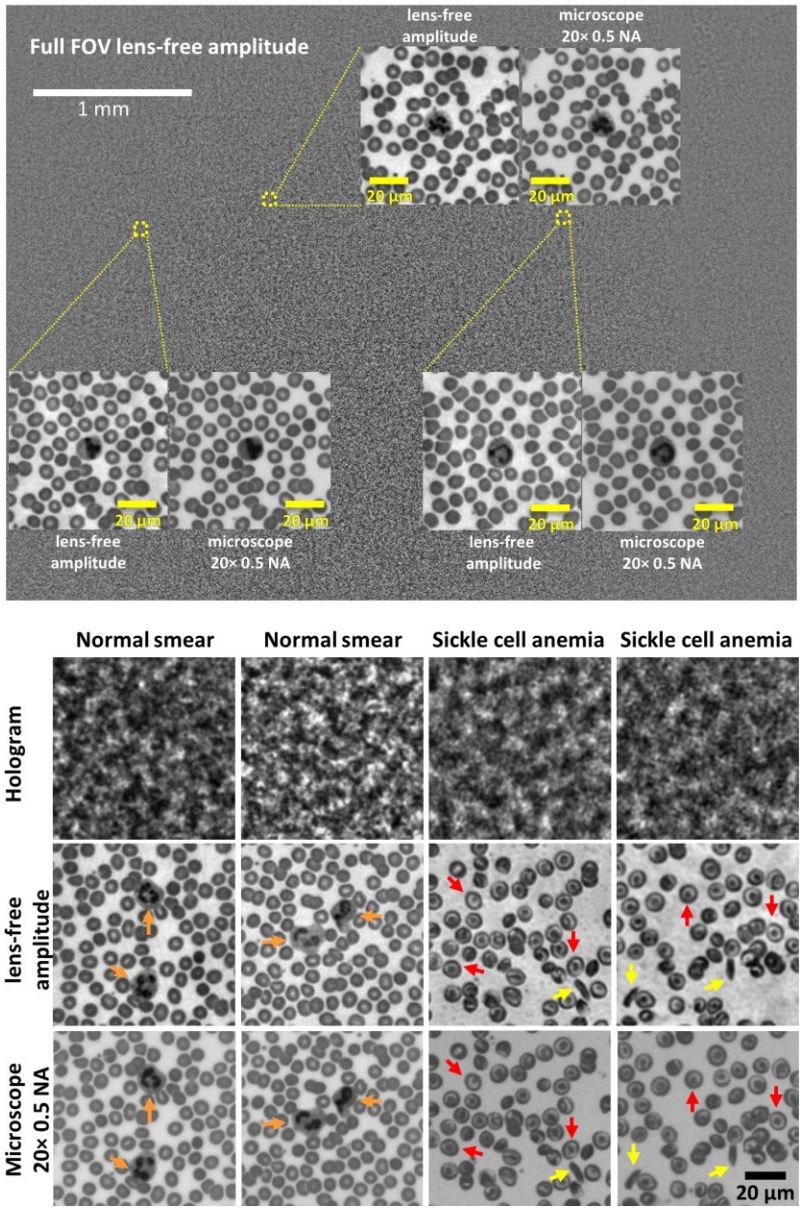

Figure 2. 7. **Lens-free imaging of normal and sickle cell anemia blood smears.** Top panel, full FOV amplitude images and zoomed-in regions of normal red and white blood cells and their 20× objective lens (0.5 NA) microscope comparisons. Bottom panel, super-resolved lens-free holograms before and after reconstruction. Normal white blood cells can be seen amidst normal red blood cells. In contrast, yellow arrows mark abnormal (sickle) red blood cells, while the red arrows mark target cells (exhibiting a bullseye appearance), which are typical for hemoglobinopathy disease. For comparison, 20× objective lens (0.5 NA) microscope images are shown directly below their holographic lens-free counterparts. Scale bars, 20 µm.

Blood smear is still considered as one of the standard methods to identify immature or abnormal cells that are indicative of various diseases, such as anemia, hemoglobin variants, and bone marrow disorders [84]. Using our lens-free on-chip microscopy platform, we imaged normal and abnormal blood smears (Fig. 2.7). The image of the blood smear (Wright's stain) was reconstructed using eight different heights (393, 411, 431, 448, 467, 484, 500, and 516 μm) and 10 multi-height phase-recovery iterations. The phase solution of TIE was used as an initial guess for the multi-height phase recovery algorithm. However random the lens-free holograms appeared before reconstruction, our reconstruction technique was able to transform these holograms to valuable images that matched visibly the microscope comparison images (Fig. 2.7). In the normal smears, mature red blood cells had uniform diameters of ~7 μm, were shaped as donuts (round with an indentation in the middle), and did not have a nucleus. In abnormal smears taken from a patient with sickle cell anemia, red blood cells that were spindle-shaped ("sickled", yellow arrows) and target cells that show a dark spot in the middle of the cell surrounded by a bright ring (red arrows) were observed. The lens-free microscope resolution also enabled the identification and classification of white blood cells present in the blood smear (Fig. 2.7).

The use of TIE to generate an initial guess

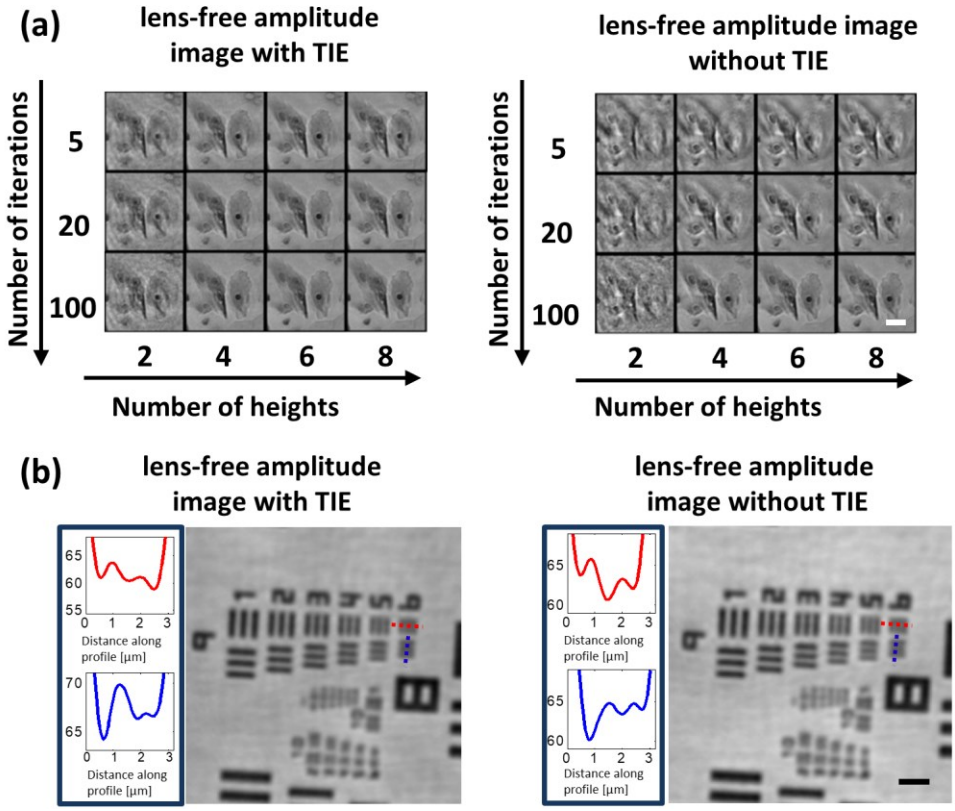

Figure 2. 8. **The effect of TIE solution on multi-height phase recovery algorithm convergence and spatial resolution. (a)** Reconstructed lens-free amplitude images as a function of the number of heights and the number of iterations. TIE or zero-phase was used as an initial phase guess for the multi-height phase-recovery algorithm. Scale bar, 20 µm. **(b)** Resolution quantification using extreme USAF test chart with and without TIE solution as an initial phase guess for the multi-height phase recovery algorithm. Green illumination wavelength (λ = 532 nm) was used to illuminate the sample and the last resolved gratings are with a line-width of 548 nm (group 9, element 6). Horizontal and vertical cross sections that show the modulation of the last resolved gratings are located to the left of each lens-free image. Scale bar, 5 µm.

In our reconstruction process, the convergence of image recovery depends on the quality of the initial phase guess. Rather than selecting a zero or random initial phase guess (which has been the standard practice [55,59,67,68,85]), here we digitally solved TIE, which provided an analytical

solution [10,60,76] to the phase of an optical wave from a series of defocused intensity images. As is shown in Fig. 2.8(a), the use of TIE dramatically reduced the number of iterations necessary for the algorithm to converge.

To validate that our spatial resolution is not compromised using TIE initial phase, we imaged extreme-USAF test chart (Ready Optics, item# 2012B), where the last element of group 9, which corresponds to a grating line-width of 548 nm, was successfully resolved using $\lambda = 532$ nm (see Fig. 2.8(b)).

The use of a low-cost axial translation stage

Fig. 2.3 depicts the challenge of using a low-end axial translation stage, e.g., with a cost of ~$10-20: each recorded hologram at a given height exhibits a different tilt between the axially translated sensor-chip and the sample plane. These uncontrolled tilts result in distortions that are apparent in the reconstructed images as can be seen in Fig. 2.3(d) upper row. To digitally mitigate these distortions (after image capture), we utilize a *rotational field transformation* technique (see the Materials and methods Section), which is a computational method that can reconstruct a complex image on any arbitrarily tilted plane [77–80]. Fig. 2.3(b) depicts the inclusion of this rotational transformation in our multi-height phase-recovery algorithm, where the current guess of each iteration (blue dashed rectangle) is projected onto the image sensor plane (green solid rectangle) to enforce the measured intensity, while retaining the phase. This tilt correction step in the forward model of our algorithm is of paramount importance in order to reconstruct the phase of the optical wave. To test the robustness of this algorithm, we recorded five interference patterns using five highly tilted planes, mimicking a poorly designed experimental set-up that is even worse than the performance of a typical inexpensive 1D translation stage. A graph that shows the sample-to-sensor distances for these five heights can be seen in Fig. 2.3(c). Without the tilt correction, the

reconstructed images are severely distorted (see Fig. 2.3(d) upper row), in contrast with the lens-free images shown in Fig. 2.3(d) lower row, which used the tilt correction process as detailed in Fig. 2.3(b). Therefore, this computational tilt correction and sample height estimation approach enables cost-effective implementations of lens-free on-chip microscopy, digitally eliminating the need for expensive scanning hardware.

Discussion

Our results demonstrate that the lens-free system based on holographic imaging provides high-resolution images of patient samples that can be used by pathologists for diagnostics. The wide FOV not only provided two orders of magnitude improvement in throughput compared to a lens-based microscope of similar resolution, but also enabled digital focusing of the image plane to different depths - a highly desired attribute that would give pathologists more degrees of freedom in their examination of the samples, since often times different parts of the specimen appear in focus at different depths for large-area pathology samples. This 3D imaging performance cannot be achieved using other on-chip microscopes that are based on contact imaging [17,86] because complex optical fields cannot be retrieved using a contact imaging geometry, which demands the objects to be flat and parallel (with sub-micron gap) with respect to the plane of the sensor chip. Pathology samples and other medically relevant biological specimens naturally have 3D features, with uncontrolled modulation of the gap between the sample and sensor planes, both of which create spatial artifacts in contact or shadow imaging. On the other hand, since holographic on-chip microscopy retrieves complex optical fields of the objects, 3D nature of specimen and uncontrolled variations in tilt and height of the specimen can be digitally corrected.

In addition to its wide FOV and 3D imaging capability, one other advantage of lens-free on-chip holographic imaging is its cost-effectiveness and design simplicity compared to a lens-based

pathology microscope. In the current set-up, we used a mechanical positioning stage mainly for two reasons. First, the positioner laterally shifts the sample for pixel super-resolution; this function of the stage can be replaced by source shifting using, for instance, an array of laser diodes (LDs) or light-emitting-diodes (LEDs), which is a cost-effective solution for achieving pixel super-resolution as we reported previously [31,56,59]. Furthermore, in our reconstructions we use an algorithm to automatically determine the relative sub-pixel shifts of each lens-free hologram, without the need for a measurement or reading from the scanning system; therefore, even a simple and inexpensive mechanical stage would work for implementing pixel super-resolution. Second, the mechanical stage was used to modulate and control the sample-to-sensor distance (Fig. 2.1(a)), so that we could capture several defocused interference patterns for our multi-height phase recovery algorithm. However, for this purpose, a simple and inaccurate one-axis translation stage is sufficient because we digitally estimate the sample-to-sensor distance as well as uncontrolled tilts of the sample using an autofocus algorithm with ~1 μm precision, without the need for stage readings. This method offered a simple way for finding the focus in an automated fashion without the need for any feedback or quantified measurement from the scanning stage or the experimental set-up, which released the alignment and complexity requirements of the system. In fact, we modified our multi-height phase recovery algorithm to digitally compensate for these uncontrolled tilts and variations in sample-to-sensor distances along our FOV, which permitted the use of a low-cost 1D translation stage (Fig. 2.3).

All the pathology slides reported in this work are reconstructed using 288 raw lens-free images (36 holograms per height to perform pixel super-resolution, and 8 heights to perform multi-height phase recovery), which can be translated into image acquisition times that are on the order of several seconds using the maximum frame rate of our opto-electronic image sensor chip (15 frames

per second). This image acquisition time can be improved using faster CMOS imager chips and/or pulsing of illumination source(s). However, for pathology applications, this is not a limiting factor because the pathology slides are fixed. In terms of the image reconstruction time, using MATLAB and eight measurement heights, the entire processing time of a 1 mm × 1 mm sub-FOV took about 4.5 minutes using a single desktop computer (Dell T3600, 16GB RAM memory and Intel Xeon processor E5-1620). Because all the reconstruction steps can be processed in parallel for different sub-FOVs, using a cluster of 20 nodes (quad-core machines), the entire FOV reconstruction can be performed within ~4.5 minutes. A cluster of Graphics Processing Units (GPUs) instead of Central Processing Units (CPUs) would speed up the total reconstruction time by a factor of 10-20-fold, as our algorithms heavily rely on fast Fourier transforms [29]. Optimized algorithms running on more efficient software languages, such as C/C++, would also improve reconstruction times. Therefore, even with a single desktop computer using GPUs, the processing time for full FOV reconstructions can be reduced to less than a few minutes.

2.4 Conclusions

In this chapter, a multi-height-based phase retrieval method is developed for lens-free microscopy of pathology slides, enabling lens-free on-chip imaging of histological tissue sections for the first time. In the presented phase retrieval method, TIE is used to generated the initial guess of the optical phase, which is then fed to an iterative multi-height phase retrieval algorithm for refinement. A digital tilt correction module is incorporated into the multi-height iterative algorithm to mitigate artifacts resulting from random tilting between the sample and the image sensor. With these methods, high-resolution imaging results of human tissues with invasive carcinoma cells, a Pap smear, and whole blood smears contained sickle cell anemia are demonstrated, which match the images from a high-end 40× benchtop microscope. In addition, a

blind test was conducted with a board-certified pathologist, which demonstrated that the images coming from the lens-free microscope could facilitate a ~99% diagnostic accuracy. These results show that the lens-free microscope holds great promise to replace the conventional microscope in digital pathology tasks, especially in resource-limited settings.

Chapter 3. Improving the color accuracy of lens-free imaging of stained tissues and cells

Holographic microscopy presents challenges for color reproduction due to the usage of narrow-band illumination sources, which especially impacts the imaging of stained pathology slides for clinical diagnosis. In this chapter, an accurate color holographic microscopy framework using absorbance spectrum estimation is presented. This method uses multispectral holographic images acquired and reconstructed at a small number (e.g., three to six) of wavelengths, estimates the absorbance spectrum of the sample, and projects it onto a color tristimulus. Using this method, the wavelength selection is optimized to holographically image 25 pathology slide samples with different tissue and stain combinations to significantly reduce color errors in the final reconstructed images. The results can be used as a practical guide for various imaging applications and, in particular, to correct color distortions in holographic imaging of pathology samples spanning different dyes and tissue types.

Part of this chapter has been submitted for publication and is under review.

3.1 Introduction

Generation of images with accurate color reproduction is one of the key requirements for a digital pathology microscope to ensure reliable and consistent diagnoses [87–90]. Among other approaches, color images can be generated by a holographic microscope through the combination of three holograms acquired at three discrete wavelengths in the red, green, and blue regions of the visible light spectrum. The three intensity images are then placed into the R, G, and B channels of an RGB image ("direct RGB combination" method). In other words, the spectral transmittance or reflectance of the sample is *discretely* sampled at three chosen wavelengths and directly used to

compose a color image. However, this approach suffers from color inaccuracies [91] compared to the color perception of the human eye, which has broad responsivity curves according to the Commission Internationale de l'Éclairage (CIE) color matching functions [92].

Prior research on improving the color accuracy of holographic imaging has mainly focused on imaging generic objects and scenes in the reflection mode. For example, Peercy *et al.* improved the accuracy of color holography for the reconstruction of macroscopic scenes based on the Gaussian quadrature and Riemann summation methods, and provided an optimal wavelength selection, showing that four wavelengths could lead to a relatively accurate color reproduction [91]. Later, Ito *et al.* presented a spectral-estimation approach based on the Wiener estimation for accurate-color holography using laser illuminations at four wavelengths [93]. While these approaches have been applied to generic objects in the reflection mode, accurate-color holographic imaging of stained pathology samples in the transmission mode remains largely unexplored. Compared to the colors of generic objects that cover a large subspace of all possible colors, the colors that occur within a stained pathology slide are by and large constrained by the dye combination that is used to stain the slide. The combination typically consists of two or three dyes and is usually known *a priori*, before the slide is imaged [94]. Consequently, it is important to develop a method to achieve accurate-color holographic imaging of pathology slides with a smaller number of wavelengths as well as better color accuracy.

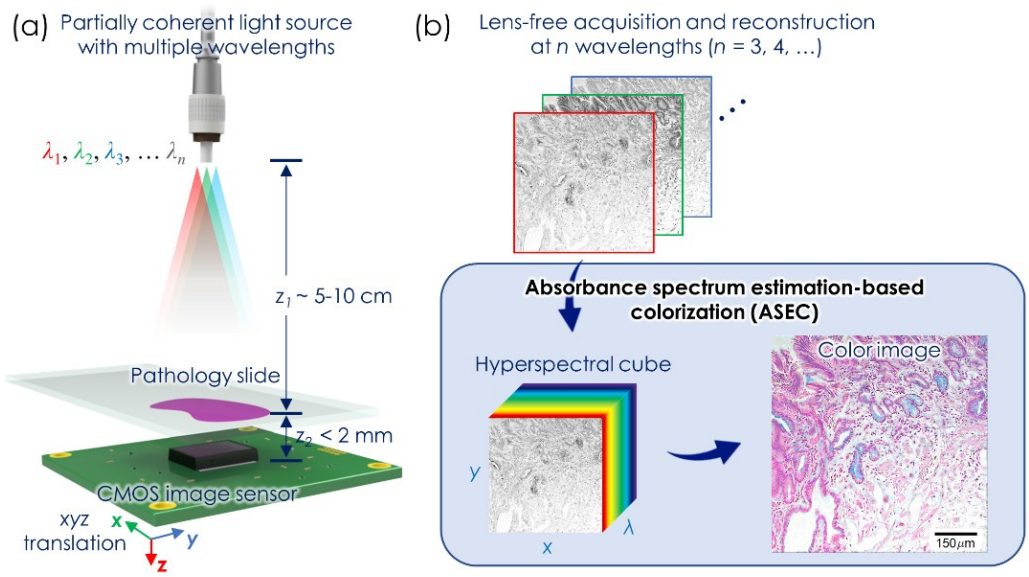

Figure 3. 1. Schematic of accurate-color lens-free holographic microscopy method. (a) Schematic of the optical setup. A partially coherent light source with multiple wavelengths illuminates the pathology slide simultaneously or sequentially (depending on the mode of operation). An image sensor is placed underneath the sample slide at a short axial distance (z_2 < 2 mm) to capture in-line holograms of the sample. **(b)** After the lens-free image acquisition and reconstruction, an absorbance spectrum estimation-based colorization (ASEC) method is applied, resulting in a color-accurate image of the sample.

In this chapter, an accurate-color holographic imaging method for pathology slide imaging is presented, which uses an absorbance spectrum estimation-based colorization (ASEC) technique. We demonstrate this technique using a lens-free on-chip holographic microscope (Fig. 3.1), but the method is broadly applicable to other holographic imaging systems. The imaging setup (Fig. 3.1(a)) uses a partially coherent source that emits narrow-band light centered at a single wavelength or multiple wavelengths *simultaneously* to illuminate the sample (e.g., a pathology slide). Further, the setup employs a complementary metal-oxide-semiconductor (CMOS) image sensor to capture the diffraction patterns (holograms) of the sample. The image sensor setup comprises a 3D translation stage to capture multiple holograms, which are processed with the subsequent pixel super-resolution (PSR) [31,48,53–56,59,95,96] and phase

recovery [35,45,55,59,70] algorithms to generate a high-resolution image of the sample under multiple illumination wavelengths. The images are then fed to the ASEC algorithm that has been pretrained on various tissue types and stains. The ASEC algorithm uses *a priori* information about the spectral statistics of each given tissue type and stain combination to estimate the absorbance spectrum of the sample at each pixel, yielding an estimated hyperspectral cube of the sample. This hyperspectral cube is then used to simulate the color response of the human eye to create a color-accurate holographic image [92].

Based on the ASEC framework, we performed wavelength optimizations for 25 pathology slides with different tissue–stain combinations using various numbers of wavelengths (n = 3, 4, 5, or 6), and tested the wavelength-optimized ASEC method on all 25 samples. The results show that using three illumination wavelengths (n = 3) is sufficient to create color-accurate reconstruction images of the samples. More wavelengths (n = 4, 5, or 6) further reduce color errors. In addition, it is demonstrated that the ASEC method can be applied in conjunction with wavelength-multiplexed holographic imaging using the demosaiced pixel super-resolution (DPSR) technique, which reduces the data acquisition time three-fold.

3.2 Materials and methods

Lens-free imaging setup

Fig. 3.1(a) shows a schematic of the optical setup, which is similar to the one in Fig. 2.1. A broad-band light source (WhiteLase Micro, NKT Photonics) filtered by an acousto-optic tunable filter (AOTF) with a spectral bandwidth of approximately 2.5 nm (full width at half maximum, i.e., FWHM) was used as illumination source. The AOTF supports simultaneously up to eight output channels at different wavelengths. All wavelength channels can be coupled into the same single-mode fiber. We directly used the emitted, uncollimated light from the single-mode fiber to

create quasi-plane-wave illumination for the sample (e.g., a pathology slide) with a light source-to-sample distance (z_1) of approximately 5–10 cm. A CMOS image sensor chip (IMX 081, Sony, pixel size of 1.12 μm) was placed below the sample with a small sample-to-sensor distance (z_2), which is typically < 2 mm. The CMOS image sensor was attached to a 3D positioning stage (MAX606, Thorlabs, Inc.). The translation was used for PSR [35,50,53,54,56,59], DPSR [48], and multi-height phase recovery techniques [35,44,54–56,59]. All the hardware was automatically controlled by LabVIEW.

Multispectral lens-free imaging at three wavelengths using wavelength multiplexing

The tunable light source was programmed to *simultaneously* output narrow-band light at three wavelengths, corresponding to the red, green, and blue regions of the visible spectrum [48]. The mechanical stage was programmed to shift the image sensor on a lateral 6 × 6 grid (step size of approximately 0.37 μm, corresponding to 1/3 of the pixel size) at each hologram acquisition height for DPSR and to N_z different heights for the multi-height phase recovery, where one "composite hologram" that results from the simultaneous three-wavelength illumination was captured by the image sensor at each of the $6 \times 6 \times N_z$ recording positions. The acquired data were then processed using DPSR, multi-height phase recovery, and ASEC, which will be detailed in the following subsections.

DPSR technique

While the color CMOS image sensor was being laterally shifted on a 6 × 6 grid with sub-pixel distances, a hologram was recorded at each position. These shifts do not need to be accurate because the actual amounts of shifting were precisely estimated using a shift estimation algorithm [46,48,50,53–56,59]. A shift-and-add based PSR method [35] was then used to synthesize four high-resolution pixel-super-resolved holograms; one for each color pixel in the

Bayer pattern (R, G_1, G_2, and B) with a resulting effective pixel size of approximately 0.37 μm [35]. Each of these four synthesized high-resolution holograms is a combined response resulting from the transmitted and diffracted light intensity at multiple wavelengths that was multiplied with the spectral responsivity of the corresponding pixel (R, G_1, G_2, or B). Demosaicing (i.e., demultiplexing) was conducted to remove the wavelength crosstalk by multiplying with the pseudoinverse of the "crosstalk matrix" [48]. The crosstalk matrix can be estimated from the three chosen wavelengths and previously measured spectral responsivities of the four-pixel types in the Bayer pattern; the two green pixels in the Bayer pattern, G_1 and G_2, have slightly different responsivities, as experimentally measured. The demosaicing process results in three high-resolution holograms without spectral crosstalk. The DPSR algorithm was accelerated using a graphics processing unit (GPU) and CUDA C++ programming.

Hologram autofocusing using the edge sparsity criterion

As will be further detailed in Chapter 4, the z-distance of a given hologram is automatically estimated through the maximization of the ToG focus criterion proposed in [97,98] as a function of the back-propagation distance. To accelerate the maximization process, we custom-wrote a search algorithm that consists of a rough scan, followed by the determination of a unimodal interval in the vicinity of the maximum and a golden-section search within the unimodal interval. More implementation details can be found in Chapter 4 and Ref. [97]. The autofocusing algorithm was accelerated using GPU and CUDA C++ programming.

Multispectral lens-free imaging through sequential wavelength scanning

The aforementioned wavelength-multiplexed lens-free imaging method is highly time- and data-efficient but mostly limited to three (or multiples of three) wavelengths that belong to the red, green, and blue regions of the visible spectrum, respectively [48]. An alternative approach to

perform multispectral (and hyperspectral) lens-free imaging at arbitrary wavelengths comprises the use of *sequential* multi-wavelength illumination, as opposed to simultaneous illumination at multiple wavelengths. At each scanning position during image acquisition for PSR and multi-height phase recovery, the wavelength-tunable illumination source was programmed to sequentially illuminate the sample at *n* wavelengths (one wavelength at a given time). The image at each wavelength was individually captured by the image sensor. The PSR and multi-height phase recovery algorithms were then applied to the data collected under each wavelength, respectively, to reconstruct the sample images at the regarding wavelength. As a special case, while performing hyperspectral imaging, the sequentially scanned illumination wavelength range spanned from 400 nm to 700 nm with a step size of 10 nm.

ASEC for holographic reconstruction of stained tissues and cells

In general, for a transmission-mode holographic imaging system that uses a single wavelength, the *reconstructed* light intensity $I(x, y)$ at the sample plane can be given by [99]

$$I(x,y) = \int S(\lambda) T(x,y;\lambda) R(\lambda) \mathrm{d}\lambda + \text{noise} \tag{3.1}$$

where λ is the optical wavelength, $S(\lambda)$ the spectral intensity distribution of the illuminant, $T(x,y;\lambda)$ the spectral transmittance of the object, and $R(\lambda)$ the spectral responsivity of a given type of image sensor pixel (R, G_1, G_2, or B). When the spectrum of the illumination source is relatively narrow (centered around λ_0) for a typical holographic system, while $T(x,y;\lambda)$ and $R(\lambda)$ are slowly varying functions of λ compared to the illumination light source bandwidth, Eq. (3.1) can be approximated as:

$$I(x,y) = S_0 T(x,y;\lambda_0) R(\lambda_0) + \text{noise} \tag{3.2}$$

where S_0 is the light intensity of the illuminant,

$$S_0 = \int S(\lambda)\,\mathrm{d}\lambda \tag{3.3}$$

The background, where no sample is present, has a transmittance equal to unity. Therefore, assuming noise is negligible, the background-normalized intensity $\tilde{I}$ of a sample can be written as:

$$\tilde{I} = \frac{I(x,y)}{I_{\text{background}}} \approx \frac{S_0 R(\lambda_0) T(x,y;\lambda_0)}{S_0 R(\lambda_0)} = T(x,y;\lambda_0) \tag{3.4}$$

which is equal to the transmittance of the sample at λ_0 and independent of the illumination source intensity and pixel responsivity.

For our wavelength-multiplexed holographic imaging system, we have n reconstructed images for n wavelengths. The reconstructed intensity at each wavelength can then be normalized on the sample plane by the empty regions to obtain the transmittance function, $T(x, y; \lambda_i)$ for $i = 1, 2, \ldots, n$. The absorbance can be calculated from the transmittance function using:

$$A(x,y;\lambda_i) = -\log_{10}\left[T(x,y;\lambda_i)\right] \tag{3.5}$$

To estimate the entire absorbance spectrum, the minimum mean-square error (MMSE) method based on the Wiener estimation was used [99,100]. Suppose we want to reconstruct the absorbance spectrum discretized at m wavelengths (e.g., $m = 31$ for spectral sample points at 400 nm, 410 nm, …, 700 nm), and we have available measurement data at n wavelengths (e.g., $n = 3$, 4, 5, or 6). The forward model, i.e., the spectral sampling operation, can be written as

$$\mathbf{g} = \mathbf{H}\mathbf{a} \tag{3.6}$$

where $\mathbf{g}$ is a $n \times 1$ vector representing the measured absorbance values at n different wavelengths (λ_i, i = 1, 2, …, n); $\mathbf{a}$ is the $m \times 1$ absorbance spectrum that we want to recover discretized at λ'_j, $j = 1, 2, \ldots, m$; $\mathbf{H}$ is an $n \times m$ "sampling matrix" - the elements of which are given by

$$h_{ij} = \begin{cases} 1 & \text{if } \lambda_i = \lambda'_j \\ 0 & \text{else} \end{cases} \tag{3.7}$$

The solution to the MMSE problem is given as [100]:

$$\hat{\mathbf{a}} = \mathbf{W}\mathbf{g} \tag{3.8}$$

$$\mathbf{W} = \mathbf{R}_{\mathbf{aa}}\mathbf{H}^{\mathrm{T}}\left(\mathbf{H}\mathbf{R}_{\mathbf{aa}}\mathbf{H}^{\mathrm{T}}\right)^{-1} \tag{3.9}$$

where $\mathbf{R}_{\mathbf{aa}}$ denotes the autocorrelation matrix of **a**. Refer to the following subsections and Eq. (3.12) for the process that is used to estimate $\mathbf{R}_{\mathbf{aa}}$. The estimated transmittance spectrum $\mathbf{t} = [t_1, t_2, \ldots, t_m]^{\mathrm{T}}$ can then be written as:

$$t_j = 10^{-\hat{a}_j} \tag{3.10}$$

where $\hat{a}_j$ is the j-th element of $\hat{\mathbf{a}}$ with $j = 1, 2, \ldots, m$. The color tristimulus can then be calculated from the estimated spectrum (see the following subsection).

Calculation of the color tristimulus from the transmittance spectrum of the sample

The tristimulus values, i.e., XYZ values [92], can be calculated from the transmittance spectrum of the sample using:

$$\begin{aligned} X &= \int \bar{x}(\lambda)T(\lambda)E(\lambda)\mathrm{d}\lambda \\ Y &= \int \bar{y}(\lambda)T(\lambda)E(\lambda)\mathrm{d}\lambda \\ Z &= \int \bar{z}(\lambda)T(\lambda)E(\lambda)\mathrm{d}\lambda \end{aligned} \tag{3.11}$$

where $\bar{x}(\lambda)$, $\bar{y}(\lambda)$, and $\bar{z}(\lambda)$ are the CIE color matching functions [92]. They represent the spectral responsivities of the cone cells of an average human eye; $E(\lambda)$ is a standard illuminant, where the CIE Standard Illuminant D65 was used in this study [92]. The resulting XYZ tristimulus values can be converted to standard RGB values using a simple linear transformation [92].

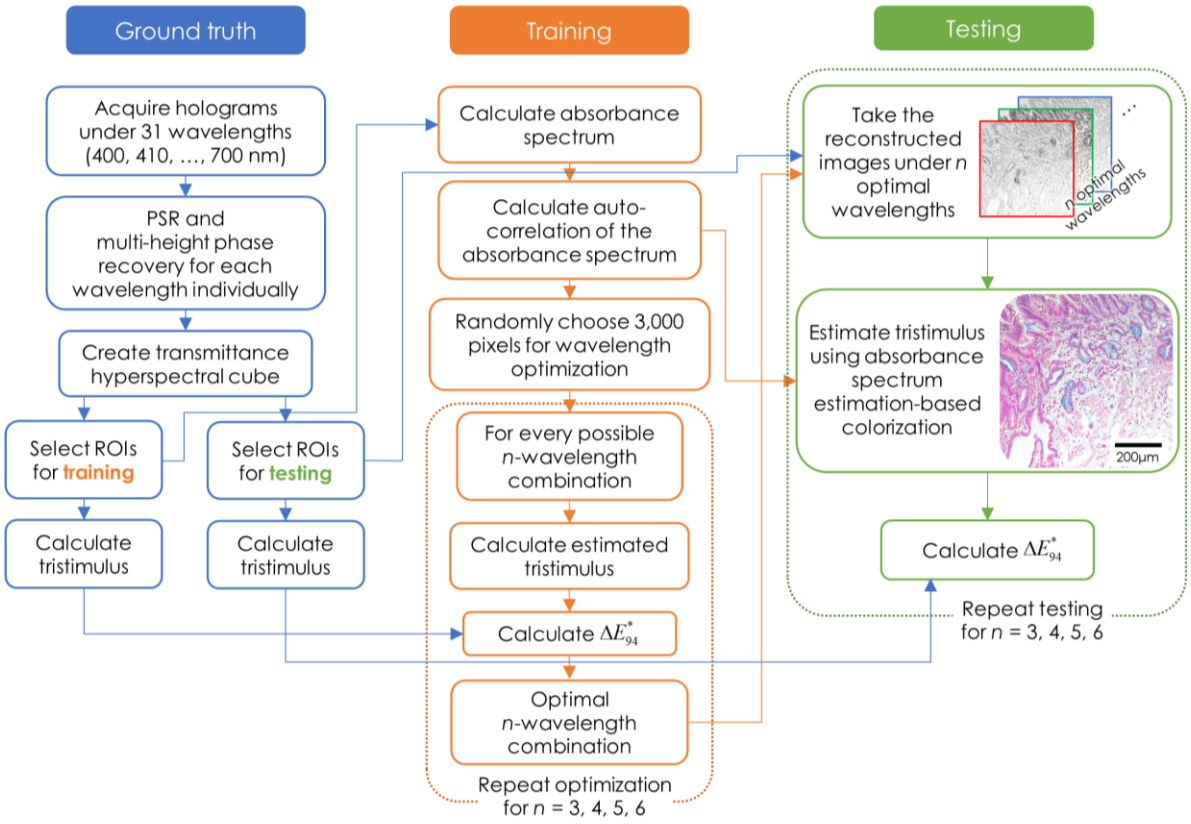

Figure 3. 2. Collection of the spectral statistics and wavelength optimization (training) as well as quantification of the average color error (testing) using the ASEC method.

Optimization of sample-specific illumination wavelengths

We developed a procedure (see Fig. 3.2) to optimize the wavelength selection for each specific tissue–stain type. The details are presented below.

(1) Acquiring the ground truth

In this study, we considered the color images that are calculated from the hyperspectral lens-free reconstructed images as the "ground truth" (left column in Fig. 3.2). It was used for the wavelength optimization and evaluation of the ASEC method. Therefore, the hyperspectral lens-free imaging and reconstruction were conducted as detailed previously. The reconstructed

hyperspectral cube was converted to the color tristimulus (CIE XYZ color space). Three 2048-by-2048-pixel regions of interest (ROIs) that represent diverse spatial features of the sample were manually picked across the entire imaging FOV and were used for training. Details related to training and testing are presented below.

(2) Collection of spectral statistics and optimization of wavelength combinations (training)

As shown in the middle column of Fig. 3.2, we converted the hyperspectral transmittance images within the three training ROIs (2048-by-2048 pixels in each) to the hyperspectral absorbance by normalizing the intensity images using their respective average background values and applying $-\log_{10}()$ (see Eqs. (3.4) and (3.5)). All the pixels within the three training ROIs (background areas excluded) were used to approximate the autocorrelation matrix

$$\mathbf{R}_{\mathbf{aa}} \approx \frac{1}{N_{\text{pixels}}} \sum_{i \in \text{P}} \mathbf{a}_i \mathbf{a}_i^{\text{T}} \tag{3.12}$$

where N_{pixels} is the total number of pixels for averaging, and P is the set of all N_{pixels} used for the $\mathbf{R}_{\mathbf{aa}}$ approximation. Once $\mathbf{R}_{\mathbf{aa}}$ is obtained for a given sample type (i.e., tissue–stain combination), it can be used to calculate $\mathbf{W}$ for any given wavelength combination for the same sample type (see Eq. (3.9)). Thus, ASEC can be readily performed when $\mathbf{R}_{\mathbf{aa}}$ is estimated.

For each combination of tissue type and stain, and given number of wavelengths (n), the optimal wavelength combination, after performing ASEC, leads to the minimum ΔE^*_{94} when compared to the ground truth color images. For each sample type, this wavelength optimization needs to be conducted only once. For this purpose, a total of 3,000 pixels were randomly chosen from the three training ROIs to be used in the wavelength optimization. An exhaustive search was conducted to obtain the globally optimal wavelength combination; i.e., for discrete wavelengths starting from 400 nm to 700 nm with 10 nm increment (31 in total), all $\binom{31}{n}$ wavelength

combinations were calculated for a given n. For each of these n-wavelength combinations, the transmittance values corresponding to the randomly chosen 3,000 pixels were collected. Afterwards, the ASEC method was applied to each of these pixels to estimate their tristimulus values (CIE XYZ color space) using the previously calculated $\mathbf{R_{aa}}$ (Eqs. (3.9)-(3.12)). The average ΔE^*_{94} was determined considering the estimated tristimulus and ground truth tristimulus values. After calculating ΔE^*_{94} for all different wavelength combinations, the ΔE^*_{94} values were sorted, and the combination corresponding to the smallest ΔE^*_{94} was selected as optimal combination.

(3) Testing of optimal wavelength combinations

The performance of the wavelength-optimized ASEC method was tested in sample areas outside the training ROIs. Two scenarios were tested in this study. Firstly, for each given number of wavelengths (n = 3, 4, 5, or 6), the corresponding optimal wavelength channels were extracted from the hyperspectral cube of the tested ROIs. Then, the procedure used to evaluate ΔE^*_{94} in the wavelength optimization step was followed: ASEC was applied to the extracted wavelength channels. The resulting estimated tristimulus values were compared against the ground truth to calculate the average ΔE^*_{94}. This represents the expected color errors when our colorization technique is applied to images outside the training ROIs. The test results for n = 3 are shown in the Results and discussion section.

Secondly, multiplexed multispectral lens-free imaging using three *simultaneous* illumination wavelengths (n = 3) was conducted for the same sample. The three illumination wavelengths were the ones previously optimized in the training step. Image reconstruction was conducted using DPSR, TIE, and multi-height phase recovery, and ASEC was performed using the previously calculated $\mathbf{R_{aa}}$. The estimated color image was registered to the "ground truth" image. A pixelwise average ΔE^*_{94} was calculated between the estimated color image and the "ground truth" color

image in the tested ROIs, which represents the expected color error of an independent imaging experiment of the sample using multiplexed illumination and reconstruction schemes.

Color-corrected lens-free holographic imaging procedure

The complete color-corrected wavelength-multiplexed lens-free imaging procedure for a new sample, whose tissue-type and stain combination is trained and optimized according to the previous subsections, is shown in Fig. 3.3. First, wavelength-multiplexed illumination was used during the image acquisition to capture holograms with xyz translations. One of the low-resolution holograms on each lateral plane was wavelength-demultiplexed, and autofocusing was applied to find its z-distance. Then, DPSR was applied to the holograms measured on each lateral plane followed by phase retrieval using the pixel-super-resolved holograms. The phase-retrieved intensity images at multiple wavelengths were transformed to a color image with the ASEC method using the previously learned statistics of this specific tissue type and stain combination. The result is a holographic color image that exhibits an accurate color reproduction.

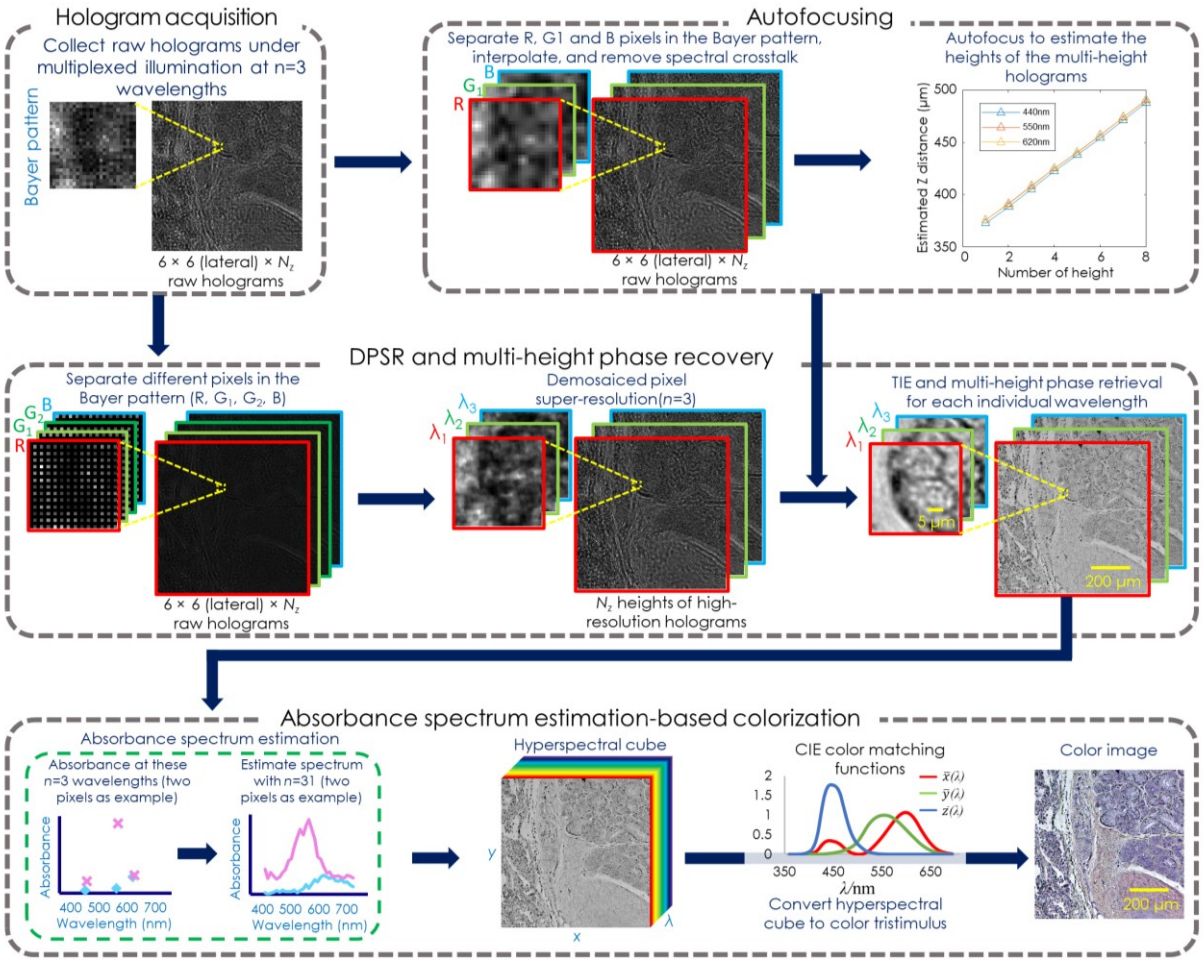

Figure 3. 3. Color-corrected and wavelength-multiplexed lens-free holographic imaging procedure. N_z is the number of the hologram measurement heights.

3.3 Results and discussion

We evaluated the ASEC performance using the testing methodology in Materials and methods. That is, the average ΔE^*_{94} value of each estimated color image with respect to the ground truth color image (i.e., from the lens-free hyperspectral imaging) was used to quantify the average color inaccuracy, owing to the capability of ΔE^*_{94} to account for the perceptual non-uniformity of widely-used color spaces [101]. However, please note that the average ΔE^*_{94} value will be partially influenced by the noise and artifacts within the image. The ASEC performance was compared to the direct RGB combination approach in Figs. 3.4-3.7. More specifically, the color

performance of the lens-free color imaging approaches using sequential or multiplexed illumination, with or without ASEC, were compared qualitatively using visual judgement and quantitatively by calculating the average ΔE^*_{94}. All three-wavelength imaging results (Figs. 3.4-3.7, Columns (a)–(d)), except Fig. 3.4(c3), used the optimal three-wavelength combinations specific to each sample type (shown in Fig. 3.9), which were identified from the wavelength optimization (training) procedure (Fig. 3.2 (middle column)). The only exception, Fig. 3.4(c3), used a suboptimal wavelength combination of 450 nm, 510 nm, and 580 nm, which is the best-performing (i.e., least-ΔE^*_{94}) wavelength combination that is compatible with DPSR; the latter requires that the three wavelengths belong to the blue, green, and red spectral regions, respectively [48]. The optimal wavelength combination for "artery H&E" (510 nm, 560 nm, and 600 nm) does not satisfy this condition.

Evidently, the images using ASEC (Figs. 3.4-3.7, Columns (b) and (d)) exhibit a better color accuracy than the corresponding images colorized with the direct RGB combination method (Columns (a) and (c)). Thus, they are in a much better agreement with the ground truth (Column (e)), both visually and quantitatively. This is reflected by the average ΔE^*_{94} values displayed in the bottom right of each individual image in Columns (a)–(d). Regarding the 25 tested samples, the average ΔE^*_{94} is improved (reduced) by approximately 2.48 and 1.73 after applying ASEC (compared to the direct RGB combination method) to approximately 1.71 and 3.83 for the sequential and multiplexed illumination cases, respectively.

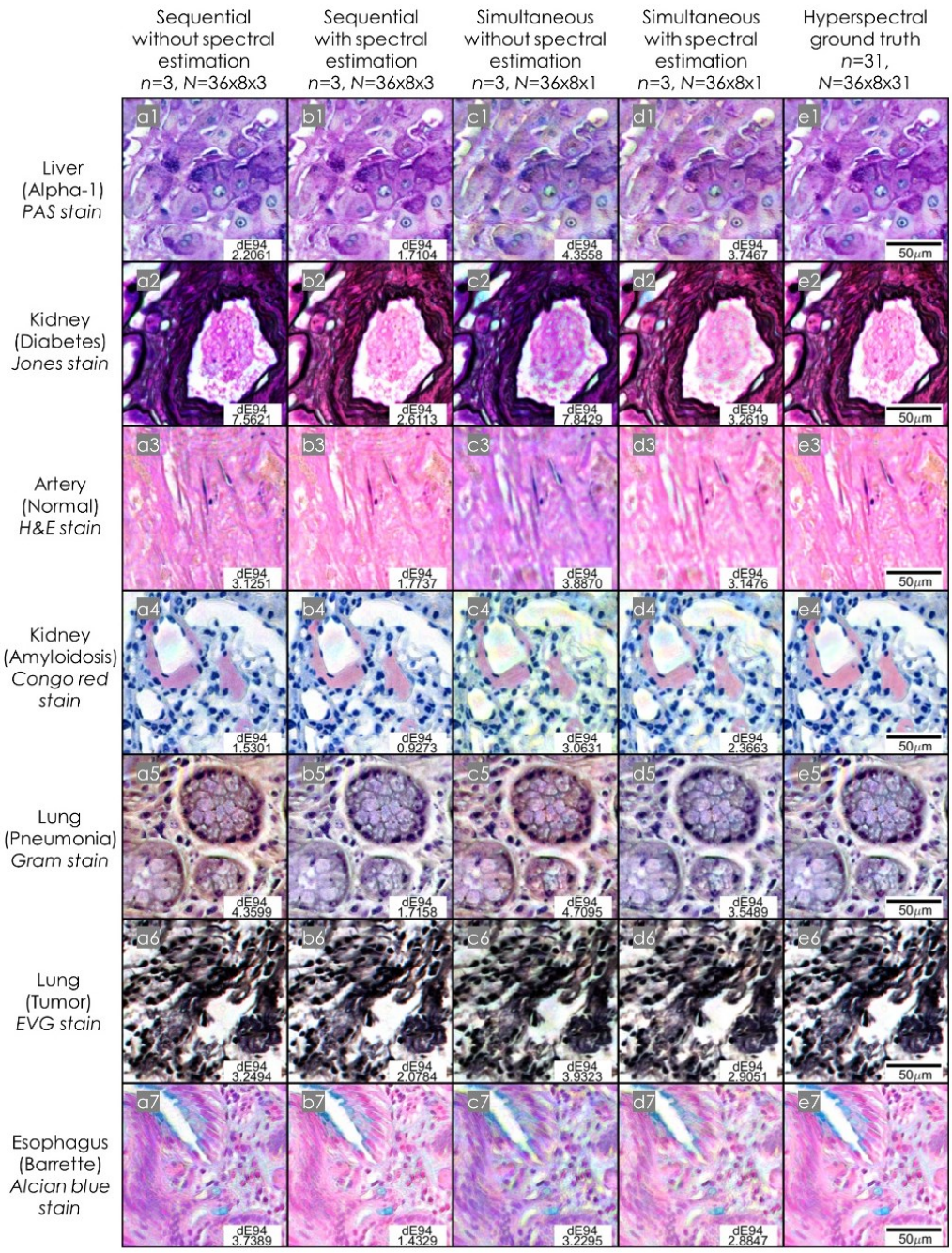

Figure 3. 4. Comparison of the performance of various lens-free imaging and colorization schemes for different samples. To the left of each row, the tissue type, its pathological condition, and its stain are specified. **Column (a):** The holographic reconstruction intensity images at the three optimal wavelengths using *sequential* illumination are directly placed into the corresponding R, G, and B channels to form an RGB image. **Column (b):** ASEC is performed on the same data as in Column (a). **Column (c):** The holographic reconstruction intensity images at the three optimal wavelengths (except c3, which uses a suboptimal combination that is compatible with DPSR) using *simultaneous*

illumination and wavelength demultiplexing are directly placed into the corresponding R, G, and B channels to form an RGB image. **Column (d):** ASEC is performed on the same data as in Column (c). **Column (e):** The ground truth color images generated from hyperspectral lens-free imaging with 31 wavelengths, ranging from 400 nm to 700 nm. The "dE94" corresponds to their respective ΔE^*_{94} value with respect to the ground truth color images in Column (e); n is the number of wavelengths; N is the number of holograms used to reconstruct the images corresponding to each column and equal to the multiplication of the number of lateral shifts for PSR or DPSR, with the number of heights, and the number of measurements per shifting position for multispectral imaging.

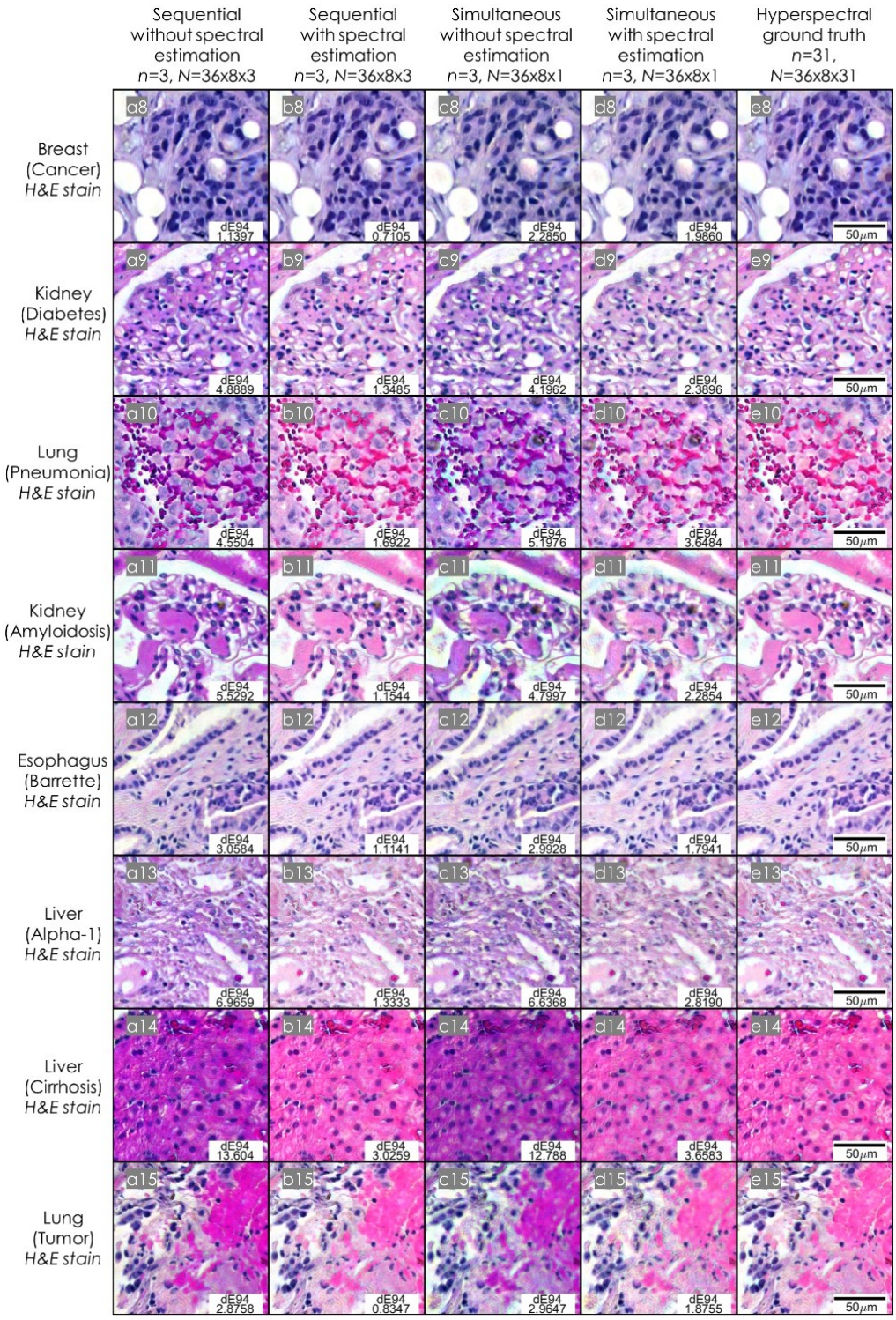

Figure 3. 5. Continuation of Fig. 3.4. Results of ASEC-based color holographic imaging using the optimal three wavelengths for each tissue type and stain combination.

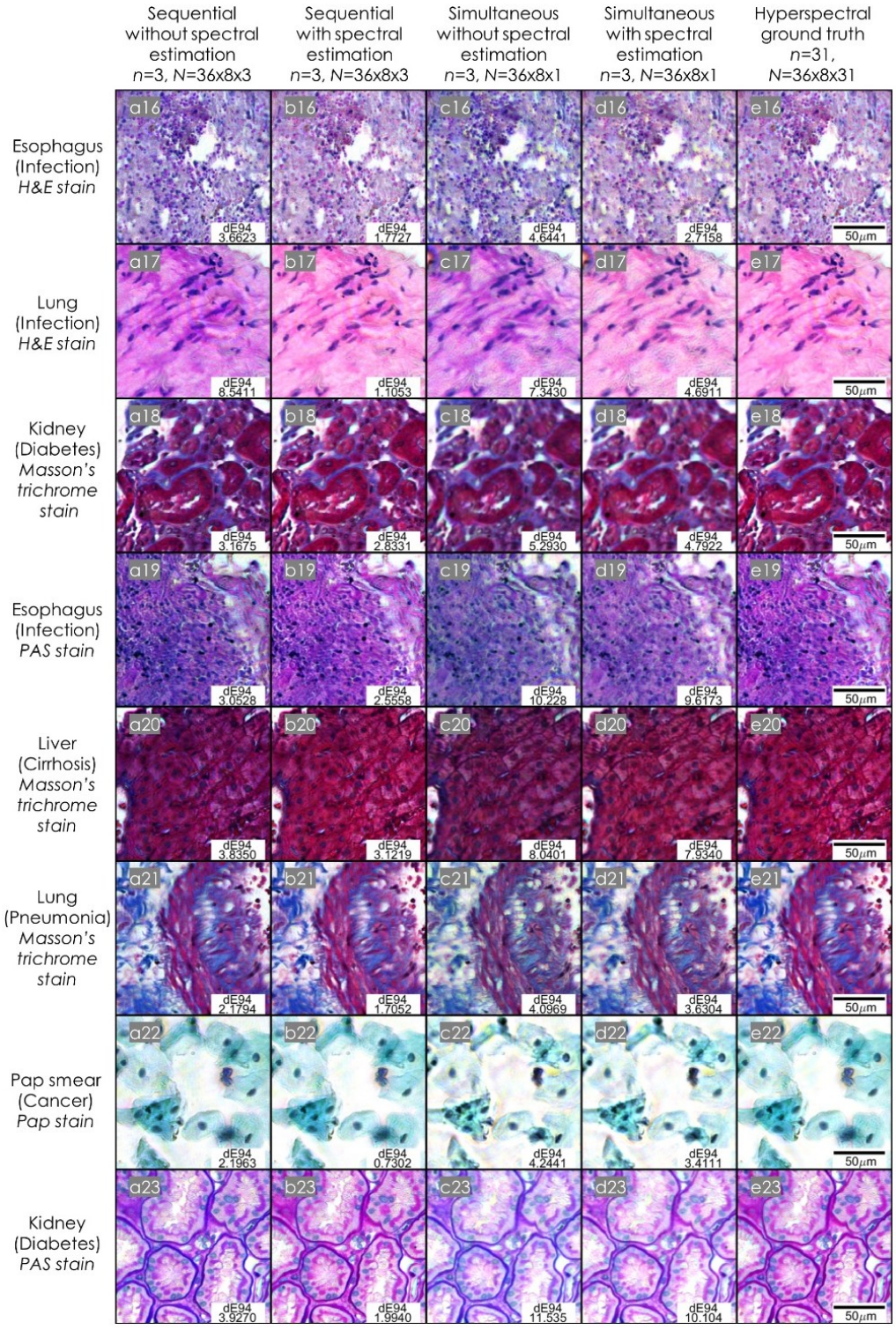

Figure 3. 6. Continuation of Fig. 3.5. Results of ASEC-based color holographic imaging using the optimal three wavelengths for each tissue type and stain combination.

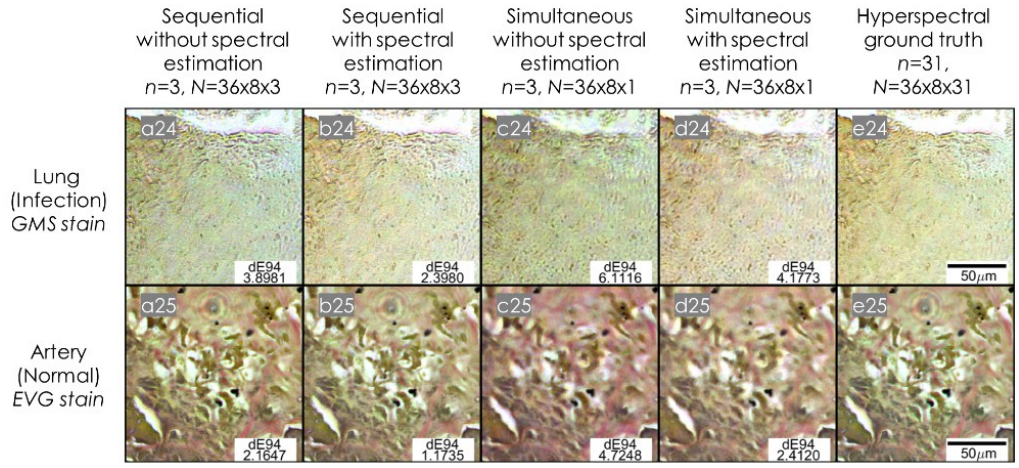

Figure 3. 7. Continuation of Fig. 3.6. Results of ASEC-based color holographic imaging using the optimal three wavelengths for each tissue type and stain combination.

The ΔE^*_{94} values of the simultaneous (i.e., multiplexed) illumination results using ASEC (Figs. 3.4-3.7, Column (d)) are, on average, larger than those with sequential illumination, by approximately 2.12 (Column (b)), which is mainly due to the additional steps involved in DPSR inevitably introducing additional error. However, for 22 of 25 samples, the ΔE^*_{94} of the simultaneous illumination results with ASEC is below 5, which demonstrates a decent color reproduction.

To further reduce the data amount required for color imaging on the basis of wavelength-multiplexed imaging and ASEC, we applied a sparsity constraint for performing multi-height phase recovery [45] and reduced the number of hologram heights from 8 to 4 and 2. The results are shown in Fig. 3.8. With the use of the sparsity constraint, the ASEC-colorized images using four heights (Column (c)) still have a decent quality, whereas those reconstructed from two heights show relatively severe reconstruction artifacts.

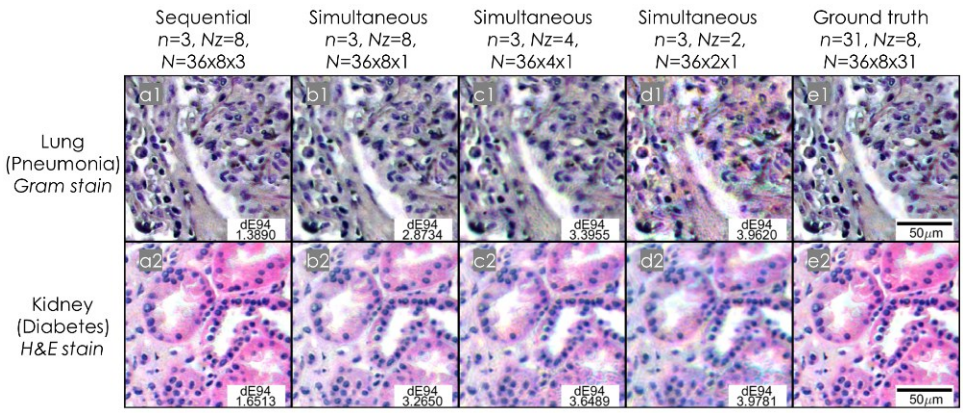

Figure 3. 8. Reducing the number of hologram heights using multi-height phase recovery with sparsity constraint. N_z is the number of the hologram measurement heights; N is the total number of acquired holograms for reconstruction.

In the ASEC method, we chose to develop our linear estimator based on the absorbance because in our transmission mode imaging system, the spectral absorbance of the sample and the amount of dye or pigment at each lateral (x, y) position within the sample follow a linear relation given by the Beer–Lambert law:

$$A(\lambda) = \sum_{j=1}^{n_{\text{species}}} A_j(\lambda) = \sum_{j=1}^{n_{\text{species}}} \varepsilon_j(\lambda) \int_0^l c_j(z)\,\mathrm{d}z \tag{3.13}$$

where $A(\lambda)$ is the absorbance of the sample at wavelength λ, $\varepsilon_j(\lambda)$ the molar attenuation coefficient or absorptivity of the attenuating species j in the sample, n_{species} refers to the total number of attenuating species within the sample, c_j the molar concentration of the attenuating species j , and l the optical path length of the illumination light going through the sample.

The optimal three-wavelength combinations of all the samples are shown in Fig. 3.9. The average wavelengths are 450.0 nm, 535.2 nm, and 605.6 nm, respectively, and represented by solid lines. Interestingly, the majority of the optimal wavelengths are clustered around these three values. Although we think that this is partially related to our wavelength optimization procedure that aims for accurate human color perception (whose peak sensitivities are approximately 446 nm, 555 nm,

and 599 nm) [102], the optimal wavelength combinations are not entirely intuitive. This is especially evident in the selection of the green wavelength: its average value (535.2 nm) is approximately 20 nm shorter than the sensitivity peak of an average human (approximately 555 nm). Moreover, a distinct outlier is presented by the artery tissue with H&E stains (dashed gray box in Fig. 3.9). Its optimized wavelengths are 510 nm, 560 nm, and 600 nm, respectively. This sample possesses larger areas with a very high absorbance for 520–540 nm, which may cause the optimization to favor the wavelength combinations with denser sampling in the green region.

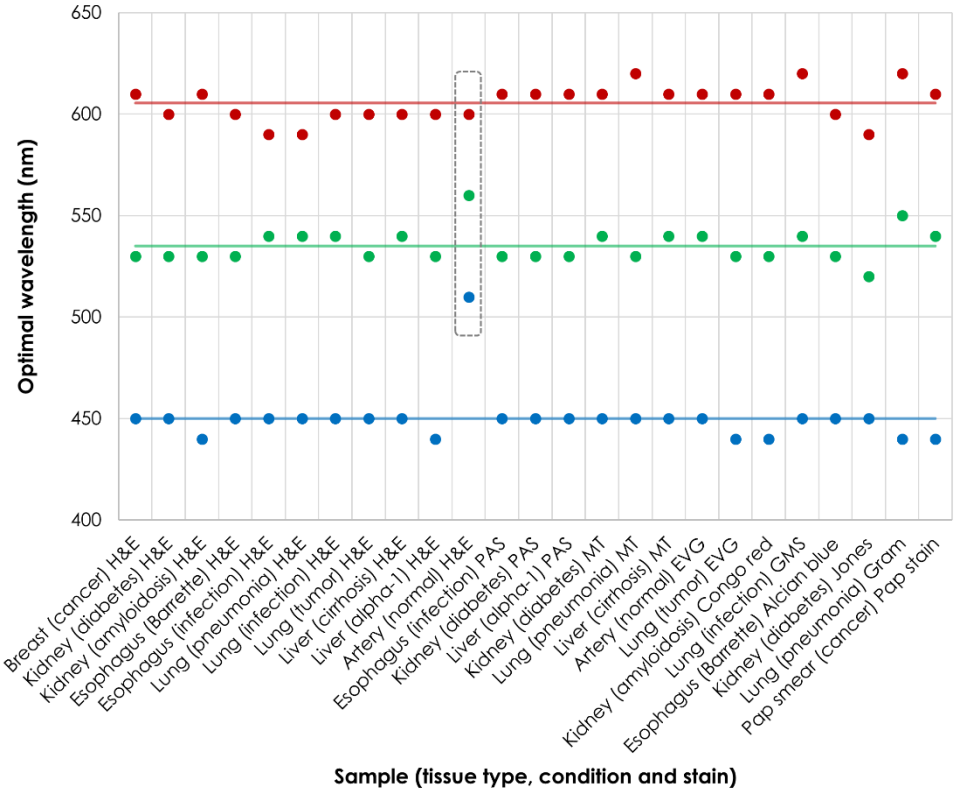

Figure 3. 9. Optimal three-wavelength combinations for various pathology samples. The solid lines represent the averaged optimal wavelengths for all the samples. The dashed gray box corresponds to an outlier: artery with H&E stain. Its optimal wavelengths deviate far from the average.

The ranked wavelength combinations obtained in the training process for all 25 samples are shown in the Tables 3.1-3.25 in the Appendix, thereby providing a practical guide to wavelength

selection for holographic imaging of various pathology slides, involving different dyes and tissue types. Due to space constraints, the top five combinations for each number of wavelengths n (n = 3, 4, 5, 6) are displayed. According to these tables, the usage of the optimal wavelength combination for a larger n always leads to more color-accurate results (i.e., lower average ΔE^*_{94}). Indeed, even the fifth-best wavelength combination of a larger n always results in more accurate colorization than the absolute best of a smaller n.

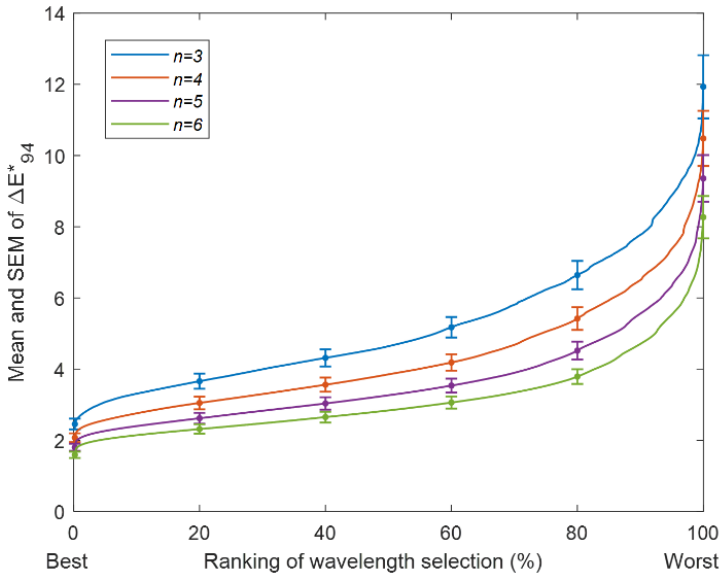

Figure 3. 10. Average ΔE^*_{94} for 25 different samples for different wavelength combinations. The x-axis presents the relative ranking for each given wavelength combination with respect to all possible n-wavelength combinations (n = 3, 4, 5, 6). Smaller relative rankings correspond to better color accuracy, i.e., lower average ΔE^*_{94}. Error bars are shown at six equally-spaced points, representing the standard error of the mean (SEM) of the average ΔE^*_{94} values regarding the 25 samples.

However, the improved color accuracy offered by using more wavelengths can still be nullified if those wavelengths are not chosen carefully. Fig. 3.10 shows the ΔE^*_{94} averaged across all the samples and plotted as a function of the relative ranking of each wavelength combination obtained in the training process, starting from the lowest ΔE^*_{94} to the highest. In other words, the x-axis

presents the rank of each wavelength combination (in an ascending order) normalized by the total number of possible combinations for a given n. The error bars represent the standard error of the mean (SEM) of the averaged ΔE^*_{94} values of the 25 samples. According to Fig. 3.10, for example the four-wavelength combination ranking at the top 2.65%, the five-wavelength combination ranking at the top 12.5%, and the six-wavelength combination ranking at the top 28.7% result in an equivalent average ΔE^*_{94} value as the best three-wavelength combination. Therefore, a poor wavelength selection will defeat the purpose to improve color accuracy with denser sampling in the optical spectrum. Moreover, even if an optimal wavelength selection is assumed, the improvement in ΔE^*_{94} by adding extra wavelengths beyond three is modest. For an average sample, the reduction in ΔE^*_{94} is 0.38 when going from three to four, 0.27 from four to five, and 0.21 from five to six wavelengths, which would be barely noticeable to the eye.

3.4 Conclusions

An ASEC method for accurate-color holographic imaging of pathology slides was presented. The method converts the holographic reconstruction images of the sample at a small number of wavelengths (n = 3, 4, 5, or 6) to an image with accurate color reproduction by computationally estimating its absorbance spectrum at each pixel position. In addition, we extracted the spectral statistics of 25 samples with different tissue–stain combinations and performed global optimization of the n-wavelength selection (n = 3, 4, 5, 6) for each sample, respectively, thereby demonstrating a significant improvement in the color accuracy compared to the direct RGB combination method. Furthermore, ASEC can be readily combined with multiplexed-wavelength holographic imaging using DPSR, leading to accurate color reproduction with a significantly reduced number of raw measurements. In conclusion, this study provides a practical guide and a database to achieve accurate-color holographic imaging of pathology slides, spanning different dyes and tissue types.

3.5 Appendix

Table 3.1. Top five *n*-wavelength combinations (*n* = 3, 4, 5, 6) for breast tissue sample with H&E stain. Pathological condition: cancer.

Sample and stain	Number of wavelengths	Wavelength combination (nm)	ΔE^*_{94} mean	ΔE^*_{94} SD
Breast(Cancer) *H&E*	6	450, 510, 530, 550, 610, 640	1.2303	0.8862
	6	450, 510, 530, 550, 610, 650	1.2415	0.8890
	6	440, 450, 520, 540, 580, 630	1.2416	0.8745
	6	450, 500, 530, 550, 610, 640	1.2417	0.8951
	6	450, 520, 530, 550, 600, 630	1.2429	0.8885
	5	440, 520, 540, 580, 630	1.3856	0.9730
	5	450, 520, 550, 600, 630	1.3893	1.0107
	5	450, 520, 540, 600, 630	1.3894	0.9919
	5	440, 520, 540, 600, 630	1.3894	0.9846
	5	450, 520, 540, 580, 630	1.3972	0.9981
	4	450, 520, 550, 610	1.5746	1.1427
	4	440, 520, 540, 610	1.5808	1.1197
	4	450, 520, 540, 610	1.5845	1.1262
	4	450, 530, 550, 610	1.5903	1.1380
	4	450, 530, 560, 610	1.5912	1.1410
	3	450, 530, 610	1.7913	1.2886
	3	440, 530, 610	1.8171	1.3374
	3	460, 530, 610	1.8484	1.3743
	3	430, 530, 610	1.8533	1.3146
	3	450, 530, 620	1.8609	1.3459

Table 3.2. Top five *n*-wavelength combinations (*n* = 3, 4, 5, 6) for kidney tissue sample with H&E stain. Pathological condition: diabetes.

Sample and stain	Number of wavelengths	Wavelength combination (nm)	ΔE^*_{94} mean	ΔE^*_{94} SD
Kidney (Diabetes) *H&E*	6	440, 460, 530, 550, 580, 620	1.1724	0.6244
	6	440, 450, 530, 550, 580, 620	1.1808	0.6357
	6	440, 450, 530, 560, 590, 620	1.1819	0.6379
	6	440, 460, 530, 560, 590, 620	1.1821	0.6431
	6	440, 460, 530, 560, 600, 620	1.1832	0.6516
	5	450, 530, 560, 590, 620	1.3206	0.7242
	5	440, 460, 530, 570, 620	1.3239	0.7167
	5	450, 530, 550, 580, 620	1.3240	0.7369
	5	450, 520, 540, 580, 620	1.3242	0.7294
	5	450, 530, 560, 610, 620	1.3276	0.7325
	4	450, 530, 570, 620	1.4551	0.7838
	4	450, 530, 560, 620	1.4567	0.7791
	4	450, 530, 580, 620	1.4621	0.7856
	4	450, 530, 560, 610	1.4631	0.7845
	4	450, 530, 570, 610	1.4677	0.7939
	3	450, 530, 600	1.7067	0.9380
	3	450, 530, 610	1.7314	0.9497
	3	440, 530, 600	1.7499	0.9662
	3	460, 530, 600	1.7548	0.9709
	3	450, 530, 620	1.7592	0.9888

Table 3.3. Top five *n*-wavelength combinations (*n* = 3, 4, 5, 6) for kidney tissue sample with H&E stain.

Pathological condition: amyloidosis.

Sample and stain	Number of wavelengths	Wavelength combination (nm)	ΔE^*_{94} mean	ΔE^*_{94} SD
Kidney (Amyloidosis) *H&E*	6	440, 450, 520, 550, 590, 620	1.0268	0.5747
	6	440, 450, 520, 540, 560, 610	1.0269	0.6074
	6	440, 450, 520, 540, 570, 610	1.0271	0.6090
	6	440, 450, 520, 550, 600, 610	1.0307	0.5882
	6	440, 450, 530, 550, 590, 620	1.0310	0.6261
	5	440, 450, 520, 550, 610	1.1698	0.6719
	5	440, 460, 520, 550, 610	1.1789	0.6800
	5	440, 450, 530, 560, 610	1.1790	0.7602
	5	440, 450, 530, 550, 610	1.1804	0.7165
	5	430, 450, 520, 550, 610	1.1856	0.6798
	4	440, 520, 550, 610	1.3111	0.7430
	4	440, 530, 550, 610	1.3194	0.7804
	4	450, 520, 550, 610	1.3219	0.7591
	4	450, 530, 550, 610	1.3265	0.7937
	4	440, 530, 560, 610	1.3267	0.8219
	3	440, 530, 610	1.5617	1.0199
	3	440, 540, 610	1.5625	0.9380
	3	450, 530, 610	1.5638	1.0275
	3	450, 540, 610	1.5685	0.9506
	3	430, 530, 610	1.5917	1.0551

Table 3.4. Top five *n*-wavelength combinations (*n* = 3, 4, 5, 6) for esophagus tissue sample with H&E stain.

Pathological condition: Barrette's esophagus.

Sample and stain	Number of wavelengths	Wavelength combination (nm)	ΔE^*_{94} mean	ΔE^*_{94} SD
Esophagus (Barrette) *H&E*	6	440, 450, 530, 540, 570, 620	1.0270	0.8018
	6	440, 450, 520, 530, 570, 620	1.0382	0.7680
	6	440, 450, 530, 540, 570, 610	1.0424	0.8263
	6	450, 460, 530, 540, 570, 620	1.0473	0.8981
	6	430, 450, 530, 540, 570, 620	1.0560	0.8261
	5	450, 530, 540, 570, 620	1.1583	0.9288
	5	450, 520, 530, 570, 620	1.1633	0.8878
	5	440, 450, 530, 570, 620	1.1675	0.8749
	5	450, 530, 540, 570, 610	1.1702	0.9468
	5	450, 520, 530, 570, 610	1.1802	0.9159
	4	450, 530, 570, 620	1.2835	0.9765
	4	450, 530, 570, 610	1.2938	0.9939
	4	450, 530, 560, 610	1.3062	0.9827
	4	450, 530, 560, 620	1.3066	0.9738
	4	450, 530, 550, 610	1.3092	0.9851
	3	450, 530, 600	1.4732	1.1521
	3	450, 530, 610	1.4869	1.1192
	3	440, 530, 600	1.4989	1.0867
	3	440, 530, 610	1.5116	1.0695
	3	430, 530, 600	1.5210	1.0624

Table 3.5. Top five *n*-wavelength combinations (*n* = 3, 4, 5, 6) for esophagus tissue sample with H&E stain.

Pathological condition: infection.

Sample and stain	Number of wavelengths	Wavelength combination (nm)	ΔE^*_{94} mean	ΔE^*_{94} SD
Esophagus (Infection) *H&E*	6	440 460 520 550 580 620	1.5024	0.8256
	6	440 450 520 550 580 620	1.5123	0.8347
	6	440 460 520 550 590 620	1.5151	0.8460
	6	450 460 520 550 580 620	1.5182	0.8315
	6	450 460 520 550 590 620	1.5210	0.8546
	5	450 520 550 580 620	1.7247	0.9595
	5	450 520 550 590 620	1.7340	0.9893
	5	450 520 550 570 610	1.7411	1.0223
	5	440 450 520 560 610	1.7466	1.0085
	5	440 460 520 560 610	1.7486	0.9921
	4	450 520 560 610	1.9506	1.1041
	4	440 520 560 610	1.9767	1.1524
	4	450 520 560 620	1.9832	1.1131
	4	450 520 550 610	1.9843	1.1451
	4	460 520 560 610	1.9870	1.1437
	3	450 540 590	2.3698	1.2840
	3	440 540 590	2.3922	1.2895
	3	450 540 600	2.4041	1.3229
	3	450 520 590	2.4057	1.3587
	3	440 540 600	2.4071	1.3198

Table 3.6. Top five *n*-wavelength combinations (*n* = 3, 4, 5, 6) for lung tissue sample with H&E stain.

Pathological condition: pneumonia.

Sample and stain	Number of wavelengths	Wavelength combination (nm)	ΔE^*_{94} mean	ΔE^*_{94} SD
Lung (Pneumonia) *H&E*	**6**	**440, 460, 520, 540, 570, 620**	**1.2246**	**0.7834**
	6	**440, 460, 530, 550, 590, 630**	**1.2310**	**0.7642**
	6	**440, 460, 520, 540, 570, 610**	**1.2315**	**0.8109**
	6	**440, 460, 530, 550, 570, 620**	**1.2343**	**0.7540**
	6	**440, 460, 530, 550, 590, 620**	**1.2354**	**0.7533**
	5	**450, 530, 550, 570, 610**	**1.3800**	**0.8773**
	5	**450, 530, 550, 590, 630**	**1.3804**	**0.8659**
	5	**450, 530, 550, 570, 620**	**1.3820**	**0.8481**
	5	**450, 520, 540, 570, 620**	**1.3821**	**0.8845**
	5	**450, 520, 540, 570, 610**	**1.3850**	**0.9117**
	4	**450, 530, 550, 610**	**1.5762**	**0.9895**
	4	**450, 530, 550, 590**	**1.5769**	**1.0492**
	4	**450, 530, 550, 600**	**1.5839**	**1.0715**
	4	**450, 530, 560, 610**	**1.5924**	**1.0179**
	4	**460, 530, 550, 610**	**1.5968**	**1.0259**
	3	**450, 540, 590**	**1.8221**	**1.2856**
	3	**440, 540, 590**	**1.8430**	**1.2953**
	3	**460, 540, 590**	**1.8499**	**1.3133**
	3	**450, 540, 600**	**1.8657**	**1.3173**
	3	**450, 540, 610**	**1.8709**	**1.2812**

Table 3.7. Top five *n*-wavelength combinations (*n* = 3, 4, 5, 6) for lung tissue sample with H&E stain. Pathological condition: infection.

Sample and stain	Number of wavelengths	Wavelength combination (nm)	ΔE^*_{94} mean	ΔE^*_{94} SD
Lung (Infection) *H&E*	6	440, 460, 520, 550, 580, 620	1.4711	0.8904
	6	440, 460, 520, 550, 590, 620	1.4722	0.9169
	6	440, 460, 520, 540, 560, 610	1.4874	0.9014
	6	440, 460, 520, 550, 600, 620	1.4883	0.9333
	6	440, 460, 520, 550, 580, 610	1.4903	0.9361
	5	440, 460, 530, 560, 610	1.6865	1.0453
	5	440, 460, 520, 560, 610	1.7069	1.0515
	5	440, 460, 520, 550, 610	1.7085	1.0810
	5	440, 460, 530, 560, 620	1.7125	1.0315
	5	440, 470, 530, 560, 610	1.7368	1.0864
	4	450, 520, 560, 610	1.9522	1.2172
	4	450, 520, 550, 610	1.9524	1.2200
	4	450, 530, 560, 610	1.9545	1.2331
	4	450, 530, 560, 620	1.9671	1.2343
	4	450, 520, 560, 620	1.9735	1.2086
	3	450, 540, 600	2.3677	1.5099
	3	450, 540, 610	2.3790	1.5231
	3	440, 540, 600	2.4309	1.4879
	3	450, 530, 600	2.4315	1.5739
	3	440, 540, 610	2.4377	1.5023

Table 3.8. Top five *n*-wavelength combinations (*n* = 3, 4, 5, 6) for lung tissue sample with H&E stain. Pathological condition: tumor.

Sample and stain	Number of wavelengths	Wavelength combination (nm)	ΔE^*_{94} mean	ΔE^*_{94} SD
Lung (Tumor) *H&E*	6	440 460 520 550 600 640	1.3910	1.0402
	6	440 460 520 550 600 620	1.4033	1.1119
	6	440 460 520 540 600 640	1.4072	1.0088
	6	430 450 530 550 570 630	1.4091	1.0659
	6	440 460 530 550 600 640	1.4092	1.1051
	5	450 530 550 600 640	1.5882	1.2388
	5	430 450 530 570 630	1.5950	1.2587
	5	450 530 550 570 630	1.6029	1.2156
	5	450 530 550 600 630	1.6040	1.2262
	5	440 450 530 570 630	1.6049	1.2968
	4	450 530 570 630	1.7672	1.3862
	4	450 530 570 620	1.8070	1.4634
	4	450 530 570 640	1.8112	1.4446
	4	450 530 600 640	1.8129	1.4830
	4	440 530 570 630	1.8269	1.4932
	3	450 530 600	2.1002	1.6564
	3	440 530 600	2.1338	1.7110
	3	450 530 610	2.1549	1.8091
	3	460 530 600	2.1673	1.6796
	3	450 520 600	2.1749	1.7741

Table 3.9. Top five *n*-wavelength combinations (*n* = 3, 4, 5, 6) for liver tissue sample with H&E stain. Pathological condition: cirrhosis.

Sample and stain	Number of wavelengths	Wavelength combination (nm)	ΔE^*_{94} mean	ΔE^*_{94} SD
Liver (Cirrhosis) *H&E*	6	450 520 530 560 610 620	1.3801	0.8127
	6	450 530 540 570 610 620	1.3807	0.8383
	6	450 460 530 560 610 620	1.3822	0.8166
	6	450 530 540 560 610 620	1.3846	0.8271
	6	450 460 530 540 570 620	1.3848	0.8217
	5	450 530 560 610 620	1.5220	0.8916
	5	450 530 540 570 620	1.5244	0.9109
	5	450 530 560 600 610	1.5291	0.9144
	5	450 530 560 610 630	1.5325	0.9061
	5	450 530 540 580 600	1.5360	0.9409
	4	450 530 560 610	1.6655	0.9730
	4	450 530 560 600	1.6863	1.0016
	4	450 530 570 620	1.6867	1.0024
	4	430 530 560 610	1.6900	0.9686
	4	440 530 560 610	1.6926	0.9373
	3	450 530 600	1.9578	1.1769
	3	430 530 600	1.9806	1.1759
	3	450 530 610	1.9833	1.2300
	3	460 530 600	1.9892	1.1856
	3	450 530 590	1.9928	1.2045

Table 3.10. Top five *n*-wavelength combinations (*n* = 3, 4, 5, 6) for liver tissue sample with H&E stain. Pathological condition: alpha-1 antitrypsin deficiency.

Sample and stain	Number of wavelengths	Wavelength combination (nm)	ΔE^*_{94} mean	ΔE^*_{94} SD
Liver (Alpha-1) *H&E*	6	440 450 530 560 600 620	1.3239	0.6968
	6	440 460 530 560 600 620	1.3247	0.7022
	6	440 460 530 560 600 630	1.3341	0.6928
	6	440 450 530 560 600 630	1.3344	0.6840
	6	440 450 530 560 610 620	1.3372	0.7062
	5	440 450 530 560 610	1.4801	0.7662
	5	440 460 530 560 610	1.4853	0.7711
	5	440 460 530 560 600	1.4885	0.7879
	5	440 450 530 560 600	1.4902	0.7801
	5	440 450 530 560 620	1.4937	0.7856
	4	450 530 560 610	1.6661	0.8712
	4	440 530 560 610	1.6739	0.8870
	4	450 530 560 620	1.6751	0.8813
	4	440 530 560 600	1.6771	0.8981
	4	450 530 560 600	1.6821	0.8844
	3	440 530 600	1.8931	0.9902
	3	440 530 610	1.9152	1.0090
	3	450 530 600	1.9182	1.0175
	3	460 530 600	1.9284	1.0220
	3	450 530 610	1.9310	1.0237

Table 3.11. Top five *n*-wavelength combinations (*n* = 3, 4, 5, 6) for artery tissue sample with H&E stain.

Pathological condition: normal.

Sample and stain	Number of wavelengths	Wavelength combination (nm)	ΔE^*_{94} mean	ΔE^*_{94} SD
Artery (Normal) *H&E*	6	440, 460, 520, 560, 580, 600	1.5234	0.8945
	6	440, 460, 520, 560, 570, 600	1.5240	0.9018
	6	450, 500, 540, 560, 570, 600	1.5266	0.9097
	6	440, 460, 520, 560, 580, 610	1.5307	0.8814
	6	440, 460, 520, 560, 570, 610	1.5335	0.9118
	5	450, 520, 560, 580, 600	1.7233	0.9721
	5	450, 520, 560, 570, 600	1.7240	0.9858
	5	450, 520, 560, 580, 610	1.7363	0.9555
	5	450, 520, 560, 570, 610	1.7403	0.9848
	5	460, 520, 560, 580, 610	1.7425	0.9483
	4	450, 520, 560, 600	1.9713	1.1805
	4	460, 520, 560, 600	1.9864	1.1675
	4	460, 520, 560, 610	2.0046	1.1493
	4	450, 520, 560, 610	2.0085	1.1611
	4	450, 510, 560, 600	2.0105	1.2801
	3	510, 560, 600	2.6371	1.7054
	3	500, 560, 600	2.6588	1.6896
	3	490, 560, 600	2.6603	1.7818
	3	510, 560, 610	2.6623	1.6740
	3	450, 510, 570	2.6797	1.8235

Table 3.12. Top five *n*-wavelength combinations (*n* = 3, 4, 5, 6) for esophagus tissue sample with PAS stain.

Pathological condition: infection.

Sample and stain	Number of wavelengths	Wavelength combination (nm)	ΔE^*_{94} mean	ΔE^*_{94} SD
Esophagus (Infection) *PAS*	6	450, 510, 530, 550, 600, 630	2.0075	1.2228
	6	450, 500, 530, 550, 600, 630	2.0185	1.2277
	6	450, 510, 530, 560, 600, 630	2.0249	1.2534
	6	450, 510, 520, 550, 600, 630	2.0261	1.2228
	6	450, 510, 530, 570, 600, 630	2.0283	1.2400
	5	450, 510, 550, 600, 630	2.2418	1.3289
	5	450, 500, 550, 600, 630	2.2598	1.3436
	5	450, 510, 540, 600, 630	2.2789	1.3260
	5	450, 510, 550, 610, 620	2.2807	1.4112
	5	450, 500, 550, 610, 620	2.2851	1.4305
	4	450, 510, 550, 610	2.5750	1.5332
	4	450, 500, 550, 610	2.5993	1.5692
	4	450, 510, 550, 620	2.6283	1.5475
	4	440, 510, 550, 610	2.6299	1.5329
	4	450, 500, 550, 620	2.6375	1.5627
	3	450, 530, 610	3.0430	1.9468
	3	440, 530, 610	3.0871	1.9174
	3	450, 540, 610	3.1009	1.9453
	3	440, 540, 610	3.1284	1.9160
	3	450, 550, 610	3.1385	2.0708

Table 3.13. Top five *n*-wavelength combinations (*n* = 3, 4, 5, 6) for kidney tissue sample with PAS stain. Pathological condition: diabetes.

Sample and stain	Number of wavelengths	Wavelength combination (nm)	ΔE^*_{94} mean	ΔE^*_{94} SD
Kidney (Diabetes) *PAS*	6	440, 470, 520, 570, 600, 630	1.4442	0.8297
	6	440, 470, 520, 560, 600, 620	1.4470	0.8273
	6	440, 470, 520, 570, 610, 630	1.4474	0.8121
	6	440, 470, 520, 560, 600, 630	1.4492	0.8099
	6	440, 470, 520, 570, 600, 620	1.4498	0.8585
	5	440, 470, 520, 570, 610	1.6364	0.9270
	5	440, 470, 520, 560, 610	1.6447	0.9344
	5	440, 520, 570, 610, 620	1.6477	0.9425
	5	440, 520, 570, 610, 630	1.6503	0.9289
	5	440, 520, 570, 600, 620	1.6518	0.9652
	4	440, 520, 570, 610	1.8225	1.0146
	4	440, 520, 560, 610	1.8396	1.0301
	4	440, 520, 580, 610	1.8618	1.0755
	4	440, 530, 560, 610	1.8653	1.0509
	4	460, 520, 560, 610	1.8679	1.1257
	3	440, 530, 610	2.1306	1.1732
	3	450, 530, 610	2.1516	1.2180
	3	460, 530, 610	2.1666	1.2963
	3	440, 520, 610	2.1900	1.2298
	3	460, 520, 610	2.2081	1.2979

Table 3.14. Top five *n*-wavelength combinations (*n* = 3, 4, 5, 6) for liver tissue sample with PAS stain. Pathological condition: alpha-1 antitrypsin deficiency.

Sample and stain	Number of wavelengths	Wavelength combination (nm)	ΔE^*_{94} mean	ΔE^*_{94} SD
Liver (Apha-1) *PAS*	6	450, 510, 540, 570, 610, 620	1.6093	0.8871
	6	450, 510, 540, 570, 610, 630	1.6142	0.8688
	6	450, 510, 530, 570, 610, 620	1.6205	0.8953
	6	450, 510, 540, 550, 610, 620	1.6290	0.8917
	6	450, 510, 530, 570, 610, 630	1.6356	0.8869
	5	450, 510, 550, 610, 620	1.8192	1.0086
	5	450, 520, 550, 610, 620	1.8264	1.0744
	5	450, 510, 550, 610, 630	1.8321	0.9917
	5	450, 520, 550, 610, 630	1.8374	1.0344
	5	450, 520, 550, 590, 640	1.8475	1.0505
	4	450, 510, 570, 620	2.0795	1.1495
	4	450, 520, 550, 610	2.0914	1.2255
	4	450, 510, 550, 620	2.1071	1.1383
	4	450, 520, 580, 610	2.1318	1.2607
	4	450, 520, 580, 640	2.1347	1.1802
	3	450, 530, 610	2.4623	1.4319
	3	440, 530, 610	2.4843	1.3968
	3	450, 530, 620	2.5135	1.4448
	3	440, 530, 620	2.5498	1.4007
	3	450, 520, 610	2.5748	1.4824

Table 3.15. Top five *n*-wavelength combinations (*n* = 3, 4, 5, 6) for kidney tissue sample with Masson's trichrome stain. Pathological condition: diabetes.

Sample and stain	Number of wavelengths	Wavelength combination (nm)	ΔE^*_{94} mean	ΔE^*_{94} SD
Kidney (Diabetes) *Masson's trichrome*	6	450, 510, 550, 580, 600, 630	1.6520	1.0100
	6	440, 510, 540, 570, 600, 630	1.6581	0.9596
	6	450, 510, 550, 580, 610, 640	1.6618	1.0213
	6	450, 510, 540, 570, 600, 630	1.6641	1.0184
	6	440, 500, 540, 570, 600, 630	1.6748	0.9795
	5	450, 510, 550, 600, 630	1.8620	1.1517
	5	450, 510, 550, 600, 610	1.8663	1.1804
	5	440, 510, 550, 600, 630	1.8773	1.1283
	5	440, 510, 550, 600, 610	1.8798	1.1621
	5	450, 520, 550, 600, 610	1.8814	1.1691
	4	450, 530, 580, 620	2.2330	1.4693
	4	440, 520, 570, 610	2.2423	1.4106
	4	450, 520, 560, 610	2.2466	1.4750
	4	450, 530, 580, 610	2.2470	1.4766
	4	450, 520, 570, 610	2.2481	1.4856
	3	450, 540, 610	2.6980	1.7645
	3	440, 540, 610	2.7240	1.7260
	3	440, 530, 610	2.7314	1.7576
	3	450, 530, 610	2.7320	1.8284
	3	450, 550, 610	2.7909	1.9070

Table 3.16. Top five *n*-wavelength combinations (*n* = 3, 4, 5, 6) for lung tissue sample with Masson's trichrome stain. Pathological condition: pneumonia.

Sample and stain	Number of wavelengths	Wavelength combination (nm)	ΔE^*_{94} mean	ΔE^*_{94} SD
Lung (Pneumonia) *Masson's trichrome*	6	440, 460, 530, 540, 590, 620	1.9865	1.1460
	6	440, 460, 510, 550, 590, 620	2.0030	1.1693
	6	440, 450, 530, 540, 590, 620	2.0038	1.1482
	6	430, 460, 530, 540, 590, 620	2.0099	1.1403
	6	450, 460, 530, 540, 590, 620	2.0130	1.1758
	5	450, 530, 540, 590, 620	2.2166	1.2855
	5	450, 530, 540, 600, 620	2.2543	1.3127
	5	450, 530, 540, 590, 610	2.2571	1.2999
	5	450, 530, 540, 600, 630	2.2706	1.3116
	5	450, 520, 550, 590, 620	2.2707	1.3197
	4	450, 530, 590, 620	2.6015	1.5341
	4	450, 530, 540, 620	2.6050	1.5043
	4	450, 520, 580, 630	2.6089	1.5448
	4	450, 530, 570, 620	2.6117	1.4915
	4	450, 530, 560, 620	2.6162	1.5058
	3	450, 530, 620	2.9994	1.7151
	3	450, 530, 610	3.0232	1.7137
	3	450, 530, 600	3.0332	1.7672
	3	450, 520, 620	3.0468	1.7530
	3	450, 520, 600	3.0533	1.7659

Table 3.17. Top five *n*-wavelength combinations (*n* = 3, 4, 5, 6) for liver tissue sample with Masson's trichrome stain. Pathological condition: cirrhosis.

Sample and stain	Number of wavelengths	Wavelength combination (nm)	ΔE^*_{94} mean	ΔE^*_{94} SD
Liver (Cirrhosis) *Masson's trichrome*	6	450, 520, 550, 580, 610, 620	1.8810	1.1275
	6	450, 510, 550, 580, 610, 620	1.8862	1.1389
	6	450, 530, 550, 580, 610, 620	1.9100	1.1457
	6	450, 520, 560, 580, 610, 620	1.9127	1.1537
	6	450, 520, 550, 580, 610, 640	1.9154	1.1415
	5	450, 520, 560, 590, 620	2.1395	1.2853
	5	450, 530, 570, 610, 620	2.1410	1.3147
	5	450, 530, 570, 600, 630	2.1487	1.2952
	5	450, 530, 570, 600, 610	2.1490	1.3142
	5	450, 530, 560, 590, 620	2.1512	1.2755
	4	450, 530, 570, 620	2.4771	1.4846
	4	450, 530, 580, 620	2.4783	1.5056
	4	450, 530, 570, 610	2.4786	1.4848
	4	450, 530, 580, 610	2.5015	1.5136
	4	450, 520, 570, 610	2.5119	1.5272
	3	450, 540, 610	3.0271	1.9556
	3	450, 530, 610	3.0435	2.0373
	3	450, 530, 600	3.0614	1.9637
	3	450, 540, 620	3.0680	2.0019
	3	450, 540, 600	3.0752	1.9389

Table 3.18. Top five *n*-wavelength combinations (*n* = 3, 4, 5, 6) for artery tissue sample with EVG stain. Pathological condition: normal.

Sample and stain	Number of wavelengths	Wavelength combination (nm)	ΔE^*_{94} mean	ΔE^*_{94} SD
Artery (Normal) *EVG*	6	430, 450, 460, 530, 550, 610	1.7535	0.9411
	6	440, 460, 530, 550, 610, 620	1.7539	0.9367
	6	440, 450, 470, 530, 550, 610	1.7549	0.9178
	6	440, 450, 460, 530, 550, 610	1.7619	0.9227
	6	440, 460, 530, 550, 610, 640	1.7631	0.9305
	5	440, 460, 530, 550, 610	1.9082	0.9930
	5	440, 460, 530, 560, 610	1.9258	1.0191
	5	440, 460, 530, 550, 620	1.9291	0.9961
	5	440, 460, 530, 560, 620	1.9454	1.0182
	5	440, 460, 530, 550, 630	1.9498	1.0058
	4	440, 460, 550, 610	2.2994	1.2245
	4	440, 460, 540, 610	2.3002	1.2530
	4	450, 530, 550, 610	2.3020	1.3087
	4	450, 530, 560, 610	2.3075	1.3152
	4	450, 530, 550, 620	2.3077	1.3136
	3	450, 540, 610	2.6551	1.5285
	3	450, 540, 620	2.6613	1.5101
	3	450, 540, 630	2.6826	1.5088
	3	450, 550, 610	2.6954	1.5084
	3	450, 550, 620	2.6979	1.5196

Table 3.19. Top five *n*-wavelength combinations (*n* = 3, 4, 5, 6) for lung tissue sample with EVG stain.

Pathological condition: tumor.

Sample and stain	Number of wavelengths	Wavelength combination (nm)	ΔE^*_{94} mean	ΔE^*_{94} SD
Lung (Tumor) *EVG*	6	440, 460, 530, 560, 600, 620	1.6935	1.2827
	6	440, 460, 520, 550, 600, 620	1.7083	1.3116
	6	440, 460, 530, 560, 610, 630	1.7189	1.3011
	6	440, 460, 530, 560, 600, 640	1.7288	1.3128
	6	440, 460, 530, 560, 600, 610	1.7353	1.2936
	5	440, 460, 530, 560, 610	2.0873	1.6408
	5	440, 460, 520, 550, 610	2.0987	1.6559
	5	440, 460, 520, 560, 610	2.1113	1.6802
	5	450, 520, 550, 600, 620	2.1233	1.5976
	5	440, 460, 530, 570, 610	2.1276	1.6583
	4	450, 520, 550, 610	2.4773	1.8636
	4	450, 530, 570, 610	2.4933	1.8732
	4	440, 460, 530, 610	2.4983	2.0272
	4	450, 520, 550, 620	2.5154	1.8381
	4	450, 530, 580, 610	2.5155	1.9499
	3	440, 530, 610	2.8605	2.2832
	3	450, 530, 610	2.8740	2.2620
	3	440, 530, 620	2.9016	2.2592
	3	450, 530, 620	2.9090	2.2414
	3	450, 520, 610	2.9498	2.3480

Table 3.20. Top five *n*-wavelength combinations (*n* = 3, 4, 5, 6) for kidney tissue sample with Congo red stain.

Pathological condition: amyloidosis.

Sample and stain	Number of wavelengths	Wavelength combination (nm)	ΔE^*_{94} mean	ΔE^*_{94} SD
Kidney (Amyloidosis) *Congo red*	6	430, 450, 520, 550, 600, 630	1.3584	0.9099
	6	440, 450, 520, 550, 610, 620	1.3716	0.9695
	6	430, 450, 530, 560, 600, 630	1.3718	0.9190
	6	430, 450, 530, 550, 600, 630	1.3725	0.8211
	6	440, 460, 520, 550, 610, 620	1.3782	0.8049
	5	440, 520, 550, 610, 620	1.5673	0.9099
	5	450, 520, 550, 610, 620	1.5782	0.9695
	5	440, 530, 550, 610, 620	1.5795	0.9190
	5	440, 510, 550, 610, 620	1.5813	0.9421
	5	430, 450, 530, 570, 630	1.5875	0.9129
	4	440, 530, 590, 620	1.7783	1.0460
	4	440, 530, 610, 620	1.7789	1.0664
	4	440, 530, 570, 620	1.7845	1.0397
	4	440, 530, 570, 630	1.7917	1.0235
	4	450, 530, 570, 620	1.8015	1.0587
	3	440, 530, 610	2.0466	1.1316
	3	450, 530, 610	2.0718	1.1794
	3	440, 530, 630	2.0986	1.1866
	3	460, 530, 610	2.1010	1.2417
	3	440, 520, 610	2.1152	1.2014

Table 3.21. Top five *n*-wavelength combinations (*n* = 3, 4, 5, 6) for lung tissue sample with GMS stain. Pathological condition: infection.

Sample and stain	Number of wavelengths	Wavelength combination (nm)	ΔE^*_{94} mean	ΔE^*_{94} SD
Lung (Infection) *GMS*	6	440, 460, 520, 530, 560, 620	mean	2.0273
	6	440, 460, 520, 550, 590, 630	2.3811	2.0938
	6	440, 460, 530, 550, 590, 630	2.3822	2.1397
	6	440, 460, 530, 540, 590, 630	2.3859	2.1109
	6	440, 460, 520, 550, 600, 630	2.3861	2.0983
	5	440, 460, 520, 560, 620	2.6255	2.3433
	5	440, 460, 530, 560, 620	2.6320	2.3270
	5	440, 460, 530, 570, 630	2.6356	2.3046
	5	440, 460, 530, 560, 630	2.6371	2.2995
	5	440, 460, 520, 550, 620	2.6413	2.3324
	4	450, 520, 550, 620	3.1171	2.7132
	4	450, 530, 560, 620	3.1239	2.7592
	4	450, 520, 560, 620	3.1250	2.7671
	4	450, 530, 550, 620	3.1265	2.7498
	4	450, 520, 560, 630	3.1385	2.7691
	3	450, 540, 620	3.5256	3.1216
	3	450, 540, 630	3.5778	3.1559
	3	450, 530, 620	3.5909	3.2012
	3	440, 540, 620	3.6053	3.2537
	3	440, 530, 620	3.6429	3.3412

Table 3.22. Top five *n*-wavelength combinations (*n* = 3, 4, 5, 6) for esophagus tissue sample with Alcian blue stain. Pathological condition: Barrette's esophagus.

Sample and stain	Number of wavelengths	Wavelength combination (nm)	ΔE^*_{94} mean	ΔE^*_{94} SD
Esophagus (Barrette) *Alcian blue*	6	440, 450, 530, 540, 570, 620	1.0270	0.8018
	6	440, 450, 520, 530, 570, 620	1.0382	0.7680
	6	440, 450, 530, 540, 570, 610	1.0424	0.8263
	6	450, 460, 530, 540, 570, 620	1.0473	0.8981
	6	430, 450, 530, 540, 570, 620	1.0560	0.8261
	5	450, 530, 540, 570, 620	1.1583	0.9288
	5	450, 520, 530, 570, 620	1.1633	0.8878
	5	440, 450, 530, 570, 620	1.1675	0.8749
	5	450, 530, 540, 570, 610	1.1702	0.9468
	5	450, 520, 530, 570, 610	1.1802	0.9159
	4	450, 530, 570, 620	1.2835	0.9765
	4	450, 530, 570, 610	1.2938	0.9939
	4	450, 530, 560, 610	1.3062	0.9827
	4	450, 530, 560, 620	1.3066	0.9738
	4	450, 530, 550, 610	1.3092	0.9851
	3	450, 530, 600	1.4732	1.1521
	3	450, 530, 610	1.4869	1.1192
	3	440, 530, 600	1.4989	1.0867
	3	440, 530, 610	1.5116	1.0695
	3	430, 530, 600	1.5210	1.0624

Table 3.23. Top five *n*-wavelength combinations (*n* = 3, 4, 5, 6) for kidney tissue sample with Jones stain. Pathological condition: diabetes.

Sample and stain	Number of wavelengths	Wavelength combination (nm)	ΔE^*_{94} mean	ΔE^*_{94} SD
Kidney (Diabetes) *Jones*	6	450, 510, 540, 560, 590, 630	3.0034	2.4221
	6	450, 510, 540, 560, 590, 620	3.0144	2.5202
	6	450, 510, 540, 560, 600, 630	3.0326	2.4133
	6	450, 510, 530, 540, 560, 600	3.0367	2.1101
	6	450, 510, 540, 560, 580, 630	3.0500	2.4474
	5	450, 510, 540, 560, 600	3.4091	2.5875
	5	450, 510, 530, 560, 600	3.4471	2.7370
	5	450, 500, 530, 560, 600	3.4884	2.8865
	5	450, 510, 540, 560, 610	3.5031	2.6354
	5	450, 500, 540, 560, 600	3.5136	2.8580
	4	450, 520, 560, 600	3.9921	3.2696
	4	450, 520, 550, 600	4.0385	3.2317
	4	450, 530, 560, 600	4.0486	3.1799
	4	450, 520, 560, 610	4.0807	3.3108
	4	450, 520, 560, 620	4.0845	3.3345
	3	450, 520, 590	4.9340	4.0862
	3	450, 530, 590	4.9921	3.9970
	3	460, 520, 590	5.0394	4.1909
	3	450, 520, 600	5.0617	4.1103
	3	440, 520, 590	5.0776	4.1770

Table 3.24. Top five *n*-wavelength combinations (*n* = 3, 4, 5, 6) for lung tissue sample with Gram stain. Pathological condition: pneumonia.

Sample and stain	Number of wavelengths	Wavelength combination (nm)	ΔE^*_{94} mean	ΔE^*_{94} SD
Lung (Pneumonia) *Gram*	6	430, 450, 460, 520, 550, 620	1.8554	1.0572
	6	430, 450, 460, 510, 550, 620	1.8628	1.0874
	6	430, 450, 460, 530, 550, 620	1.8717	1.0710
	6	430, 450, 460, 530, 560, 620	1.8737	1.0687
	6	430, 450, 460, 530, 570, 620	1.8762	1.1040
	5	430, 450, 520, 550, 620	2.1207	1.2615
	5	430, 450, 530, 550, 620	2.1233	1.2423
	5	430, 450, 530, 560, 620	2.1234	1.2643
	5	440, 460, 520, 560, 620	2.1366	1.2333
	5	430, 450, 530, 570, 620	2.1376	1.2771
	4	440, 520, 550, 620	2.4706	1.5909
	4	440, 510, 550, 620	2.4737	1.5932
	4	440, 520, 560, 620	2.4873	1.5872
	4	440, 530, 560, 620	2.4979	1.5611
	4	440, 530, 570, 620	2.4994	1.6074
	3	440, 550, 620	2.8927	1.7386
	3	440, 550, 610	2.8985	1.7692
	3	440, 550, 630	2.9580	1.7524
	3	450, 540, 610	2.9582	1.8089
	3	450, 530, 610	2.9686	1.9252

Table 3.25. Top five *n*-wavelength combinations (*n* = 3, 4, 5, 6) for Papanicolaou smear sample with Papanicolaou stain. Pathological condition: cervical cancer.

Sample and stain	Number of wavelengths	Wavelength combination (nm)	ΔE^*_{94} mean	ΔE^*_{94} SD
Pap smear (Cancer) *Pap stain*	6	440, 460, 520, 550, 590, 630	1.7420	1.4599
	6	440, 460, 520, 550, 600, 630	1.7515	1.4732
	6	440, 460, 530, 550, 590, 630	1.7558	1.6221
	6	440, 460, 520, 540, 580, 630	1.7670	1.6372
	6	440, 460, 530, 550, 600, 630	1.7683	1.6720
	5	440, 460, 520, 560, 610	2.0165	1.9927
	5	440, 460, 520, 550, 610	2.0207	1.6979
	5	440, 460, 530, 550, 610	2.0544	1.8744
	5	440, 470, 520, 560, 610	2.0560	2.0230
	5	450, 460, 520, 550, 610	2.0593	1.7388
	4	440, 520, 560, 610	2.3213	2.2830
	4	440, 520, 550, 610	2.3284	2.0345
	4	450, 520, 550, 610	2.3439	2.0231
	4	440, 530, 550, 610	2.3569	2.1608
	4	450, 520, 560, 610	2.3663	2.2963
	3	440, 540, 610	2.7606	2.4589
	3	440, 540, 630	2.7980	2.6536
	3	450, 540, 610	2.7985	2.5172
	3	440, 540, 620	2.8319	2.4943
	3	450, 540, 630	2.8473	2.7261

Chapter 4. Edge sparsity-based robust autofocusing algorithm

Autofocusing, i.e., the automatic estimation of the sample-to-sensor distance, is essential to digital holographic imaging. The previously discussed hologram reconstruction and phase retrieval methods in Chapters 1-2 all require the accurate focus distance of the hologram as a prerequisite. Previously used autofocusing criteria exhibit challenges when applied to, e.g., connected objects with different optical properties. Furthermore, in some of the earlier autofocusing criteria the polarity, i.e., whether to search for the peak or the valley as a function of depth, changes for different types of samples, which creates another challenge. In this chapter, a robust and accurate autofocusing criterion is introduced that is based on the edge sparsity of the complex optical wavefront, which is termed as the Sparsity of the Gradient (SoG). The success of SoG was demonstrated by imaging a wide range of objects, including resolution test targets, stained and unstained Papanicolaou smears, stained tissue sections, and blood smears.

Part of this chapter has been previously published in: Y. Zhang, H. Wang, Y. Wu, M. Tamamitsu, and A. Ozcan, "Edge sparsity criterion for robust holographic autofocusing," Optics Letters **42**, 3824 (2017) (reused with permission from Ref. [97], Optical Society of America).

4.1 Introduction

Digital holography [103] enables computational refocusing within a 3D sample volume after the image acquisition. This unique advantage has made it a useful technique in various applications such as bio-fluid analysis [40], dynamic 3D tracking of sperms [30], monitoring of living cells [104], among many others. Recently, it was also shown that digital holography in a lensless in-line format can achieve high-throughput imaging of tissue slides and cell smears on a chip [35,70], as discussed in Chapters 2-3.

Digital refocusing and reconstruction of holograms rely on the precise knowledge of the defocus distance (i.e., the "*z* distance") of the object of interest. A widely-accepted autofocusing method involves digital refocusing of a hologram using various *z* distances, where a certain function, i.e., an autofocusing criterion, is evaluated based on this set of refocused images. The *z* distance that corresponds to the maximum (or sometimes the minimum) of this criterion is used as the focus distance of the object for that given hologram. A good autofocusing criterion should in general be unimodal over a wide range of *z* distances, and be accurate for various types of samples [105].

There have been numerous autofocusing criteria demonstrated so far for different holographic imaging applications and they were successfully used to image various samples [104,106–112] . For example, Gillespie *et al.* proposed to use self-entropy (SEN) as an autofocusing criterion in digital holography and successfully applied it to some test images [106]. As an alternative, Liebling *et al.* used the sparsity of the Fresnelet coefficients (FRES) as an autofocusing criterion and applied it for imaging resolution test targets [107]. Dubois *et al.* used the integrated amplitude (AMP) as an autofocusing criterion for pure amplitude and pure phase objects, with opposite polarities [108]. Later a modified version of AMP was also proposed using integrated high-pass filtered amplitude (HPA), which was demonstrated to lead to a minimum for both amplitude and phase objects [109]. Langehanenberg *et al.* compared four different autofocusing criteria for imaging of pure-phase objects, including the summed weighted power spectrum (SPEC), variance (VAR), summed gradient (GRA), and summed Laplacian (LAP) to validate the applicability of SPEC and GRA on pure-phase objects [104]. Memmolo *et al.* proposed to use the contrast texture measure (i.e., the Tamura coefficient, TC) as an autofocusing criterion and demonstrated successful results based on off-axis holography using macroscopic objects [110]. Later, Memmolo

et al. also used a sparsity measure, i.e., the Gini index (GI), as an autofocusing criterion to image microscopic objects, e.g., cells [111]. Recently, Lyu *et al.* have used the axial magnitude differential (DIF) as another autofocusing criterion and discussed its applicability to amplitude-contrast and phase-contrast samples [112].

Despite all this wide variety of available autofocusing criteria, the choice of the specific criterion is, unfortunately, still highly *subjective* depending on the object type or application of interest. Development of a robust and accurate autofocusing criterion for digital holography that works universally well for different types of samples is a challenging task for several reasons. *First*, the coherent diffraction of light in holography results in complex interference patterns, in addition to speckle and multiple reflection related interference artifacts, instead of providing homogeneous smoothening as in the case of incoherent microscopy and photography. Therefore, the sharpness or the high-frequency spatial content of a holographic image does not necessarily diminish with defocusing. Moreover, without phase retrieval, the twin image artifact in in-line holography makes autofocusing more challenging. These explain some of the failures of directly applying autofocusing criteria developed for incoherent imaging to holography. *Second*, different mechanisms of light-matter interaction result in different complex-valued transmission functions corresponding to the samples. For example, a phase object such as a transparent and unlabeled cell interacts with the illumination light mainly through perturbations to the optical phase of the transmitted wavefront, leaving its amplitude mostly unchanged. On the other hand, an amplitude object such as a metal-coated resolution test target, mainly modulates the amplitude of the transmitted wave, whereas a *stained* cell or tissue section that is semitransparent would both modulate the phase and amplitude. These variations among different types of objects make some of the autofocusing criteria that are based on e.g., the sharpness of the features, contrast, sparsity

or other properties of the amplitude channel of the complex field less robust. Furthermore, many of these criteria change polarity for amplitude-contrast vs. phase-contrast samples, and fail or perform sub-optimal for mixed amplitude- and phase-contrast samples [108,112]. Some of the previous work also explored applying a criterion on the phase channel of the complex field for autofocusing [106], but these approaches suffer from the same limitations discussed earlier, besides facing phase wrapping related challenges.

4.2 Materials and methods

Here we propose a robust autofocusing criterion for digital holography that performs accurate depth focusing across a wide range of samples, including amplitude-only, phase-only and mixed object types. We termed this criterion as Sparsity of the Gradient (SoG), which is based on the ***edge sparsity*** of an object's in-focus image. SoG of a complex optical wavefront U is defined as,

$$\mathrm{SoG}(U) = \mathrm{S}(|\nabla U|) \tag{4.1}$$

where ∇ is the gradient operator, $|\cdot|$ is the modulus operator, and $\mathrm{S}(\cdot)$ is a sparsity measure. $|\nabla U|$ can be calculated for a complex-valued image as $\left|\nabla U\right|_{i,j}^2 = \left|U_{i,j} - U_{i,j-1}\right|^2 + \left|U_{i,j} - U_{i-1,j}\right|^2$.

Under the SoG framework, we used two different sparsity measures, GI and TC. which we term as Gini of the Gradient (GoG) and Tamura of the Gradient (ToG), respectively. One should note that TC has been recently proven to be a sparsity measure [98]. These two sparsity measures (GI and TC) were chosen to quantify the edge sparsity of a complex image since they exhibit advantages, such as invariance under scaling, compared to other sparsity measures [98,113].

GI is defined for a real and non-negative image (C) as:

$$\mathrm{GI}(C) = 1 - 2\sum_{k=1}^{N} \frac{a_{[k]}}{\mathrm{sum}(C)}\left(\frac{N-k+0.5}{N}\right) \tag{4.2}$$

where $a_{[k]}$ is the k-th sorted entry of the image matrix, C, in ascending order, $k = 1, \ldots N$, and sum(C) is the sum of all the entries of the image. TC is defined as:

$$\mathrm{TC}(C) = \sqrt{\sigma(C)/\langle C \rangle} \tag{4.3}$$

where $\sigma(\cdot)$ is the standard deviation, and $\langle \cdot \rangle$ is the mean.

The design of the SoG criterion for autofocusing assumes that the images of natural objects are mostly composed of flat regions and sharp edges, a widely accepted assumption utilized in image compression, image denoising, etc. When a refocused complex optical wavefront corresponding to a physical object is *in focus*, sharp edges should be sparse i.e., the sharpest transitions in the image should only take up a small fraction of the image's total area.

As opposed to most of the other autofocusing criteria that operate on the amplitude channel of a refocused image, SoG operates directly on the *complex* refocused image, which makes it much more general and robust for amplitude-contrast, phase-contrast, or mixed object types. The gradient operator in the definition of SoG can sense the sharp changes in an image regardless of the specific amplitude and/or phase-contrast mechanism of the object of interest. As a consequence, SoG is expected to always reach its ***maximum*** at the correct focus distance regardless of the type of the object, which is another advantage over some of the previously reported autofocusing criteria that usually exhibit opposite polarity for amplitude- vs. phase-contrast objects and an ambiguous polarity for mixed amplitude/phase-contrast objects.

4.3 Results and discussion

To compare the performance of GoG and ToG against the state-of-the-art, we selected 8 previously proposed autofocusing criteria including SEN, FRES, HPA, SPEC, GRA, TC, GI, and DIF. Note that VAR and LAP [104] criteria are analogous to TC and GRA [104,110], respectively,

and therefore they were not duplicated in our comparison. We used 5 different types of quasi-planar samples to validate our method, including a USAF resolution test target, an unstained Pap smear, a stained Pap smear (Pap stain, ThinPrep preparation), a 4 μm thick H&E-stained lung tissue section, and a Wright-stained whole blood smear. Among these objects, the USAF test target can be considered as an amplitude-contrast object, the unstained Pap smear can be considered as a phase-contrast object, while the others can be considered as mixed amplitude- and phase-contrast objects. We validated that both GoG and ToG outperform the existing autofocusing criteria, providing superior accuracy and robustness for different types of amplitude-contrast, phase-contrast and mixed amplitude- and phase-contrast objects.

Moreover, all the digital autofocusing experiments reported here were performed without any phase-retrieval using in-line holograms of spatially-connected samples that violate the "weakly-scattering" condition; stated differently, the refocused images were severely contaminated by the twin image artifact, making autofocusing much more challenging. This demonstrates that GoG and ToG are robust and accurate even under noisy conditions, and also illustrates their practical usefulness for in-line holography, where the knowledge of the z distances is usually a prerequisite for the subsequent phase retrieval step, and therefore autofocusing on the non-phase-retrieved hologram is usually an inevitable initial step for image reconstruction [35,70]. We also tested GoG and ToG on various phase-retrieved holograms, where they also performed very well [98]. Therefore, we believe GoG and ToG (or SoG in general) can also be applied to off-axis holographic imaging.

The raw holograms corresponding to the test objects were captured using a lens-free in-line holography setup, with pixel super-resolution implemented on a chip [35], achieving an effective pixel size of ~0.37 μm at both the hologram and object reconstruction planes. To create the "ground

truth" focus distance for each sample, we took the following two steps: first, multi-height phase retrieval [35] using 8 hologram heights was performed using manually found *relative* z distances with respect to the first hologram height. The relative z distances were found such that their refocused images looked most alike. Second, we used the *phase-retrieved complex-valued hologram* at the plane closest to the sample to perform manual refocusing to create the ground truth *absolute* focus distance based on visual judgement. We used z increments of ~1 μm, as any change in z below 1 μm is hardly noticeable to the human eye for this imaging system.

For each autofocusing criterion that we used in our comparison, in order to rapidly find the resulting focus distance, to be compared with the ground truth focus distance discussed earlier, we custom-wrote a search algorithm based on the golden-section search method [114], composed of 5 steps. (1) Using the selected autofocusing criterion, conduct a rough scan between z = 100 μm and z = 800 μm with a step size of 10 μm. z = 0 μm defines the plane of the imager chip. (2) Define a 40 μm search range around the maximum (or minimum, depending on the selected criterion) of the rough scan in (1). (3) Evaluate the focus criterion at $4M$+1 equally spaced z distances spanning the search range defined in (2). Identify the maximum (or minimum) of the search. We used M = 3. (4) Check unimodality based on these $4M$+1 points. If not unimodal, shrink the search range in half around the maximum (or minimum) point, where $2M$ new points need to be evaluated. Repeat until unimodality is reached. (5) After unimodality is confirmed, conduct iterative golden-section search within the search range to identify the maximum (or minimum). The search stops when the search range is < 0.01 μm.

Based on this evaluation process, the autofocusing accuracies of 10 different criteria (GoG, ToG, HPA, GRA, SEN, GI, SPEC, DIF, TC and FRES) were compared to the gold standard focus distances for different objects (Table 4.1). To overcome the ambiguity of polarity based on the

sample type, we automatically searched for both the peaks ("Max") and valleys ("Min") for all the criteria, except for GoG, ToG, and FRES (only Max) and HPA (only Min). To better visualize the results, we color-coded Table 4.1 with a colormap, representing the errors made in focus distances, ranging between 0 and 10 µm. In the same table, >10 µm errors were colored as gray, considered as "*failure*". "NaN" represents a case where Max/Min criterion is found at the boundary of the search range. Evidently, GoG and ToG performed very well for all the sample types. Their largest errors (1.66 µm and 1.52 µm, respectively) occurred for the stained Pap smear, which are comparable to the 1 µm uncertainty resulting from human error in manual focusing.

Table 4. 1. Absolute errors (in µm) of various autofocusing criteria on different samples. For all criteria except GoG, ToG, HPA and FRES, both minimum and maximum were searched.

Method	GoG	ToG	HPA	GRA		SEN		GI		SPEC		DIF		TC		FRES
Polarity	Max	Max	Min	Min	Max	Min	Max	Min	Max	Min	Max	Min	Max	Min	Max	Max
USAF target	0.96	1.02	1.11	494.1	0.07	0.84	505.2	NaN	0.34	518.1	12.52	NaN	179.6	NaN	0.18	1.33
Unstained Pap Smear	0.10	0.04	0.98	0.06	104.3	10.54	436.0	0.70	NaN	0.00	148.5	127.0	0.06	0.93	NaN	NaN
Stain Pap Smear	1.66	1.52	0.75	3.14	9.27	NaN	79.00	68.66	NaN	130.9	12.32	227.4	353.9	71.52	NaN	6.28
Lung tissue	0.12	0.54	NaN	2.35	6.97	16.46	296.1	17.59	NaN	NaN	6.93	19.90	334.4	18.64	NaN	4.09
Blood smear	1.08	1.10	19.78	4.38	2.90	5.21	81.77	41.02	7.14	NaN	0.89	2.23	282.1	41.00	7.85	NaN

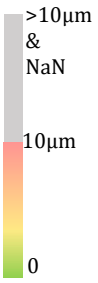

For the other autofocusing criteria, first let us focus on their performance on the USAF test target (an amplitude-contrast object) and the unstained Pap smear (a phase-contrast object). If we consider the smaller error of the two polarities (Max vs. Min) wherever applicable, HPA, GRA, GI and TC had errors less than or around 1 µm. We also observed polarity inversion for GRA, GI and TC when switched from the USAF test target to an unstained Pap smear sample, which has also been reported in the literature [111,112]. The other criteria, SEN, SPEC, DIF and FRES, failed for at least one of the two samples (Table 4.1). As for the performance of these autofocusing criteria for the other three samples, including the stained Pap smear, lung tissue and blood smear

samples, we see that HPA, SEN, GI, SPEC, DIF, TC, and FRES each failed for at least one sample. GRA had >2 μm but <4 μm errors for all three samples, but the polarity changed among the objects, which might be due to the relative extent of amplitude-contrast and phase-contrast of each sample.

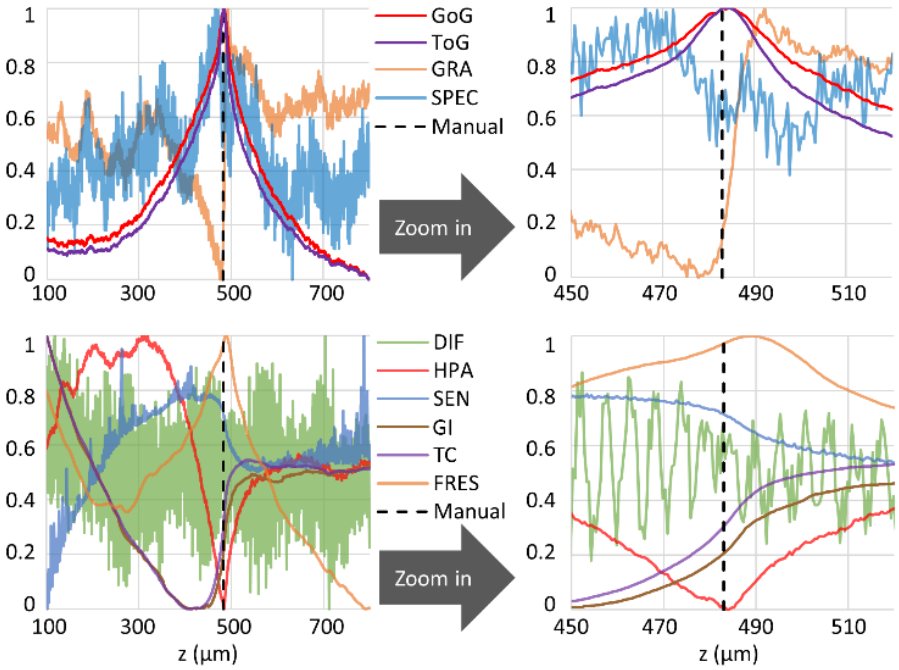

Figure 4. 1. Different autofocusing criteria as a function of *z*, using a stained Pap smear sample. To ensure the visibility of the curves, the criteria were divided in two parts (upper and lower panels). The correct z distance is shown with a dashed line.

To get more insights into the behavior of different autofocusing criteria, we took the stained Pap smear sample as an example, and plotted the values of each criterion against *z*, as shown in Fig. 4.1. The SPEC, SEN, and DIF exhibit significant oscillations which make it difficult to search for a peak or valley. GI and TC do not have a peak/valley at the actual z, but they both have a large slope around it. GRA has a peak and a valley on the opposite sides of the correct z value, and the curve is also slightly fuzzy. FRES and HPA each have a peak/valley near the correct z, but are not unimodal. GoG and ToG, on the other hand, are overall smooth, unimodal, and each have a strong global peak close to the correct z value, as desired.

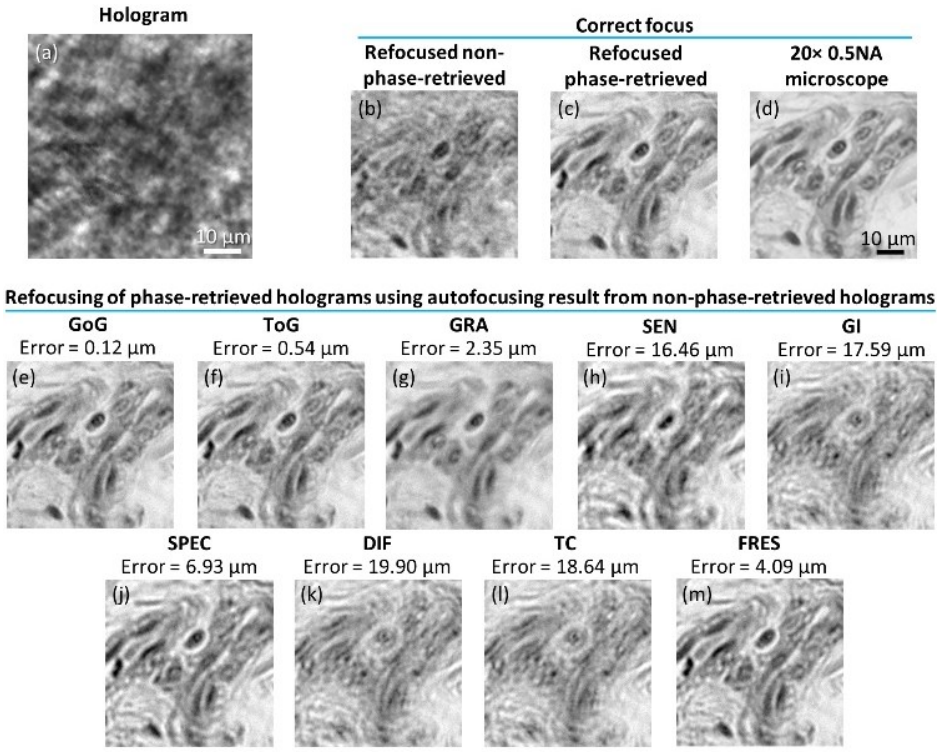

Figure 4. 2. Comparison of the autofocusing accuracy of different criteria using a lung tissue sample. (a) Hologram intensity. **(b-d)** Holographic and 20× 0.5NA microscope images at the correct focus. **(e-m)** Refocused image amplitude using all the autofocusing criteria except HPA, which failed to find a minimum. The smaller autofocusing error between the Min and Max is displayed, wherever applicable.

Fig. 4.2 further provides a comparison of the refocusing results based on these different criteria that we used. To enable a better visual judgement, the phase-retrieved hologram of a lung tissue sample using 8 sample heights was refocused, where each focus distance was estimated from the non-phase-retrieved hologram. Fig. 4.2 (e-m) clearly shows that GoG and ToG provide the best in-focus images, which contain sharp features of the cells and the tissue morphology that agree well with a 20× 0.5NA microscope objective image.

Summarizing this comparison, all the criteria other than GoG, ToG and GRA failed for at least one sample. The average errors for GoG, ToG and GRA for all the samples were 0.78 μm, 0.84 μm and 1.70 μm, respectively, where the smaller errors between Min and Max were considered

for quantification of the error in GRA (to its advantage). Polarity inversion was observed among different sample types as a disadvantage of GRA, which may cause confusion when autofocusing an unknown sample. An additional challenge with any autofocusing criterion that has polarity inversion is that there can be a particular specimen that has a certain level of amplitude- and phase-contrast such that it is exactly at (or close to) the point of polarity inversion, which can create a singularity point and the correct z cannot be determined.

Although GoG and ToG performed very similarly for dense objects, we also noticed that for naturally sparse samples of small size, such as dilute *Giardia lamblia* cysts and sperm cells, the user sometimes needs to choose a region of interest that tightly bounds the object of interest when using GoG. This constraint is relaxed when using ToG, leading to more flexibility. Mathematical origins of this different behavior of GoG and ToG for naturally sparse samples are discussed in detail in [98].

In addition to the autofocus criteria discussed so far, we also tested the recently proposed Complex Ratio [115], which failed for some of the samples. We also tried cascading existing criteria onto the gradient of the complex refocused image, creating various new criteria such as "AMP of the Gradient", "SEN of the Gradient", "SPEC of the Gradient", etc. These also failed for some of the samples, and therefore were not included in our comparison.

Table 4. 2. Comparison of computation times.

Method	GoG	ToG	HPA	GRA	SEN	GI	SPEC	DIF	TC	FRES
Time(ms)	177	134	106	97	170	142	109	190	114	392

Computational efficiency is another important feature of an autofocus criterion that needs to be considered. We performed a comparison of the run-times of different autofocusing criteria using a laptop computer equipped with an Intel Core i7-7700HQ CPU @ 2.80 GHz and 16 GB of

memory; GPU acceleration was not used. The total time required to refocus a hologram of 1024×1024 pixels and evaluate each autofocusing criterion is summarized in Table 4.2. For this image size, GoG and ToG are ~1.8 and ~1.4 times slower, respectively, compared to the most computationally efficient focusing criterion tested here (GRA).

4.2 Conclusions

In conclusion, we demonstrated a robust and accurate holographic autofocusing criterion that is based on the edge sparsity of the complex wavefront, termed Sparsity of Gradient (SoG). Under the SoG framework, two individual metrics, i.e., Tamura coefficient of Gradient (ToG) and Gini index of Gradient (SoG) are proposed. Analysis showed that it outperforms existing autofocusing approaches for a wide range of objects with different amplitude- and phase-contrast compositions, at the cost of a modest increase in computation time.

Chapter 5. Three-dimensional lens-free microscopy of optically cleared tissue

In Chapters 2-3, lens-free computational microscopy of thin-sectioned and stained histological tissue sections is presented. However, high-throughput sectioning and optical imaging of tissue samples using traditional immunohistochemical techniques can be costly and inaccessible in resource-limited areas. In this chapter, 3D imaging and phenotyping in optically transparent tissue using lens-free holographic on-chip microscopy is demonstrated as a low-cost, simple, and high-throughput alternative to conventional approaches. The tissue sample is passively cleared using a simplified CLARITY method and stained using diaminobenzidine to target cells of interest, enabling brightfield optical imaging and 3D sectioning of thick samples. The lens-free computational microscope uses pixel super-resolution and multi-height phase recovery algorithms to digitally refocus throughout the cleared tissue and obtain a 3D stack of complex-valued images of the sample, containing both phase and amplitude information. We optimized the tissue clearing and imaging system by finding the optimal illumination wavelength, tissue thickness, sample preparation parameters and the number of heights of the lens-free image acquisition, and implemented a sparsity-based denoising algorithm to maximize the imaging volume and minimize the amount of the acquired data, while also preserving the contrast-to-noise ratio of the reconstructed images. As a proof-of-concept, we achieved 3D imaging of neurons in a 200 μm-thick cleared mouse brain tissue over a wide field-of-view (FOV) of 20.5 mm^2. The lens-free microscope also acquired more than an order-of-magnitude less amount of raw data compared to a conventional scanning optical microscope imaging the same sample volume. Being low cost, simple, high throughput and data-efficient, we believe that this CLARITY-enabled computational

tissue imaging technique could find numerous applications in biomedical diagnosis and research in low-resource settings.

Part of this chapter has been previously published in: Y. Zhang, Y. Shin, K. Sung, S. Yang, H. Chen, H. Wang, D. Teng, Y. Rivenson, R. P. Kulkarni, and A. Ozcan, "3D imaging of optically cleared tissue using a simplified CLARITY method and on-chip microscopy," Science Advances **3**, e1700553 (2017) (reused with permission from Ref. [36], AAAS).

5.1 Introduction

Chronic diseases such as cancer are increasing in the developing world [116,117]. To accurately diagnose and treat such diseases, tissue biopsies are necessary and widely considered among the gold standard techniques. However, in many developing countries, the infrastructure to process tissue biopsies may be limited which can lead to delays and inaccuracies in diagnosis and thus cause more advanced diseases [118]. The current gold standard diagnostic methods, e.g., tissue biopsy and histopathological analysis, require tissue preparation facilities and complex procedures. The high cost of equipment and the lack of trained healthcare professionals may result in delays in diagnosis. Although technological advances have allowed for physicians to remotely access medical data to perform diagnosis, there still remains an urgent need for reliable and inexpensive means for disease identification, particularly in low-resource settings, for pathology, biomedical research, and related applications.

The CLARITY technique offers a unique method for whole tissue biopsies to be labeled and imaged without the need for serial sectioning [119–121]. This technique preserves spatial relationships and tissue microstructures by forming a tissue-hydrogel hybrid with increased permeability for deep optical interrogation, which can be useful for 3D mapping and identification of rare markers [119,122]. The simplified CLARITY method (SCM) [123] creates optically

transparent tissue with proteins and nucleic acids intact using an easy-to-follow protocol without the need for any additional equipment. Based on the passive CLARITY technique (PACT) [124], SCM forms a hydrogel matrix throughout the tissue with the polymerization of acrylamide to maintain tissue integrity [123,124]. The light-scattering due to endogenous lipids within the tissue are then passively eliminated using an inexpensive detergent solution, and the intact tissue can be specifically labeled for multiple markers of interest.

Fluorescent microscopy has been typically used to image CLARITY samples, as most tissue clearing methods have been developed for labeling using fluorescent probes [125–128]. However, many laboratories in resource-limited settings have little or no access to high-cost microscopy equipment and filter sets required for fluorescence imaging. Colorimetric staining [123] serves as an alternative and cost-effective method of specific labeling that is compatible with brightfield 3D imaging modalities, also enabling the use of portable imaging devices. In addition, it allows for the specimen to be imaged repeatedly without any degradation in quality, while photobleaching and signal fading may occur in a fluorescently stained sample [129].

Lens-free holographic on-chip microscopy can be an ideal complementary technique to enable colorimetric phenotyping of cleared tissue using SCM in low resource settings [30,34,35,44,47–50,53,55,59,63,130]. Our lens-free on-chip microscope design (see Fig. 5.1(a)) works in the brightfield transmission mode, where the sample is illuminated by a partially coherent light source, with a large illumination aperture that is placed 5-10 cm above the sample (z_1 distance), and the holographic shadow of the sample is captured by the image sensor chip positioned in close proximity to the sample (z_2 distance < 1-2 mm). The light that is scattered by the sample volume interferes with the unscattered light, forming the sample's in-line hologram [8,131–136]. For highly scattering and/or absorbing samples such as *uncleared* tissue, the sample needs to be

sectioned into thin slices, typically under 10 µm, to be successfully imaged in transmission mode [35,44,49]. If the sample is too thick, the photons that are transmitted will likely have undergone multiple random scattering events along their path, causing loss of useful information as well as a reduction in signal-to-noise ratio. The CLARITY process greatly reduces such unwanted scattering and absorption by removing most lipids while maintaining proteins and

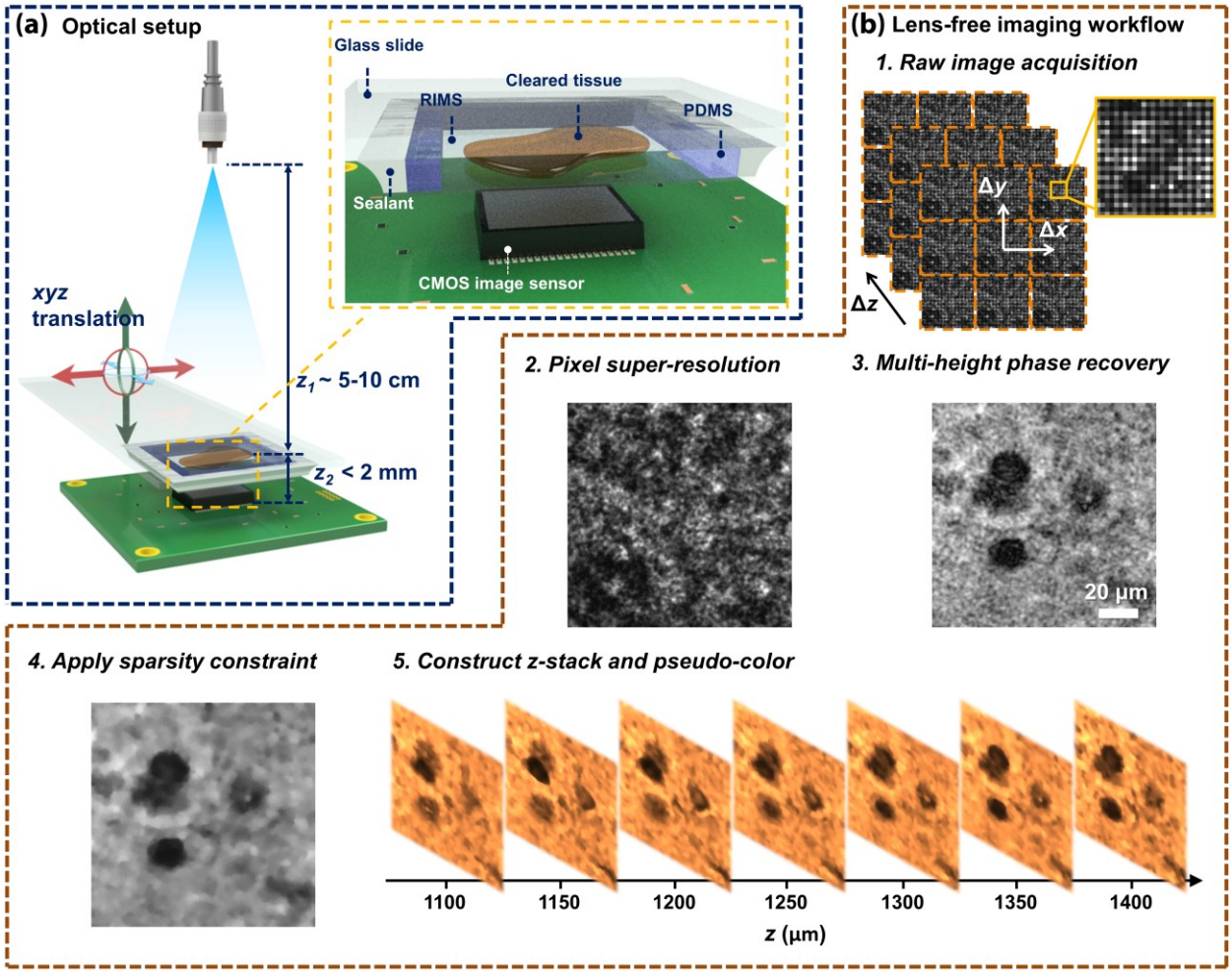

Figure 5. 1. Lens-free on-chip microscopy setup and image processing steps. (a) Schematic of the lens-free on-chip imaging setup. The cleared tissue is loaded in a PDMS/glass chamber filled with a refractive index matching solution. A sealant is applied on the sides to avoid evaporation and leakage. **(b)** Lens-free image processing workflow is outlined.

nucleic acids intact, thus increasing the effective imaging depth (i.e., the sample thickness that can be reconstructed/imaged).

Here, we demonstrate lens-free 3D imaging of SCM-prepared tissue samples stained with 3,3'-Diaminobenzidine (DAB), which reduces the cost and complexity associated with traditional CLARITY techniques, while also introducing portability. To maximize the volume of the imaged tissue by our on-chip microscope and minimize the amount of acquired data, while also preserving a good contrast-to-noise ratio (CNR) in our images, we optimized the illumination wavelength, tissue thickness, pH of the staining solution, and the number of heights used in lens-free on-chip image acquisition. Furthermore, we exploited the natural sparsity of the holographically reconstructed images to effectively remove image artifacts resulting from random scattering of the background and the interference from out-of-focus cells. Based on these optimizations, we achieved 3D holographic imaging of a 200 μm-thick section of mouse brain tissue over a FOV ~ 20.5 mm^2 using parvalbumin, a common protein found in a subset of neurons, as the target marker. We also confirmed that the holographically reconstructed sections of the brain tissue agree well with the images acquired using a high-end scanning optical microscope. Moreover, to image the same 3D tissue volume, the lens-free microscope acquires ~21 times fewer number of raw images (corresponding to ~11 times less image data), and can be over two orders of magnitude faster compared to a conventional scanning optical microscope that images the same sample volume. With the advantages of being low cost, simple, high throughput and data-efficient, this SCM-enabled computational tissue imaging method can potentially be used for disease diagnosis and biomedical research in resource-limited environments.

5.2 Materials and Methods

Tissue clearing

Whole mouse brains were harvested according to the UCLA Institutional Animal Care and Use Committee (IACUC) guidelines, and all experimental procedures were approved by the IACUC. Mice were anesthetized with pentobarbital and perfused transcardially with saline followed by 4% paraformaldehyde in 1X phosphate-buffered saline (PBS). Brains were removed, postfixed overnight at 4°C, and embedded in 3% Bactoagar. Free-floating coronal sections (50, 100, 200 μm) were collected using a vibratome (Leica Microsystems). Alternatively, the 200 μm thickness can be manually cut using a razor blade with spacers to reduce equipment complexity.

The tissue sections were incubated overnight at 4°C in a 4% acrylamide solution (Bio-Rad) containing 0.5% w/v of the photoinitiator 2,2'-Azobis[2-(2-imidazolin-2-yl)propane]dihydrochloride (VA-044, Wako Chemicals Inc., USA). Polymerization of the acrylamide was then initiated with an incubation at 37°C for 3 hours with gentle shaking. After rinsing with 1X PBS, the tissue sections were placed into a clearing solution containing 8% w/v sodium dodecyl sulfate (SDS, Sigma Aldrich) and 1.25% w/v boric acid (Fisher) (pH 8.5) and incubated at 37°C with gentle shaking until cleared. Residual SDS was removed with a 24-hour 1X PBS wash.

Tissue sections were placed in a refractive index matching solution (RIMS) for long-term storage and for imaging of the stained samples. To prepare RIMS, 40 grams of Histodenz (Sigma) was dissolved in 30 mL 0.02M phosphate buffer (Sigma) with 0.05% w/v sodium azide (Sigma). The pH was adjusted using NaOH. The solution was syringe filtered through a 0.2 μm pore filter and stored at room temperature.

DAB staining

The cleared mouse brain sections were incubated in 200 µL of diluted rat monoclonal anti-mouse parvalbumin primary antibody (Immunostar) and washed with 1X PBS for 24 hours. A secondary incubation was done in 200 µL of diluted goat monoclonal anti-rat antibody conjugated with horseradish peroxidase (HRP) enzyme (Thermo Scientific Pierce Antibodies) for 48 hours with a following 24 hour 1X PBS wash. Both primary and secondary antibodies were diluted 1:200 v/v with a blocking solution comprised of 1% v/v normal goat serum and 0.1% v/v Tween-20 in PBS. All incubation steps were performed with rotation at room temperature.

The chromogenic staining solution was formulated with 250 µL of 1% w/v 3,3'-Diaminobenzidine tetrahydrochloride (Sigma), 250 µL of 0.3% hydrogen peroxide solution (Sigma), and 4.5 mL of DI water. The solution was then adjusted to the appropriate pH using NaOH. The tissue sections were placed in the staining solution for 3 minutes and washed with 1X PBS to remove any excess DAB solution.

Slide mounting

The cleared and stained tissue is loaded into a sealed chamber filled with RIMS to be imaged by the lens-free on-chip microscope. The sample chamber is illustrated in Fig. 5.1(a). A piece of PDMS sheet with dimensions of ~ 18 mm × 18 mm and a thickness of ~ 1 mm with a square hole of ~ 10 mm × 10 mm in the middle is placed on one end of a piece of glass slide. The cleared tissue is placed at the center, and RIMS is pipetted into the chamber to ensure that it is filled entirely. A piece of No. 1 coverslip is placed on the top of the chamber. Finally, epoxy is applied to all the edges of the chamber as sealant.

Lens-free on-chip imaging setup and image acquisition

The lens-free imaging setup is illustrated in Fig. 5.1(a). A single-mode optical fiber-coupled broadband light source (WhiteLase-Micro, Fianium Ltd, Southampton, UK) is used as a partially coherent illumination source with a spectral bandwidth of ~ 2.5 nm. Similarly, a light-emitting-diode (LED) with a thin-film filter at the optimal illumination wavelength could also be used as a source [31,56,59]. Below the light source, a piece of cleared tissue sample loaded in a custom-made chamber (see the previous subsection for details) is mounted on a 3D positioning stage (NanoMax 606, Thorlabs, Inc., New Jersey, US), and is positioned on top of a complementary metal-oxide-semiconductor (CMOS) image sensor chip (IMX081, 1.12 μm pixel size, 16.4 megapixels, Sony Corp., Japan). Before starting the lens-free image acquisition, we manually adjust the positioning stage so that there is minimal gap between the image sensor and the sample slide, based on visual inspection. During the image acquisition process, the positioning stage moves the sample in x, y and z directions to enable PSR and multi-height based phase recovery. These two functions (PSR and multi-height phase recovery) can also be implemented using a field-portable system as demonstrated in our former work [56,59]. The entire set-up is controlled using a custom-written LabVIEW interface. The acquired holographic images are raw format images, as shown in Fig. 5.1(b), step 1.

Multiple hologram exposures to extend dynamic range

A high dynamic range (HDR) imaging technique was used to avoid under or overexposure of the acquired holograms. Three images were taken sequentially with exposure times of t, $4t$ and $16t$, where t was adjusted (e.g., 10-20 ms) so that there were no saturated pixels at the shortest exposure time. An HDR image was then synthesized from these three images by replacing the saturated

pixels of the longer exposure image by the unsaturated shorter-exposure image pixels, digitally scaled to the same exposure time.

Pixel super-resolution (PSR) algorithm

As detailed in Chapter 1, in order to reduce pixelation related spatial artifacts due to the finite pixel size of the image sensor and to improve the spatial resolution of the reconstructed images, multiple sub-pixel shifted holograms were recorded and digitally combined into a "pixel super-resolved" hologram [31,35,44,47,48,50,53,55,56,59,95]. The x-y motors in the positioning stage were programmed to shift the sample on a regular grid with a grid size of 0.37 μm in the x-y plane, equal to a third of the image sensor pixel pitch. In an alternative configuration, source shifting could also be used to induce sub-pixel level shifts at the hologram plane, which can also be achieved using an array of LEDs, without the need for any mechanical motion, as demonstrated in our former work [31,56,59]. Although the increased sample thickness could pose challenges due to different levels of sub-pixel shifts encountered for different depths in the sample, illumination source shifting is still a viable solution for less thick samples [29]. For thick samples, where illumination source shifting or LED array-based solutions face challenges, cost-effective piezoelectric actuators can also be used to deliver sample motion in the micrometer range. It is important to emphasize that the x and y translations need not be precise, as they are estimated accurately by a computational shift estimation algorithm after image acquisition [57].

A 6-by-6 grid was used, in order for one channel of the Bayer image sensor to cover the period of the Bayer pattern. The color channel (R, G or B) that is the most sensitive to the illumination wavelength is used. In the case of 470 nm illumination wavelength, it is the B channel that exhibits the best sensitivity. The resulting $6 \times 6 = 36$ raw holograms are synthesized into an optimal higher-resolution hologram in the maximum likelihood sense, using a computationally efficient

optimization algorithm [35,58]. One should note that if we were to use a monochrome image sensor with the same pixel pitch, only a 3-by-3 grid could replace the 6-by-6 scan. An example of the pixel super-resolved hologram is shown in Fig. 5.1(b), step 2.

Autofocusing algorithm

An autofocusing algorithm is used to accurately find the sample-to-sensor distance (z_2). Random dust particles on the measured lens-free hologram are used as targets for autofocusing. First, an area with dust particles far away from the cleared tissue sample is identified. The holographic pattern of a dust particle is characterized by a set of circular concentric rings and is easy to identify. Next, this part of the hologram is digitally propagated using the angular spectrum approach to a range of z distances, and a focus criterion, i.e., the Tamura coefficient [110,111] is used to estimate the sample-to-sensor distance. For this, we used the golden-section search algorithm [114] as our search method.

Acceleration of the image reconstruction using CUDA

To speed up the data processing, the image reconstruction was implemented in CUDA C/C++ and was run on a graphics processing unit (GPU) server with an Nvidia Tesla K20c computation accelerator. Software libraries based on CUDA such as CUFFT, CUBLAS and thrust provided by Nvidia were utilized. Since operations such as the digital back-propagation of optical waves involves fast Fourier transform/inverse fast Fourier transform (FFT/IFFT) pairs and these operations are repeated hundreds, and even thousands of times, utilizing the FFT/IFFT provided by CUFFT resulted in a significant speedup, which was measured to be ~60-fold faster compared to the MATLAB version of our code based on a central processing unit (CPU). Basic operations such as real/complex image arithmetic and downsampling/upsampling were all implemented through our own CUDA kernel functions.

The entire FOV (5.215 mm × 3.940 mm) of our on-chip microscope was digitally divided into 12 square tiles (4 columns, 3 rows) each measuring approximately 1.5 mm × 1.5 mm with some spatial overlap. PSR and multi-height phase recovery steps were done sequentially for each tile, and the reconstructed images were digitally stitched together at the end.

Sparsity-based image denoising using total variation (TV) regularization

TV denoising [137] was applied on our reconstructed and refocused lens-free images to remove the noise resulting from out-of-plane interference and speckle, without significantly reducing the sharpness of the images. This is achieved by solving the following minimization problem:

$$\min_{\mathbf{I}} \mathrm{TV}(\mathbf{I}) + \frac{\eta}{2}\|\mathbf{I}_0 - \mathbf{I}\|_2^2 \tag{5.1}$$

where $\mathbf{I}_0$ is the amplitude of the digitally refocused lens-free reconstruction image (noisy), and η is a regularization parameter. The total variation of the solution, $\mathbf{I}$, is defined as:

$$\mathrm{TV}(\mathbf{I}) \triangleq \sum_{i,j} \sqrt{\left|{}_{,j} - I_{i,j}\right|^2 + \left|I_{i,j+1} - I_{i,j}\right|^2} \tag{5.2}$$

where $I_{i,j}$ is the (i, j)-th element of $\mathbf{I}$. Eq. (5.2) is solved by applying the Chambolle's iterative method [138] using 50 iterations. In this work, $\eta = 4$ was chosen to effectively remove noise while keeping the image details including cell boundaries and morphology. An example of the TV-denoised lens-free amplitude image is shown in Fig. 5.1(b), step 4.

Digital rendering of the lens-free reconstructed z-stack and pseudo-coloring of the sample images

The phase-recovered lens-free hologram is digitally propagated to a series of z distances to construct a depth-resolved image stack of the cleared tissue. The amplitudes of the back-

propagated lens-free images are normalized and pseudo-colored [35,48,54,56,139] to obtain a similar color compared to a regular brightfield microscope. In this pseudo-coloring step, we assume that the ratio between R, G and B channels is constant. Thus, the amplitude of the holographic reconstruction for a given sample is used as the "B" channel of an RGB image, while the "R" and "G" channels are simply set to 3.44 and 2.01 times of the "B" channel, respectively. These ratios are empirically learned from a microscope image of an SCM-prepared mouse brain tissue (stained with DAB) by averaging the R/B and G/B channel ratios of the image. An example of the resulting lens-free z-stack is illustrated in Fig. 5.1(b), step 5.

Hyperspectral lens-free imaging by wavelength scanning

To optimize the illumination wavelength for SCM-prepared tissue samples, we used hyperspectral imaging (see Results and discussion). At each position of the mechanical stage, a lens-free hologram is captured for each one of the 31 wavelengths ranging from 400 nm to 700 nm with a step size of 10 nm. In the processing step, PSR and multi-height phase recovery were performed individually for each wavelength, resulting in 31 lens-free reconstructed images at different wavelengths. After this optimization process, a single illumination wavelength (i.e., 470 nm) was used for imaging of all the subsequent samples.

5.3 Results and discussion

Optimization of the illumination wavelength

In this work, since we used a single dye for staining the target cells, it is sufficient to use only one illumination wavelength, which reduces the amount of data to be processed and stored. To identify the ideal illumination wavelength in our experiments, we performed CNR optimization as

a function of the illumination wavelength using a 50 µm-thick tissue sample (refer to the Materials and methods section). We defined CNR as:

$$CNR = \left| \frac{S_b - S_c}{\sigma_b} \right| \tag{5.3}$$

where S denotes the average of the reconstructed image amplitude, σ denotes the standard deviation of the amplitude, and subscripts c and b denote the stained *cell* of interest and its local *background*, respectively. Because the stained cells absorb more light, we expect that $S_b > S_c$ for a transmission imaging system.

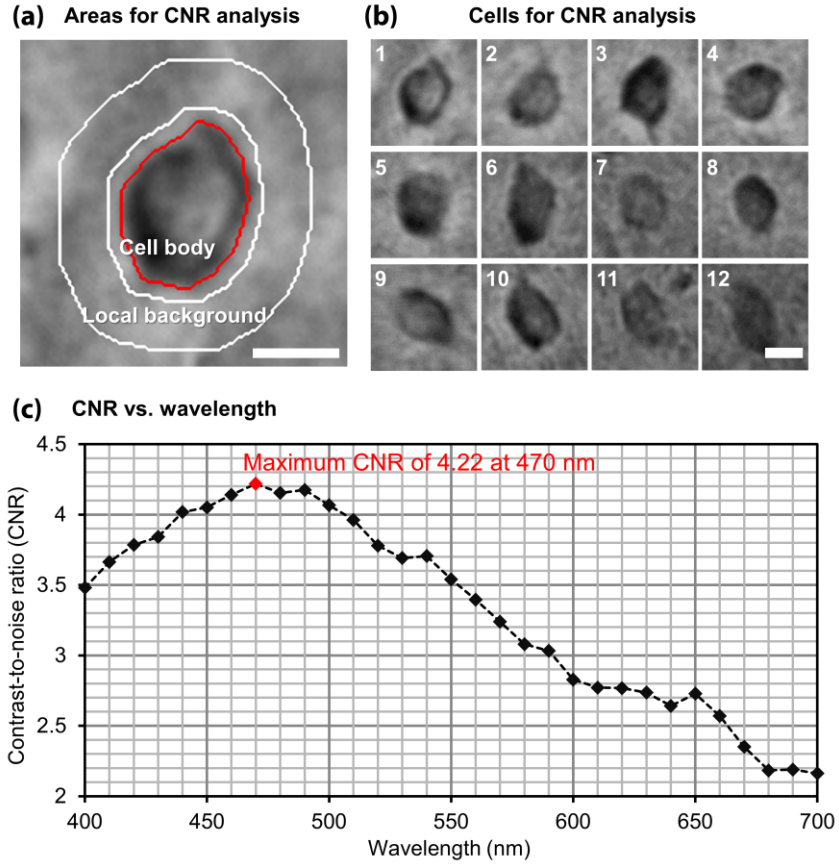

Figure 5. 2. Illumination wavelength optimization using a 50 µm thick tissue sample. Scale bars: 10 µm. **(a)** A neuron cell body and the local background regions are used for CNR analysis. **(b)** A few examples of the cells that we used for CNR analysis. **(c)** CNR as a function of the illumination wavelength, with the peak occurring at 470 nm.

For this CNR analysis and illumination wavelength optimization, the boundaries of 12 distinct neurons (see Fig. 5.2) were manually drawn to define the spatial support of the cells. The background region for each cell was defined locally as the region that was within 20 pixels from each cell's boundary and at least 5 pixels away from the boundary (Fig. 5.2(a)). The CNR for each cell was calculated using its own spatial support and its local background to reduce the effect of global intensity variations in the image. The average CNR of all the cells at each illumination wavelength is shown in Fig. 5.2(c). We observe that CNR is almost a unimodal function of wavelength, and its peak occurs at around 470 nm, based on which, we selected our illumination wavelength to be 470 nm. To better understand this observation, we compared the CNR-wavelength plot with the absorption spectrum of DAB reported in the literature [140], which confirmed that the shapes of these two functions agree very well, and that the DAB absorption spectrum also reaches its peak at approximately 470 nm.

Increasing the thickness of the 3D imaged tissue

The CLARITY process greatly reduces the background scattering and absorption of the tissue, resulting in clearer images of the cells. However, there is still non-specific staining of the background as well as random refractive index variations within the sample that will scatter the photons and distort the optical wavefront, resulting in an increased background noise and a reduced image quality at larger tissue thicknesses. We experimentally investigated the effect of the increased tissue thickness on our lens-free reconstruction quality, where 50 μm, 100 μm and 200 μm thick tissue samples, after clearing, were imaged using the lens-free on-chip microscope, and the CNRs of a number of cells were measured for each reconstructed image. These samples were all prepared under a pH of 7.4. Based on the number of cells that were available in the reconstructed FOVs, we randomly chose 12 cells from the 50 μm-thick tissue, 11 cells from the 100 μm-thick

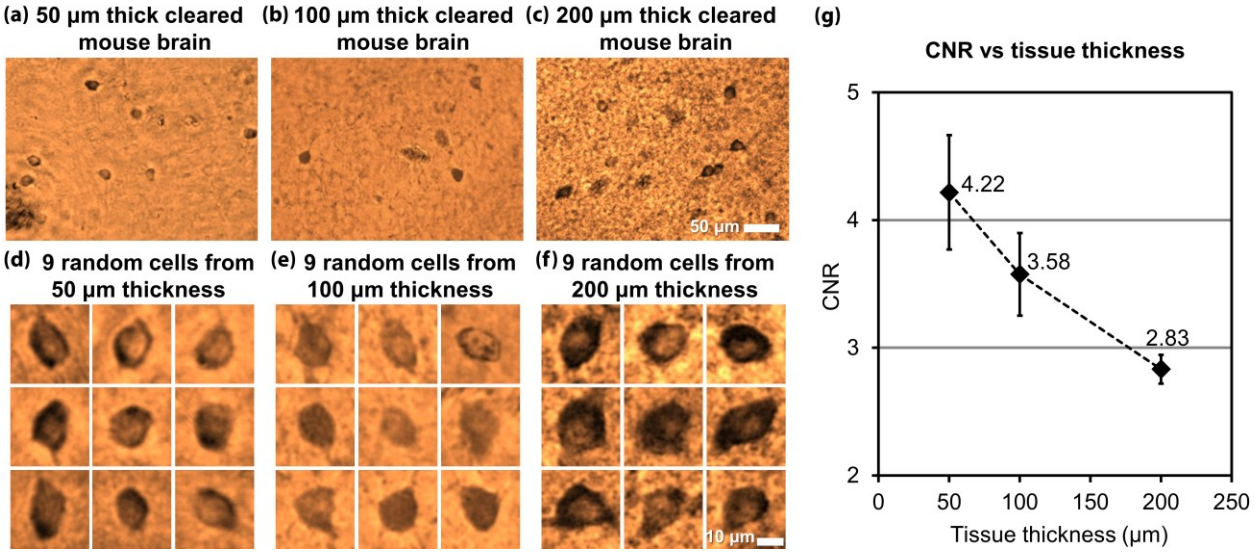

Figure 5. 3. Imaging comparison of different thicknesses of cleared tissue. (a-c) Sub-FOVs of the pseudo-colored lens-free reconstructed images of a 50 µm-thick, 100 µm-thick and 200 µm-thick cleared mouse brain tissue. Each one of these images was digitally focused to a few arbitrary cells located within the sample. The 50 µm-thick sample is the same sample shown in Fig. 5.2. **(d-f)** 9 randomly selected cells from each sample thickness are illustrated. **(g)** Mean CNR of the reconstructed neurons within the cleared tissue as a function of its thickness. Error bars represent the standard error of the mean, which is equal to the standard deviation divided by the square root of the number of sampled cells.

tissue and 19 cells from the 200 µm-thick tissue, which were randomly scattered within the tissue thickness with no bias towards the top or bottom of the tissue section. The closest vertical distances (z_2) from the cells to the image sensor plane in these three samples were: ~820 µm, ~680 µm and ~890 µm, respectively, which were measured by digital back-propagation and auto-focusing. Some of these pseudo-colored cell images (a random subset of 9 cells for each thickness) are shown in Fig. 5.3(d-f), and their mean CNR values are reported in Fig. 5.3(g) with the error bars representing the standard error of the mean. As expected, Fig. 5.3(g) reveals that CNR drops as the thickness of the tissue increases. At 200 µm tissue thickness, a mean CNR of 2.83 is obtained. We expect the CNR to further decrease if thicker tissue samples are imaged. Since larger tissue thicknesses

also result in a longer clearing time, which is less desirable for point-of-care and related medical applications, we chose 200 μm as the maximum tissue thickness that we imaged using the technique reported here. Future work will focus on further improving the tissue thickness with more rapid clearing methods and less background staining.

Optimization of pH for tissue staining

Decreasing the pH of the staining solution slows the reaction between the horseradish peroxidase (HRP) enzyme and the DAB substrate, which in turn, results in less production of the insoluble brown precipitate [141]. Consequently, this reduces the amount of the reaction product that may diffuse out and non-specifically bind to the tissue. A lower pH may also eliminate any endogenous peroxidase and pseudoperoxidase activity, as these are known to react with the DAB substrate and are present at varying levels in all tissue types [142]. However, this may also cause a loss of sensitivity in the specific staining of the parvalbumin neurons.

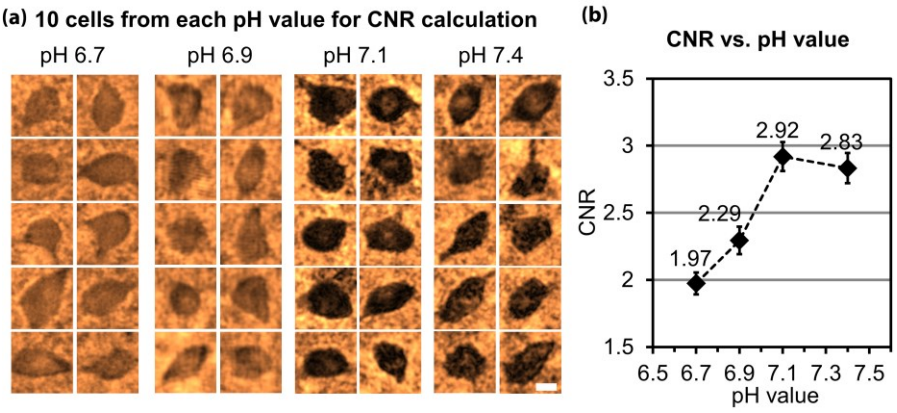

Figure 5. 4. Optimization of pH for tissue staining. (a) Randomly selected cells that are reconstructed using lens-free on-chip microscopy corresponding to four cleared tissue samples (each 200 μm thick) stained with pH values of 6.7, 6.9, 7.1, and 7.4, respectively. Scale bar: 10 μm. **(b)** Average CNR as a function of the pH value, with the peak CNR occurring at a pH value of 7.1. Error bars represent the standard error of the mean.

In an attempt to search for the optimum condition that lowers the background staining and increases CNR, we prepared 200 μm thick tissue samples, stained using four different pH values – 6.7, 6.9, 7.1, and 7.4, where 16, 22, 27 and 19 cells were randomly chosen within the reconstructed lens-free images to calculate the CNR for each pH value. A random subset of 10 reconstructed cells for each pH value is shown in Fig. 5.4(a), and the mean CNR values calculated from all the cells are plotted in Fig. 5.4(b). Based on these experiments, an optimal CNR of 2.92 was achieved at a pH value of 7.1, which can be considered as a "sweet spot", where the amount of non-specific background staining is reduced, while the sensitivity due to the specific staining of the parvalbumin neurons is not largely compromised.

Optimization of the number of heights in lens-free on-chip imaging and sparsity-based image denoising

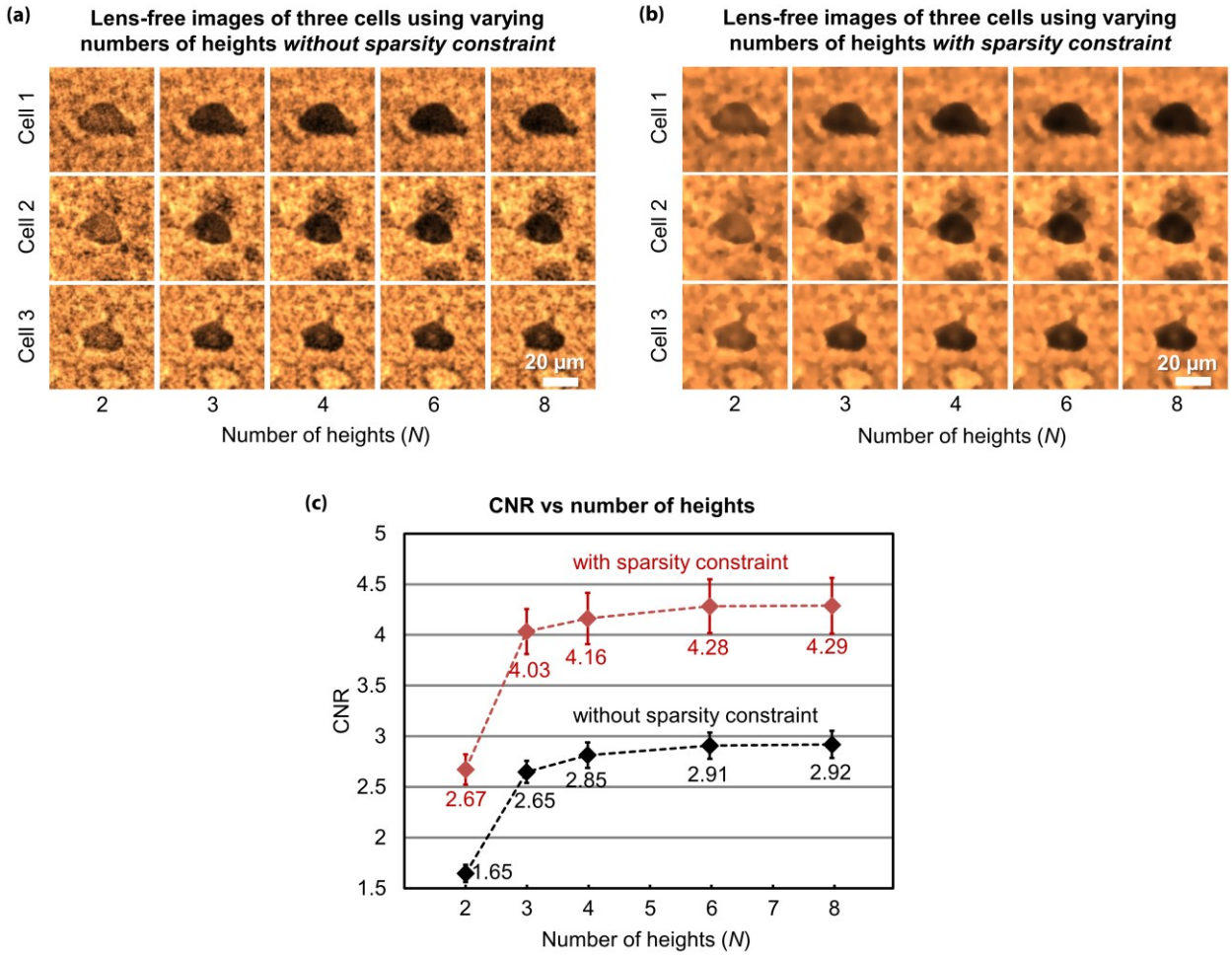

Figure 5. 5. Effect of the number of heights and the sparsity-based image denoising algorithm on the CNR of the reconstructed lens-free images corresponding to a 200 µm thick cleared tissue sample stained under a pH of 7.1. **(a, b)** Sample lens-free images of three randomly selected cells as the number of heights varies from 2 to 8, before and after applying the sparsity constraint, respectively. **(c)** Average CNR calculated using the reconstructed lens-free images of 27 cells plotted against the number of heights, before (black curve) and after (red curve) applying the sparsity constraint. Error bars represent the standard error of the mean. Using the sparsity constraint significantly improves the CNR of the lens-free images.

The number of heights used in our multi-height phase recovery method directly increases the amount of data that is acquired. A larger number of heights also leads to a longer image reconstruction time. Therefore, a reduction in the number of heights would reduce the overall imaging time and the data storage burden. Towards this goal, we evaluated the average CNR of the reconstructed neurons as a function of the number of heights that is used in our reconstruction process. Furthermore, for a given number of heights, we also implemented a sparsity-based image denoising algorithm to improve the CNR of the reconstructed cell images (see the Materials and methods section for details).

In this analysis, lens-free images at eight heights were captured for a 200-μm thick cleared mouse brain tissue that is stained under a pH value of 7.1 (the same sample as in Fig. 5.4(a), pH 7.1). The vertical separation between these heights was ~15 μm. Within this acquired lens-free holographic image data, we chose subsets of N heights from all the measurements (N = 2, 3, 4, 6, and 8) and performed lens-free reconstructions for these images. To illustrate this process, three sample cells are shown in Figs. 5.5(a, b) to visualize the impact of the number of heights, N, as well as the sparsity-based denoising on the quality of the reconstructed images. Average CNR values corresponding to 27 randomly selected cells are also plotted as a function of N in Fig. 5.5(c). Figs. 5.5(a, b) clearly show that by implementing a sparsity-based denoising step, speckle and interference related image noise that results from random background scattering from the hydrogel structure as well as out-of-focus cells is effectively reduced without significantly affecting the image quality. As a result, the average CNR value with sparsity-based denoising is significantly improved for each N as illustrated in Fig. 5.5(c). We also observed that as N exceeds three, the CNR improvement is differential. Therefore, in order to minimize the data acquisition and the

reconstruction time, while also preserving the image quality, we have chosen to use $N = 3$ and the sparsity-based denoising method in our experiments that will be reported next.

3D imaging of cleared mouse brain tissue

Based on the optimized parameters discussed in the previous subsections, here we present the 3D imaging results of a 200 μm thick cleared tissue of the mouse brain. The same sample is also imaged using an automated scanning microscope (IX83, Olympus Corp.) with a 20× 0.75NA objective lens by z-scanning with a step size of 1 μm in air. The full FOV of the lens-free on-chip microscope (20.5 mm^2) is >70 times larger than a 20× objective's FOV (0.274 mm^2), shown in Fig. 5.6(a). In Fig. 5.6(b), we show the minimum intensity projection (MIP) image of the lens-free reconstructed z-stack (pseudo-colored and zoomed in over a smaller FOV), where each image in the stack corresponds to the lens-free reconstruction that is digitally refocused to a different z-distance/depth within the sample volume. The same figure also shows the MIP of the z-stack of an automated scanning microscope for comparison, where the scanning range (computational for the lens-free microscope and mechanical for the scanning microscope) spans ~387 μm, encompassing the entire cleared tissue thickness with some extra volume on each side. As desired, the MIP images from both modalities show consistent cell distributions in the x and y directions. A total of 19 distinct cells in this sample region were digitally refocused and shown in Fig. 5.6(c), with the lens-free images shown on top of the corresponding 20× objective based microscope comparison images, which provide a decent match to each other.

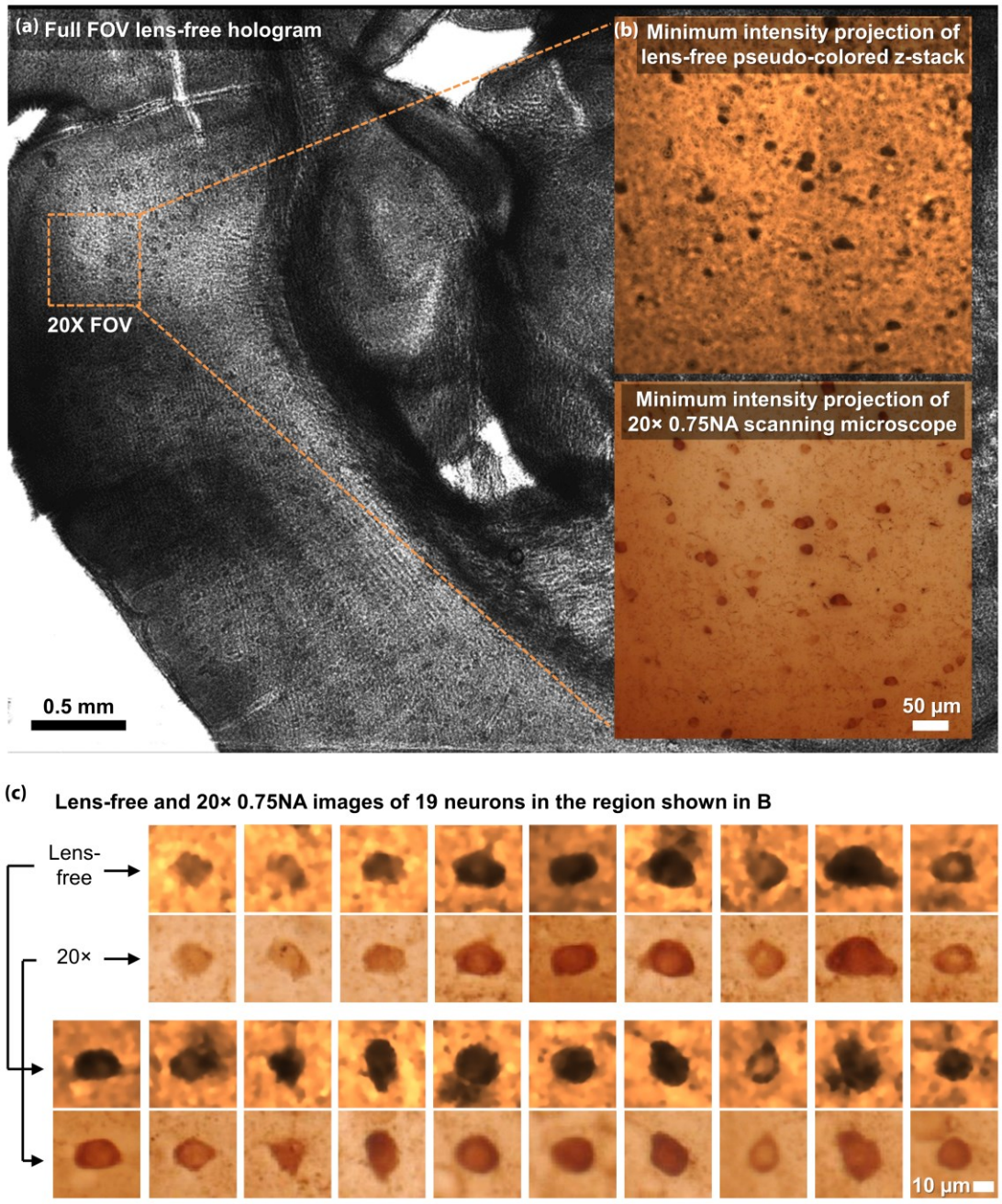

Figure 5. 6. Lens-free 3D imaging of a cleared, DAB-stained 200-µm thick mouse brain tissue. (a) Full FOV lens-free hologram. **(b)** A zoomed-in region corresponding to a 20× microscope objective FOV. Minimum intensity projection images of the lens-free pseudo-colored z-stack and the scanning microscope's z-stack (obtained with a 20× 0.75NA objective) are presented. **(c)** Comparison of lens-free images of 19 neurons against the images obtained with a 20× 0.75NA objective lens.

Data efficiency

Table 5. 1. Data and timing efficiency. *Left*: Comparison of the number of images and the amount of acquired image data between a lens-free on-chip microscope and a typical scanning optical microscope with a 20× objective lens. *Right*: Computation time corresponding to the full-FOV (20.5 mm^2) image reconstruction routine implemented in CUDA using an Nvidia Tesla K20c GPU (released in November 2012). This total computation time can be further improved by more than an order of magnitude by using a GPU cluster.

Data efficiency comparison

Lens-free microscope

HDR	PSR	Heights	# of images	Data (GB)
3	36	3	324	3.5

Conventional scanning microscope 20× 0.5NA

Lateral scan	Axial scan	# of images	Data (GB)
92	73	6716	39.4

Timing of lens-free image reconstruction

Subroutine	Time (s)
Read images from hard drive	7.0
Autofocus	10.2
Pixel super-resolution (PSR)	91.0
Image alignment	54.6
Multi-height phase recovery	94.6
Total	257.4

A comparison between the number of images that is required by the lens-free on-chip microscope and a conventional scanning brightfield optical microscope (20× 0.5NA) to image the same sample volume clearly demonstrates the advantage of the 3D imaging capability of lens-free on-chip microscopy. 20× 0.5NA is specifically chosen for this comparison to approximately match the resolution of the presented lens-free microscope [35]. In order to image a 20.5 mm^2 FOV spanning a depth of ~200 μm in the z direction, our lens-free on-chip microscope utilized 3 × 36 × 3 = 324 raw lens-free holograms, where the first "3" represents three different hologram exposure times, "36" represents 6-by-6 pixel super-resolution, which could have been reduced to 3 × 3 = 9 using a monochrome image sensor. See the Materials and methods section for implementation details of pixel super-resolution (PSR). The second "3" represents $N = 3$ heights for multi-height phase recovery. In order for a conventional scanning optical microscope to image the same volume, assuming a typical 10% overlap between lateral scans for digital image

alignment and stitching, ~92 images are needed to cover the same 20.5 mm^2 FOV. As for the number of axial scans, we assume that the z-step size should be no more than the depth of field of the objective lens, and assuming $n = 1.46$, $\lambda = 470$ nm and $NA = 0.5$, at least ~73 axial steps would be needed to cover a tissue thickness of 200 μm using a scanning optical microscope with a 20× objective lens [143,144]. This number of axial steps would increase proportional to the square of the numerical aperture of the objective lens that is used, and therefore higher NA objectives would need to scan much larger number of axial planes within the sample volume. Combining these lateral and axial scans, in order to create a 3D image of this sample volume one would require at least 92 × 73 = 6,716 images using a scanning optical microscope, which is ~21 and ~84 times more than the number of images required by a lens-free on-chip microscope using a color (RGB) and monochrome image sensor chip, respectively. Also note that there is typically natural warping and tilting of cleared tissue samples, and as a result of this, the required z-scanning range for a 200 μm-thick sample can be much larger than 200 μm. Therefore, the calculated number of images for a typical scanning optical microscope (i.e., 6,716) is a conservative lower bound. On the other hand, this warping and tilting effect will not result in more captured images for the lens-free on-chip microscope, which is another important advantage of its holographic operation principle.

Our lens-free microscope's image sensor captures 10-bit raw images and stores each image as a 16-bit raw format binary file. Therefore, after high dynamic range (HDR, see the Materials and methods section) synthesis using three image exposures, the effective bit depth is 14-bit, which can still be stored inside a single 16-bit binary file. Because the HDR process can be easily performed during the data acquisition process, only a total of 36 × 3 = 108 raw images, each having 16.4 megapixels and 16 bits per pixel, need to be stored before the image reconstruction step, resulting in approximately 3.5 GB of data for the entire sample volume (~ 0.2 mm × 20.5 mm^2).

On the other hand, the scanning optical microscope that we used for comparison in this work stores 24-bit TIFF files, each having a size of ~5.87 MB, resulting in a total of 39.4 GB of captured data, which is ~11 times larger than the lens-free microscope data size required for imaging of the same sample volume (see Table 5.1).

Image acquisition and data processing times

Using a color (RGB) CMOS imager chip with a relatively low-speed USB 2.0 imaging board, acquisition of 324 raw holograms (3 exposures per lateral position, 36 lateral positions per height, N = 3 heights) would typically take ~30 min. This can be significantly improved by using monochrome and higher-speed image sensors, faster data interfaces such as USB 3.1 (10 Gbit/s) and solid-state drives (SSD, ~500 MB/s write speed). These improvements would permit reaching the maximum frame rate of the imager chip, which in our case is ~15 fps, and the entire image acquisition time can be reduced to ~21.6 sec for 324 raw holograms.

As for the image computation time, we used CUDA to speed up the full-FOV (20.5 mm^2) image reconstruction algorithm (see the Materials and Methods section for details). Table 5.1 also presents the timing of different stages of the CUDA routine during the sample reconstruction. Using a *single* GPU (Nvidia Tesla K20c, released in November 2012), the full FOV was reconstructed in 257.4 sec. This total time currently does not include HDR processing and 3D z-stack rendering for the final display of the results. HDR has very low computational burden and can be easily performed during the image acquisition process. The 3D stack rendering mainly involves digital propagation and denoising, which can be efficiently implemented on the GPU. The adoption of GPUs in our computational imaging system will not result in an increase in the overall cost, as nowadays consumer-grade GPUs provide high-performance at a low-cost. For example, a standard gaming GPU (e.g., Nvidia GeForce GTX 1060) can deliver similar

performance compared to the GPU that we used in this this work, costing no more than $200. A laptop computer equipped with such a GPU can be bought at approximately $1000, which is expected to significantly reduce in a matter of 1-2 years.

This entire image processing routine can be further accelerated by using a GPU cluster. As an example, a GPU cluster that has 12 GPUs will provide a ~12× speedup (the data communication overhead is almost negligible with high-throughput communication standards such as InfiniBand), resulting in only ~21 sec for the entire image reconstruction process. By using more recent generations of high-performance GPUs, the image processing time can be reduced even further. As a consequence, the total image/data acquisition and processing time, combined, for an ideally designed lens-free on-chip microscope can be lower than ~40 seconds.

In comparison to a lens-free on-chip microscope, it would take more than 5,075 seconds (that is, 84.6 minutes) for a scanning optical microscope using a 20× objective lens to capture the same volume using 92 × 73 = 6,716 raw images, as detailed earlier. This calculation is based on that scanning a z-stack of 73 images takes 55.16 seconds on average, with e.g., the microscope that we used in this work. Ignoring the additional time required for lateral translation of the sample, this time is multiplied by 92, the number of lateral scans to match the FOV, yielding a total imaging time of at least 84.6 min. This estimate, in addition to lateral translation time, also ignores the computational step that is required for digital stitching of the acquired set of images together, and therefore should be considered as a conservative estimate. As a result, lens-free microscopy is estimated to be more than two orders of magnitude faster than a typical lens-based scanning optical microscope in terms of the image acquisition time.

Limitations and future work

Demonstrating that optically cleared tissue samples can be imaged in 3D with a high throughput on-chip microscope, this work serves as a proof of concept for CLARITY technique to be merged with computational microscopy tools that can reduce the cost of inspection of tissue samples and diagnosis as well as improve access to 3D tissue imaging and related research even in resource constrained settings. However, we would like to also mention a few limitations of this research and current state of our results.

Unlike confocal microscopy, holography in general is not a 3D tomographic imaging modality, and can suffer from shadowing and other spatial artifacts due to absorption and/or phase aberrations within a 3D sample. For 3D tomographic imaging using holography, different layers/sections of a sample volume will need to experience, at least approximately, the same *illumination wavefront* that is only phase shifted due to wave propagation inside the sample volume. Stated differently, any significant complex-valued refractive index modulation within the sample volume will result in illumination of the subsequent layers of the sample volume with distorted wavefronts that suffer from unknown phase and amplitude variations compared to previous layers. This is similar to a "Chicken and Egg" problem, since understanding of such wavefront aberrations within the sample volume is possible by the measurement of 3D complex refractive index values of the sample, which remain unknown, i.e., to be imaged and measured/inferred. There are various assumptions and simplifications that can make this problem more approachable, including e.g., weakly scattering and absorbing sample assumption, which can be easier to satisfy especially when the sample is spars [2,145]. The imaged samples in this work partially satisfy these constraints, since we used optical tissue clearing and the colorimetrically labeled cells within the sample volume were sparse in 3D.

The tissue clearing and staining protocol presented here can be further optimized to reduce background scattering and reduce tissue processing times, which can enable imaging even thicker tissues using this technique. Recently emerging deep learning based holographic image reconstruction methods [70] that improve suppression of image artifacts using neural networks can also be utilized to further increase the tissue thickness that can be imaged. Furthermore, protocols for multiplexed staining need to be established and optimized, where different cells/structures will be specifically stained with different dyes. This will enable the imaging of multiple cell types in the same tissue sample by performing lens-free imaging at different illumination wavelengths, depending on the dye spectra. This will also enable identification of structures of interest, such as visualization of cell nuclei using counter-staining, which is a routine technique in standard histopathological practice.

We used mouse brain tissue as a proof-of-concept in this paper because it has been well-established across various CLARITY techniques. This made it easier for us to optimize both the clearing and staining for this specific application, because we were able to identify whether the optical clearing or the staining process needed to be altered in order to produce a good holographic image. However, optical tissue clearing has been used on many different types of tissue samples, from whole mouse hearts to unsectioned tumor tissues [123,124]. Future work will explore modification and optimization of the presented approach for other tissue types.

Finally, the CLARITY method is relatively new and protocols have not yet been fully established for disease diagnosis facilitated by optical tissue clearing. Therefore, as a further step, future efforts will be needed to clinically validate the feasibility of using the presented method for disease diagnosis and pathological investigation of human tissue, which is an emerging field of current research [124,146–148].

5.4 Conclusions

In this chapter, a low-cost and simple tissue clearing and imaging system that combines SCM and lens-free on-chip 3D imaging is demonstrated, which can be field-portable and used in low-resource environments. SCM adopts a colorimetric staining method, which involves inexpensive and easy-to-use materials and methods. The tissue clearing can be performed passively with minimal reagents while preserving the natural antigens, which can then be stained with DAB for imaging with the portable lens-free microscope. The lens-free microscope uses PSR and multi-height phase recovery algorithms to reconstruct an optical wave field with amplitude and phase information and can be digitally refocused to any plane within the sample to generate a 3D image stack. We optimized the system parameters including the illumination wavelength, tissue thickness, pH of staining solution, and the number of measurement heights, and applied a sparsity-based image denoising step to ensure a high CNR while maximizing the imaged tissue volume and minimizing the amount of captured data. With the optimized system, a 200-μm-thick cleared mouse brain tissue was imaged in 3D, where the individual neurons at different depths agreed well with 20× 0.7NA brightfield microscope images. Moreover, in order to image the same 3D extent of the cleared tissue, the lens-free microscope only requires 21 times fewer images (11 times less data). This simple, low-cost and portable system could potentially provide an alternative solution to tissue-based diagnosis and biomedical research in low-resource settings.

Chapter 6. Polarization-sensitive lens-free microscopy for detection of gout and pseudogout crystals

Gout is a form of crystal arthropathy where monosodium urate (MSU) crystals deposit and elicit inflammation in a joint. Diagnosis of gout relies on identification of MSU crystals under a compensated polarized light microscope (CPLM) in synovial fluid aspirated from the patient's joint. The detection of MSU crystals by CPLM is enhanced by their birefringent properties. However, CPLM partially suffers from the high-cost and bulkiness of conventional lens-based microscopy, and its relatively small field-of-view (FOV) limits the efficiency and accuracy of gout diagnosis. In this chapter, a lens-free polarized microscope is presented which adopts a novel differential and angle-mismatched polarizing optical design achieving wide-field and high-resolution holographic imaging of birefringent objects with a color contrast similar to a standard CPLM. The performance of this computational polarization microscope is validated by imaging MSU crystals made from a gout patient's tophus and steroid crystals used as negative control. This lens-free polarized microscope, with its wide FOV (>20 mm^2), cost-effectiveness and field-portability, can significantly improve the efficiency and accuracy of gout diagnosis, reduce costs, and can be deployed even at the point-of-care and in resource-limited clinical settings.

Part of this chapter has been previously published in: Zhang, Y. *et al.* Wide-field imaging of birefringent synovial fluid crystals using lens-free polarized microscopy for gout diagnosis. *Scientific Reports* **6,** 28793 (2016) (reused from Ref. [63] under the Creative Commons Attribution 4.0 International License, CC BY 4.0, https://creativecommons.org/licenses/by/4.0/).

6.1 Introduction

Gout is a type of crystal arthropathy, which is caused by the deposition of monosodium urate (MSU) crystals in the joints and periarticular structures such as the tendons and ligaments. During an acute gout attack, the patient experiences severe pain and swelling of the affected structures, which can often be debilitating for the patient [149,150]. The prevalence of gout has been gradually increasing by as much as fourfold for the past five decades, and is the most common type of inflammatory arthritis in the United States affecting over 8 million adults, 3.9% of the entire population [151].

The pathogenesis of gout is complex, involving abnormalities in both metabolism and immunity. The key components include hyperuricemia and MSU crystallization [152]. Uric acid is a byproduct of purine metabolism, degraded by the enzyme uricase by most mammals. However, humans lack this enzyme because of multiple evolutional mutations of its coding gene and hence have higher levels of serum urate than other mammals [153]. Once serum urate rises above 6.8 mg/dL, urate can form MSU crystals under certain environmental factors (typically in and around joints), which then act as a potent trigger of inflammation in the joints [154,155].

The gold standard for the diagnosis of gout is identification of MSU crystals within the synovial fluid aspirated from the joints of a gout patient using a compensated polarized light microscope (CPLM) [156,157]. Compared to a standard brightfield light microscope, a CPLM has a pair of linear polarizers using the cross-polarized configuration, and a full-wave retardation plate (red compensator) to convert birefringence of the objects into color variations. MSU crystals have needle-like shape and strong negative birefringence, i.e., the fast axis is along the axial direction of the crystal, which, when observed under a CPLM, appear *yellow* (or *blue*) when the MSU crystal is aligned *parallel* (or *perpendicular*) with the slow axis of the full-wave retardation plate, upon a

red/magenta background color. Although polarized microscopy has been considered as the "gold standard" for diagnosis of gout since 1961, recent studies show that joint aspiration is not regularly performed in primary care clinics [158,159]. In some observational studies, only about 10% of primary care physicians performed polarizing microscope examination in diagnosing gout patients [160,161]. Among other reasons, limitations of traditional CPLM play an important role. Most critically, conventional lens-based microscopes have relatively small FOV, especially when high-numerical aperture (NA) and high-magnification objective lenses are used. For example, in the identification of MSU crystals, routinely a 40× (e.g., 0.75NA) objective lens is used to observe the morphology of the crystals, resulting in an extremely small FOV (~ 0.2 mm^2) which leads to long examination times by diagnosticians. In particular, when there is only a limited number of crystals present in a synovial fluid sample taken from the patient, the examination of the entire sample can be not only time-consuming but also can produce a non-reliable diagnostic result because of operator-dependent bias in detecting the crystals over a limited FOV [162]. The concentration of crystals directly correlates with diagnosticians' ability to positively identify crystals [163]. Furthermore, the reliability of CPLM for detection of MSU crystals can vary widely depending on the examiner's level of training [164]. These drawbacks of the current method call for a newer method to detect birefringent crystals that is higher-throughput, easier to use and ideally automated.

Invented to address the limitations of the conventional lens-based light microscopes, lens-free on-chip microscopy based on digital in-line holography has gone through significant developments in the past decade [13,29,30,33–35,40,42,49,53,55,59,64,95,96,165–172]. Taking advantage of the rapid increase in mega pixel counts and the reducing costs of optoelectronic image sensors as well as the exponential improvements in computation capabilities of consumer electronic devices,

lens-free on-chip microscopy can perform wide-field imaging without the need for lenses or objectives in a compact, cost-effective and field-portable setup [56,59,62]. In a lens-free on-chip imaging set-up, a transparent sample is positioned above an image sensor chip (e.g., a complementary metal-oxide semiconductor (CMOS) or charged-coupled device (CCD) chip) where the sensor-to-sample distance (i.e., z_1) is less than a millimeter whereas the source-to-sample distance (z_2) is e.g., 5-10 cm. This imaging geometry has unit magnification and as a result of this, the entire active area of the imager chip serves as the object FOV, which can easily reach >20-30 mm^2 and >10-20 cm^2, using commercially available CMOS or CCD imager chips, respectively. Therefore the FOV of the lens-free microscope can be 2-3 orders of magnitude larger than a conventional lens-based microscope with a similar resolution level [13]. One disadvantage of unit magnification geometry is that the diffraction patterns or in-line holograms of samples are typically undersampled due to the relatively large pixel size at the sensor plane. This limitation has been mitigated using pixel super-resolution (PSR) and synthetic aperture techniques to achieve submicron resolution over large FOVs, breaking the resolution limit imposed by the pixel size of the image sensor chips, also achieving a space-bandwidth product that is larger than 1 billion [13,15,47,49,50,53,57,58,71].

Due to these advantages, lens-free computational microscopy can be a potential solution to the efficiency and reliability issues of gout diagnosis using the conventional CPLM. However, the adaptation of the current bright-field lens-free microscopy setup to polarized imaging is not straightforward: the cross-polarized configuration used in CPLM can totally extinct the background light that is not modified by the birefringent sample, and therefore is not applicable to lens-free holography where reference light is necessary to form interference [52,62]. Moreover, the color contrast of birefringent objects as generated by a conventional CPLM is challenging to

replicate by a lens-free microscope which inherently uses narrow-band illumination sources, unless multiple wavelengths are used.

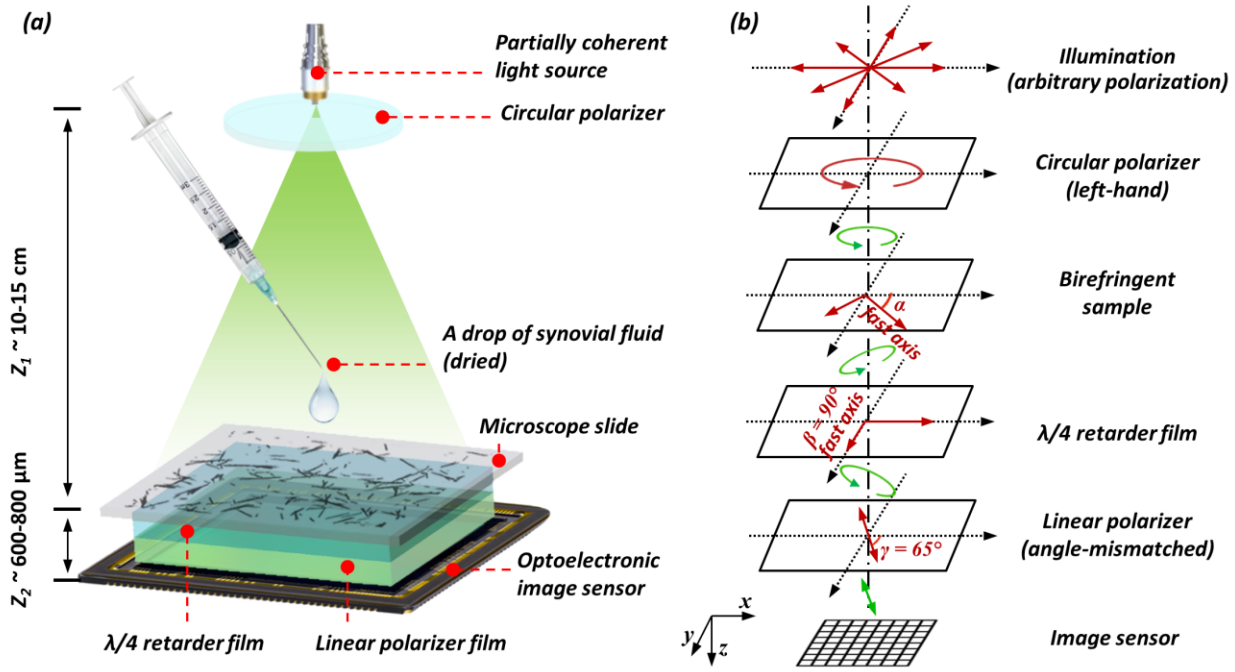

Figure 6. 1. Optical design. (a) Schematic setup of lens-free differential holographic polarized microscopy. **(b)** Design of the polarization in this system. The light, which is propagating from top to bottom, passes through a left-hand circular polarizer, the birefringent sample, a λ/4 retarder film, a linear polarizer and reaches the image sensor. The orientations of the polarizing components are illustrated with red arrows, and the polarization states of the light between components are illustrated with green arrows.

To face these challenges and create a lens-free microscope that can be used in gout diagnosis, we designed a novel *lens-free differential holographic polarized imaging* platform, which can achieve wide-field imaging of birefringent objects on an image sensor chip with sub-micron resolution (see Fig. 6.1(a)). In this design, a partially coherent light source is passed through a circular polarizer and is incident on the transparent sample that contains the synovial fluid taken from a patient. A CMOS optoelectronic image sensor is placed right below the sample, with a polarization analyzer unit composed of a λ/4 retarder film and a linear polarizer film positioned

above the image sensor, which utilizes the entire active area of the image sensor as our imaging FOV (~ 20.5 mm^2). The holographic diffraction patterns of the sample captured by the image sensor are processed by reconstruction algorithms including PSR [31,35,53,55,56,59,95] and multi-height based phase recovery [35,55,56,59] which generate both amplitude and phase images of the sample. In this work, we also employed a differential imaging strategy where we subtract two reconstructed images (where the analyzer was rotated by 90° between each image acquisition) to eliminate possible ambiguities between birefringent objects and absorptive objects that might randomly appear in the sample FOV. The detailed polarization design of our lens-free on-chip microscope is also shown in Fig. 6.1(b). The analyzer unit is modified from a standard cross-polarized configuration by changing the orientation of the linear polarizer from +45° with respect to the *x*-axis to +65°, to pass a certain fraction of the background light for hologram formation.

We optimized this lens-free polarization imaging design first using numerical simulations based on the Jones calculus [173], and then experimentally validated its effectiveness by imaging MSU crystal samples made from a gout patient's tophus and a fabricated steroid crystal sample (used as a negative control). Our lens-free polarized imaging results, after a digital pseudo-coloring step, achieved close agreement to gold-standard images obtained using CPLM with a 40× 0.75NA objective lens, both in color contrast and spatial details of the samples. Three board-certified rheumatologists also confirmed the image quality and the resolution of the lens-free polarized microscope images for crystal identification in gout diagnosis. With a substantial increase in the imaging FOV coupled with high resolution and contrast, this computational imaging technique is a promising approach to increase the efficiency and accuracy of gout diagnosis. This system can also potentially be used for pseudogout diagnosis, with the causative calcium pyrophosphate dihydrate (CPPD) crystals having positive-birefringence and rhomboid or rod shape. We believe

that with its cost-effectiveness, compactness and field-portability, this lens-free polarization imaging technology shows great promise to be deployed at point-of-care and low-resource settings for gout disease and related clinical needs. Other future clinical applications of this platform could include diseases caused by crystals that can be detected by a conventional CPLM. For example, ureteral stones can be diagnosed by detecting birefringent crystals in urine samples.

6.2 Materials and methods

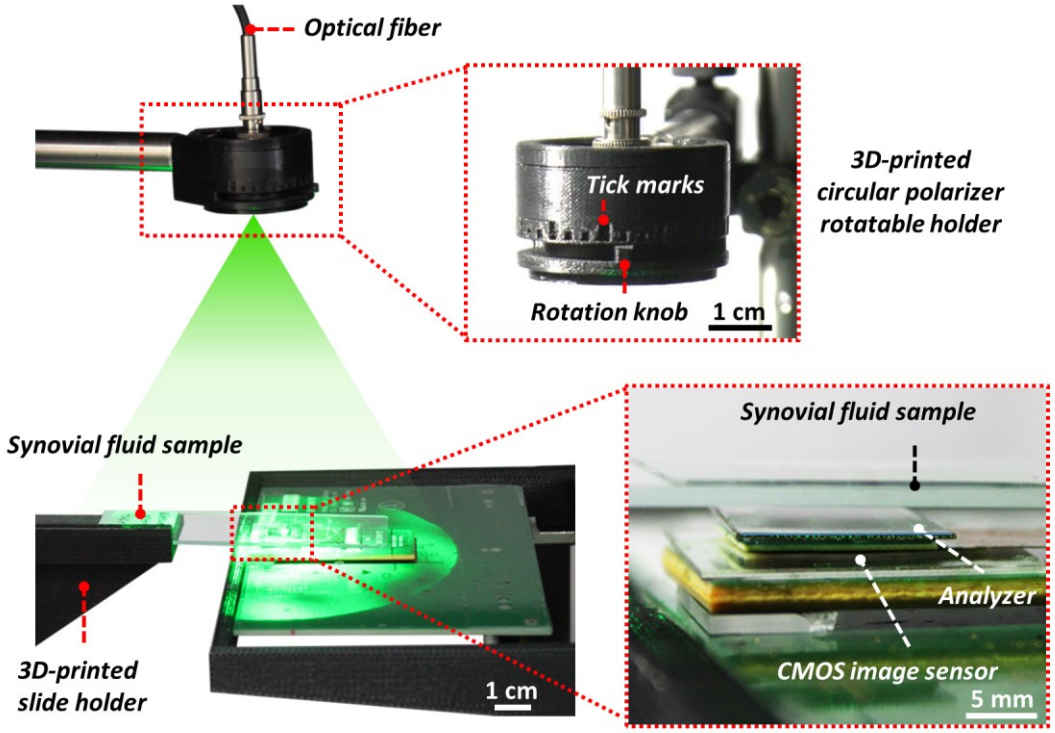

Figure 6. 2. Experimental setup.

Lens-free polarized on-chip imaging setup

A broad band source (WhiteLase-Micro, Fianium Ltd, Southampton, UK) is used to provide illumination at a wavelength of 532 nm, with a spectral bandwidth of ~2.5 nm and an optical power of ~ 20 µW. The source is coupled to a single-mode optical fiber and the light is emitted at the end of this fiber without any collimation, as shown in Fig. 6.2. A circular polarizer mounted in a 3D-

printed rotatable holder is attached to the optical fiber, such that the light first passes through the circular polarizer. Approximately 10 cm (z_1 distance) under the illumination fiber tip, a microscope slide with a drop of synovial fluid (dried) is held in place by a 3D-printed slide holder. A CMOS image sensor (Sony, IMX081, 1.12 μm pixel size) with an analyzer film on top is placed under the sample and is connected to a 3D positioning stage (Thorlabs, NanoMax 606) for x-y-z movement to achieve PSR and multi-height based phase recovery. The analyzer film is directly placed on top of the image sensor with immersion oil in between. The function of the immersion oil is to mitigate interference fringes caused by the thin air gap between the analyzer and the image sensor surfaces. The distance between the CMOS image sensor photosensitive layer to the sample (z_2 distance) is ~ 600 μm.

Before image acquisition, the orientation of the circular polarizer is rotated manually to maximize the total illumination power on the sample by observing the histogram of the live readout from the image sensor. This alignment step does not need to be repeated for further imaging experiments if the illumination part remains unchanged. For an unpolarized light source, no such alignment is necessary.

At the first stage of the image acquisition, the long side of the analyzer unit is aligned with the long side (i.e., horizontal direction) of the image sensor chip. After PSR and multi-height hologram acquisition, we rotate the analyzer unit by 90°, and repeat the same PSR and multi-height hologram acquisition process. Since the rotation of the analyzer is equivalent to the rotation of the sample, in an alternative design, one can permanently bond the analyzer unit to the image sensor chip and rotate the sample between the two imaging runs.

Fabrication of the analyzer unit using low-cost polymeric polarizing and retardation films

A 1.8 cm-by-1.5 cm piece of λ/4 retarder film (75 μm thickness, Edmund Optics) is cut out from a larger sheet, with the long side parallel to the slow axis. A piece of linear polarizing film (180 μm thickness, Edmund Optics) of the same dimensions is cut, with the long side at -65° with respect to the polarization direction. Then the two pieces are aligned and bonded together using ultraviolet (UV)-curable adhesive (NOA 68, Norland Products, Cranbury, NJ) with the λ/4 retarder on top, and cured under a UV lamp.

Fabrication of the circular polarizing unit

In general for an unpolarized light source, a piece of circular polarizer placed in front of the light source is sufficient to generate circularly polarized light, without the need for alignment. However, in our experimental set-up the light generated by the tunable illumination source is close to linearly polarized light. Therefore, the orientation of the circular polarizer in our set-up translates into output light intensity variations. To better utilize the power of the illumination source, we designed a 3D-printed rotatable holder for the circular polarizer to achieve free manual rotation with a range of 180°. First, a circular polarizer piece is cut from a larger sheet (left-handed plastic circular polarizer, Edmund Optics), and is glued to a 3D-printed rotary piece with a handle. Then the rotary piece is placed inside a 3D-printed outer shell with openings on the top and at the bottom, and with tick marks for 10° increments. Finally, an optical fiber holder is embedded inside the same outer shell, on top of the rotary piece.

Processing of lens-free polarized images

As depicted in Fig. 6.3, after PSR and multi-height-based phase recovery and image reconstruction of the two hologram stacks with the analyzer unit undergoing a 90° rotation in between, two sets of reconstructed complex images of the objects are obtained. In order to combine

them into a single lens-free polarized image with pseudo color-contrast, the following steps are sequentially applied:

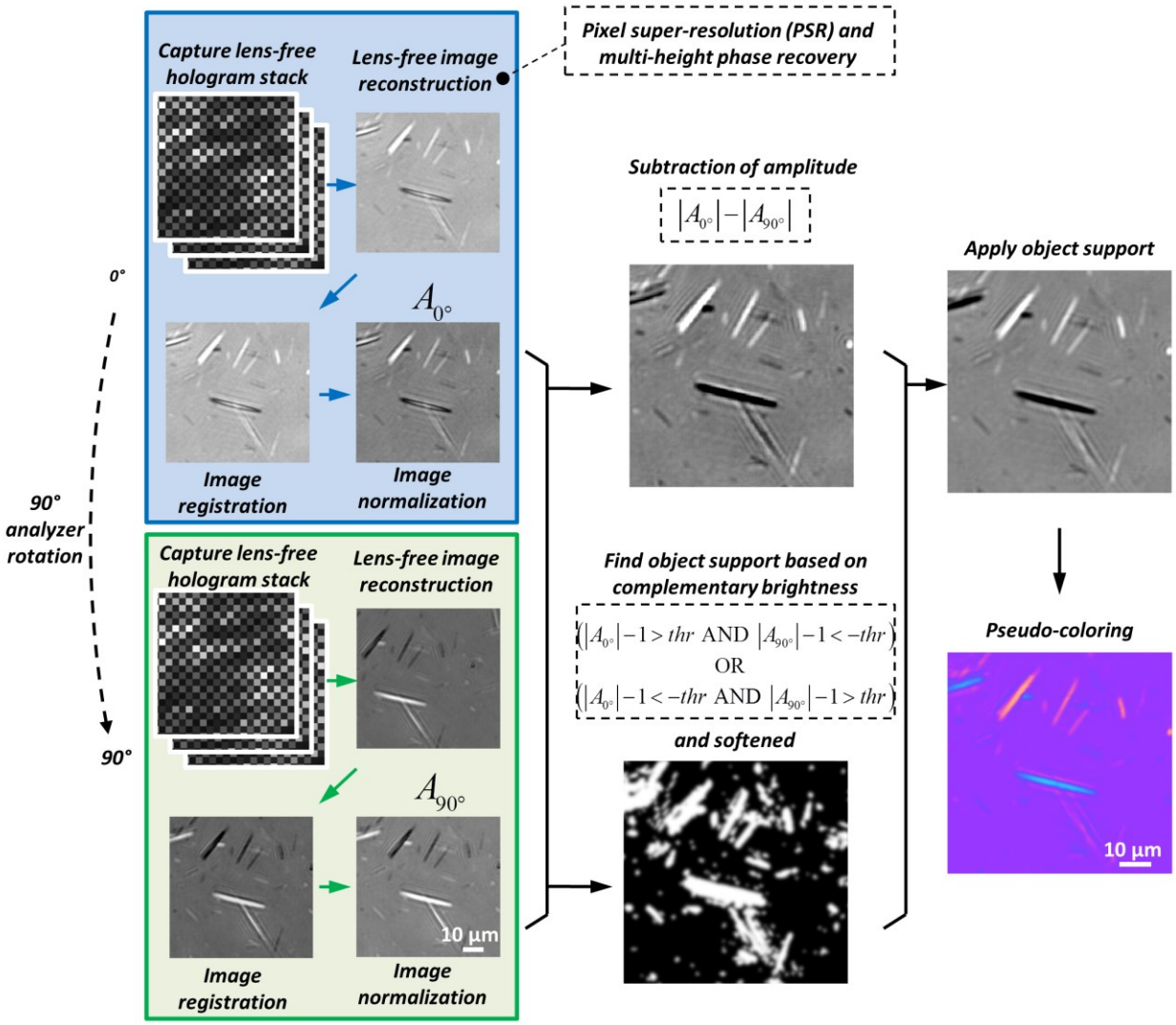

Figure 6. 3. Image processing flow chart. The blue box and the green box depict the processing of the lens-free hologram stack with the analyzer positioned at 0° and 90°, respectively. Then the image processing results are used in combination to obtain the amplitude-subtracted (differential) image and the object support. Finally, the object support is applied to obtain a grayscale image, and pseudo-coloring is performed to create color contrast similar to a CPLM.

(1) Image registration. We utilize the automated feature-matching algorithm in the Computer Vision System Toolbox™ of MATLAB® to calculate a geometric transform between the two sets

of complex images assuming a similarity relationship, based on which the 90° image is aligned to the 0° image. Note that this feature matching requires that the inputs are real-valued images. Therefore, we used the absolute-background-subtracted versions of the two complex images for feature extraction purposes:

$$O_j^s = \left| O_j - \bar{O}_j \right| \tag{6.1}$$

where O_j (j = {0°, 90°}) denotes the two complex images to be aligned, $\bar{O}_j$ denotes the mean value of O_j.

(2) Image normalization. Both the 0° and 90° complex images after image registration in step *(1)* are divided by their respective mean values, such that the discrepancy between their brightness is minimized. This step results in two normalized complex images A_j (j = {0°, 90°}).

(3) Subtraction of image amplitudes. We then calculate $A_s = \left|A_{0°}\right| - \left|A_{90°}\right|$, resulting in a differential image A_s whose values are centered around 0.

(4) Birefringent object support calculation. To further exploit the information about the object support, i.e., the specific positions and maps of birefringent objects within the sample FOV, we take advantage of the complementary brightness property of this optical design, where *the brighter-than-background pixels caused by birefringence in the 0° image will roughly correspond to darker-than-background pixels in the 90° image*, and vice versa. Based on this, the object support map (M) for birefringent objects in our imaging FOV can be calculated using the following binary operation:

$$\begin{gathered} M = \left(\left|A_{0°}\right| - 1 > thr \text{ AND } \left|A_{90°}\right| - 1 < -thr \right) \\ \text{OR} \\ \left(\left|A_{0°}\right| - 1 < -thr \text{ AND } \left|A_{90°}\right| - 1 > thr \right) \end{gathered} \tag{6.2}$$

where *thr* is a predefined threshold value, e.g., 0.1, AND and OR refer to pixel-wise logical operators. The object support mask is then softened using a Gaussian function with σ = 0.56 μm, resulting in a new mask:

$$M_b = M * \frac{1}{\sqrt{2\pi}\sigma} e^{-\frac{x^2+y^2}{2\sigma^2}} \tag{6.3}$$

where $*$ denotes two-dimensional convolution operation.

(5) Application of object support. After the calculation of the birefringent object support map M_b, we then create a grayscale differential image $A_M = A_s \circ$, where $\circ$ denotes pixel-wise multiplication of two images.

(6) Pseudo-coloring of the lens-free image. In this final step, the grayscale differential image A_M is mapped into a color image *C* to create a similar color contrast compared to a conventional CPLM image for the ease of a rheumatologist to inspect our lens-free images. This color map is statistically learned using a sample lens-free grayscale differential image from step *(5)* and a corresponding CPLM image (40× 0.75NA) of the same sample. First these two images (lens-free and CPLM) are aligned with respect to each other using image registration. Then, a set of 128 bins are created for the sample lens-free grayscale differential image, spanning the entire range of its values:

$$\text{bin}_k = \left[a + (k-1)w, a + kw \right) \tag{6.4}$$

where k = 1, …, 128, a is the minimum value of the sample lens-free grayscale differential image (A_M), and a+128w is equal to the maximum value of A_M. For each one of these bins, we then perform the following:

a) Find the set of pixels in the sample lens-free grayscale differential image that fall into the *k*th bin.

b) For this set of pixels found in step a, find the corresponding pixels in the sample CPLM image, and calculate the mean R, G and B values for these pixels.

After steps a and b, we create the mapping between the pixel values of the sample lens-free differential image with respect to the R, G and B components of the corresponding CPLM image. We finally use a piecewise linear function to approximate these 3 mapping functions (for R, G and B channels) to avoid rapid fluctuations due to insufficient sampling. For values that can potentially occur outside the range of these bins, linear extrapolation method is used.

PSR technique to improve the resolution of lens-free on-chip microscopy

As detailed in Chapter 1, the pixel size of the image sensor array imposes a physical limit on the resolution of a lens-free on-chip microscope, according to the Nyquist sampling theorem [174]. The PSR technique is applied to break this undersampling related resolution limit by capturing multiple subpixel-shifted low-resolution holograms and synthesizing them into a single high-resolution hologram [13,31,35,53,55,56,59,95]. During the lens-free hologram acquisition, a positioning stage is used to shift the image sensor chip on an 8-by-8 orthogonal grid with a grid size of 0.28 μm. Note that these subpixel shifts do not need to be precise or known a priori, as we use a digital shift estimation algorithm to accurately estimate these sub-pixel shifts after image capture [95]. Then a conjugate gradient method is used to find the optimal high-resolution hologram that is statistically consistent with all the low-resolution pixelated holograms that are undersampled at the sensor array [95].

Autofocus algorithm to identify the sample height on the sensor chip

An autofocus algorithm is used to automatically find the z_2 distance (i.e., the sample-to-sensor distance) for a PSR hologram by solving a maximization problem, with the objective function being a focus criterion, and the variable being the propagation distance. The focus criterion we

used in this work is the negative of the Tamura coefficient [111] calculated for the amplitude of the complex image, which is found to give a distinct peak at the correct z_2 distance. The hologram is digitally propagated to a range of z_2 distances with the focus criterion evaluated at each height, and the corresponding maximum is found. Next, a smaller range of z_2 distances are evaluated around this maximum point, with the scanning resolution also refined. These steps are repeated until the scanning resolution falls below a predefined threshold (e.g., 0.01 μm). The edge sparsity-based metric presented in Chapter 4 can also be used here.

Multi-height phase recovery for elimination of twin-image artifact

As detailed in Chapter 2, a multi-height iterative phase recovery algorithm [35,55,56,59,67] with 10 heights is used to retrieve the optical phase of the holograms, in order to mitigate the twin image artifact caused by the loss of phase information at the sensor array. These heights are separated by ~ 15 μm. An initial guess of the complex optical wave is calculated using the back-propagation of the hologram at the first measurement height, assuming that the heights are ordered in ascending order (i.e., the closest z_2 corresponds to the first height). Then, this initial guess is propagated to the second height, where its amplitude is averaged with the square root of the measured hologram at the second height, and the phase is kept unchanged. Next, this updating process is repeated at the subsequent heights and then backwards after it reaches the last height. Each one of these digital round-trips among these different heights counts as one iteration, and after ~ 10-20 iterations the optical phase converges, yielding us a unique complex wave for each one of the measurement heights. The converged complex wave of any one of these heights is finally propagated to the plane of the sample to obtain the complex image of the sample. Note that the transport of intensity equation (TIE) [10,35,60] is not used here as it is known that TIE is more sensitive to low-frequency components, whereas the multi-height based iterative phase recovery

is more sensitive to high-frequency components. In this work, since the birefringent crystals of interest in synovial fluid are relatively small and sharp, the multi-height iterative phase recovery converges rather quickly without the need for using a solution of TIE.

Preparation of MSU and steroid crystals

The reference slides containing MSU crystals were anonymously prepared from a surgically resected large tophus without a link to any subject related information. The tophus was obtained when a patient with confirmed gout received resection surgery of the tophus located in the olecranon bursa. The surgery was routine elective surgery to alleviate the symptom, as part of standard clinical care and unrelated to this study. The tophus was cut in half, revealing a soft semi-liquid center. A smear sample was prepared (touch-prep method), and a small amount of adhesive mounting medium (Cytoseal™, Richard Allan Scientific, Kalamazoo, Michigan) was applied onto the sample. Finally, the slide was cover-slipped.

For the slides of steroid crystals (used as negative controls), a mixture of methylprednisolone acetate suspension (Depo-Medrol® 40mg/ml, Pfizer, New York) and 1 cc of 1% lidocaine was made. Twenty microliters of this mixture was placed onto a slide and smeared, and then air-dried. Adhesive mounting medium was not used for the steroid crystals slides, because applying the medium to steroid crystals had a tendency of creating bubbles next to the crystals, which was not observed in the MSU sample preparation.

All biologic samples were obtained after de-identifying the patients' information. The methodology for obtaining these samples was reviewed by UCLA Institutional Review Board (IRB) and deemed exempt.

6.3 Results and discussion

Design, numerical simulation and analysis of lens-free polarized on-chip microscopy for imaging birefringent crystals

In order to model our optical design, we can effectively decompose the presented lens-free polarized imaging system into two sections that deal with *polarization* and *diffraction*. In the *polarization* related part, the circular polarizer, birefringent sample and the analyzer are assumed to be thin and the vertical gaps between these components are assumed to be negligible. In the *diffraction* part, the light that exits the *analyzer* diffracts to be sampled by the sensor chip, after a propagation distance of z_2.

We formulated the polarization part of this lens-free on-chip imaging system using Jones calculus [173] and simulated it in MATLAB®. The Jones representation of the respective elements of our imaging system can be written as:

a) Input left-hand circularly polarized (LHCP) light:

$$\mathbf{W} = \frac{1}{\sqrt{2}}\begin{bmatrix} 1 \\ -i \end{bmatrix} \tag{6.5}$$

where $i = \sqrt{-1}$.

Particular attention should be paid to the convention of handedness: the LHCP used in this paper is defined *from the point of view of the source*, i.e., *if one looks away from the source, along the direction of light propagation, the temporal rotation of the field at a given point in space is counterclockwise.*

b) Birefringent sample:

$$\mathbf{S} = \begin{bmatrix} e^{-i\varphi/2}\cos^2\alpha + e^{i\varphi/2}\sin^2\alpha & \left(e^{-i\varphi/2} - e^{i\varphi/2}\right)\cos\alpha\sin\alpha \\ \left(e^{-i\varphi/2} - e^{i\varphi/2}\right)\cos\alpha\sin\alpha & e^{-i\varphi/2}\sin^2\alpha + e^{i\varphi/2}\cos^2\alpha \end{bmatrix} \tag{6.6}$$

where φ is the relative phase retardation induced by the object birefringence after the sample plane, and α is the orientation of the fast axis of the birefringent sample with respect to the *x*-axis.

c) λ/4 retarder:

$$\mathbf{Q} = e^{-i\pi/4}\begin{bmatrix} \cos^2\beta + i\sin^2\beta & (1-i)\sin\beta\cos\beta \\ (1-i)\sin\beta\cos\beta & \sin^2\beta + i\cos^2\beta \end{bmatrix} \tag{6.7}$$

where β is the orientation of the fast axis of the λ/4 retarder with respect to the *x*-axis.

d) Linear polarizer:

$$\mathbf{L} = \begin{bmatrix} \cos\gamma & \sin\gamma \end{bmatrix} \tag{6.8}$$

where γ is the polarization orientation of the linear polarizer with respect to the *x*-axis. Note that we write $\mathbf{L}$ as a row vector instead of a 2-by-2 matrix, such that $p = \mathbf{LQSW}$ can be a scalar complex output.

Based on these definitions, the variables of interest in our lens-free optical design for polarization imaging are *α, β, γ,* and *φ*. In our simulations, we approximated the shape of the MSU crystals as a cylinder. We further assumed that the lower bound on the diameter of the MSU crystal is 0.5 μm [175], and the lower bound on the birefringence is $|\Delta n| = 0.1$ with the fast axis being the axis of the cylinder; therefore the relative birefringence induced phase retardation at the center of the cylinder at a wavelength of 532 nm can be approximated as $\varphi \sim 0.19\pi$. As the incident wave is circularly polarized, without loss of generality, we select β to be equal to 90°. In order to detect birefringence as well as its sign (+/-) similar to a CPLM image, ideally the brightness in the output image should vary when the MSU crystal takes different orientations in the sample FOV. More specifically, when the MSU crystals are aligned with a certain direction, the output should appear brighter than the background; when perpendicular to the same direction, the output should appear

darker than the background. In this way, if the sign of the birefringence changes, the brightness variation will invert, helping us to determine the sign of the birefringence of the sample.

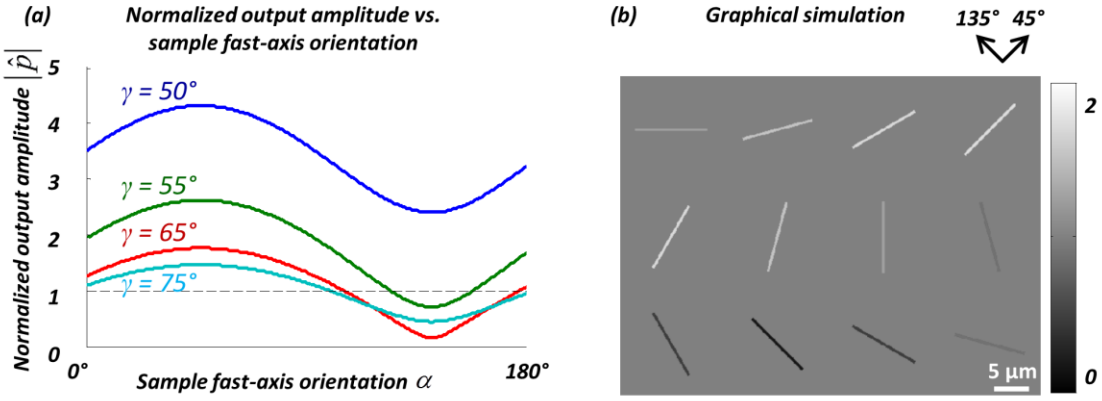

Figure 6. 4. Optimization of the orientation angle of the linear polarizer (γ). (a) The normalized output amplitude $|\hat{p}|$ is plotted as a function of the sample fast-axis orientation, α, for different linear polarizer orientations (γ = 50°, 55°, 65°, 75°). **(b)** The simulated normalized output images of MSU crystals at varying orientations, using γ = 65°. The MSU crystals are simulated as cylinders with a birefringence of $|\Delta n|$ = 0.1, diameter of 0.5 µm, length of 10 µm, and the fast axis is along the long axis of the crystals.

With these in mind, we scanned the remaining two parameters α and γ, and calculated the normalized output ($\hat{p}$) against α while varying γ, i.e.:

$$\hat{p} = \frac{p}{p_0} = \frac{\mathbf{LQSW}}{\mathbf{LQIW}} = \frac{\mathbf{LQSW}}{\mathbf{LQW}} \tag{6.9}$$

where in the calculation of p_0, the Jones matrix of the birefringent sample is replaced by the identity matrix **I** representing no sample being present. As can be seen in Fig. 6.4 (a), all the curves corresponding to different choices of γ exhibit a modulation of $|\hat{p}|$ as a function of α, and the maximum values of these curves occur at α = 45° while the minimum values occur at α = 135°. Among all of these curves shown in Fig. 6.4(a), the red curve, representing γ = +65°, has the largest modulation depth, implying the best sensitivity for the current parameters simulated. Moreover,

the red curve is almost symmetrically distributed around unity, and thus, the brighter-than-background orientations of the MSU crystal roughly correspond to $0° < \alpha < 90°$, whereas the darker-than-background orientations of the MSU crystal roughly correspond to $90° < \alpha < 180°$. This feature gives advantage to the determination of the sign of the birefringence of the objects which is important for gout diagnosis and inspection of synovial fluids, and therefore in our experimental design, we chose $\gamma = +65°$ as the optimal configuration. Based on this choice, Fig. 6.4(b) also shows the graphical simulation of the image of a 0.5 μm diameter MSU crystal having different orientations: as expected, the crystal brightness is maximum when aligned in the 45° direction, and minimum when aligned in the 135° direction.

Next, we further simulated the behavior of four different types of objects with the same cylindrical morphology with a diameter of 0.5 μm:

1) Transparent and negatively birefringent ($\varphi = 0.19\pi$, fast axis is along the cylinder axis);

2) Transparent and positively birefringent ($\varphi = 0.19\pi$, fast axis is perpendicular to the cylinder axis);

3) Transparent and non-birefringent ($\varphi = 0$);

4) Absorptive and non-birefringent ($\varphi = 0$ and transmission light intensity is attenuated by 36% per micron).

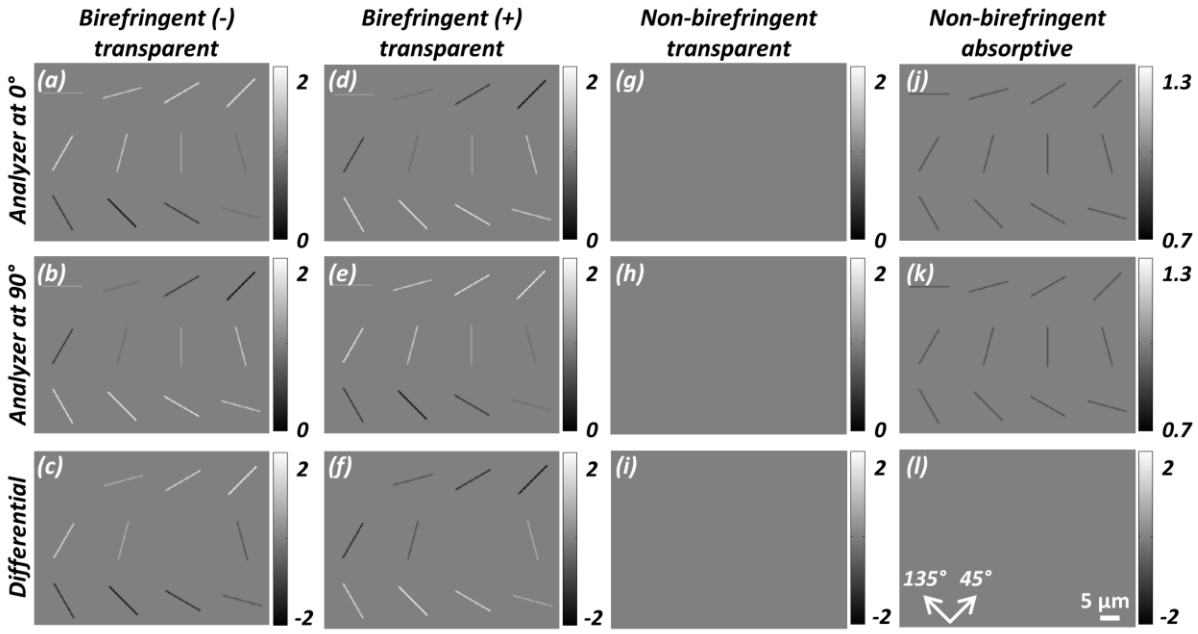

Figure 6. 5. Simulated images of four different types of particles with the same needle-like morphology: negatively birefringent and transparent (first column), positively birefringent and transparent (second column), non-birefringent and transparent (third column), non-birefringent and absorptive (fourth column), imaged under two different analyzer orientations (0°: first row, 90°: second row) and the subtraction of the amplitudes (labeled as *differential*) at these two orientations (third row). The differential step (third row) results in cancellation of non-birefringent particles that normally appear in both orientations of the analyzer.

These numerical simulations were performed to better understand how different target objects would appear in our imaging design as compared to potential false positive objects, and the results are summarized in Fig. 6.5. As can be seen in the first row, Fig. 6.5 (a) and Fig. 6.5 (d), having opposite signs of birefringence show inversion of brightness; for example for α = 45°, negative birefringence translates to maximum brightness while positive birefringence translates to minimum brightness; for α = 135°, negative birefringence translates to minimum brightness while positive birefringence translates to maximum brightness. As expected, a non-birefringent and transparent object (see Fig. 6.5 (g)) results in zero signal, whereas a non-birefringent and absorptive object (see Fig. 6.5 (j)) results in reduced brightness.

A close observation of Fig. 6.5 (panels a, d, and j) reveals a potential ambiguity of crystal analysis. Although it is safe to declare brighter-than-background objects as birefringent, darker-than-background objects need additional analysis before they can be described as birefringent since an absorptive object could have the same appearance upon single viewing. To resolve this ambiguity, we adopted a differential imaging strategy as also detailed in the Materials and methods section. In addition to a single analyzer/sample orientation, we rotate the analyzer or the sample by 90°, then repeat the lens-free imaging experiment, and finally subtract the amplitudes of the two reconstructed images, resulting in the differential output $\hat{p}_s = |\hat{p}_{0^\circ}| - |\hat{p}_{90^\circ}|$, where the subscripts 0° and 90° denote the images before and after analyzer/sample rotation, respectively. Fig. 6.5 middle row depicts the second set of reconstructed images with the analyzer rotated by 90°, and Fig. 6.5 bottom row shows the subtraction results. *As shown in Fig. 6.5 (c, f and l), the signals due to birefringence are enhanced while the signals due to absorption are exactly canceled out, as desired*. This differential image $\hat{p}_s$, in combination with the original lens-free images, $\hat{p}_{0^\circ}$ and $\hat{p}_{90^\circ}$, help us remove potential false positive objects while also sensitively detecting birefringent objects and determining their sign. One should note that if a specific birefringent crystal is aligned either at 0° or 90°, the difference lens-free image $\hat{p}_s$ will not show its signature; this is also the case for the standard CPLM and would not constitute a limitation since the individual images at each analyzer position will show the presence of such birefringent crystals (see e.g., Fig. 6.5(a-f)).

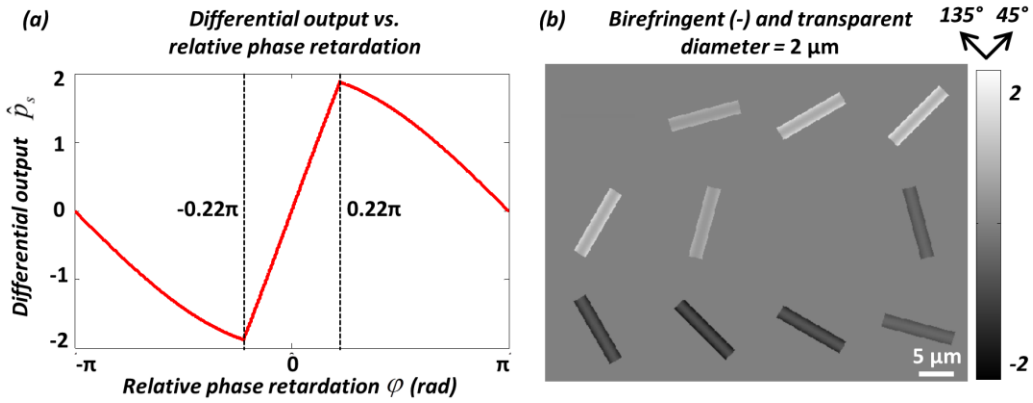

Figure 6. 6. Simulation of linearity. (a) Simulation of the differential output $\hat{p}_s$ as a function of the relative phase retardation φ, with the crystals aligned at 45° ($\alpha = 45°$). $\hat{p}_s$ almost linearly reaches to the maximum/minimum when $|\varphi|$ increases from 0 to ~ 0.22π, then turns backwards towards 0 as $|\varphi|$ further increases to π. **(b)** Simulated image of an MSU crystal with larger diameter (2 μm) compared to Fig. 6.4 and Fig. 6.5. The effect of the nonlinearity is manifested by the hollow appearance of the simulated images. Nevertheless, the intense (bright/dark) edges provide enough contrast for crystal detection and identification.

For this differential lens-free imaging design, it is also important to understand and quantify the linearity of the differential output signal $\hat{p}_s$ with respect to the relative birefringent phase retardation φ. Here, the crystals are assumed to be aligned at 45° ($\alpha = 45°$). Since $\hat{p}_s$ is a periodic function of φ with a period of 2π, we only need to investigate $\hat{p}_s$ with respect to φ varying between –π and π, where $0 < \varphi < \pi$ implies that the fast axis is along 45°, and $-\pi < \varphi < 0$ implies that the slow axis is along 45°. As shown in Fig. 6.6 (a), for small φ ($|\varphi|<0.22\pi$), the differential output $\hat{p}_s$ is almost perfectly linear as a function of φ. However, this linearity does not hold for larger $|\varphi|$. In fact, beyond the turning points $|\varphi| \approx 0.22\pi$, the curve moves backwards and reaches zero at $|\varphi| = \pi$. This is an interesting observation that is revealed by our numerical simulations and analysis, and it should not affect the sensitivity of our imaging platform for gout diagnosis or detection of

MSU crystals. The thickness of the needle-shaped MSU crystal gradually increases from its edge (approximately zero thickness) to the middle (largest thickness), so that the relative phase retardation φ also gradually increases from 0 to its maximum value. Therefore, it is guaranteed that even for a thick MSU crystal with a large maximum φ value, there will be a strong linear birefringence signal toward the edges of the crystal for its detection and identification. This is also verified by the simulation results shown in Fig. 6.6(b), where the diameter of the cylindrical crystal model is increased to 2 μm, and therefore the maximum relative phase retardation is increased to approximately 0.75π. It is shown that, even though at the middle of the crystals the images appear less intense, the strong signal contrast toward the edges is maintained. The same behavior is also verified experimentally, as will be detailed in the next subsection.

Experimental results on lens-free polarized imaging of MSU crystals

To demonstrate the imaging capabilities of our lens-free polarized on-chip microscopy platform to be used in gout diagnosis, we imaged MSU crystal samples made from the tophus of a de-identified patient (refer to the Methods section for details) using our lens-free microscope and compared our images against the gold standard images captured using a benchtop CPLM (Olympus BX51 with additional polarization components: drop-in polarizer U-POT and gout analyzer U-GAN) with a 40× 0.75NA objective lens. Fig. 6.7(a) shows a full-FOV lens-free hologram, captured with the analyzer at 0°. The circular FOV of a typical 40× objective lens (see the yellow dashed circle) is ~ 0.24 mm^2, which is around two orders of magnitude smaller compared to the lens-free FOV. This large FOV of lens-free microscopy offers an important advantage for screening of large areas in the search for scarce crystals, potentially helping to reduce the false-negative rate of diagnosticians. By digitally zooming into a sub-region of the lens-free image (see Fig. 6.7(b)), one can clearly see that, as expected, the MSU crystals appear brighter

compared to the background when their orientations are close to 45° and darker when their orientations are close to 135°. Three regions of interest (ROI) are further selected and zoom-in images are shown to the right of Fig. 6.7. The lens-free pseudo-colored images (Fig. 6.7(f-h)) are digitally processed from the lens-free grayscale differential reconstruction results (Fig. 6.7(c-e)) as detailed in the Materials and methods section. Comparing Fig. 6.7(f, g) to the corresponding images of the benchtop CPLM (Fig. 6.7(i, j)), we notice that not only the most prominent objects with strongly yellow or blue colors agree well in each set of images, but even the weak signals are picked up (pointed by the white arrows) by both microscopes; in fact the image contrast of these weak crystals captured by the lens-free microscope is much stronger than the CPLM images. This stronger image contrast suggests the potential enhanced sensitivity of the lens-free polarized microscope. In Fig. 6.7(h), we also notice that two relatively thicker crystals (pointed by the yellow arrows) result in "hollow" appearances, verifying the predictions of our numerical simulations (see Fig. 6.6(b)). Although Fig. 6.7(h) appears somewhat different compared to Fig. 6.7(k), it should not pose a problem for identification of MSU crystals or gout diagnosis, as these thick MSU crystals are clearly defined by their strong yellow/blue periphery enclosing a hollow interior, with a needle-shaped morphology. For the same thicker crystals, we also notice that the lens-free images contain some fringes along the crystals that do not exist in the traditional CPLM images. These artifacts result due to diffraction and form a signature of thicker birefringent crystals in lens-free images. However, because of the fact that these fringes will only occur around these thick and strongly birefringent objects and that non-birefringent objects (transparent or absorptive) are canceled out in our differential holographic images, this will not affect the sensitivity of our computational gout imaging method.

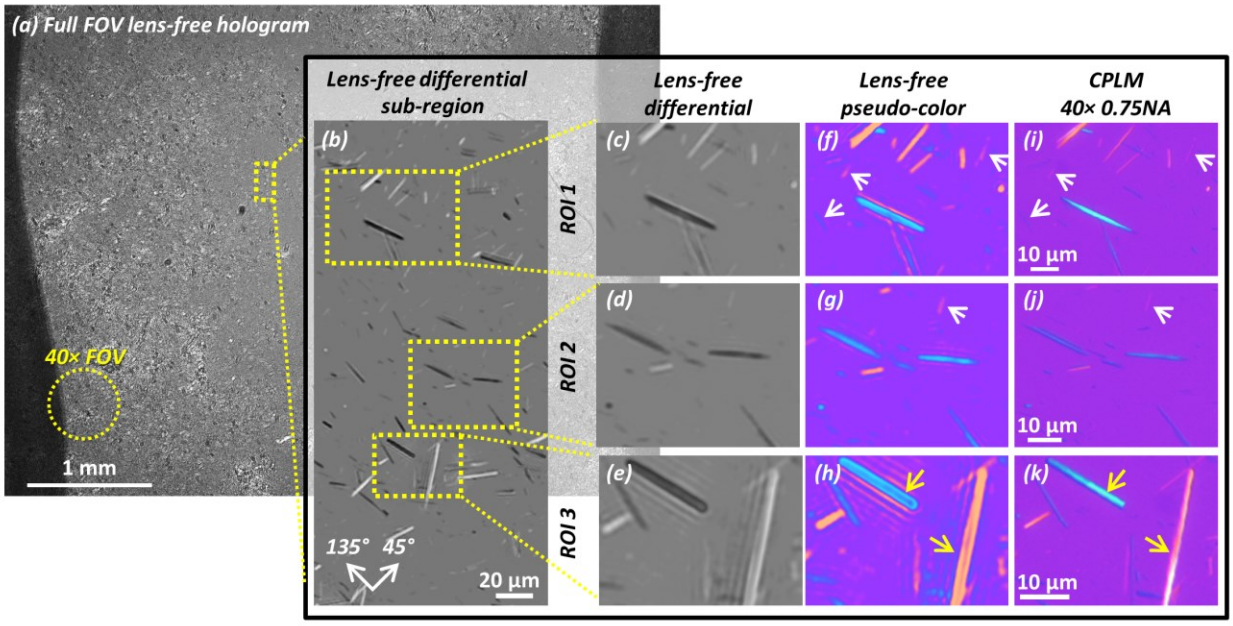

Figure 6. 7. Experimental imaging result of a MSU crystal sample from a patient's tophus, compared to a 40× 0.75NA CPLM. (a) The full FOV of the lens-free hologram is 20.5 mm^2 which is ~2 orders of magnitude larger compared to the FOV of a typical 40× microscope objective lens (see yellow dashed circle). **(b)** A sub-region showing the lens-free differential polarized image. Clearly the crystals oriented close to 45° (see orientation guide in the bottom left) appear brighter than the background, and those close to 135° appear darker. **(c-e)** Lens-free grayscale differential image of 3 ROIs taken from (b). **(f-h)** Pseudo-colored images of (c-e). **(i-k)** 40× 0.75NA CPLM images of the same regions as (f-h). White arrows: crystals that result in a weak signature have better contrast in the lens-free pseudo-color images (f, g) than the CPLM images (i, j). Yellow arrows: thick MSU crystals in the lens-free pseudo-color image (h) have hollow appearances, slightly different from the CPLM image (k).

Experimental results on lens-free polarized imaging of steroid crystals

Next, in order to test the performance of our lens-free holographic imaging method to differentiate other types of birefringent crystals from MSU crystals, we imaged steroid crystal samples as negative control. Corticosteroid crystals are birefringent crystals that can be found in some patients' joint fluids following a corticosteroid injection and sometimes can lead to false positives in gout diagnosis. Their irregular shape provides a means to differentiate them from MSU

crystals. As shown in Fig. 6.8, the pseudo-color lens-free polarized microscope images (b, e, g, i) of these crystals show consistent morphology that agrees well with the benchtop CPLM images of the same samples (c, f, h, j). Because of the large thicknesses of these steroid crystals, there exists some glowing artifacts around the crystals' lens-free images (b, e, yellow arrows), due to similar reasons previously discussed. In particular, the ROI 3 shown in Fig. 6.8 (g-j) contains multiple steroid crystal particles, whose surfaces reside at different depths/heights. We use the digital re-focusing capability of the lens-free polarized microscope to show some of the in-focus images of these respective crystal particles at different z-distances from the sensor chip. In Fig. 6.8 (g, i), the lens-free image was digitally refocused to relative Δz distances of 0 μm and 8.3 μm. At these respective planes, the particles on the lens-free images pointed by the white arrows are at the best focus, showing distinct and clear shapes that are also consistent with Figs. 6.8 (h, j), which had to be manually refocused to the same particles due to the extremely narrow depth of focus of the objective lens used in CPLM. For example, the blue-colored irregularly shaped crystal particle on the top right of ROI 3, pointed by the white arrow in Fig. 6.8 (g), is best visualized at $\Delta z = 0$ μm, and the sharp corner at the bottom of the blue-colored crystal particle, pointed by the white arrow in Fig. 6.8 (i), is best visualized at $\Delta z = 8.3$ μm.

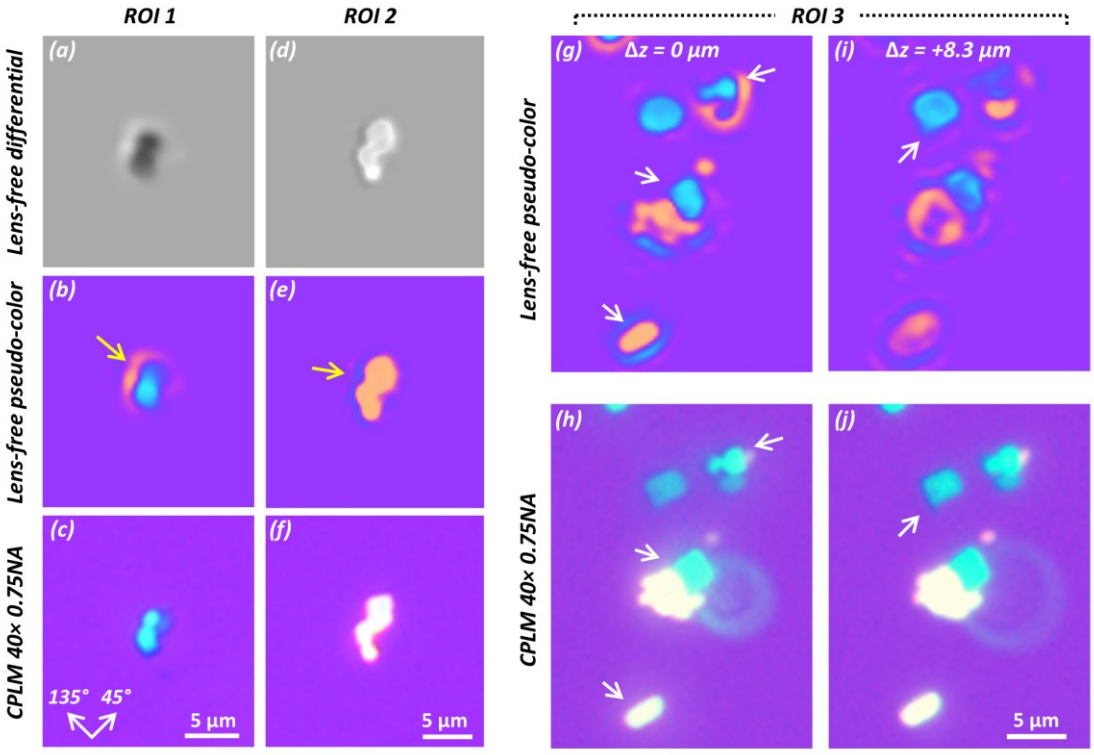

Figure 6. 8. Experimental imaging result of a steroid crystal sample, compared to a 40× 0.75NA CPLM. (a, d) Lens-free grayscale differential images of ROI 1 and ROI 2. **(b, e)** Pseudo-colored images of (a, d). The yellow arrows point to the glowing effect around crystals, resulting from the large thicknesses of the crystal particles. **(c, f)** 40x 0.75NA CPLM images of the same regions as (b, e). **(g, i)** The lens-free images of ROI 3 digitally refocused to the best relative focus distances (Δz) for different crystal particles, pointed by white arrows. **(h, j)** CPLM images corresponding to (g, i), manually refocused to the best focus distances for the respective particles pointed by white arrows.

This digital re-focusing capability of the lens-free holographic polarized microscope is an important feature and an advantage for the diagnosis of gout since microscopic samples are usually not perfectly planar – they inevitably have height variations on the order of tens of microns. Moreover, when the user of a conventional microscope translates the sample stage to observe different regions of the sample, the sample can easily get out of focus as the movement of the sample stage is not perfectly horizontal. For a regular sample, since one can constantly refocus the

microscope, these issues may be acceptable (at the cost of diagnostician time). But when screening a sample with scarce crystals using a standard benchtop CPLM, there can be scenarios where there are simply not enough birefringent targets to focus on [176]. This would be less of an issue for the lens-free holographic polarized microscope described in this work because of its enhanced depth of field which can span several hundred microns as well as its large FOV that is >20 mm^2. [52] The lens-free holograms over a large sample area can thus be easily brought into focus by autofocusing and digital back-propagation algorithms detailed in our Materials and methods section.

Discussion

One of the major advantages of the presented lens-free polarization imaging approach is its larger FOV and cost-effectiveness compared to a standard CPLM. Using state-of-the-art CMOS imager chips that are also found in mobile phone cameras, a large FOV of >20-30 mm^2 can be routinely achieved using the lens-free imaging technology, whereas a standard objective-lens with a similar resolution level would typically have ~0.2 mm^2 FOV. Furthermore, a field-portable and light-weight version of our lens-free microscope with PSR capabilities [59] can be put together under $250-300 including all the components except the computer interface, while a standard CPLM [177] costs more than $10K and is significantly more bulky and heavy (>15 kg), also excluding the PC.

The imaging time of a large sample FOV is also of importance for this lens-free polarization microscopy technique to be used for synovial fluid screening in clinical settings. The image acquisition and processing speeds of the presented platform are currently not optimized to fully utilize the capabilities of the image sensor chip and the computer used in our work. In the image acquisition step, typically 1280 raw (i.e., lower-resolution) holograms are captured in each

experiment for PSR (64 raw holograms per height), multi-height phase recovery (10 heights) and differential imaging (2 analyzer angles). However, a significant reduction in the number of raw holograms that need to be acquired can be achieved as illustrated in Fig. 6.9: a similar image quality is retained in our lens-free MSU crystal images by using e.g., 4×4=16 raw holograms for PSR, 3 multi-height measurements at 2 analyzer angles, resulting in 96 raw holograms in total, which presents more than 13-fold reduction in the number of raw hologram measurements (96 vs. 1280). The CMOS image sensor chip that we used in our experiments has a maximum frame rate of ~15 frames per second; however, a much faster image acquisition can be achieved by adopting higher frame rate image sensors already available on the market.

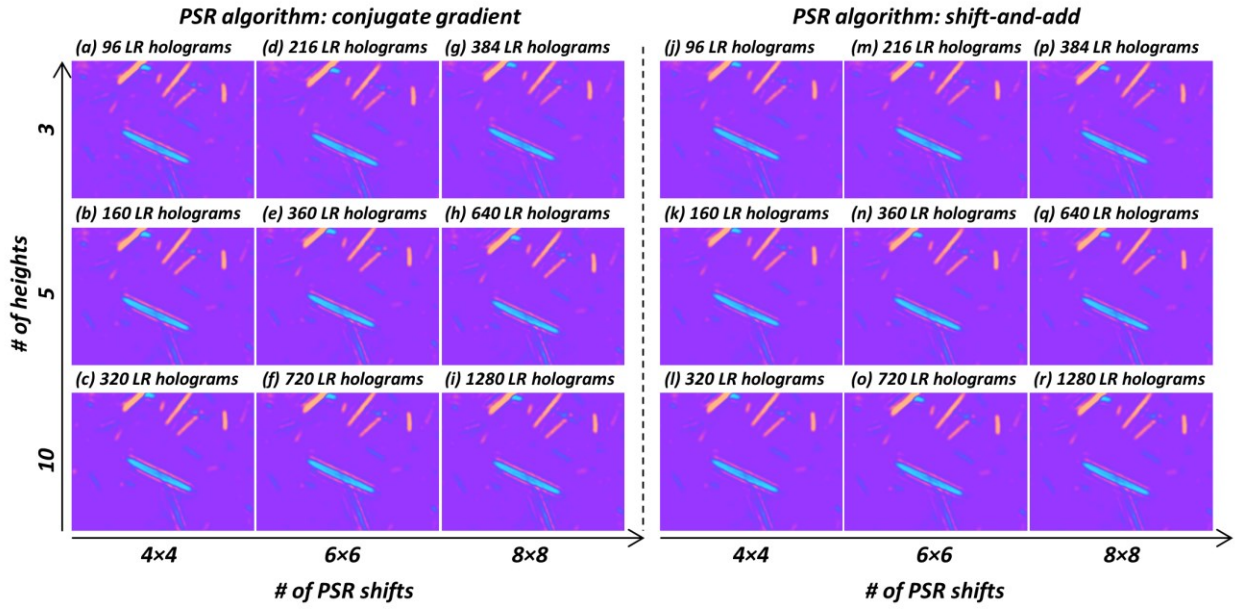

Figure 6. 9. Comparison of lens-free polarized imaging results using different numbers of low-resolution (LR) raw holograms. The left panel uses the conjugate gradient algorithm for implementing PSR, while the right panel uses the shift-and-add algorithm. Columns: different numbers of sub-pixel shifted raw holograms are used to synthesize a high-resolution hologram using PSR. Rows: different numbers of heights are used to perform multi-height phase recovery. The total number of LR raw holograms used to generate each image also includes a factor of 2 due to the two analyzer orientations.

Fig. 6.9 also compares the performance of two different PSR algorithms (i.e., the conjugate gradient algorithm [56,57,59] vs. the shift-and-add algorithm [35,53,58]) as a function of the number of raw holograms used in phase recovery and final image reconstruction, both of which provide very similar imaging results. Using the shift-and-add algorithm for PSR, which is in general faster than the conjugate gradient algorithm, the entire image reconstruction of a 1 mm^2 FOV (including PSR with 64 sub-pixel shifts and multi-height phase recovery with 10 heights, used in Fig. 6.9(r)) for one analyzer orientation can be completed within ~2.5 min using a desktop PC (OptiPlex 9010, Dell Inc.), without GPU programming. The time cost of the subsequent image processing steps (image registration, image subtraction, pseudo-coloring, etc.) are much smaller compared to PSR and multi-height phase recovery steps. Therefore, a computer cluster with approximately 40 nodes can process an entire FOV of ~20 mm^2 in ~2.5 min by dividing it into 1 mm^2 tiles. This time is reduced to ~20 seconds for PSR with 16 sub-pixel shifts and multi-height phase recovery with 3 heights, used in Fig. 6.9(j). To further improve the image processing speed, a cluster of GPUs can be used instead of CPUs, which can speed up the reconstruction time by at least another factor of 10-fold.

6.4 Conclusions

The design of a lens-free differential holographic polarized imaging platform is presented, which integrates cost-effective polymeric polarizing films with lens-free on-chip microscopy to achieve wide-field and high-resolution imaging of birefringent crystals. This computational imaging system is designed and further optimized through numerical simulations using Jones calculus. Lens-free imaging experiments corresponding to MSU crystal samples prepared from a gout patient's tophus and steroid crystals (as negative control) demonstrated that our reconstructed images have resolution, color and contrast that are highly consistent with the performance of a

gold-standard CPLM (40× 0.75NA). With ~2 orders of magnitude larger FOV than a CPLM, the presented technique has the potential to largely improve the efficiency and accuracy of gout diagnosis, while also reducing costs. Furthermore, as the lens-free imaging set-up can be cost-effective and field-portable, the presented method is especially promising for automated diagnosis of crystal arthropathy at the point of care or in resource-limited clinical settings.

Chapter 7. Lens-free time-resolved speckle imaging for high-throughput detection of motile parasites in bodily fluids

Parasitic infections form a major global public health issue. Existing screening methods based on manual microscopic examination often struggle to provide sufficient volumetric throughput and sensitivity to facilitate early diagnosis. In this chapter, a motility-based label-free computational imaging platform is demonstrated to rapidly detect motile parasites in optically dense bodily fluids by utilizing the locomotion of the parasites as a specific biomarker and endogenous contrast mechanism. Based on this principle, a cost-effective and mobile instrument was built, which rapidly screens ~3.2 mL of fluid sample in three dimensions (3D) to automatically detect and count motile microorganisms using their holographic time-lapse speckle patterns. We demonstrate the capabilities of our platform by detecting trypanosomes, a motile protozoan parasite, with various species that cause deadly diseases affecting millions of people worldwide. Using a holographic speckle analysis algorithm combined with deep learning-based classification, we show sensitive and label-free detection of trypanosomes within spiked whole blood and artificial cerebrospinal fluid (CSF) samples, achieving a limit-of-detection of ten trypanosomes per mL of whole blood (~five-fold better than the current state-of-the-art parasitological method) and three trypanosomes per mL of CSF. We further demonstrate that this platform can be used to detect other motile parasites by imaging *Trichomonas vaginalis,* the causative agent of trichomoniasis, which affects 275 million people worldwide. With its cost-effective, portable design and rapid screening time, this unique platform has the potential to be used for sensitive and timely diagnosis of neglected tropical diseases caused by motile parasites and other parasitic infections in resource-limited regions.

Part of this chapter has been submitted for publication and is under review.

7.1 Introduction

Parasitic infections affect billions of people globally, resulting in massive socioeconomic burden [178–181]. Although usually associated with low-income countries, parasitic infections are also becoming an increasing health concern in developed countries. In the United States alone, millions of people are affected by various parasites, which can lead to severe illnesses and even death [178]. Motility is common among disease-causing organisms, from unicellular pathogenic bacteria and parasitic protozoa to multicellular parasitic worms and ectoparasites. The ability of an organism to move itself from one location to another has obvious benefits for successful infection and transmission, and motility is often central to virulence [182–184]. Despite the importance of motility for a parasitic lifestyle, parasite motility remains an understudied area of research and motility-based diagnostics are largely underexplored.

Human African trypanosomiasis (HAT), also known as sleeping sickness, and Chagas disease (i.e., American trypanosomiasis) are examples of neglected tropical diseases caused by motile protozoan parasites. Neglected tropical diseases have historically been given little attention, disproportionately affect the world's poorest people, and lack adequate medical interventions for diagnosis and treatment. There are no vaccines, and existing chemotherapeutics suffer from high toxicity and drug resistance [185–188]. These two devastating diseases, HAT and Chagas disease, are caused by related trypanosome parasites [189]. *Trypanosoma brucei* (*T. brucei gambiense and T. brucei rhodesiense* subspecies) is responsible for HAT [186,187], and related species cause animal diseases that present a substantial economic burden in some of the poorest areas of the world. The parasite is transmitted to humans by the tsetse fly and survives extracellularly in blood and tissues, with dramatic impacts on the central nervous system [186,187]. HAT is endemic in ~30 sub-Saharan Africa countries with ~65 million people at risk of infection [181]. The number

of reported cases has dropped to historic lows, but past declines in case numbers have been followed by major epidemics. Therefore, HAT remains an important human health risk [190]. Chagas disease, on the other hand, is caused by *Trypanosoma cruzi* (*T. cruzi*), which invades and replicates inside host cells causing severe pathology within host tissues [191]. Chagas disease is mostly transmitted by the bite of triatomine bugs, but other transmission routes include blood transfusion and ingestion of contaminated food or drink [192]. The disease is endemic in Latin America where it affects over 6 million people [188,192,193]. It is estimated that more than 300,000 people are infected in the United States [194] with further increases expected as globalization and climate change impact the distribution of disease-transmitting vectors.

Both trypanosomiases can be classified into an initial stage during which trypanosomes circulate in the bloodstream and medical treatment is most effective (stage I HAT and acute Chagas disease), and a later stage that is exceedingly more difficult, if not impossible, to cure (stage II HAT and chronic Chagas disease). Therefore, *early detection is crucial* for both diseases. However, rapid and sensitive diagnosis remains challenging, particularly in resource-limited settings [195]. In the diagnosis of HAT, it is also essential to assess the stage of the disease to determine the appropriate therapeutic strategy. While trypanosomes remain in the blood and lymph in stage I HAT, stage II HAT is characterized by trypanosomes crossing the blood-brain barrier and invading the central nervous system, causing neurological symptoms and eventually death if untreated. Because the drugs used to treat stage I and stage II are not interchangeable, and drugs for stage II may be more toxic, it is very important to identify the stage of the disease to inform the selection of treatment regimen. Stage determination is currently done by collecting cerebrospinal fluid (CSF) via a lumbar puncture and examining the CSF under a microscope for presence of white blood cells (WBCs) and trypanosomes.

Both trypanosome species are typically ~20 μm in length and ~3 μm in width, and use flagellum-mediated motility for parasite propulsion [186,196,197]. Detection of these motile parasites in large volume bodily fluids such as blood and CSF is an important clinical challenge. For decades, the standard screening test for *T. b. gambiense* HAT has been the card agglutination test for trypanosomiasis (CATT), which detects the presence of antibodies against a specific parasite antigen [181]. However, CATT suffers from practical limitations as well as low specificity and sensitivity in some areas [181]. Moreover, a positive CATT test must typically be confirmed with direct visual observation in blood samples. Several molecular and immunological detection methods have been developed including polymerase chain reaction (PCR) and rapid diagnostic tests (RDTs), but these methods are limited by insufficient specificity or sensitivity, the need for sophisticated equipment and highly trained personnel, or high production costs [181,198,199]. Thus, microscopic evaluation is still widely used for primary or secondary diagnosis, and direct observation of CSF remains the sole method for HAT stage determination [181,199]. Each milliliter of whole blood typically contains billions of red blood cells (RBCs), millions of WBCs and hundreds of millions of platelets. In contrast, blood parasitemia fluctuates during the course of infection and often is below 100 parasites/mL [195,200,201], making microscopic identification of trypanosomes a *needle-in-a-haystack* problem. The low sensitivity of direct observation methods therefore requires analytical separation devices such as centrifugation or ion exchange purification, which partially limit analysis in resource-limited settings [202–204]. Thus, there is still a major need for development of new methods with high sensitivity and throughput that can reduce costs and simplify diagnosis.

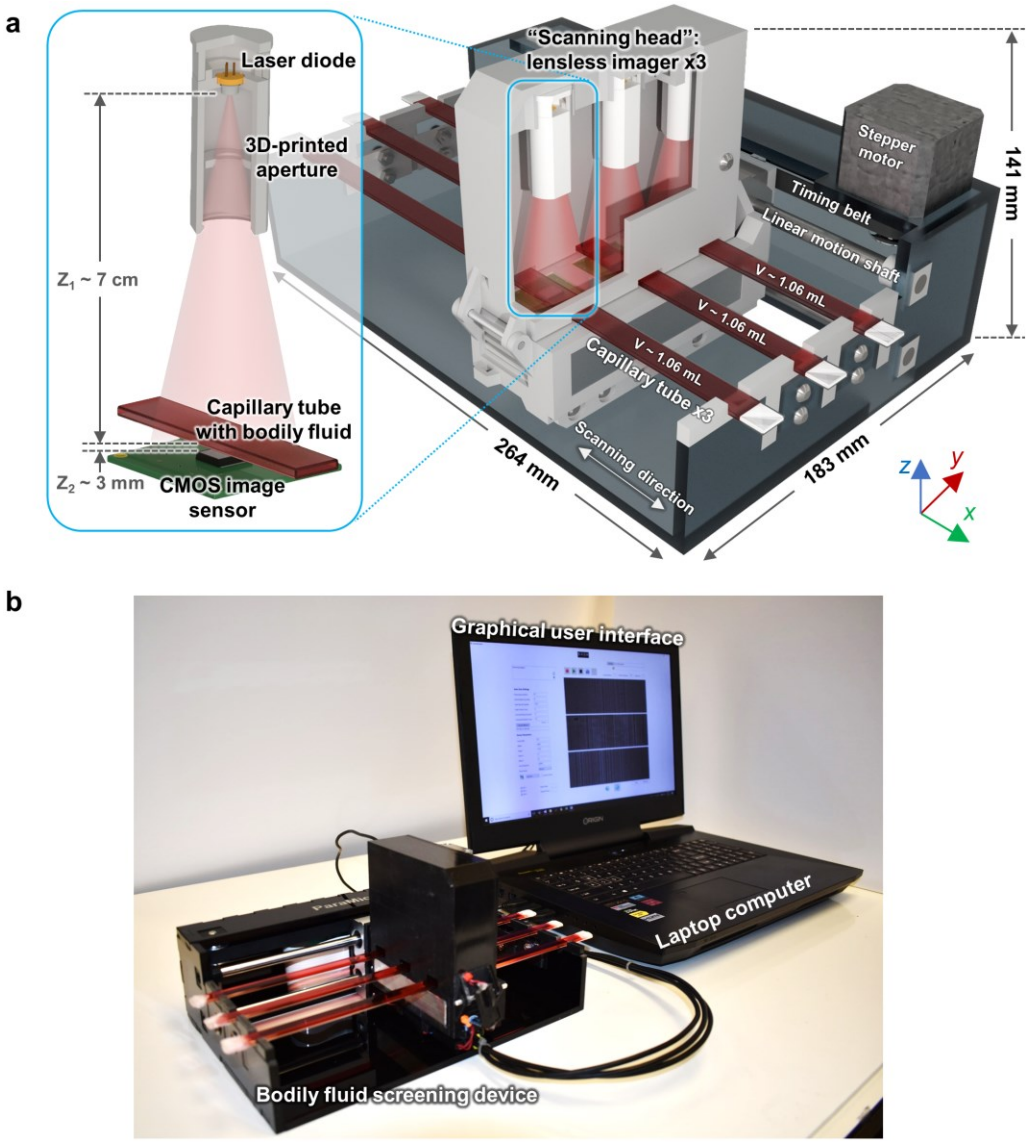

Figure 7. 1. High-throughput bodily fluid screening device, which screens and analyzes ~3.2 mL of fluid sample within ~20 min. (a) Schematic illustration of the device based on lensless holographic time-resolved speckle imaging. **(b)** Photograph of the device, controlled by a laptop, which is also used for processing of the acquired data.

To address this important challenge, here we demonstrate a cost-effective and field-portable optical device (Fig. 7.1) based on lensless time-resolved holographic speckle imaging, for label-free, high-throughput and sensitive detection of motile parasites in various bodily fluids and turbid media. Instead of staining a target analyte or using molecular biomarkers, our technique utilizes the locomotion of self-propelling parasites (or other motile microorganisms) as a biomarker and

endogenous contrast mechanism. As a result, the sample preparation is very simple and fast, does not require any benchtop-scale sample processing device/equipment and does not require refrigeration, centrifugation or purification. As shown in Fig. 7.1(a), the fluid sample to be screened is illuminated by a coherent light source (e.g., a laser diode), and a complementary metal-oxide-semiconductor (CMOS) image sensor is placed below the sample to record the time-varying holographic speckle patterns of the sample. This image sequence is then analyzed by a custom-written computational motion analysis (CMA) algorithm based on holography to generate a three-dimensional (3D) contrast map that is specific to the locomotion of the parasites in the sample volume. Finally, a deep learning-based classifier is used to automatically detect and count the signal patterns of the parasites using the reconstructed 3D locomotion map.

To increase the throughput and reduce the limit of detection (LoD) for rapid screening of large fluid volumes (~3.2 mL), we constructed a prototype that consists of three identical lensless speckle imaging modules mounted on a linear translation stage to screen three individual sample tubes in parallel (Fig. 7.1(a)). Each imaging module is translated to different sections of the capillary tube containing the liquid sample, where the CMOS image sensor captures high-frame-rate video sequences before moving on to the next section. Using this approach, ~3.2 mL of fluid sample is prepared, screened and analyzed, all within ~20 min, using the setup shown in Fig. 7.1. Compared to standard benchtop optical microscopes, our design provides orders of magnitude increase in the screened sample volume (which is very important for the detection of parasites at low concentrations) and is significantly more compact and light-weight (1.69 kg). Furthermore, since a large sample volume is screened computationally in the axial direction, our imaging device does not need high precision in its opto-mechanical design, which also makes our platform highly

cost-effective, where its parts cost less than $1,850 in total even under very low volume manufacturing.

We used trypanosomes to test our mobile platform and demonstrated its capability to detect parasites in spiked whole blood and CSF samples, which are important for the diagnosis and stage determination of HAT as well as the diagnosis of acute Chagas disease. We performed spiking experiments at a series of concentrations using *T. brucei brucei* (a non-human infectious subspecies of *Trypanosoma*) as a model parasite for *T.b. gambiense*, *T.b. rhodesiense* and *T. cruzi*. Through deep learning-based classification, we showed that as low as 10 parasites per mL of whole blood and 3 parasites per mL of CSF can be reliably detected using our platform. Furthermore, we demonstrated the success of our platform to detect other motile parasites in bodily fluids by imaging *Trichomonas vaginalis* (*T. vaginalis*), the protozoan parasite responsible for trichomoniasis, which is the most common, non-viral sexually transmitted disease affecting 3.7 million people in the United States and 275 million worldwide [205]. We believe that this label-free, motility-based parasite detection platform can provide a cost-effective and portable approach for rapid and sensitive screening of trypanosomes and other motile parasites in resource-limited settings, or as a high-throughput analytical research tool to study motile organisms in 3D.

7.2 Materials and methods

Sample preparation

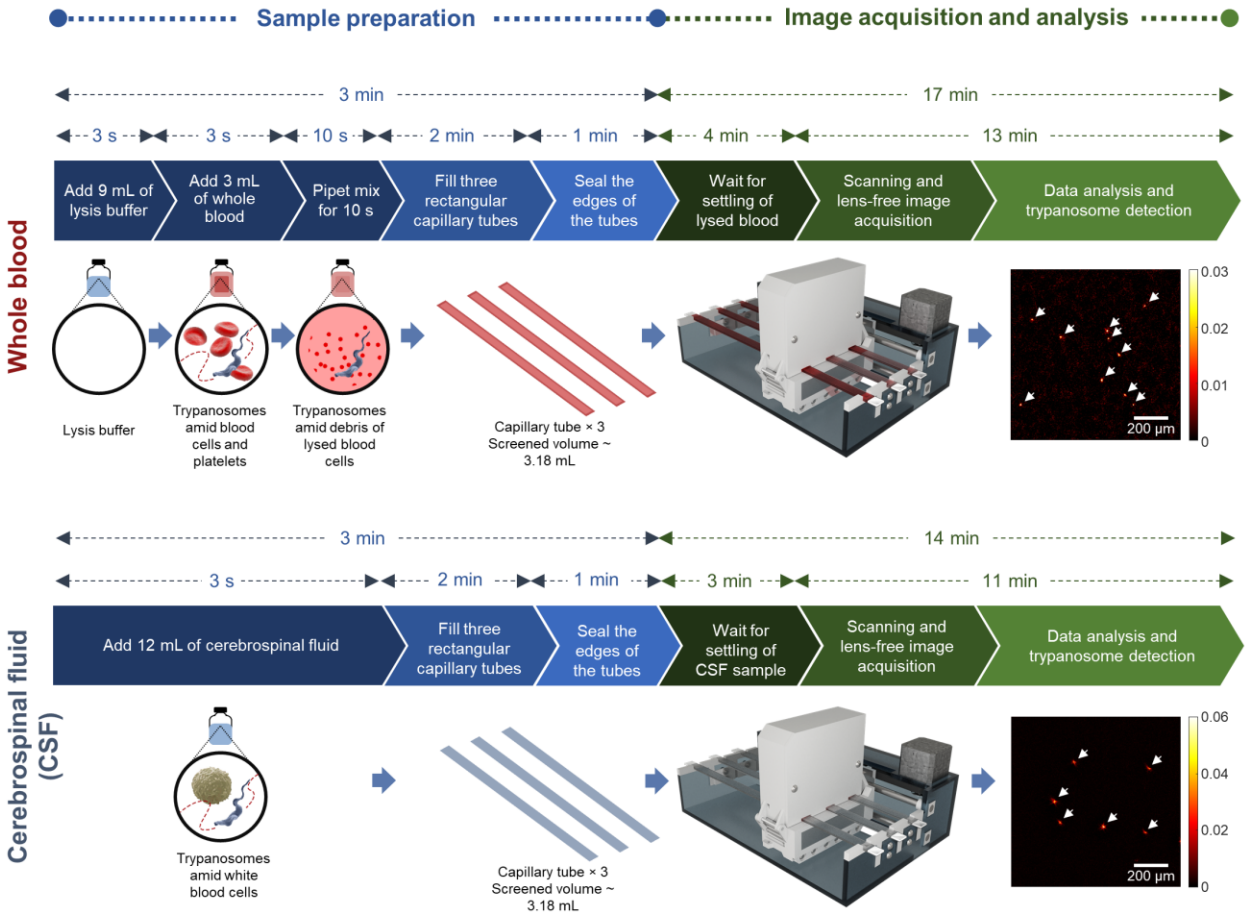

Figure 7. 2. Sample preparation and imaging process.

Lysis buffer preparation: 44 mM sodium chloride (product no. 71379, Sigma Aldrich (Missouri, USA)), 57 mM disodium phosphate (product no. 30412, Sigma Aldrich), 3 mM monopotassium phosphate (product no. 60220, Sigma Aldrich), 55 mM glucose (product no. G8270, Sigma Aldrich), and 0.24 % (w/v) sodium dodecyl sulfate (product no. L4390, Sigma Aldrich) in reagent grade water (product no. 23-249-581, Fisher Scientific (New Hampshire, USA)) were mixed for 2 h using a magnetic stir bar on a magnetic mixer. The solution was then filtered using a disposable filtration unit (product no. 09-740-65B, Fisher Scientific) for sterilization and

was stored at room temperature. This buffer solution lyses all the components of whole blood including RBCs and WBCs but does *not* lyse the trypanosomes [206].

Artificial CSF preparation: According to a previous method [207], 1.25 M sodium chloride, 260 mM sodium bicarbonate (product no. SX0320-1, EMD Millipore), 12.5 mM sodium phosphate monobasic (product no. S6566, Sigma Aldrich), and 25 mM potassium chloride (product no. P5405, Sigma Aldrich) were mixed well, and 10 mM magnesium chloride (product no. 208337, Sigma Aldrich) was added to make 10X artificial CSF. The solution was then filtered using a disposable filtration unit for sterilization. 10X stock solution was diluted ten-fold with reagent grade water to make 1X artificial CSF [207].

Culturing trypanosomes: 427-derived bloodstream single marker trypanosomes (*T. b. brucei*) were cultivated at 37 °C with 5% CO_2 in HMI-9 medium with 10% heat-inactivated fetal bovine serum (product no. 10438026, Gibco (Massachusetts, USA)) as described in ref. [208].

Collection of trypanosome infected mouse blood: All experiments involving mice were carried out in accordance with the guidelines and regulations of the UCLA Institutional Animal Care and Use Committee (IACUC), NIH Public Health Service Policy on Humane Care and Use of Animals, USDA Animal Welfare regulations, and AAALAC International accreditation standards under IACUC-approved protocol ARC# 2001-065. Mouse infections were performed as described in ref. [209] with the following modifications: Female BALB/cJ mice (product no. 000651, Jackson Laboratory, age 11-24 weeks) were injected intraperitoneally with 5×10^5-1×10^6 parasites in 0.1-0.2 mL ice-cold phosphate buffered saline with 1% glucose (PBS-G). Parasitemia was monitored by counting in a hemacytometer, and infected blood samples were collected when parasitemia reached ~10^7-10^8 parasites/mL. Infected blood was collected from either the saphenous vein or by cardiac puncture after euthanasia into heparinized capillary tubes (product no. 22-260950, Fisher

Scientific) or heparinized collection tubes (product no. 8881320256, Covidien (Dublin Republic of Ireland)).

Separation of WBCs from human blood: We used Ficoll-Paque PREMIUM (product no. 45-001-751, Fisher Scientific) for in vitro isolation of mononuclear cells from blood using density gradient separation according to manufacturer's instructions. Human blood samples were acquired from UCLA Blood and Platelet Center after de-identification of patients and related information and were used in the separation of WBCs from blood. We mixed 2 mL ethylenediaminetetraacetic acid (EDTA)-treated blood with 2 mL sterile PBS (product no. 10-010-049, Fisher Scientific) in a 5 mL centrifuge tube (product no. 14-282-300, Fisher Scientific) by drawing the mixture in and out of a pipette. We put 3 mL of Ficoll-Paque PREMIUM in a 15 mL conical centrifuge tube (product no. 14-959-53A, Fisher Scientific) and carefully layered the diluted blood sample on the Ficoll-Paque PREMIUM. The suspension was centrifuged at 400×g for 40 min at 19 ºC using a centrifuge with swing-out rotors (Allegra X-22R, Beckman-Coulter (California, USA)). After centrifugation, the upper layer containing plasma and platelets was removed and mononuclear cells were transferred to a sterile centrifuge tube. To wash the cell isolate, it was mixed in 6 mL PBS and centrifuged at 400×g at 19 ºC for 13 min. The washing step was repeated twice, and the pellet was suspended in 1 mL PBS. The concentration of WBC was determined by counting in a hemacytometer and diluted accordingly to a stock solution of 8×10^5 WBC/mL in PBS.

Protocol for calibration curve analysis for blood samples: Freshly collected trypanosome-infected mouse blood was diluted in uninfected mouse blood (Balb/C, female, pooled, sodium heparin, Charles River Inc. (Massachusetts, USA)) to a concentration of approximately 10^6 parasites/mL. A sample of this trypanosome-infected blood was lysed with 3 volumes of lysis buffer and the trypanosome concentration was determined by counting in a hemacytometer. The

trypanosome-infected blood was then diluted accordingly with uninfected blood to achieve the desired concentrations for calibration curve analysis.

Protocol for calibration curve analysis for CSF samples: Cultured trypanosomes were freshly harvested for each measurement to ensure consistent parasite motility. Trypanosomes were grown to a concentration of ~1×10^6-1.5×10^6 cells/mL and harvested by centrifugation at 1200×g for 5 min. The cell pellet was resuspended in 1 mL of PBS-G and diluted approximately 10-fold to 10^5 cells/mL in PBS-G. The trypanosome concentration was determined by counting in a hemacytometer and the sample was then diluted accordingly into 1X artificial CSF to achieve the desired concentrations for calibration curve analysis.

Sample preparation for imaging: We did experiments using blood and artificial CSF samples (Fig. 7.2). Borosilicate capillary tubes (inner dimensions: 1 mm height × 10 mm width × ~30 cm length; product no. LRT-1-10-67, Friedrich & Dimmock, Inc. (New Jersey, USA)) were prepared by dipping one end of the capillary tube into Vaseline jelly to plug the end. Plastic capillaries, e.g., those made of acrylic, can also be used instead of glass. Excess jelly was removed using a Kimwipe (product no. 06-666, Fisher Scientific) and the tube end was sealed with parafilm (product no. 13-374-12, Fisher Scientific). For each tube, we prepared 4 mL of sample. For blood samples, 3 mL of lysis buffer was mixed with 1 mL of uninfected or infected whole blood in a centrifuge tube. For CSF samples, we put 100 μL WBC stock solution into trypanosome-infected artificial CSF to have 2×10^4 WBCs/mL (i.e., 20 WBCs/μL) in the final mixture. Each sample was mixed well by drawing the mixture in and out of a pipette before loading into the capillary tube. The open end of the capillary tube was then sealed using the jelly and parafilm. The glass capillary was then cleaned using a Kimwipe moistened with methanol (product no. A452SK-4, Fisher Scientific) and put on the device.

Culturing T. vaginalis: *T. vaginalis* strain G3 (Beckenham, UK 1973, ATCC-PRA-98) was cultured in modified TYM media supplemented with 10% horse serum (Sigma), 10U/ml penicillin-10 μg/ml streptomycin (Invitrogen (California, USA)), 180 μM ferrous ammonium sulfate, and 28 μM sulfosalicylic acid at 37 °C [210]. Culture was passaged daily and maintained at an approximate concentration of 1×10^6 cells/mL.

Design of the high-throughput lensless time-resolved speckle imaging platform

As shown in Fig. 7.1(a), the device is made up of five main modules: (1) a "scanning head" consisting of three lensless holographic speckle imagers, (2) linear translation stage, (3) housing, (4) circuit, and (5) control program, each of which is detailed below.

(1) Scanning head: Three identical lensless imagers are built next to each other, housed by 3D-printed plastic using a 3D printer (Objet30 Pro, Stratasys (Minnesota, USA)). As shown in Fig. 7.1(a) inset, each lensless imager uses a 650-nm laser diode (product no. AML-N056-650001-01, Arima Lasers Corp. (Taoyuan, Taiwan)) as the illumination source, which has an output power of ~1 mW. The emitted light is passed through a 3D-printed aperture to limit its emission angle and avoid light leakage into the adjacent imagers. The sample, a glass capillary tube filled with the bodily fluid to be screened, is placed ~7 cm (z_1 distance) below the laser diode. The sample's diffraction pattern is imaged by a 10-megapixel CMOS image sensor (product no. acA3800-14um, Basler (Ahrensburg, Germany)) with a 1.67 μm pixel size and an active area of 6.4 mm × 4.6 mm (29.4 mm^2), placed below the capillary tube. The air gap between the image sensor and the bottom surface of the glass capillary tube is ~1-1.5 mm to reduce the heat transfer from the image sensor to the sample. Because each image sensor has multiple circuit boards that generate heat, custom-made aluminum heat sinks are inserted between the circuit boards and arranged on the sides of the scanning head to dissipate heat and prevent image sensor malfunction.

(2) Linear translation stage: A linear translation stage is built from two linear motion shafts (product no. 85421, Makeblock Co., Ltd. (Shenzhen, China)), two linear motion sliders (product no. 86050, Makeblock Co., Ltd. (Shenzhen, China)), a timing belt (product no. B375-210XL, ServoCity (Kansas, USA)), two timing pulleys (product no. 615418, ServoCity (Kansas, USA)) and a stepper motor (product no. 324, Adafruit Industries LLC. (New York, USA)). The scanning head is mounted onto the sliders using screws.

(3) Housing: The housing of the scanning head is made from 3D-printed plastic. The outer shell of the device is made from laser-cut ¼-inch acrylic sheets.

(4) Circuit: A printed circuit board (PCB) is custom-built to automate the device, which contains a microcontroller (Teensy LC, PJRC (Oregon, USA)) connected to the laptop computer via USB 2.0, laser diode driver circuits built from constant current circuits (product no. LM317DCYR, Texas Instruments (Texas, USA)), and a stepper motor driver circuit (product no. TB6612, Adafruit). The laser diodes and the stepper motor are powered using a 12 V power adapter. Various digital switches built from metal-oxide-semiconductor field-effect transistors (MOSFETs) are controlled by the digital outputs from the microcontroller to cut the power to the laser diodes and the image sensors when they are unused. Specifically, to cut the power to the image sensor, the power wire of the USB 3.0 cable of the image sensor is cut and a MOSFET-based digital switch is inserted into the power line.

(5) Control program: A Windows application written in C# with a graphical user interface (GUI) enables the user to initiate the screening of the current sample in addition to various other functionalities, such as customizing image acquisition parameters, performing a live view of the diffraction patterns, taking a snapshot, and stopping the acquisition.

Image acquisition

After the sample is loaded onto the device and has settled for a 3-4 min waiting time (4 min for lysed whole blood and 3 min for artificial CSF, see Fig. 7.2 for details), the user presses the "record" button on the GUI to start acquisition. During screening, our device is programmed to scan the capillary tubes at 36 discrete positions, with a distance of ~4.7 mm between spatially adjacent ones. This results in a total screening volume of 36 (discrete scanning positions) × 29.4 mm^2 (FOV of the image sensor) × 1 mm (channel height of the capillary tube) ≈ 1.06 mL per lensless speckle imager, and ~3.18 mL for the three parallel imagers combined. At each of the 36 positions, to achieve a high frame rate (~26.6 fps), the image sensor's FOV is split into two halves (i.e., the upper 1374 rows and the lower 1374 rows of the pixels), with each half capturing 61 frames (for lysed blood) or 41 frames (for CSF) sequentially (see the following subsections for optimization of frame numbers).

The image sensor's temperature rises when it is powered, leading to temperature gradient-induced convection flow of the liquid sample. To mitigate these problems, two measures are taken. First, instead of scanning the 36 positions unidirectionally, the device scans in *a back-and-forth fashion*. Let the 36 positions be represented by positions #1, #2, …, #36, which are spatially ordered. Instead of scanning in the order of #1, #2, …, #36, we programmed the device to scan with a larger step size of 9 positions, and whenever the scanning head cannot move forward with this step size, it comes back to the unscanned position with the smallest position number. That is, the device first scans positions #1, #10, #19, and #28. Then, the scanning head comes back to position #2, followed by #11, #20, and #29, and so on. This scanning pattern largely prevents heat accumulation at a given section of the capillary tube, which has sufficient time to cool down before the scanning head comes back to its vicinity. As a second measure, a 6 s "downtime" is added

between scanning positions to allow the image sensor to cool down. After completing the acquisition at a given position, the power to the image sensor is cut by a MOSFET-based digital switch added into the USB 3.0 cable. After a 6 s wait time, the stepper moves the scanning head to the next position, where the power to the image sensor is restored to capture the next set of images.

Table 7. 1. Image processing time.

Processing step	Single GPU		Dual GPUs	
	Time per image sequence (ms) Blood / CSF	Total time per test (min) Blood / CSF	Time per image sequence (ms) Blood / CSF	Total time per test (min) Blood / CSF
Copy data from CPU memory to GPU memory	316.7 / 212.7	1.14 / 0.77	346.2 / 231.7	0.62 / 0.42
Image normalization	44.3 / 30.0	0.16 / 0.11	49.0 / 32.5	0.09 / 0.06
Autofocusing	523.0 / NA	1.88 / NA	680.8 / NA	1.23 / NA
Computational motion analysis	6205.0 / 5515.7	22.34 / 19.86	6137.8 / 5561.5	11.05 / 10.01
Post image filtering	106.7 / 136.0	0.38 / 0.49	108.2 / 138.3	0.19 / 0.25
Segmentation	10.1 / 10.1	0.04 / 0.04	10.1 / 10.1	0.02 / 0.02
Deep learning-based classification	9.8 / 10.3	0.04 / 0.04	9.8 / 10.3	0.02 / 0.02
Total	7215.6 / 5914.8	25.98 / 21.29	7341.9 / 5984.4	13.22 / 10.77

During our testing, we save the acquired images to a hard drive for processing. All three image sensors, capturing uncompressed 8-bit images, generate a total data rate of ~421 MB/s, which slightly exceeds the average write-speed of our solid-state drive (SSD). Therefore, a queue is created in the random-access memory (RAM) for each image sensor to temporarily buffer the incoming image data, and another thread is created to constantly move the image data from the buffer into the SSD. However, because all the remaining image data can be fully saved to the SSD

during the aforementioned downtime between positions, the total image acquisition time per test is not increased due to the limited write-speed. As a more time-efficient alternative, the acquired images can be temporarily stored in the RAM, while they are constantly moved to the GPUs for processing in batches corresponding to each image sequence. In this way, the image processing can be performed concurrently with the image acquisition, reducing the total time per test (see the Results and discussion section, Fig. 7.2, and Table 7.1).

Image processing using CMA and deep learning-based identification

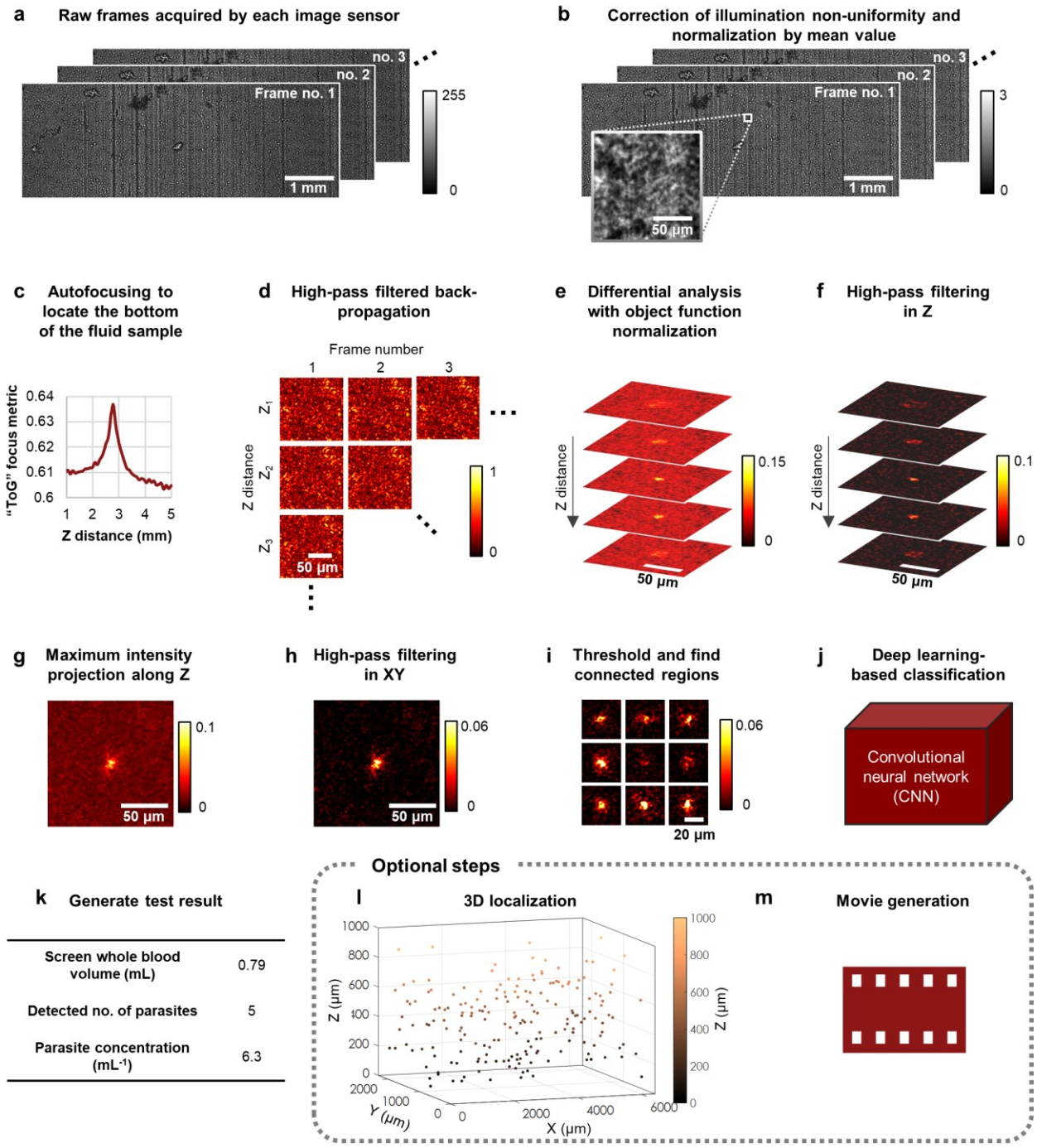

Figure 7. 3. CMA algorithm with OFN, combined with deep learning-based identification, for sensitive and label-free detection of trypanosomes in lysed blood. The steps are performed in the same order as listed here.

We developed CMA to generate 3D contrast from particle locomotion in noisy holograms and speckled interference patterns, and applied deep learning-based classification to identify the signals corresponding to the parasite of interest. As an example, Fig. 7.3 depicts the procedure we used to detect trypanosomes from lysed whole blood, whereas in other application settings (e.g., trypanosome detection in CSF), we applied minor changes to the procedure, detailed below. The algorithm takes the raw holographic diffraction patterns acquired by each image sensor at each scanning position as input. We denote $\mathbf{A}_i$ (i = 1, …, N_F) as the raw frames, where N_F is the total number of recorded frames in each sequence. The algorithm consists of the following steps:

1. ***Hologram preprocessing to mitigate the variations and non-uniformity of the illumination***

For every 8-bit raw image acquired by each image sensor (Fig. 7.3(a)), it is divided by a "background" intensity pattern representing the non-uniformity of the laser diode illumination source, which was previously computed from Gaussian-smoothed and averaged raw images in a negative control experiment and stored to be used by other experiments. After this, the hologram is further normalized (divided) by its own mean value, yielding the illumination-corrected holograms $\tilde{\mathbf{A}}_i$ (i = 1, …, N_F) (Fig. 7.3(b)).

2. ***Determining the range of axial-distances of the fluid sample under test***

In the case of lysed blood, because most of the cell debris tend to fully sediment within the 4 min wait time (Fig. 7.2), we applied "Tamura coefficient of the gradient" (ToG) autofocusing criterion [97,98] to automatically determine the z-distance of the bottom of the fluid sample (Fig. 7.3(c)), denoted as z_b. Then, we defined our range of digital z-scanning as [z_b – 200 μm, z_b + 1200 μm] with a 50 μm step size. Note that in addition to the 1 mm expected channel height, we gave an extra scanning range of ±200 μm to allow for possible errors in the channel height, tilting of the

channel, errors in autofocusing, etc. This makes our hardware much less complicated and inexpensive as we do not need tight tolerances in our scanner design and sample holder placement.

In the case of clear media such as CSF where objects/particles are sparse, autofocusing to the bottom of the channel can be challenging. Therefore, we pre-calibrated the z_b distance of each capillary tube (see Appendix) and used it throughout our experiments. Because z_b is pre-calibrated, i.e., not adaptively calculated for each sample, we specify a larger range of digital z-scanning, [z_b – 500 μm, z_b + 1500 μm], also with a 50 μm step size. Note that z_b is slightly different for each of the three channels of the device and is calibrated respectively.

3. *CMA algorithm to generate contrast from locomotion*

We denote the z-distances to be scanned as z_j ($j = 1, \ldots, N_z$) as determined by the previous step. We digitally propagate each element of $\tilde{\ }$ to each of z_j with a high-pass filtered coherent transfer function (Fig. 7.3(d)); see Appendix for details) to obtain

$$\mathbf{B}_{i,j} = \mathrm{HP}\left[\mathcal{P}\left(\tilde{\ }\right.\right. \quad \left.\left._{,\,\lrcorner}\right. \tag{7.1}$$

where P represents the angular spectrum-based back-propagation [52], HP represents high-pass filtering, and $i = 1, \ldots, N_F$, $j = 1, \ldots, N_z$.

Next, time-averaged differential analysis with OFN is applied (Fig. 7.3(e)), which yields:

$$\mathbf{C}_j = \frac{1}{N_F - \delta_F} \sum_{i=1}^{N_F - \delta_F} \frac{\left|\mathbf{B}_{i+\delta_F,j} - \mathbf{B}_{i,j}\right|}{\exp\left[\gamma \cdot \frac{1}{2}\left|\mathbf{B}_{i+\delta_F,j} + \mathbf{B}_{i,j}\right|\right]} \tag{7.2}$$

where δ_F is the subtraction frame interval, $\exp\left[\gamma \cdot \frac{1}{2}\left|\mathbf{B}_{i+\delta_F,j} + \mathbf{B}_{i,j}\right|\right]$ is the OFN factor, γ is a parameter related to OFN that is respectively tuned for lysed blood ($\gamma = 2$) and CSF experiments ($\gamma = 3$). Time-averaging significantly improves the SNR by smoothing out random image noise as well as random motion of unwanted particles/objects while preserving the true signals of motile

microorganisms. OFN further suppresses potential false positive signals resulting from e.g., strongly scattering, unwanted particles/objects such as cell debris (see Appendix and Figs. 7.9 and 7.10). The result of this step, $\mathbf{C}_j$, is a three-dimensional image stack.

4. ***Post-image processing and segmentation***

The z-stack $\mathbf{C}_j$ (j = 1, …, N_z) suffers from a low-spatial-frequency background that mainly results from high-frequency noise in the raw images, which remains when performing high-pass filtered back-propagation and frame subtraction. Therefore, as shown in Fig. 7.3(f-h), the 3D z-stack $\mathbf{C}_j$ is first high-pass filtered in the z-direction by a mean-subtracted Gaussian kernel (σ_z = 250 μm) and the negative pixels are clipped to zero, yielding $\mathbf{D}_j$ (j = 1, …, N_z). It is then projected into a 2D image, **E**, using maximum intensity projection (MIP). High-pass filtering is applied again in 2D (mean-subtracted Gaussian kernel, $\sigma_x = \sigma_y$ = 25 μm) to remove the residual background, and the negative pixels are again clipped to zero, yielding **F**.

Segmentation of candidate signal points within **F** is performed by 2D median filtering (3×3 pixel window, pixel size = 1.67 μm), thresholding (threshold = 0.01 for detecting trypanosomes in lysed blood and 0.02 for detecting trypanosomes in CSF) followed by dilation (disk-shape structuring element, radius = 2 pixels, pixel size = 1.67 μm) and searching for connected pixel regions. Connected regions that are smaller than 5 pixels are discarded. 64-by-64 pixel image patches centered around the pixel-value-weighted centroids of these connected regions are cropped from **F** (without 2D median filtering), and are used for the downstream identification by a deep learning-based classifier.

5. ***Deep learning-based classifier for detection of motile trypanosomes***

A CNN that consists of three convolution blocks followed by two fully-connected layers is built and trained to identify true signal spots created by motile trypanosomes. The detailed network

structure is shown in Fig. 7.12, which is separately trained for trypanosome detection from lysed blood and CSF samples (see the Appendix for details).

6. *Generation of test results*

The image processing steps (Fig. 7.3(a-j)) are repeated for each captured image sequence and each image sensor. The total detected number of trypanosomes from all the positions are summed up and divided by the total screened volume (~3.18 mL) to calculate the detected parasitemia. For lysed blood, it is further multiplied by a factor of 4, i.e., the dilution factor introduced by lysis, to calculate the parasitemia in the original whole blood sample.

7. *3D localization of motile microorganisms and movie generation*

Our technique also offers the capability to locate the motile microorganisms in 3D and generate in-focus amplitude and phase movies of them for a close-up observation, using the following steps. For each signal spot that is classified as positive by the CNN classifier, we go back to the corresponding z-stack $\mathbf{D}_j$ ($j = 1, \ldots, N_z$) and only crop out a "column" that is 30 × 30 pixels in x-y, centered around this spot, while spanning the entire z-range (N_z layers). Then, an autofocusing metric is used to evaluate each of the N_z layers, and the layer that corresponds to the maximum value of the autofocusing metric corresponds to its in-focus position. We tried ToG and Tamura coefficient-based criteria [97,98,110], and both work very well for this purpose. While the current z-localization accuracy is limited by the z-step size we chose (Δz = 50 μm), it can be further improved through finer z-sectioning. Using the currently found z-localization distance as an initial guess, we perform high-pass filtered back-propagation and differential analysis (detailed in Step 3) over a z-range of ±100 μm around the initial guess with a finer z-step size of 5 μm. However, OFN is disabled this time; in other words, the exponential normalization factor in Eq. (7.2) is removed, owing to OFN's side effect of slightly weakening the signal at the optimal focus distance,

where the object function of the microorganism is the strongest. Autofocusing is performed again over the same 30 × 30-pixel region over different z-layers similarly as before. The previously determined x-y centroid, in addition to the newly found z-distance, is used as the 3D location of this motile microorganism. Because the additional high-pass filtered back-propagation and differential analysis may be only performed on a smaller region-of-interest (ROI) around each given spot (e.g., in our case, an ROI of 512×512 pixels is used), the 3D localization is computationally efficient. The 3D localization capability can be used to generate movies (detailed below), or to study microorganism behavior in biological or biomedical research settings.

Using the obtained 3D position of each motile microorganism, the movie of each detected microorganism can be generated by digitally back-propagating (without high-pass filtering) each frame of the recorded raw image sequence $\mathbf{A}_i$ ($i = 1, \ldots, N_F$) or the illumination-corrected version $\tilde{\ }$ to the corresponding z-coordinate. The amplitude and phase channels of the back-propagated images are displayed side by side. The generated movies can potentially be used as an additional way to confirm the detection result of this platform when trained medical personnel are available.

Timing of image processing algorithm

In this work, we used a laptop equipped with an Intel Core i7-6700K central processing unit (CPU) @ 4.00 GHz, 64 GB of RAM, and two Nvidia GTX 1080 GPUs for image processing. Table 7.1 summarizes the time required for our image processing workflow, using a single GPU or using two GPUs simultaneously. Here, we assume that during image acquisition, the images captured by the imaging device are temporarily stored in the CPU RAM and are constantly moved to the GPU memory in batches corresponding to the scanning positions, where it is processed by the GPU (or GPUs). In this way, image processing can be performed concurrently during image acquisition, shortening the time requirement per test. We mimic this situation by pre-loading

existing data from the hard drive into the RAM of the computer before starting the timer, which provides a reasonable estimation of the time cost of our processing. Because the number of acquired images and the image processing workflow for lysed blood and CSF are different (see previous subsections and Appendix), their timing results are calculated individually. In Table 7.1, timing results for lysed blood and CSF are separately by "/".

7.3 Results and discussion

Detection of parasite locomotion in 3D using holographic speckle analysis

To sustain a high frame rate (~26.6 fps) which is essential to our parasite detection technique, we chose to split the full field of view (FOV) of the image sensor in two halves, each ~14.7 mm^2. Fig. 7.4(a-c) shows the raw speckle patterns of a lysed, trypanosome-spiked whole blood sample captured by our image sensor. Even though this simple lysis process has significantly reduced the density of the blood sample, the interference patterns (e.g., Fig. 7.4(b-c)) are still highly dense due to the random light scattering resulting from the cell debris in the lysed blood. As a result, the diffraction patterns of the optically transparent and weakly scattering trypanosomes (Fig. 7.4(c), yellow arrows) are buried under the speckle patterns, making their direct detection extremely challenging.

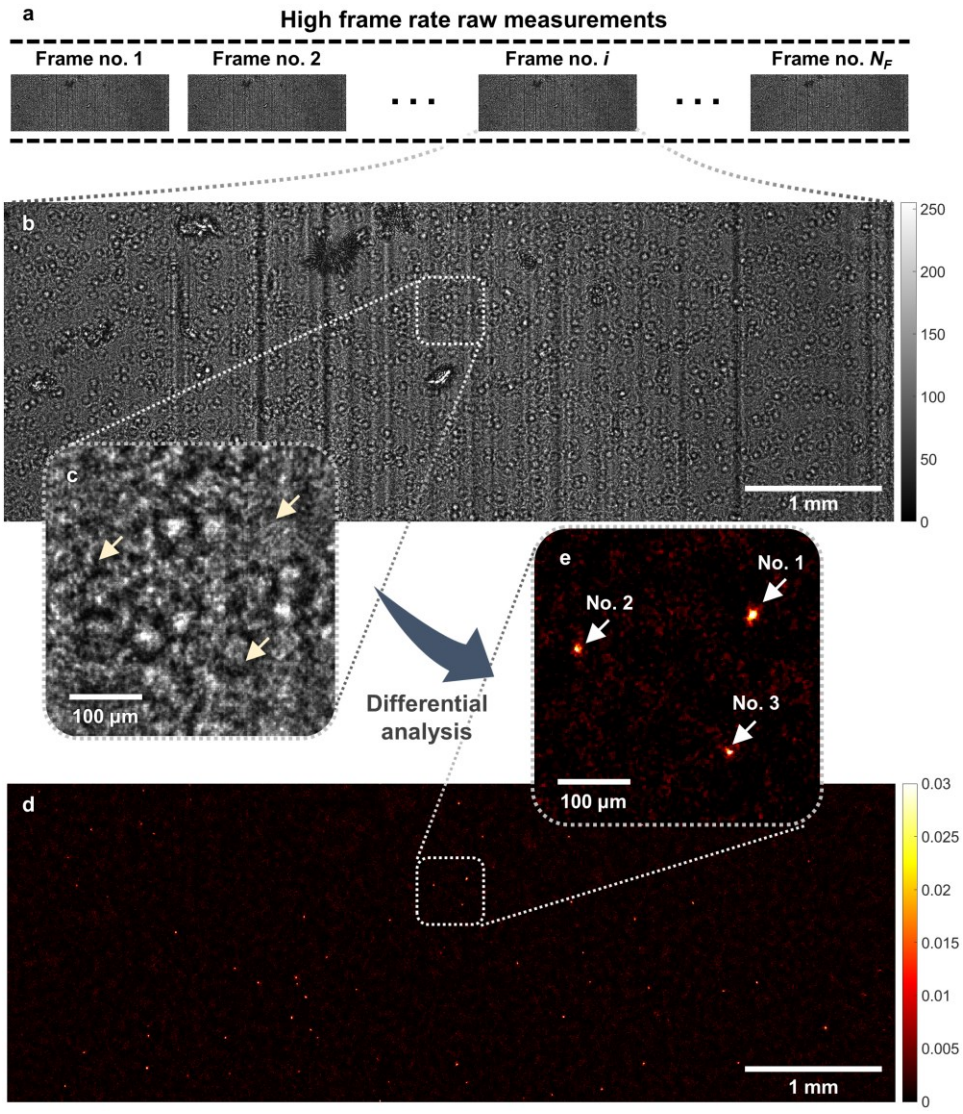

Figure 7. 4. Experimental demonstration of applying the CMA algorithm and OFN to a lysed blood sample spiked with motile trypanosome parasites, over an FOV of ~14.7 mm^2. (a) A time-sequence of the diffraction patterns of the sample is captured. **(b, c)** One of the frames in the raw image sequence is shown. The diffraction pattern is severely speckled due to the light scattering by the cell debris, making the parasites invisible (yellow arrows in **(c)**). **(d, e)** After being processed by the CMA algorithm, motile parasites can be detected.

To address this challenge, the spatial-temporal variations in the detected speckle patterns due to the rapid locomotion of motile trypanosomes within blood can be utilized. We took advantage of this and developed a CMA algorithm, which involves holographic back-propagation,

differential imaging (with an optimally-adjusted frame interval for trypanosome locomotion), and temporal averaging, conducted at each horizontal cross section within the sample volume. Object function normalization (OFN) was introduced into each differential imaging step to suppress potential false positives due to unwanted, strongly scattering objects within the sample. The algorithm was then followed by post-image processing and deep learning-based classification to identify the signals caused by trypanosomes (see the Methods section for details). Fig. 7.4(d-e) exemplify the result of this computational process, where the "hotspots" in the processed images correspond to motile trypanosomes. To better illustrate this, based on the calculated 3D locations of the three hotspots in Fig. 7.4(e) (indicated by white arrows), we created in-focus movies of the amplitude and phase channels of the back-propagated diffraction patterns. Rapid locomotion of these trypanosomes can be observed in this video, although partially obscured by the interference patterns created by the other non-motile objects (e.g., cell debris) in the sample.

Similarly, the results of imaging trypanosomes within WBC-spiked artificial CSF samples are shown in Fig. 7.5. Because CSF is mostly a clear medium, the background noise level caused by quasi-static scatterers in the medium is significantly lower compared to the motile trypanosome signal level (i.e., the hotspots in Fig. 7.5(b)).

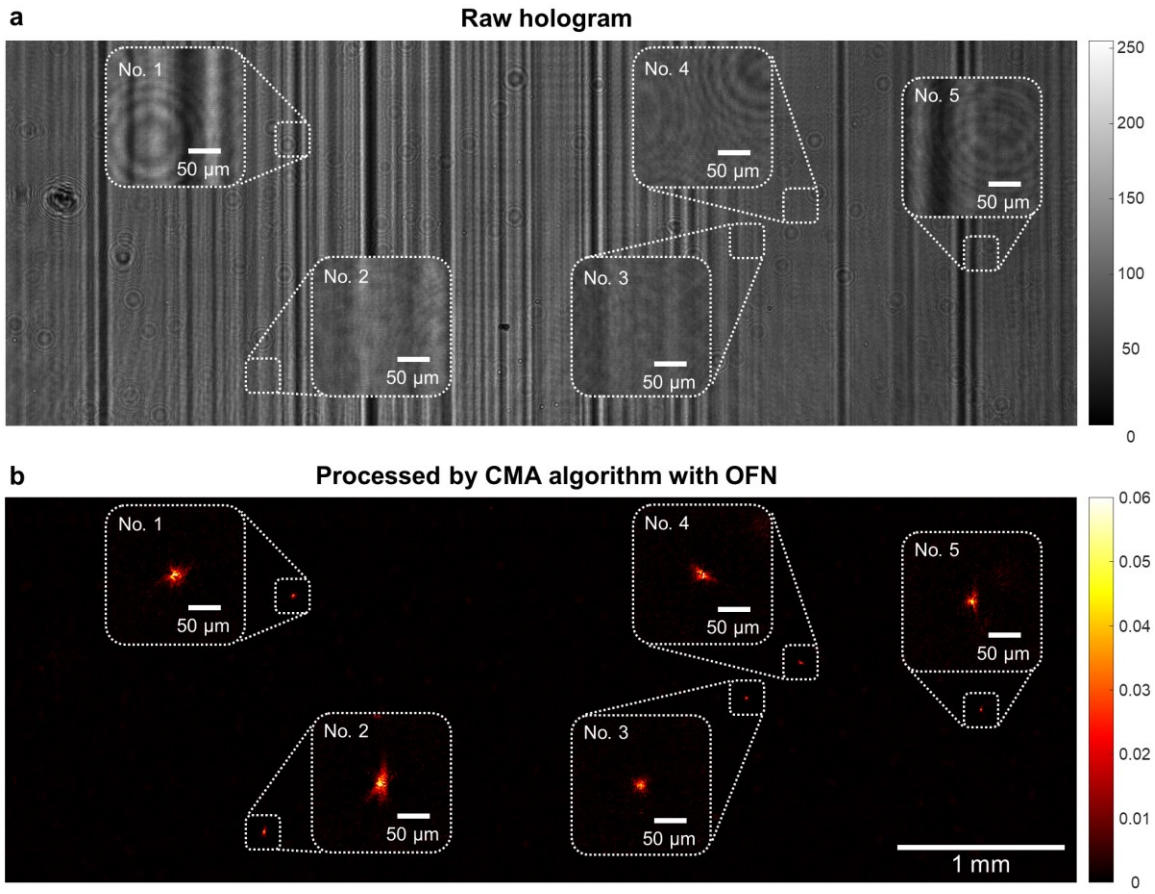

Figure 7. 5. Imaging result of trypanosomes within artificial CSF spiked with WBCs. (a) One of the raw holograms in the image sequence. **(b)** Image that is processed by the CMA algorithm with OFN.

As detailed in Table 7.1, >80% of the total image processing time to image and detect these trypanosomes is spent on the CMA algorithm, which involves thousands of fast Fourier transforms of ~6-megapixel images for each recorded image sequence (see the Materials and methods section for details). Therefore, graphics processing unit (GPU) based parallel computing is essential for the speed-up of the CMA algorithm. Using a single GPU, the entire image processing task for one experiment (216 image sequences in total for the three parallel image sensors) takes ~26 min and ~21 min for blood and CSF samples, respectively. When using two GPUs, because each GPU is given a separate image sequence to process at a given time, there is minimal interference between the GPUs and maximal parallelism can be achieved. Therefore, ~2-fold speed-up is observed when

using two GPUs, resulting in a total image processing time of ~13 min and ~11 min for blood and CSF experiments, respectively. Combined with all the other sample preparation steps, the total detection time per test amounts to ~20 min and ~17 min for blood and CSF samples, respectively (see Fig. 7.2 for details).

Quantification of the LoD for trypanosomes

We determined the LoD of our platform for detecting trypanosomes in lysed whole blood by performing serial dilution experiments, and the results are shown in Fig. 7.6(a-b). We spiked trypanosome-infected mouse blood into uninfected blood to generate a series of parasite concentrations, including 0 mL^{-1} (negative control), 10 mL^{-1}, 100 mL^{-1}, 1000 mL^{-1}, 10,000 mL^{-1} and 100,000 mL^{-1}, where $N = 3$ replicate experiments were performed at each concentration. As shown in Fig. 7.6(a), no false positives were found in the three negative control samples, while for the three 10 mL^{-1} experiments, our detected concentration was 7.55 ± 3.70 mL^{-1}. Therefore, we conclude that our LoD is ~10 trypanosomes per mL of whole blood, which is 5× better than the best parasitological detection method currently available (i.e., the mini anion exchange centrifugation technique, mAECT [202]). Fig. 7.6 also reveals that the recovery rate (detected trypanosome concentration divided by the spiked concentration) of our technique ranges from ~68%-76% (at the lower end of our tested concentrations) to ~38%-39% (at the higher end). This concentration-dependent recovery rate is possibly related to the proximity of trypanosomes to each other at higher concentrations, which results in more than one trypanosome in a 64×64-pixel cropped image that might be misclassified as negative by the deep learning-based classifier (see the Materials and methods section for details), leading to underestimation of the true number of trypanosomes in the sample. This drop in the recovery rate observed at high concentrations can be potentially compensated through calibration.

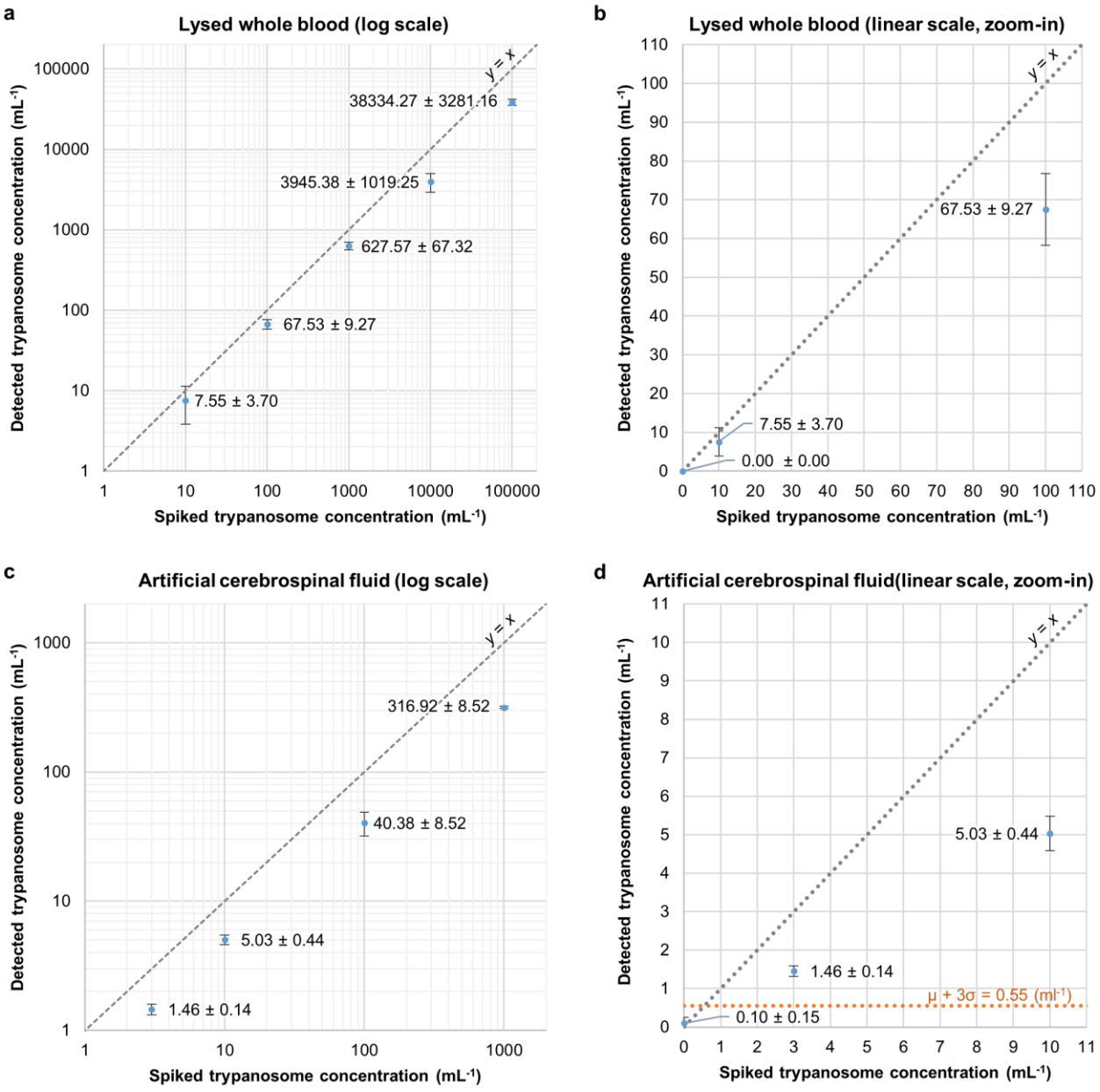

Figure 7. 6. Quantification of the LoD of our platform for detecting trypanosomes in lysed whole blood and artificial CSF samples. (a) Calibration curve for trypanosome detection in lysed whole blood (logarithmic scale). Dashed line indicates expected values ($y = x$). Measured values are indicated by blue data points. Error bars show the standard deviation of 3 independent measurements. **(b)** Zoom-in of **(a)** showing the low concentration measurements (linear scale), including the negative control (no trypanosomes). No false positives were found in the three negative control samples. **(c, d)** Calibration curves for trypanosome detection in artificial CSF, similar to **(a, b)**. Orange dashed line in **(d)** corresponds to the mean + 3×standard deviation of the negative control result.

For *T. brucei*, stage determination is critical for determining the most appropriate treatment regimen. This is currently done by collecting CSF via a lumbar puncture and examining the CSF under a microscope. Patients with ≤5 μL^{-1} WBCs and no trypanosomes in the CSF are classified as stage I; otherwise, if there are >5 μL^{-1} WBCs or if trypanosomes are found in the CSF, they are classified as stage II (ref. [181]). To address this need for high-throughput CSF screening, we also quantified the LoD of our platform to detect trypanosomes in CSF. For this purpose, we used an artificial CSF [207] sample that is spiked with human WBCs, where cultured trypanosomes were spiked into the artificial CSF solution at concentrations of 3 mL^{-1}, 10 mL^{-1}, 100 mL^{-1}, and 1000 mL^{-1}, in addition to a negative control ($N = 3$ for each concentration). The concentration of spiked human WBCs was selected as 20 WBCs/μL to evaluate the performance of the device to detect trypanosomes in a scenario where the WBC concentration was four times higher than the 5 μL^{-1} threshold used in stage determination. Unlike the blood sample, the CSF solution is optically clear and lysis was not needed, which helped us further improve our LoD: as shown in Fig. 7.6(c-d), our platform was able to detect trypanosomes spiked in CSF with a very low LoD of 3 trypanosomes per mL.

Detection of T. vaginalis parasites

Although we chose to validate our motility-based detection approach on *T. brucei*, we anticipate this approach to be broadly applicable for the detection of a variety of motile microorganisms. As a preliminary test of the performance of our device on a completely different motile parasite, we chose *T. vaginalis*, the protozoan parasite responsible for trichomoniasis, which is the most common non-viral sexually transmitted disease in the United States and worldwide [205,211–213]. *T vaginalis* infects the urogenital tract of both women and men. Although often asymptomatic, *T. vaginalis* infection has been associated with increased risk

related to other health conditions including human immunodeficiency virus infection, pre-term labor, pelvic inflammatory disease and prostate cancer [179,212]. For the diagnosis of trichomoniasis, cell culture followed by microscopy remains the gold standard, which is highly sensitive and can detect *T. vaginalis* from an inoculum containing as few as three parasites per mL [211]. However, it is limited by the high cost, inconvenience, a long examination time, as well as susceptibility to sample contamination. The most common diagnostic method, wet-mount microscopy, suffers from poor sensitivity (51%-65%) [213,214]. Thus, our highly sensitive lensless time-resolved holographic speckle imaging method could be of substantial benefit.

With only minor adjustments to our algorithm (see the Materials and methods section), we demonstrated that our platform can detect *T. vaginalis* in phosphate-buffered saline (PBS) solution and culture medium (see Figs. 7.6 and 7.7). Based on these experiments, we observe that *T. vaginalis* creates significantly stronger signal intensities compared to trypanosomes in CSF (Fig. 7.5), which is related to the intense locomotion and strong light scattering of *T. vaginalis*. This suggests that our platform can potentially be used to achieve a similar, if not better, sensitivity level for *T. vaginalis*, e.g., reaching ≤ 3 parasites per mL. More testing is needed to establish the LoD of *T. vaginalis* from different environments such as culture medium and urine, corresponding to different clinical needs, such as the detection of *T. vaginalis* from diluted vaginal secretion or directly from urine.

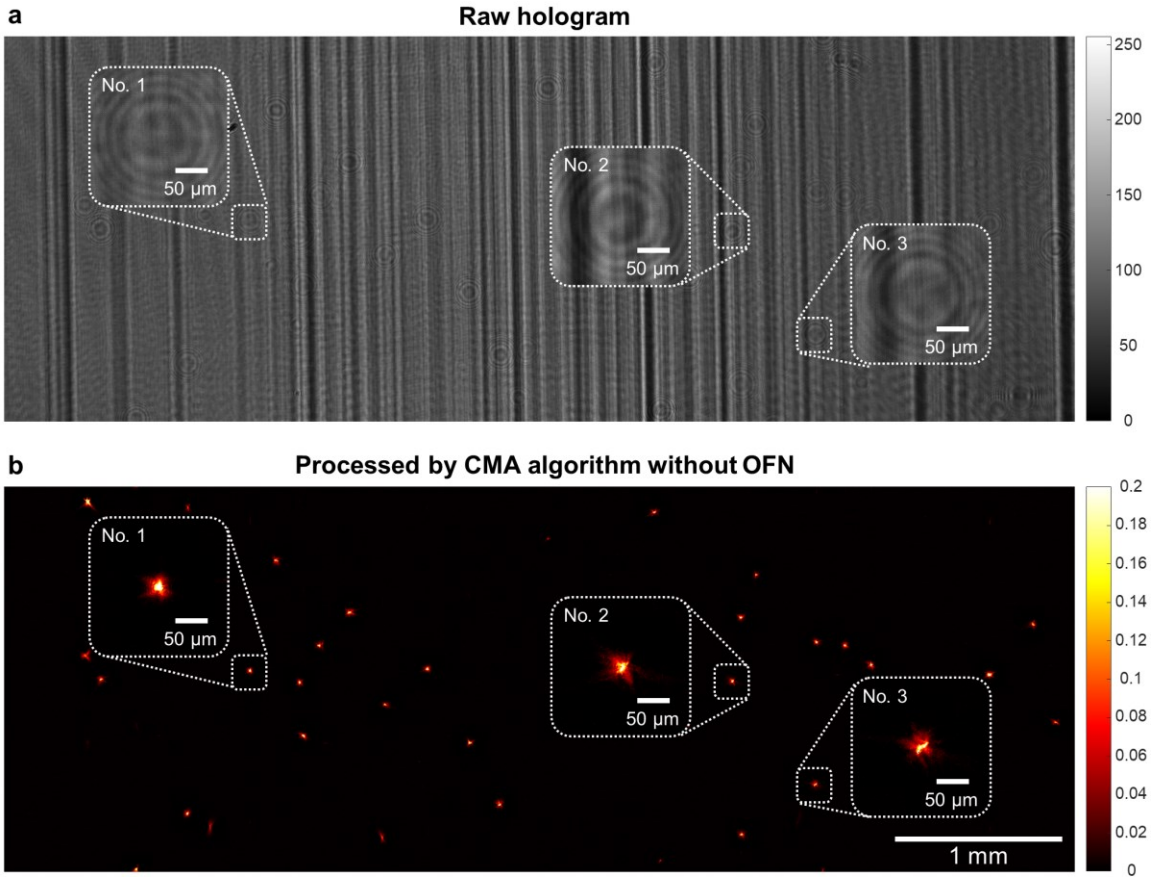

Figure 7. 7. Imaging result of *Trichomonas vaginalis* (*T. vaginalis*) within phosphate buffered saline (PBS). (a) One of the raw holograms in the image sequence. **(b)** Image that is processed by the CMA algorithm. Because trichomonas has a strong optical phase, OFN is not applied here.

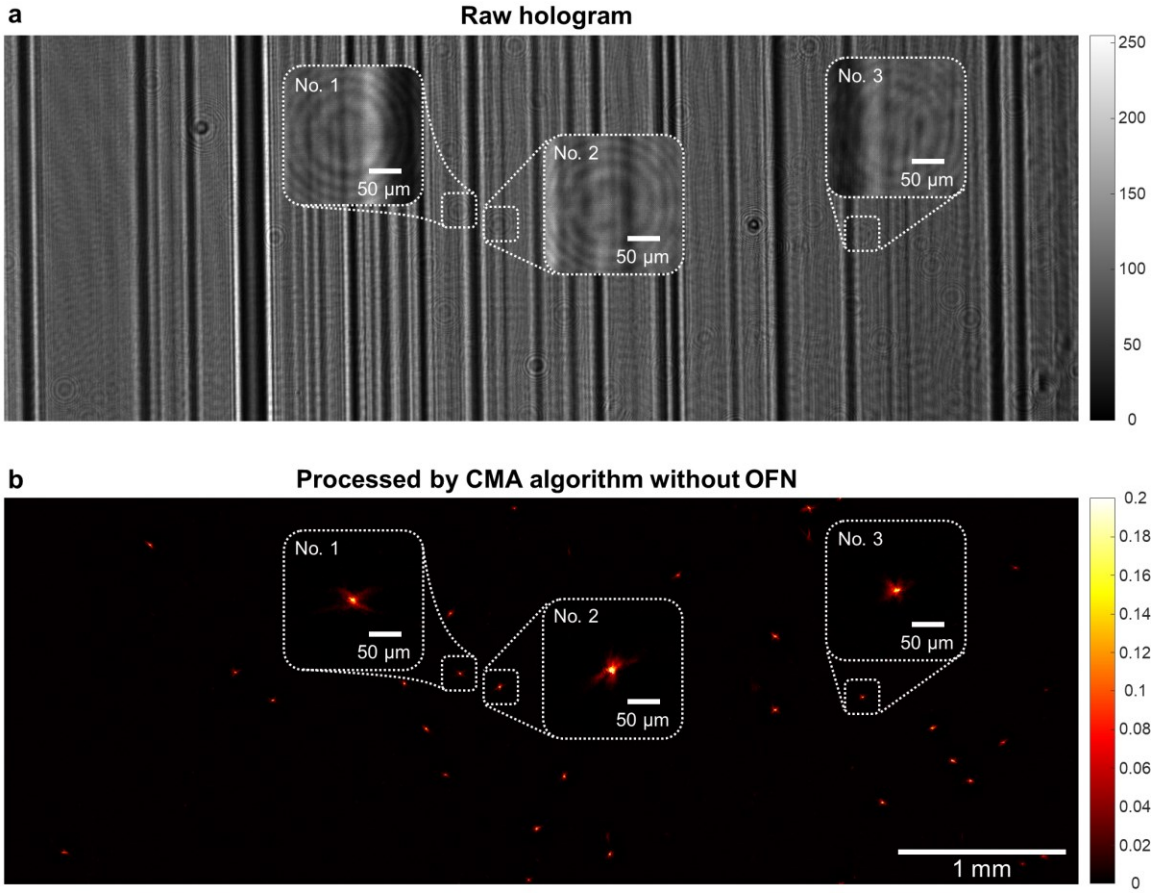

Figure 7. 8. Imaging result of *T. vaginalis* within culture medium. (a) One of the raw holograms in the image sequence. **(b)** Image that is processed by the CMA algorithm without OFN.

Discussion

We presented a new method of motility-based parasite detection, based on lensless time-resolved holographic speckle imaging, and demonstrated that it is effective for rapid detection of trypanosomes within lysed blood and CSF, achieving an LoD that is better than the current parasitological methods [181,195,202,215–224]. This automated technique has the potential to improve parasite screening efficiency, while reducing the need for highly specialized and expensive equipment and expertise that are essential to PCR-based or microscopic detection methods. The total cost for all the parts of our instrument, excluding the laptop, is less than $1850; and this cost can be easily reduced to $500-1000 under large volume manufacturing. Our total

analysis time, including all the sample preparation steps, is only ~20 min, which is comparable to or faster than most existing methods. This motility-based method achieves high sensitivity without requiring specialized detection reagents, refrigeration, centrifugation or purification, making it more versatile for the analysis of different types of samples (e.g., blood, CSF) and less susceptible to differences between parasite sub-species or isolates from different regions of the world. Therefore, the presented prototype could be readily adapted to any established or mobile clinic with access to electricity or battery power, representing an advancement that could be a useful addition to existing diagnostic methods.

This diagnostic method could also be beneficial for improving the diagnosis of bloodstream HAT or Chagas infection, or facilitating earlier identification of stage II HAT cases, when the parasitemia in the CSF is under the LoD of traditional methods and when the WBCs in the CSF are still scarce. Such a platform may also be useful for follow-up after disease treatment in order to screen patients for earlier and more sensitive detection of relapse. These advances could result in improved treatment outcomes for patients and increase the cure rate of disease. In addition to HAT, animal trypanosomiasis severely limits economic development. Therefore, applying motility-based detection to aid screening of infected livestock and development of vector control options could help to raise endemic areas out of poverty [225]. In the case of Chagas disease, this technique could be adapted for screening of blood donors or blood products as well as sugarcane juice and acai juice products to help reduce various routes of transmission. Given the large populations at risk, the ability to rapidly analyze various types of samples/liquids in a simple and automated fashion will be particularly critical for developing a viable strategy to screen samples in regions where disease incidence declines owing to eradication efforts.

Our device and label-free detection method take advantage of the locomotion patterns of parasites to maximize the detection signal-to-noise ratio (SNR). Trypanosomes are known for their incessant motion, and motility is crucial to their survival as well as their virulence in the host [184]. The swimming behavior of trypanosomes is highly complex [196,226]. Because the flagellum is laterally attached to the cell body, parasite translocation is accompanied by cell body rotation, resulting in a "corkscrew" swimming pattern. Moreover, in addition to cell translocation, the flagellum generates rapid, three-dimensional beating patterns. The average beating frequency of *T. brucei* is estimated as 18.3±2.5 Hz in forward moving cells and 13.1±0.8 Hz in backward moving ones, whereas the rotational frequency of forward moving cells is 2.8±0.4 Hz [227]. The frame rate that matches the average beating frequency (forward moving), according to the Nyquist sampling rate, is equal to 36.6 fps. In other words, a frame rate of at least 36.6 fps is able to record the speckle changes corresponding to each flagellar stroke; and even higher frame rates can record the speckle changes with finer time resolution, corresponding to different time points during a flagellar stroke. Assuming optimal subtraction time interval (Δt) and time window (T) are used (see Materials and methods, Appendix and Fig. 7.11), a higher frame rate leads to richer time-resolved information of speckle changes induced by motile parasites as well as more frames that can be used for averaging, thus can improve the SNR overall. However, because our goal is to generate contrast based on locomotion rather than high-fidelity recording of the beating patterns, frame rates that are below 36.6 fps are also acceptable for detection purposes. Considering the scanning time and the amount of acquired data, we chose to use a frame rate of ~26.6 fps for our platform. For future versions of the platform, faster image sensors and data interfaces can be used to achieve higher frame rates, thereby improving the SNR without increasing the data acquisition time.

T.b. brucei is widely used as a model microorganism for the study of trypanosomes because it is non-pathogenic to humans and therefore safe to conduct experiments on. We anticipate that this approach will be readily applicable to *T.b. gambiense*, *T.b.rhodesiense* and *T. cruzi*, since their movements are fundamentally similar, however direct testing will need to be done on human-infectious trypanosomes. Mouse blood and an artificial CSF solution were used throughout our testing due to safety concerns, but our lysis buffer also works with human blood. Future research will focus on testing patient samples from endemic regions to establish the sensitivity and specificity of our presented technique for the diagnosis of various trypanosomiases.

Numerous motile organisms can cause infections in humans [182,183,228]. The current state of our technique does not differentiate different parasites automatically. However, the amplitude and phase movie that is generated for each detected signal (Fig. 7.3(m)) can potentially allow a trained clinician to distinguish different motile parasites based on the morphology, size, and motility pattern, which is analogous to observing each live parasite under a brightfield and phase-contrast microscope. Prevalence of particular pathogens in the region can also aid in this regard. Moreover, a trained video classifier based on, e.g., a convolutional neural network (CNN) or a recursive neural network (RNN) can potentially distinguish and automatically identify various parasites, if sufficient training data are provided.

In this work, we utilized trypanosomes to demonstrate the feasibility of lensless time-resolved holographic speckle imaging to be employed in detection of parasitic infection. While our approach capitalized on the motility of trypanosomes, this platform is broadly applicable to other motile parasites, including other eukaryotic parasites such as *T. vaginalis* (see Figs. 7.7 and 7.8), and other fluid samples beyond those tested here. In principle, this platform can also be used for the detection of *Loa loa* (*L. loa*) microfilariae in blood samples, which are significantly larger

(~0.2-0.3 mm in length) compared to the parasites that we studied here. For such large motile parasites, as an alternative approach, D'Ambrosio *et al.* used a cellphone-based detection method by taking advantage of the displacement of the RBCs caused by the collision with *L. loa* microfilariae in an imaging chamber [229]. This design is very compact and cost-effective, however it suffers from a much smaller detection volume (~0.01 mL) compared to our method which screens and automatically processes ~0.8 mL of whole blood or ~3.2 mL of CSF, and it would be very challenging for it to be used for the detection of parasitic protozoa such as trypanosomes which have more than an order-of-magnitude smaller size and mass, lower parasitemia, as well as much weaker light scattering compared to *L. loa*.

Motile bacteria also cause a number of human diseases [183]. Although bacteria are typically much smaller than trypanosomes, the concept of motility-based detection combined with optical magnification could also be explored for label-free detection of bacterial pathogens. There may be potential uses of motility-based detection for screening of other bodily fluids such as urine or diluted mucosal secretions and stool samples. Therefore, we believe that this presented approach has considerable potential to impact various global health challenges. Lastly, we believe that using motility as a biomarker and endogenous contrast can create new possibilities beyond clinical diagnostics. As a label-free 3D imaging modality that is robust to light-scattering and optically-dense media, it can potentially be employed to study motile microorganisms within various fluid environments in a high-throughput manner.

7.4 Conclusions

In conclusion, a high-throughput and sensitive platform for detecting motile parasites in bodily fluids is presented, which uses a novel computational imaging approach named lensless time-resolved holographic speckle imaging. In this method, high-frame-rate holographic recordings of

the body fluid sample were used to computationally detect motile parasites within the sample volume in 3D. A compact and cost-effective imaging device has been built, which can rapidly examine ~3.2 mL of fluid sample within ~20 min. CNN-based classifier is trained to automatically identify the patterns caused by trypanosomes. The LoD of the technique has been established to be <10 trypanosomes per ml in whole blood and <3 per ml in CSF, which is significantly better than the current state-of-the-art parasitological method. This unique imaging technique and optical platform can find numerous applications, including the rapid detection of various motile parasites within bodily fluids as well as biological research.

7.5 Appendix

Pre-calibration of the z-distance range

To pre-calibrate the z-distance range for each of the three channels of our device, we placed one capillary tube whose bottom outer surface was purposely made dirty. We then captured three holograms when the scanning head is at the two ends of its scanning range as well as in the middle, and autofocused to the dirty surface using the three holograms respectively [97,98]. The expected z_b in this case was calculated from the averaged autofocusing distance by adding the wall thickness of the glass capillary tube. The calibration step needs to be done only once.

High-pass filtered computational back-propagation

We back-propagated the diffraction patterns to the given z-distances using the angular spectrum method [52], involving a 2D fast Fourier transform (FFT), a matrix multiplication in the spatial frequency domain with the free-space transfer function, and an inverse FFT. However, because the approximate size of the trypanosomes is known, we added a high-pass filter into the transfer function in the spatial frequency domain to suppress other noises and artifacts.

The coherent transfer function of free-space propagation is given by

$$H(f_x, f_y; z) = \begin{cases} \exp\left[j \frac{2\pi z}{\lambda} \sqrt{1 - (\lambda f_x)^2 - (\lambda f_y)^2} \right], & \sqrt{f_x^2 + f_y^2} \le \frac{1}{\lambda} \\ 0, \quad \text{others} \end{cases} \tag{7.3}$$

where z is the propagation distance, λ is the optical wavelength, f_x and f_y are spatial frequencies in x and y, respectively.

On top of H, we added two high-pass filters, H_1 and H_2, which are used to suppress unwanted interference patterns. H_1 is a 2D Gaussian high-pass filter, which is used to suppress the low-frequency interference patterns owing to the reflection from the various surfaces in the light path, including the protective glass of the image sensor and the various interfaces of the capillary tube loaded with fluids. H_1 is given by

$$H_1\left(f_x, f_y\right) = 1 - \exp\left[-\frac{1}{2} \sigma_1^2 \left(f_x^2 + f_y^2 \right) \right] \tag{7.4}$$

where σ_1 = 25.05 μm. H_2 is used to suppress the interference patterns caused by the unwanted grooves of the manufactured glass capillary tubes. Because the grooves are oriented along the axial direction of the capillary tubes, corresponding to the y-direction in the captured images, their energy is mostly concentrated close to the f_x axis in the spatial frequency domain. Therefore, H_2 performs high-pass filtering to f_y, which is given by

$$H_2\left(f_x, f_y\right) = 1 - \exp\left[-\frac{1}{2} \sigma_2^2 f_y^2 \right] \tag{7.5}$$

where σ_2 = 116.9 μm.

The final coherent transfer function, which combines H, H_1 and H_2, is given by

$$\tilde{I}(\quad\quad;\quad) = H\left(f_x, f_y; z\right) \cdot \min\left\{ H_1\left(f_x, f_y\right), H_2\left(f_x, f_y\right) \right\} \tag{7.6}$$

where $\min\{H_1, H_2\}$ chooses the smaller filter value from H_1 or H_2.

Object function normalization (OFN) to remove potential false positives

OFN is essential to reduce potential false positives owing to strongly scattering particles/objects within the sample (see Figs. 7.9 and 7.10 for a comparison of results with and without OFN). Under slightly time-varying illumination and drifting of the fluid, strongly scattering particles/objects such as cells that are not lysed, clumps of cell debris, spiked white blood cells (WBCs) in the CSF samples or even air bubbles can create strong contrast (hotspots) when processed by CMA. These hotspots can resemble those created by trypanosomes, leading to false positive detections. Therefore, in order to distinguish parasites of interest (especially trypanosomes) that have *weak scattering* and *strong locomotion* from other unwanted objects that have *strong scattering* and *weak locomotion*, we use the object function itself to normalize the frame subtraction corresponding to Eq. (7.2). An exponential function with a properly selected γ further selectively suppresses strongly scattering objects. For trypanosome detection in lysed blood, we chose $\gamma = 2$ based on visual judgement of the resulting distinction between "true positive" signals versus potential "false positive" signals; for trypanosome detection in CSF, $\gamma = 3$.

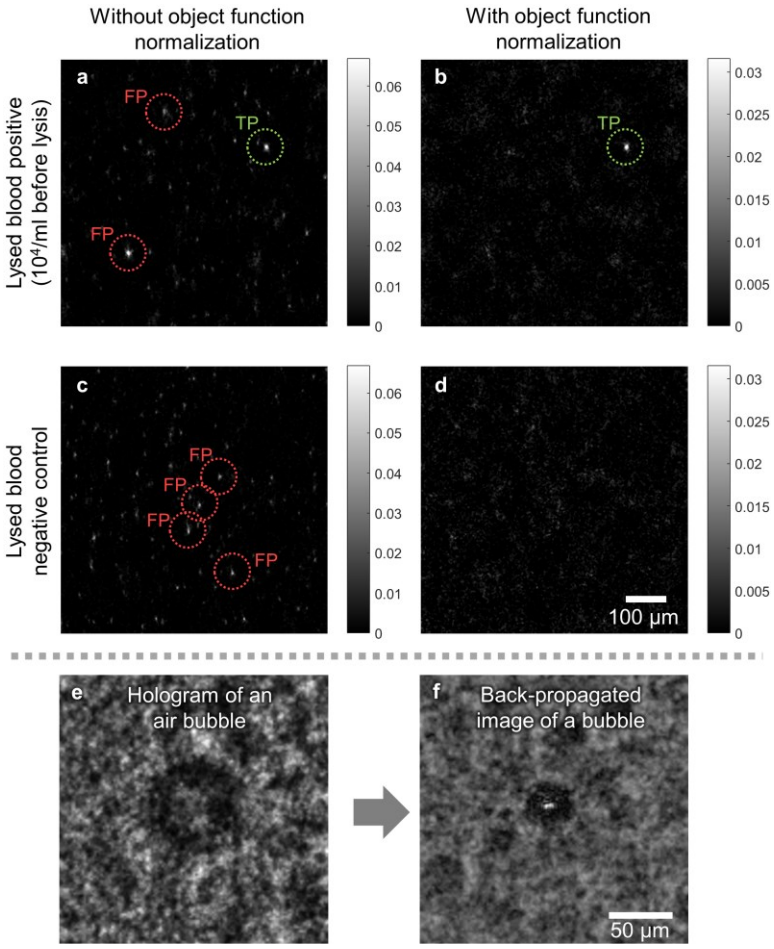

Figure 7. 9. OFN suppresses potential "false positives" due to strongly scattering particles, demonstrated in lysed blood. TP: true positive spots corresponding to trypanosomes; FP: false positives. The false positives in the negative control sample **(c)** are suppressed after applying OFN **(d)**, whereas the true positive signal is preserved ("TP" in **(a)** and **(b)**). In the positive sample, a strong false positive is created due to an air bubble ("FP" in the bottom left of **(a)**), whose hologram and back-propagated amplitude image are shown in **(e)** and **(f)**, respectively. It is, however, effectively eliminated by OFN, as shown in **(b)**.

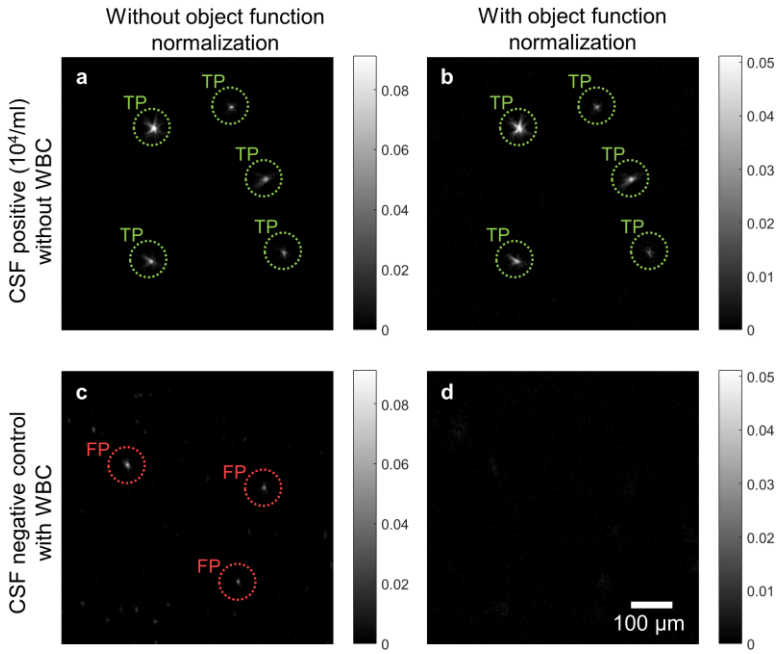

Figure 7. 10. OFN suppresses potential "false positives" due to strongly scattering particles, demonstrated in artificial CSF. TP: true positive spots corresponding to trypanosomes; FP: false positives. The false positives due to spiked WBCs that are evident in the negative control sample **(c)** are suppressed after applying OFN **(d)**, whereas the true positives are preserved in the positive sample **(a, b)**.

Optimization of the subtraction frame interval δ_F and total analyzed frames N_F in the computational motion analysis (CMA) algorithm with object function normalization (OFN)

The subtraction frame interval δ_F and total analyzed frames N_F are parameters that should be optimized for the parasite (or microorganism) to be detected. δ_F and N_F are related to the subtraction *time* interval Δt and the total analyzed *time* T through

$$\delta_F = \Delta t \cdot R \tag{7.7}$$

$$N_F = T \cdot R \tag{7.8}$$

where R is the frame rate of the recorded sequence (i.e., 26.6 fps in our system). By optimally choosing δ_F (or Δt), the signal from the characteristic locomotion of the microorganism of interest can be amplified with respect to the noise, which includes image sensor noise in addition to

unwanted random motion of the background objects/particles in the sample. N_F (or T), on the other hand, determines the window of time-averaging. A larger N_F, in general, will result in reduction of the random background noise through averaging; but at the same time, it can potentially also weaken the useful signal if the microorganism swims away from its original location during T due to directional motion.

We optimized δ_F and N_F for trypanosome detection by evaluating the average signal-to-noise ratio (SNR) of the processed images by CMA with OFN (corresponding to Fig. 7.3(h)), for blood and cerebrospinal fluid (CSF). Signal is defined as the maximum value of the segmented hotspot, whereas noise is defined as the average value of the background, excluding signal regions. SNR is calculated as $20 \cdot \log_{10}$(Signal/Noise) (dB). 20 hotspots were randomly chosen from one imaged field of view (FOV) of a 10^4/mL trypanosome-spiked blood experiment, and 40 hotspots were randomly chosen from a 10^4/mL trypanosome-spiked artificial CSF experiment. The SNRs were averaged for blood and CSF, respectively. We varied δ_F and N_F to observe their effects on average SNR (Fig. 7.11). The same set of hotspots were used consistently for average SNR calculations as we varied δ_F and N_F for either blood and CSF, respectively.

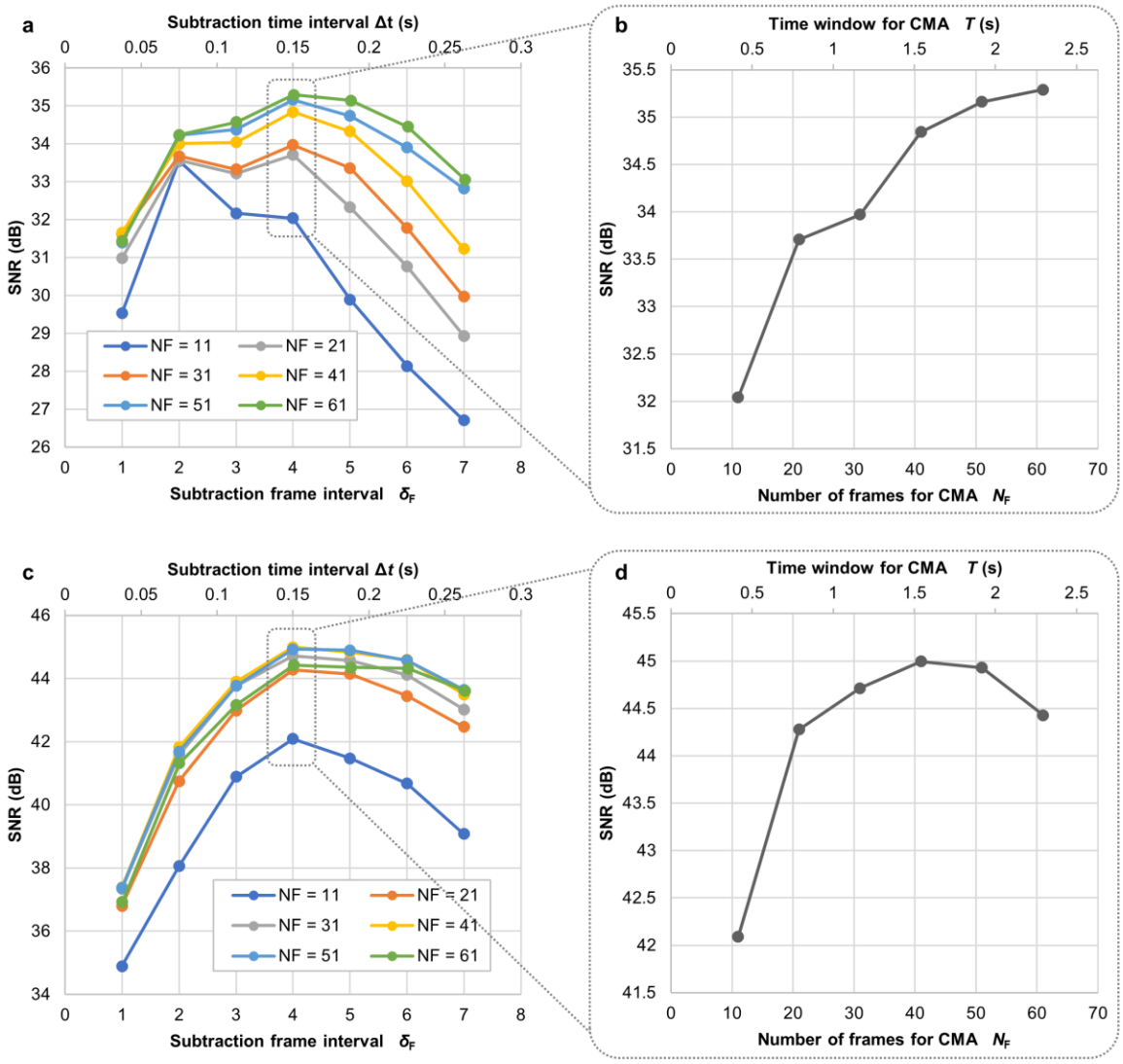

Figure 7. 11. Optimization of the subtraction frame interval δ_F and total analyzed frames N_F for differential analysis. The SNR is used as the criterion for optimization. **(a, b)** Optimization for trypanosome detection in lysed blood. $\delta_F = 4$ and $N_F = 61$ leads to the optimal SNR of 35.29 dB. **(c, d)** Optimization for trypanosome detection in CSF. $\delta_F = 4$ and $N_F = 41$ leads to the optimal SNR of 45.00 dB.

As shown in Fig. 7.11(a-b), for lysed blood, $\delta_F = 4$ ($\Delta t = 0.15$ s) and $N_F = 61$ frames ($T = 2.29$ s) leads to the highest SNR of 35.29 dB. Fig. 7.11(b) implies that the average SNR could still increase if a larger N_F (T) is used. However, due to practical time constraints of this platform as a diagnostic tool as well as heating of the sample over time, we only recorded 61 frames per image sequence.

For CSF (Fig. 7.11(c-d)), a similar effect is observed about δ_F, which maximizes the SNR at $\delta_F = 4$. However, Fig. 7.11(d) shows that the SNR drops as a function of N_F when $N_F > 41$, and therefore, the optimal N_F is chosen as $N_F = 41$. In addition, the optimal SNR for CSF ($\delta_F = 4$, $N_F = 41$) is 45.00 dB, which is ~10 dB higher than the optimal SNR in blood. Based on these observations, we conclude that because CSF is a clear medium (as compared to the lysed blood), less averaging (i.e., a smaller N_F) is needed to achieve a low noise and high SNR. Therefore, for N_F beyond 41, the benefit in SNR from more averaging is diminished, whereas other factors that decrease SNR start to become dominant, mainly due to the gradual displacement of microorganisms from their original locations.

Construction and training of the convolutional neural network (CNN) for the identification of trypanosomes

Generation of positive images for training/validation

Positive images are manually identified from experimental data with a relatively high concentration of spiked trypanosomes. For blood, one test (i.e., one scanning experiment with three capillary tubes) with a spiked trypanosome concentration of ~10^4/mL was used (no overlap with the data reported in Fig. 7.6). For CSF, one test with a spiked trypanosome concentration of ~10^4/mL in artificial CSF was used, and the sample was not spiked with WBCs as was done for

testing. For each bodily fluid type, the images were processed using CMA with OFN followed by post image filtering and segmentation (see Materials and methods for details), and movies were generated for the first 4000 detected candidate spots. Two human annotators jointly viewed these movies and judged the existence of a motile trypanosome in each movie characterized by a slender body and rapid beating. The resulting label for each movie was either "positive" (with a high confidence that there existed a moving trypanosome), "negative", or "uncertain". Multiple trypanosomes that co-exist in a single video are labeled as "negative" to avoid confusing the network during training. It was much easier to annotate the movies related to CSF due to the high quality of the holographic reconstruction in the clear medium; whereas for blood, the resulting labels were mostly either "positive" or "uncertain", because it was difficult to affirm that the movie did not contain a trypanosome. After manual annotation, only those that were labeled as "positive" were kept in training/validation. The "uncertain" and "negative" were discarded. This resulted in 3697 positive images for blood and 3890 positive images for CSF. Note that the movies are solely for the purpose of labeling, and the 2D maximum intensity projection (MIP) image patches resulting from CMA are used to construct the training/validation library. The images were then randomly split into training and validation sets using a four-to-one ratio. Finally, data augmentation was performed to increase the number of training images by mirroring the images horizontally, vertically, and both horizontally and vertically, resulting in 4× larger positive training libraries for blood and CSF, respectively.

Generation of negative images for training/validation

Negative training/validation images entirely came from negative control experiments (no overlap with the data reported in Fig. 7.6). One negative control test was used to populate the training/validation library for blood; two negative control tests were used for CSF because of fewer

"false positives" per test. When segmenting the negative images, a lower intensity threshold was used (0.008 for blood and 0.015 for CSF) to generate more images, resulting in 5834 negative images for blood and 2586 images for CSF experiments. The images were randomly split into training and validation sets using a four-to-one ratio for blood and CSF, respectively. Data augmentation was performed to the negative training libraries similarly to the positive set by mirroring the images in three different ways, resulting in a 4× enlargement of the negative training library size. In addition, to improve the robustness of the trained classifier to unseen data, we also performed augmentation by replicating the negative images and multiplying by a factor of 1.5. Thus, the total enlargement factor for the negative training libraries is 8×.

Network architecture

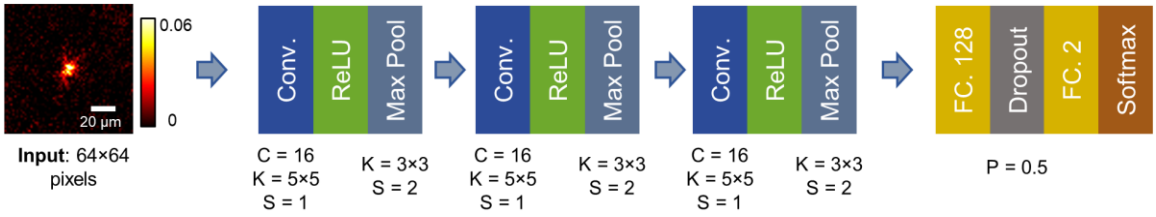

Figure 7. 12. Structure of the CNN to automatically detect the signals created by trypanosomes. C: number of channels; K: convolutional filter size; S: stride; P: probability of dropout.

In this work, we constructed a CNN with three convolutional blocks and two fully connected (FC) layers (see Fig. 7.12). Each convolutional block consists of a convolutional layer (filter size = 5×5, stride = 1, 16 channels) followed by a rectified linear unit (ReLU) layer and a max-pooling layer (filter size = 3×3, stride = 2). The first FC layer has 128 output nodes, and the second FC layer has 2 output nodes, representing the two classes (trypanosome and non-trypanosome). The outputs are then passed through a softmax layer to generate the class probabilities. Dropout (p = 0.5) is added to the first FC layer during training. The same network architecture is separately trained to identify trypanosome signals within blood and CSF.

Network training

The CNN was implemented in TensorFlow (version 1.7.0) and Python (version 3.6.2). The convolutional kernels were initialized using a truncated normal distribution (mean = 0, standard deviation = 5.5×10^{-3}). The weights of the FC layers were initialized using the Xavier initializer [230]. All network biases were initialized as zero. The learnable parameters were optimized using the adaptive moment estimation (Adam) optimizer [231] with a learning rate of 10^{-3}. A batch size of 64 was used, and the network was trained for ten thousand iterations until converged.

CUDA acceleration of the CMA algorithm

The CMA algorithm was accelerated using CUDA C++ and was run on a laptop computer with dual Nvidia GTX 1080 graphics processing units (GPUs). The most computationally intensive mathematical operations in the CMA algorithm were fast Fourier transforms (FFTs) and inverse FFTs (IFFTs). The Nvidia CUDA Fast Fourier Transform library (cuFFT) library was used to perform these operations. Thrust library was used to perform reduction (i.e., summation of all elements) of an image, which was further used to calculate the mean value of the image for normalization. Other various basic mathematical operations on real or complex-valued images were implemented using custom-written CUDA kernel functions. The CUDA code was carefully optimized to parallelize computation, maximize efficiency and minimize GPU memory usage. For instance, when performing back-propagation of the diffraction patterns to each z-distance, the high-pass-filtered coherent transfer function (Eqs. (7.3-7.6)) was only calculated once per z-distance, which was reused for all the frames in the time sequence. When performing time-averaged differential analysis with OFN (Eq. (7.2)), only ($\delta_F + 1$) back-propagated images (i.e., $\mathbf{B}_i$) needed to be stored in the GPU memory at each given time without sacrificing performance, which

reduced the GPU memory usage and made it possible to process even larger-scale problems (e.g., image sequences with more frames, or performing CMA at more z-distances) or to use lower-end GPUs with less memory.

Before performing FFTs, the raw images (vertical: 1374 pixels, horizontal: 3840 pixels) were padded to a size of 1536 × 4096 pixels. The padded pixels were assigned the mean value of the unpadded image to reduce artifacts from discontinuities. Because the new dimensions are powers of 2 and 3 ($1536 = 2^9 \times 3$ and $4096 = 2^{12}$), the FFT operation was accelerated by a factor of ~2.4× compared to without padding. After IFFT was complete, the images were cropped back to the original size for other image processing steps.

COMSOL simulation of sample heating due to the image sensor

The image sensor's temperature rises when it is turned on, creating a temperature gradient above it. Therefore, the fluid within the glass tube will gradually start to flow, also causing the particles within the glass tube to move directionally [232]. As a result, the signal of motile microorganisms generated by the CMA algorithm will weaken due to a "smearing" effect; and in the meantime, the movement of the other unwanted particles will increase the background noise and false positive detections, which is undesirable. The fluid velocity due to convection is related to the height of the fluid channel. Due to the drag force near the channel wall, a thinner channel will lead to a reduced fluid velocity at a given time after the onset of heating. However, as a tradeoff, a thinner channel also results in a reduced screening throughput.

We used COMSOL simulation to estimate the flow speed inside the channel. As shown in Fig. 7.13(a), we created a channel (1 mm inner height, 10 mm inner width, surrounded by a silica wall with a uniform thickness of 0.67 mm) filled with water. A 6 cm section of the channel was selected as the region of interest for simulation. At the center of the channel, a CMOS image sensor

(modeled as a constant heat source with a surface temperature of 313 K) was placed 1 mm below the channel's bottom surface. ~313 K was the highest temperature of the image sensor during image acquisition (see Materials and methods), experimentally measured by an infrared camera (FLIR C2). The reference temperature (room temperature) was set to be 293 K. Non-isothermal flow was used to model the water inside the channel and the air outside the channel.

Fig. 7.13(b-c) show the result of this simulation. The maximum fluid velocity magnitude inside the channel is shown, representing a worst-case scenario. As expected, the fluid velocity increases as a function of the time after onset of heating and the channel height (see Fig. 7.13(b)). We further plotted the relation between the maximum fluid velocity and the channel height in Fig. 7.13(c), at t = 7 s after the onset of heating, which approximately corresponds to the duration of image acquisition (there is a time gap when switching from the upper half to the lower half of the image sensor's FOV). Again, the fluid velocity at t = 7 s represents a worst-case scenario, where the fluid velocity is largest. As shown in Fig. 7.13(c), at a channel height of 1 mm, the fluid velocity is ~2.9 μm/s. Over the duration of a single image sequence of 61 frames (~2.3 s), the displacement due to fluid flow is upper-bounded by ~6.7 μm, which is acceptable when compared with the length of the trypanosome. On the contrary, if the channel height is 2 mm, the displacement will be upper-bounded by ~28 μm, which will lead to strong smearing and reduction of the signal. As a result, the channel height in this work was chosen as 1 mm.

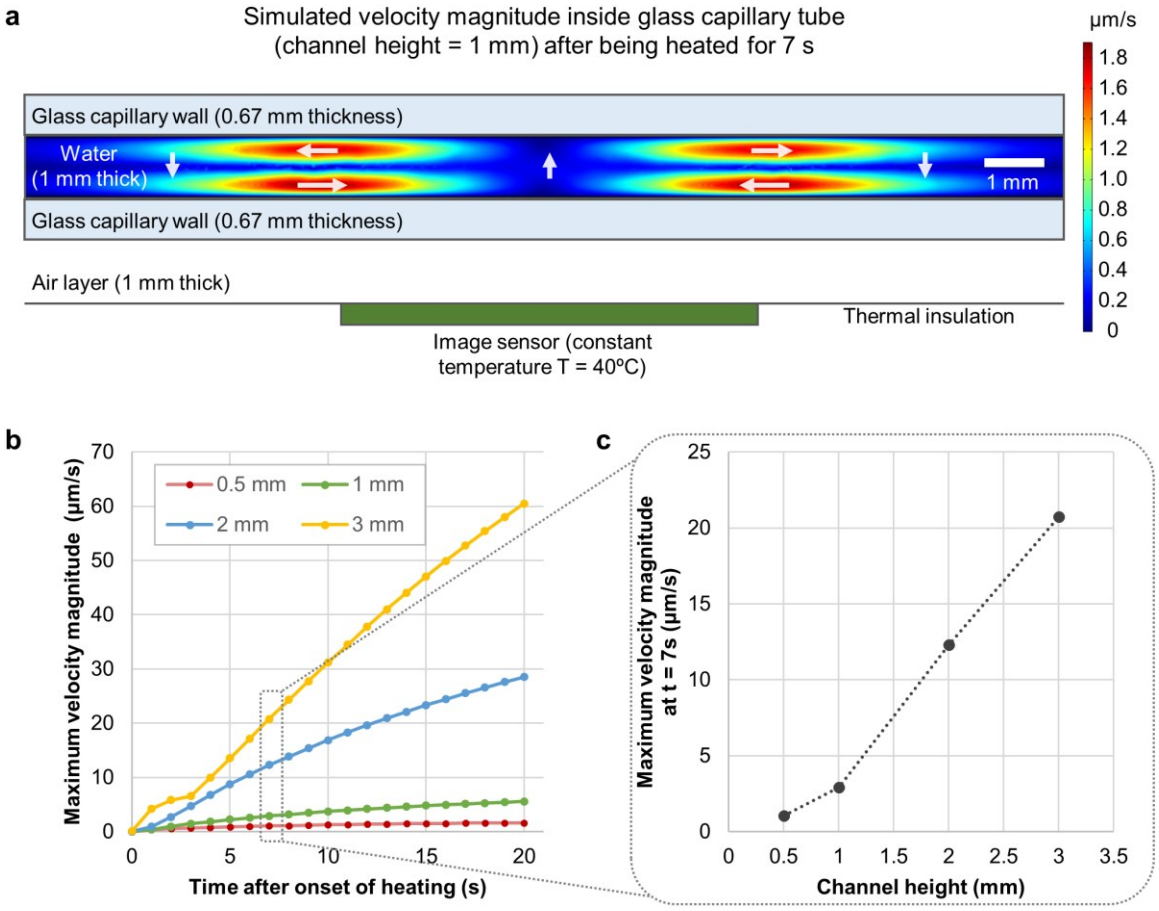

Figure 7. 13. Simulation of the velocity field inside the glass tube due to convection after being heated by the image sensor. (a) Velocity magnitude distribution after the 1 mm-height glass tube is heated for 7 s (side view). The middle cross section of the glass tube is shown. **(b)** Maximum fluid velocity magnitude within the glass tube, as a function of time being heated. Different curves correspond to different inner height of the glass tube. **(c)** Maximum fluid velocity magnitude as a function of the channel height, after being heated for 7 s.

Chapter 8. Conclusions

Optical microscopy has been an indispensable tool for medical diagnosis, owing to its unique capability to visualize structures of clinical significance that are too small to be seen normally. The recent developments in semiconductor-based optoelectronic image sensor technologies and the abundance of computational resources have stimulated the advancement of computational microscopy, which endeavors to overcome the limitations of the conventional optical microscope by incorporating new jointly-designed imaging hardware and software. This dissertation has focused on one of the computational microscopy modalities, namely *lens-free computational microscopy*. Due to its low cost, wide field of view, high throughput, field-portability, amplitude-and-phase-imaging capability, and volumetric imaging capability, it has shown great promise to be applied to various medical imaging and sensing tasks.

Looking back, I summarize that my contribution to lens-free computational microscopy is mainly the development of new techniques and methods applied to three different domains.

(1) Pathology. While it had been challenging for lens-free microscopy to image dense and connected samples such as pathology slides, I contributed to the development of a hybrid multi-height-based phase retrieval method that combines the transport-of-intensity equation, iterative multi-height phase retrieval and tilt correction, which achieved lens-free microscopy of stained and unstained tissue sections and cell smears (Chapter 2). Later, I improved the color accuracy of lens-free microscopy of stained tissues and cells by developing an absorbance spectrum estimation-based color correction method (Chapter 3). I also created a robust holographic autofocusing algorithm that improved the automation of the lens-free post-processing pipeline (Chapter 4). In Chapter 5, lens-free 3D microscopy of optical cleared tissues is presented, which

demonstrates cell phenotyping in intact thick tissues, but also suggests important implications to future pathology diagnosis and imaging of tumor tissues.

(2) Gout/pseudogout diagnosis (rheumatology). Borrowing some of the successful techniques that were developed for pathology slide imaging, e.g., multi-height-based phase retrieval, autofocusing, etc., I led the construction of a polarized lens-free microscope for the rapid and high-throughput imaging of synovial fluid that potentially contains birefringent MSU and CPPD crystals (Chapter 6), for the diagnosis of gout and pseudogout.

(3) Parasite detection in bodily fluids (microbiology). As another major technical breakthrough, I led the development of a novel optical imaging technique, *lensless time-resolved holographic speckle imaging*, that capitalize on the motility of parasites for their rapid and high-throughput detection in bodily fluids (such as blood and cerebrospinal fluid) using an analytic and deep-learning-based approach. Based on this technique, I have built a cost-effective and portable device that has shown potential to be used for field diagnosis of parasitic infections.

Looking forward, I believe that many of these presented techniques and platforms have the potential to be translated to clinical diagnosis, leading to cost-effective and powerful imaging solutions. This would bring a significant reduction in the cost of health care, especially diagnosis, and it could potentially lead to improvement in the cure rate of certain diseases, such as parasitic infections, in less-developed countries and resource-limited settings. Additionally, we have already seen an increasing trend to bring together the recent advances in imaging and artificial intelligence (AI). Combined with the rapid development of AI, the lens-free microscope could become even more cost-effective, accessible, autonomous, and personalized.

References

1. J. Hahn, S. Lim, K. Choi, R. Horisaki, and D. J. Brady, "Video-rate compressive holographic microscopic tomography," Opt. Express **19**, 7289–7298 (2011).

2. D. J. Brady, K. Choi, D. L. Marks, R. Horisaki, and S. Lim, "Compressive Holography," Opt. Express **17**, 13040 (2009).

3. S. R. P. Pavani, M. A. Thompson, J. S. Biteen, S. J. Lord, N. Liu, R. J. Twieg, R. Piestun, and W. E. Moerner, "Three-dimensional, single-molecule fluorescence imaging beyond the diffraction limit by using a double-helix point spread function," Proc. Natl. Acad. Sci. **106**, 2995–2999 (2009).

4. E. Betzig, G. H. Patterson, R. Sougrat, O. W. Lindwasser, S. Olenych, J. S. Bonifacino, M. W. Davidson, J. Lippincott-Schwartz, and H. F. Hess, "Imaging Intracellular Fluorescent Proteins at Nanometer Resolution," Science **313**, 1642–1645 (2006).

5. J. Rosen and G. Brooker, "Non-scanning motionless fluorescence three-dimensional holographic microscopy," Nat. Photonics **2**, 190–195 (2008).

6. Z. Wang, D. L. Marks, P. S. Carney, L. J. Millet, M. U. Gillette, A. Mihi, P. V. Braun, Z. Shen, S. G. Prasanth, and G. Popescu, "Spatial light interference tomography (SLIT)," Opt. Express **19**, 19907–19918 (2011).

7. Y. Kikuchi, D. Barada, T. Kiire, and T. Yatagai, "Doppler phase-shifting digital holography and its application to surface shape measurement," Opt. Lett. **35**, 1548–1550 (2010).

8. Z. Wang, L. Millet, M. Mir, H. Ding, S. Unarunotai, J. Rogers, M. U. Gillette, and G. Popescu, "Spatial light interference microscopy (SLIM)," Opt. Express **19**, 1016–1026 (2011).

9. Y. Rivenson, A. Stern, and B. Javidi, "Overview of compressive sensing techniques applied in holography [Invited]," Appl. Opt. **52**, A423 (2013).

10. L. Waller, L. Tian, and G. Barbastathis, "Transport of Intensity phase-amplitude imaging with higher order intensity derivatives," Opt. Express **18**, 12552–12561 (2010).

11. A. M. Maiden, J. M. Rodenburg, and M. J. Humphry, "Optical ptychography: a practical implementation with useful resolution," Opt. Lett. **35**, 2585 (2010).

12. A. M. Maiden, M. J. Humphry, F. Zhang, and J. M. Rodenburg, "Superresolution imaging via ptychography," J. Opt. Soc. Am. A **28**, 604–612 (2011).

13. A. Greenbaum, W. Luo, T.-W. Su, Z. Göröcs, L. Xue, S. O. Isikman, A. F. Coskun, O. Mudanyali, and A. Ozcan, "Imaging without lenses: achievements and remaining challenges of wide-field on-chip microscopy," Nat. Methods **9**, 889–895 (2012).

14. A. Uzan, Y. Rivenson, and A. Stern, "Speckle denoising in digital holography by nonlocal means filtering," Appl. Opt. **52**, A195 (2013).

15. O. Mudanyali, E. McLeod, W. Luo, A. Greenbaum, A. F. Coskun, Y. Hennequin, C. P. Allier, and A. Ozcan, "Wide-field optical detection of nanoparticles using on-chip microscopy and self-assembled nanolenses," Nat. Photonics **7**, 247–254 (2013).

16. A. Ozcan, "Mobile phones democratize and cultivate next-generation imaging, diagnostics and measurement tools," Lab. Chip **14**, 3187 (2014).

17. G. Zheng, S. A. Lee, Y. Antebi, M. B. Elowitz, and C. Yang, "The ePetri dish, an on-chip cell imaging platform based on subpixel perspective sweeping microscopy (SPSM)," Proc. Natl. Acad. Sci. **108**, 16889–16894 (2011).

18. U. Balis, J. Hipp, T. Flotte, J. Monaco, J. Cheng, A. Madabhushi, Y. Yagi, J. Rodriguez-Canales, M. Emmert-Buck, M. Dugan, S. Hewitt, M. Toner, R. Tompkins, D. Lucas, and J. Gilbertson, "Computer aided diagnostic tools aim to empower rather than replace pathologists: Lessons learned from computational chess," J. Pathol. Inform. **2**, 25 (2011).

19. J. Rosen, G. Brooker, G. Indebetouw, and N. T. Shaked, "A Review of Incoherent Digital Fresnel Holography," J. Hologr. Speckle **5**, 124–140 (2009).

20. G. Brooker, N. Siegel, V. Wang, and J. Rosen, "Optimal resolution in Fresnel incoherent correlation holographic fluorescence microscopy," Opt. Express **19**, 5047–5062 (2011).

21. J. Rosen, N. Siegel, and G. Brooker, "Theoretical and experimental demonstration of resolution beyond the Rayleigh limit by FINCH fluorescence microscopic imaging," Opt. Express **19**, 26249–26268 (2011).

22. E. J. Candès, J. K. Romberg, and T. Tao, "Stable signal recovery from incomplete and inaccurate measurements," Commun. Pure Appl. Math. **59**, 1207–1223 (2006).

23. S. G. Adie, B. W. Graf, A. Ahmad, P. S. Carney, and S. A. Boppart, "Computational adaptive optics for broadband optical interferometric tomography of biological tissue," Proc. Natl. Acad. Sci. **109**, 7175–7180 (2012).

24. C. P. Fleming, J. Eckert, E. F. Halpern, J. A. Gardecki, and G. J. Tearney, "Depth resolved detection of lipid using spectroscopic optical coherence tomography," Biomed. Opt. Express **4**, 1269–1284 (2013).

25. B. J. Vakoc, R. M. Lanning, J. A. Tyrrell, T. P. Padera, L. A. Bartlett, T. Stylianopoulos, L. L. Munn, G. J. Tearney, D. Fukumura, R. K. Jain, and B. E. Bouma, "Three-dimensional microscopy of the tumor microenvironment in vivo using optical frequency domain imaging," Nat. Med. **15**, 1219–1223 (2009).

26. P. Marquet, B. Rappaz, P. J. Magistretti, E. Cuche, Y. Emery, T. Colomb, and C. Depeursinge, "Digital holographic microscopy: a noninvasive contrast imaging technique allowing quantitative visualization of living cells with subwavelength axial accuracy," Opt. Lett. **30**, 468–470 (2005).

27. Z. Monemhaghdoust, F. Montfort, Y. Emery, C. Depeursinge, and C. Moser, "Off-axis digital holographic camera for quantitative phase microscopy," Biomed. Opt. Express **5**, 1721–1730 (2014).

28. X. Yang, Y. Pu, and D. Psaltis, "Imaging blood cells through scattering biological tissue using speckle scanning microscopy," Opt. Express **22**, 3405–3413 (2014).

29. S. O. Isikman, W. Bishara, S. Mavandadi, F. W. Yu, S. Feng, R. Lau, and A. Ozcan, "Lens-free optical tomographic microscope with a large imaging volume on a chip," Proc. Natl. Acad. Sci. **108**, 7296–7301 (2011).

30. T.-W. Su, L. Xue, and A. Ozcan, "High-throughput lensfree 3D tracking of human sperms reveals rare statistics of helical trajectories," Proc. Natl. Acad. Sci. **109**, 16018–16022 (2012).

31. W. Bishara, U. Sikora, O. Mudanyali, T.-W. Su, O. Yaglidere, S. Luckhart, and A. Ozcan, "Holographic pixel super-resolution in portable lensless on-chip microscopy using a fiber-optic array," Lab. Chip **11**, 1276 (2011).

32. I. Navruz, A. F. Coskun, J. Wong, S. Mohammad, D. Tseng, R. Nagi, S. Phillips, and A. Ozcan, "Smart-phone based computational microscopy using multi-frame contact imaging on a fiber-optic array," Lab. Chip **13**, 4015 (2013).

33. O. Mudanyali, C. Oztoprak, D. Tseng, A. Erlinger, and A. Ozcan, "Detection of waterborne parasites using field-portable and cost-effective lensfree microscopy," Lab. Chip **10**, 2419 (2010).

34. T.-W. Su, A. Erlinger, D. Tseng, and A. Ozcan, "Compact and Light-Weight Automated Semen Analysis Platform Using Lensfree on-Chip Microscopy," Anal. Chem. **82**, 8307–8312 (2010).

35. A. Greenbaum, Y. Zhang, A. Feizi, P.-L. Chung, W. Luo, S. R. Kandukuri, and A. Ozcan, "Wide-field computational imaging of pathology slides using lens-free on-chip microscopy," Sci. Transl. Med. **6**, 267ra175-267ra175 (2014).

36. Y. Zhang, Y. Shin, K. Sung, S. Yang, H. Chen, H. Wang, D. Teng, Y. Rivenson, R. P. Kulkarni, and A. Ozcan, "3D imaging of optically cleared tissue using a simplified CLARITY method and on-chip microscopy," Sci. Adv. **3**, e1700553 (2017).

37. M. Veli and A. Ozcan, "Computational Sensing of *Staphylococcus aureus* on Contact Lenses Using 3D Imaging of Curved Surfaces and Machine Learning," ACS Nano **12**, 2554–2559 (2018).

38. W. Bishara, H. Zhu, and A. Ozcan, "Holographic opto-fluidic microscopy," Opt. Express **18**, 27499–27510 (2010).

39. W. Bishara, S. O. Isikman, and A. Ozcan, "Lensfree Optofluidic Microscopy and Tomography," Ann. Biomed. Eng. **40**, 251–262 (2012).

40. S. Seo, S. O. Isikman, I. Sencan, O. Mudanyali, T.-W. Su, W. Bishara, A. Erlinger, and A. Ozcan, "High-Throughput Lens-Free Blood Analysis on a Chip," Anal. Chem. **82**, 4621–4627 (2010).

41. T.-W. Su, S. O. Isikman, W. Bishara, D. Tseng, A. Erlinger, and A. Ozcan, "Multi-angle lensless digital holography for depth resolved imaging on a chip," Opt. Express **18**, 9690–9711 (2010).

42. G. Stybayeva, O. Mudanyali, S. Seo, J. Silangcruz, M. Macal, E. Ramanculov, S. Dandekar, A. Erlinger, A. Ozcan, and A. Revzin, "Lensfree Holographic Imaging of Antibody Microarrays for High-Throughput Detection of Leukocyte Numbers and Function," Anal. Chem. **82**, 3736–3744 (2010).

43. A. Feizi, Y. Zhang, A. Greenbaum, A. Guziak, M. Luong, R. Y. L. Chan, B. Berg, H. Ozkan, W. Luo, M. Wu, Y. Wu, and A. Ozcan, "Rapid, portable and cost-effective yeast cell viability and concentration analysis using lensfree on-chip microscopy and machine learning," Lab Chip **16**, 4350–4358 (2016).

44. Y. Zhang, A. Greenbaum, W. Luo, and A. Ozcan, "Wide-field pathology imaging using on-chip microscopy," Virchows Arch. **467**, 3–7 (2015).

45. Y. Rivenson, Y. Wu, H. Wang, Y. Zhang, A. Feizi, and A. Ozcan, "Sparsity-based multi-height phase recovery in holographic microscopy," Sci. Rep. **6**, (2016).

46. H. Wang, Z. Göröcs, W. Luo, Y. Zhang, Y. Rivenson, L. A. Bentolila, and A. Ozcan, "Computational out-of-focus imaging increases the space–bandwidth product in lens-based coherent microscopy," Optica **3**, 1422–1429 (2016).

47. W. Luo, Y. Zhang, Z. Göröcs, A. Feizi, and A. Ozcan, "Propagation phasor approach for holographic image reconstruction," Sci. Rep. **6**, (2016).

48. Y. Wu, Y. Zhang, W. Luo, and A. Ozcan, "Demosaiced pixel super-resolution for multiplexed holographic color imaging," Sci. Rep. **6**, (2016).

49. W. Luo, A. Greenbaum, Y. Zhang, and A. Ozcan, "Synthetic aperture-based on-chip microscopy," Light Sci. Appl. **4**, e261 (2015).

50. W. Luo, Y. Zhang, A. Feizi, Z. Göröcs, and A. Ozcan, "Pixel super-resolution using wavelength scanning," Light Sci. Appl. **5**, e16060 (2016).

51. T.-W. Su, I. Choi, J. Feng, K. Huang, E. McLeod, and A. Ozcan, "Sperm Trajectories Form Chiral Ribbons," Sci. Rep. **3**, (2013).

52. J. W. Goodman, *Introduction to Fourier Optics*, 3rd ed (Roberts & Co, 2005).

53. A. Greenbaum, W. Luo, B. Khademhosseinieh, T.-W. Su, A. F. Coskun, and A. Ozcan, "Increased space-bandwidth product in pixel super-resolved lensfree on-chip microscopy," Sci. Rep. **3**, (2013).

54. A. Greenbaum, A. Feizi, N. Akbari, and A. Ozcan, "Wide-field computational color imaging using pixel super-resolved on-chip microscopy," Opt. Express **21**, 12469 (2013).

55. A. Greenbaum and A. Ozcan, "Maskless imaging of dense samples using pixel super-resolution based multi-height lensfree on-chip microscopy," Opt. Express **20**, 3129 (2012).

56. A. Greenbaum, N. Akbari, A. Feizi, W. Luo, and A. Ozcan, "Field-Portable Pixel Super-Resolution Colour Microscope," PLoS ONE **8**, e76475 (2013).

57. R. C. Hardie, K. J. Barnard, J. G. Bognar, E. E. Armstrong, and E. A. Watson, "High-resolution image reconstruction from a sequence of rotated and translated frames and its application to an infrared imaging system," Opt. Eng. **37**, 247–260 (1998).

58. M. Elad and Y. Hel-Or, "A fast super-resolution reconstruction algorithm for pure translational motion and common space-invariant blur," IEEE Trans. Image Process. **10**, 1187–1193 (2001).

59. A. Greenbaum, U. Sikora, and A. Ozcan, "Field-portable wide-field microscopy of dense samples using multi-height pixel super-resolution based lensfree imaging," Lab. Chip **12**, 1242 (2012).

60. M. Reed Teague, "Deterministic phase retrieval: a Green's function solution," J. Opt. Soc. Am. **73**, 1434 (1983).

61. M. W. Davidson and M. Abramowitz, "Optical Microscopy," in *Encyclopedia of Imaging Science and Technology* (John Wiley & Sons, Inc., 2002).

62. O. Mudanyali, D. Tseng, C. Oh, S. O. Isikman, I. Sencan, W. Bishara, C. Oztoprak, S. Seo, B. Khademhosseini, and A. Ozcan, "Compact, light-weight and cost-effective microscope based on lensless incoherent holography for telemedicine applications," Lab. Chip **10**, 1417 (2010).

63. Y. Zhang, S. Y. C. Lee, Y. Zhang, D. Furst, J. Fitzgerald, and A. Ozcan, "Wide-field imaging of birefringent synovial fluid crystals using lens-free polarized microscopy for gout diagnosis," Sci. Rep. **6**, 28793 (2016).

64. S. B. Kim, H. Bae, K. -i. Koo, M. R. Dokmeci, A. Ozcan, and A. Khademhosseini, "Lens-Free Imaging for Biological Applications," J. Lab. Autom. **17**, 43–49 (2012).

65. J. R. Fienup, "Phase retrieval algorithms: a comparison," Appl. Opt. **21**, 2758 (1982).

66. J. R. Fienup, "Reconstruction of an object from the modulus of its Fourier transform," Opt. Lett. **3**, 27 (1978).

67. L. J. Allen and M. P. Oxley, "Phase retrieval from series of images obtained by defocus variation," Opt. Commun. **199**, 65–75 (2001).

68. L. J. Allen, W. McBride, N. L. O'Leary, and M. P. Oxley, "Exit wave reconstruction at atomic resolution," Ultramicroscopy **100**, 91–104 (2004).

69. Z. Jingshan, R. A. Claus, J. Dauwels, L. Tian, and L. Waller, "Transport of Intensity phase imaging by intensity spectrum fitting of exponentially spaced defocus planes," Opt. Express **22**, 10661–10674 (2014).

70. Y. Rivenson, Y. Zhang, H. Günaydın, D. Teng, and A. Ozcan, "Phase recovery and holographic image reconstruction using deep learning in neural networks," Light Sci. Appl. **7**, 17141 (2018).

71. S. Farsiu, M. Elad, and P. Milanfar, "Multiframe demosaicing and super-resolution of color images," IEEE Trans. Image Process. **15**, 141–159 (2006).

72. Sung Cheol Park, Min Kyu Park, and Moon Gi Kang, "Super-resolution image reconstruction: a technical overview," IEEE Signal Process. Mag. **20**, 21–36 (2003).

73. R. E. Bank, *PLTMG, a Software Package for Solving Elliptic Partial Differential Equations: Users' Guide 6.0*, Frontiers in Applied Mathematics No. vol. 7 (Society for Industrial and Applied Mathematics, 1990).

74. C. Johnson, *Numerical Solution of Partial Differential Equations by the Finite Element Method* (Dover Publications, 2009).

75. S. S. Gorthi and E. Schonbrun, "Phase imaging flow cytometry using a focus-stack collecting microscope," Opt. Lett. **37**, 707 (2012).

76. D. Paganin, A. Barty, P. J. McMahon, and K. A. Nugent, "Quantitative phase-amplitude microscopy. III. The effects of noise," J. Microsc. **214**, 51–61 (2004).

77. S. De Nicola, A. Finizio, G. Pierattini, P. Ferraro, and D. Alfieri, "Angular spectrum method with correction of anamorphism for numerical reconstruction of digital holograms on tilted planes," Opt. Express **13**, 9935 (2005).

78. N. Delen and B. Hooker, "Free-space beam propagation between arbitrarily oriented planes based on full diffraction theory: a fast Fourier transform approach," J. Opt. Soc. Am. A **15**, 857 (1998).

79. S. J. Jeong and C. K. Hong, "Pixel-size-maintained image reconstruction of digital holograms on arbitrarily tilted planes by the angular spectrum method," Appl. Opt. **47**, 3064 (2008).

80. K. Matsushima, "Formulation of the rotational transformation of wave fields and their application to digital holography," Appl. Opt. **47**, D110 (2008).

81. K. Matsushima, H. Schimmel, and F. Wyrowski, "Fast calculation method for optical diffraction on tilted planes by use of the angular spectrum of plane waves," J. Opt. Soc. Am. A **20**, 1755 (2003).

82. J. Garcia-Sucerquia, "Color lensless digital holographic microscopy with micrometer resolution," Opt. Lett. **37**, 1724–1726 (2012).

83. Z. Göröcs, L. Orzó, M. Kiss, V. Tóth, and S. T\Hokés, "In-line color digital holographic microscope for water quality measurements," in *Laser Applications in Life Sciences 2010* (International Society for Optics and Photonics, 2010), pp. 737614–737614.

84. B. J. Bain, "Diagnosis from the Blood Smear," N. Engl. J. Med. **353**, 498–507 (2005).

85. A. Anand and B. Javidi, "Three-dimensional microscopy with single-beam wavefront sensing and reconstruction from speckle fields," Opt. Lett. **35**, 766 (2010).

86. Z. Gorocs and A. Ozcan, "On-Chip Biomedical Imaging," IEEE Rev. Biomed. Eng. **6**, 29–46 (2013).

87. W. C. Revie, M. Shires, P. Jackson, D. Brettle, R. Cochrane, and D. Treanor, "Color Management in Digital Pathology," Anal. Cell. Pathol. Amst. **2014**, (2014).

88. W. S. Campbell, G. A. Talmon, K. W. Foster, S. M. Lele, J. A. Kozel, and W. W. West, "Sixty-five thousand shades of gray: importance of color in surgical pathology diagnoses," Hum. Pathol. **46**, 1945–1950 (2015).

89. P. Bautista, N. Hashimoto, and Y. Yagi, "Color standardization in whole slide imaging using a color calibration slide," J. Pathol. Inform. **5**, 4 (2014).

90. P. Shrestha and B. Hulsken, "Color accuracy and reproducibility in whole slide imaging scanners," J. Med. Imaging **1**, 027501–027501 (2014).

91. M. S. Peercy and L. Hesselink, "Wavelength selection for true-color holography," Appl. Opt. **33**, 6811 (1994).

92. D. Pascale, "A review of rgb color spaces... from xyy to r'g'b'," Babel Color (2003).

93. Y. Ito, Y. Shimozato, P. Xia, T. Tahara, T. Kakue, Y. Awatsuji, K. Nishio, S. Ura, T. Kubota, and O. Matoba, "Four-Wavelength Color Digital Holography," J. Disp. Technol. **8**, 570–576 (2012).

94. G. Orchard and B. Nation, eds., *Histopathology*, Fundamentals of Biomedical Science (Oxford University Press, 2012).

95. W. Bishara, T.-W. Su, A. F. Coskun, and A. Ozcan, "Lensfree on-chip microscopy over a wide field-of-view using pixel super-resolution," Opt. Express **18**, 11181 (2010).

96. S. O. Isikman, W. Bishara, and A. Ozcan, "Lensfree On-chip Tomographic Microscopy Employing Multi-angle Illumination and Pixel Super-resolution," J. Vis. Exp. (2012).

97. Y. Zhang, H. Wang, Y. Wu, M. Tamamitsu, and A. Ozcan, "Edge sparsity criterion for robust holographic autofocusing," Opt. Lett. **42**, 3824 (2017).

98. M. Tamamitsu, Y. Zhang, H. Wang, Y. Wu, and A. Ozcan, "Comparison of Gini index and Tamura coefficient for holographic autofocusing based on the edge sparsity of the complex optical wavefront," ArXiv170808055 Physicsoptics (2017).

99. P. Xia, Y. Ito, Y. Shimozato, T. Tahara, T. Kakue, Y. Awatsuji, K. Nishio, S. Ura, T. Kubota, and O. Matoba, "Digital Holography Using Spectral Estimation Technique," J. Disp. Technol. **10**, 235–242 (2014).

100. H. Haneishi, T. Hasegawa, A. Hosoi, Y. Yokoyama, N. Tsumura, and Y. Miyake, "System design for accurately estimating the spectral reflectance of art paintings," Appl. Opt. **39**, 6621–6632 (2000).

101. B. Hill, T. Roger, and F. W. Vorhagen, "Comparative analysis of the quantization of color spaces on the basis of the CIELAB color-difference formula," ACM Trans. Graph. **16**, 109–154 (1997).

102. G. Wyszecki and W. S. Stiles, *Color Science: Concepts and Methods, Quantitative Data, and Formulae*, Wiley classics library ed, Wiley Classics Library (John Wiley & Sons, 2000).

103. U. Schnars and W. Jueptner, *Digital Holography: Digital Hologram Recording, Numerical Reconstruction, and Related Techniques* (Springer, 2010).

104. P. Langehanenberg, B. Kemper, D. Dirksen, and G. von Bally, "Autofocusing in digital holographic phase contrast microscopy on pure phase objects for live cell imaging," Appl. Opt. **47**, D176 (2008).

105. F. C. A. Groen, I. T. Young, and G. Ligthart, "A comparison of different focus functions for use in autofocus algorithms," Cytometry **6**, 81–91 (1985).

106. J. Gillespie and R. A. King, "The use of self-entropy as a focus measure in digital holography," Pattern Recognit. Lett. **9**, 19–25 (1989).

107. M. Liebling and M. Unser, "Autofocus for digital Fresnel holograms by use of a Fresnelet-sparsity criterion," J. Opt. Soc. Am. A **21**, 2424 (2004).

108. F. Dubois, C. Schockaert, N. Callens, and C. Yourassowsky, "Focus plane detection criteria in digital holography microscopy by amplitude analysis," Opt. Express **14**, 5895 (2006).

109. F. Dubois, A. El Mallahi, J. Dohet-Eraly, and C. Yourassowsky, "Refocus criterion for both phase and amplitude objects in digital holographic microscopy," Opt. Lett. **39**, 4286 (2014).

110. P. Memmolo, C. Distante, M. Paturzo, A. Finizio, P. Ferraro, and B. Javidi, "Automatic focusing in digital holography and its application to stretched holograms," Opt. Lett. **36**, 1945–1947 (2011).

111. P. Memmolo, M. Paturzo, B. Javidi, P. A. Netti, and P. Ferraro, "Refocusing criterion via sparsity measurements in digital holography," Opt. Lett. **39**, 4719 (2014).

112. M. Lyu, C. Yuan, D. Li, and G. Situ, "Fast autofocusing in digital holography using the magnitude differential," Appl. Opt. **56**, F152–F157 (2017).

113. N. Hurley and S. Rickard, "Comparing Measures of Sparsity," IEEE Trans. Inf. Theory **55**, 4723–4741 (2009).

114. W. H. Press, S. A. Teukolsky, W. T. Vetterling, and B. P. Flannery, "Golden section search in one dimension," Numer. Recipies C Art Sci. Comput. **2**, (1992).

115. S. Grare, S. Coetmellec, D. Allano, G. Grehan, M. Brunel, and D. Lebrun, "Dual wavelength digital holography for 3D particle image velocimetry," J. Eur. Opt. Soc. Rapid Publ. **10**, (2015).

116. D. O. Abegunde, C. D. Mathers, T. Adam, M. Ortegon, and K. Strong, "The burden and costs of chronic diseases in low-income and middle-income countries," The Lancet **370**, 1929–1938 (2007).

117. M. E. Daniels, T. E. Donilon, and T. J. Bollyky, eds., *The Emerging Global Health Crisis: Noncommunicable Diseases in Low- and Middle-Income Countries*, Independent Task Force Report No. no. 72 (Council on Foreign Relations, 2014).

118. "Cancer in Developing Countries - INCTR – International Network for Cancer Treatment and Research," http://www.inctr.org/about-inctr/cancer-in-developing-countries/.

119. K. Chung and K. Deisseroth, "CLARITY for mapping the nervous system," Nat. Methods **10**, 508–513 (2013).

120. R. Tomer, L. Ye, B. Hsueh, and K. Deisseroth, "Advanced CLARITY for rapid and high-resolution imaging of intact tissues," Nat. Protoc. **9**, 1682–1697 (2014).

121. K. Chung, J. Wallace, S.-Y. Kim, S. Kalyanasundaram, A. S. Andalman, T. J. Davidson, J. J. Mirzabekov, K. A. Zalocusky, J. Mattis, A. K. Denisin, S. Pak, H. Bernstein, C. Ramakrishnan, L. Grosenick, V. Gradinaru, and K. Deisseroth, "Structural and molecular interrogation of intact biological systems," Nature **497**, 332–337 (2013).

122. D. S. Richardson and J. W. Lichtman, "Clarifying Tissue Clearing," Cell **162**, 246–257 (2015).

123. K. Sung, Y. Ding, J. Ma, H. Chen, V. Huang, M. Cheng, C. F. Yang, J. T. Kim, D. Eguchi, D. Di Carlo, T. K. Hsiai, A. Nakano, and R. P. Kulkarni, "Simplified three-dimensional tissue clearing and incorporation of colorimetric phenotyping," Sci. Rep. **6**, (2016).

124. B. Yang, J. B. Treweek, R. P. Kulkarni, B. E. Deverman, C.-K. Chen, E. Lubeck, S. Shah, L. Cai, and V. Gradinaru, "Single-Cell Phenotyping within Transparent Intact Tissue through Whole-Body Clearing," Cell **158**, 945–958 (2014).

125. T. Kuwajima, A. A. Sitko, P. Bhansali, C. Jurgens, W. Guido, and C. Mason, "ClearT: a detergent- and solvent-free clearing method for neuronal and non-neuronal tissue," Development **140**, 1364–1368 (2013).

126. H. Lee, J.-H. Park, I. Seo, S.-H. Park, and S. Kim, "Improved application of the electrophoretic tissue clearing technology, CLARITY, to intact solid organs including brain, pancreas, liver, kidney, lung, and intestine," BMC Dev. Biol. **14**, 48 (2014).

127. R. D. Spence, F. Kurth, N. Itoh, C. R. L. Mongerson, S. H. Wailes, M. S. Peng, and A. J. MacKenzie-Graham, "Bringing CLARITY to gray matter atrophy," NeuroImage **101**, 625–632 (2014).

128. H. Zheng and L. Rinaman, "Simplified CLARITY for visualizing immunofluorescence labeling in the developing rat brain," Brain Struct. Funct. **221**, 2375–2383 (2016).

129. K. Toman, "What are the advantages and disadvantages of fluorescence microscopy," Toman's Tuberc. Case Detect. Treat. Monit. Answ. 2nd Ed Geneva World Health Organ. 31–34 (2004).

130. R. A. Terborg, J. Pello, I. Mannelli, J. P. Torres, and V. Pruneri, "Ultrasensitive interferometric on-chip microscopy of transparent objects," Sci. Adv. **2**, e1600077 (2016).

131. Y. Rivenson, A. Stern, and B. Javidi, "Compressive Fresnel Holography," J. Disp. Technol. **6**, 506–509 (2010).

132. J. Garcia-Sucerquia, W. Xu, S. K. Jericho, P. Klages, M. H. Jericho, and H. J. Kreuzer, "Digital in-line holographic microscopy," Appl. Opt. **45**, 836–850 (2006).

133. H. N. Chapman and K. A. Nugent, "Coherent lensless X-ray imaging," Nat. Photonics **4**, 833–839 (2010).

134. Y. Sung, N. Lue, B. Hamza, J. Martel, D. Irimia, R. R. Dasari, W. Choi, Z. Yaqoob, and P. So, "Three-Dimensional Holographic Refractive-Index Measurement of Continuously Flowing Cells in a Microfluidic Channel," Phys. Rev. Appl. **1**, 014002 (2014).

135. E. Mathieu, C. D. Paul, R. Stahl, G. Vanmeerbeeck, V. Reumers, C. Liu, K. Konstantopoulos, and L. Lagae, "Time-lapse lens-free imaging of cell migration in diverse physical microenvironments," Lab. Chip **16**, 3304–3316 (2016).

136. P. Memmolo, L. Miccio, M. Paturzo, G. Di Caprio, G. Coppola, P. A. Netti, and P. Ferraro, "Recent advances in holographic 3D particle tracking," Adv. Opt. Photonics **7**, 713–755 (2015).

137. L. I. Rudin, S. Osher, and E. Fatemi, "Nonlinear total variation based noise removal algorithms," Phys. Nonlinear Phenom. **60**, 259–268 (1992).

138. A. Chambolle, "An Algorithm for Total Variation Minimization and Applications," J. Math. Imaging Vis. **20**, 89–97 (2004).

139. Y. Zhang, Y. Wu, Y. Zhang, and A. Ozcan, "Color calibration and fusion of lens-free and mobile-phone microscopy images for high-resolution and accurate color reproduction," Sci. Rep. **6**, 27811 (2016).

140. P. Haub and T. Meckel, "A Model based Survey of Colour Deconvolution in Diagnostic Brightfield Microscopy: Error Estimation and Spectral Consideration," Sci. Rep. **5**, 12096 (2015).

141. S.-R. Shi, S. A. Imam, L. Young, R. J. Cote, and C. R. Taylor, "Antigen retrieval immunohistochemistry under the influence of pH using monoclonal antibodies.," J. Histochem. Cytochem. **43**, 193–201 (1995).

142. M. T. T. Wong-Riley, "Endogenous peroxidatic activity in brain stem neurons as demonstrated by their staining with diaminobenzidine in normal squirrel monkeys," Brain Res. **108**, 257–277 (1976).

143. S. Liu and H. Hua, "Extended depth-of-field microscopic imaging with a variable focus microscope objective," Opt. Express **19**, 353–362 (2011).

144. T. S. Tkaczyk, *Field Guide to Microscopy*, The SPIE Field Guides (SPIE Press, 2010).

145. Y. Rivenson, A. Stern, and J. Rosen, "Reconstruction guarantees for compressive tomographic holography," Opt. Lett. **38**, 2509–2511 (2013).

146. A. Feuchtinger, A. Walch, and M. Dobosz, "Deep tissue imaging: a review from a preclinical cancer research perspective," Histochem. Cell Biol. **146**, 781–806 (2016).

147. P. H. Neckel, U. Mattheus, B. Hirt, L. Just, and A. F. Mack, "Large-scale tissue clearing (PACT): Technical evaluation and new perspectives in immunofluorescence, histology, and ultrastructure," Sci. Rep. **6**, 34331 (2016).

148. E. Olson, M. J. Levene, and R. Torres, "Multiphoton microscopy with clearing for three dimensional histology of kidney biopsies," Biomed. Opt. Express **7**, 3089–3096 (2016).

149. R. Wortmann, ed., *Crystal-Induced Arthropathies: Gout, Pseudogout, and Apatite-Associated Syndromes* (Taylor & Francis, 2006).

150. T. Neogi, T. L. T. A. Jansen, N. Dalbeth, J. Fransen, H. R. Schumacher, D. Berendsen, M. Brown, H. Choi, N. L. Edwards, H. J. E. M. Janssens, F. Lioté, R. P. Naden, G. Nuki, A. Ogdie, F. Perez-Ruiz, K. Saag, J. A. Singh, J. S. Sundy, A.-K. Tausche, J. Vaquez-Mellado, S. A. Yarows, and W. J. Taylor, "2015 Gout Classification Criteria: An American College of Rheumatology/European League Against Rheumatism Collaborative Initiative," Arthritis Rheumatol. **67**, 2557–2568 (2015).

151. Y. Zhu, B. J. Pandya, and H. K. Choi, "Prevalence of gout and hyperuricemia in the US general population: The National Health and Nutrition Examination Survey 2007–2008," Arthritis Rheum. **63**, 3136–3141 (2011).

152. N. W. McGill and P. A. Dieppe, "Evidence for a promoter of urate crystal formation in gouty synovial fluid.," Ann. Rheum. Dis. **50**, 558–561 (1991).

153. M. Oda, Y. Satta, O. Takenaka, and N. Takahata, "Loss of Urate Oxidase Activity in Hominoids and its Evolutionary Implications," Mol. Biol. Evol. **19**, 640–653 (2002).

154. R. W. Fiddis, N. Vlachos, and P. D. Calvert, "Studies of urate crystallisation in relation to gout.," Ann. Rheum. Dis. **42**, 12–15 (1983).

155. R. E. Sours, D. A. Fink, and J. A. Swift, "Dyeing Uric Acid Crystals with Methylene Blue," J. Am. Chem. Soc. **124**, 8630–8636 (2002).

156. D. J. McCarthy and J. L. Hollander, "Identification of urate crystals in gouty synovial fluid," Ann. Intern. Med. **54**, 452–460 (1961).

157. E. Pascual, E. Batlle-Gualda, A. Martínez, J. Rosas, and P. Vela, "Synovial Fluid Analysis for Diagnosis of Intercritical Gout," Ann. Intern. Med. **131**, 756–759 (1999).

158. B. Pal, M. Foxall, T. Dysart, F. Carey, and M. Whittaker, "How is Gout Managed in Primary Care? A Review of Current Practice and Proposed Guidelines," Clin. Rheumatol. **19**, 21–25 (2000).

159. L. R. Harrold, K. M. Mazor, A. Negron, J. Ogarek, C. Firneno, and R. A. Yood, "Primary care providers' knowledge, beliefs and treatment practices for gout: results of a physician questionnaire," Rheumatology **52**, 1623–1629 (2013).

160. M. Underwood, "Diagnosis and management of gout," BMJ **332**, 1315–1319 (2006).

161. H. Amer, A. Swan, and P. Dieppe, "The utilization of synovial fluid analysis in the UK," Rheumatology **40**, 1060–1063 (2001).

162. H. R. Schumacher, M. S. Sieck, S. Rothfuss, G. M. Clayburne, D. F. Baumgarten, B. S. Mochan, and J. A. Kant, "Reproducibility of synovial fluid analyses. A study among four laboratories," Arthritis Rheum. **29**, 770–774 (1986).

163. C. Gordon, A. Swan, and P. Dieppe, "Detection of crystals in synovial fluids by light microscopy: sensitivity and reliability.," Ann. Rheum. Dis. **48**, 737–742 (1989).

164. J. W. Park, D. J. Ko, J. J. Yoo, S. H. Chang, H. J. Cho, E. H. Kang, J. K. Park, Y. W. Song, and Y. J. Lee, "Clinical factors and treatment outcomes associated with failure in the detection of urate crystal in patients with acute gouty arthritis," Korean J. Intern. Med. **29**, 361–369 (2014).

165. E. McLeod, T. U. Dincer, M. Veli, Y. N. Ertas, C. Nguyen, W. Luo, A. Greenbaum, A. Feizi, and A. Ozcan, "High-Throughput and Label-Free Single Nanoparticle Sizing Based on Time-Resolved On-Chip Microscopy," ACS Nano **9**, 3265–3273 (2015).

166. D. Tseng, O. Mudanyali, C. Oztoprak, S. O. Isikman, I. Sencan, O. Yaglidere, and A. Ozcan, "Lensfree microscopy on a cellphone," Lab. Chip **10**, 1787 (2010).

167. O. Mudanyali, W. Bishara, and A. Ozcan, "Lensfree super-resolution holographic microscopy using wetting films on a chip," Opt. Express **19**, 17378 (2011).

168. S. O. Isikman, A. Greenbaum, W. Luo, A. F. Coskun, and A. Ozcan, "Giga-Pixel Lensfree Holographic Microscopy and Tomography Using Color Image Sensors," PLoS ONE **7**, e45044 (2012).

169. E. McLeod, W. Luo, O. Mudanyali, A. Greenbaum, and A. Ozcan, "Toward giga-pixel nanoscopy on a chip: a computational wide-field look at the nano-scale without the use of lenses," Lab. Chip **13**, 2028–2035 (2013).

170. J. Weidling, S. O. Isikman, A. Greenbaum, A. Ozcan, and E. Botvinick, "Lens-free computational imaging of capillary morphogenesis within three-dimensional substrates," J. Biomed. Opt. **17**, 126018–126018 (2012).

171. S. V. Kesavan, F. Momey, O. Cioni, B. David-Watine, N. Dubrulle, S. Shorte, E. Sulpice, D. Freida, B. Chalmond, J. M. Dinten, X. Gidrol, and C. Allier, "High-throughput monitoring of major cell functions by means of lensfree video microscopy," Sci. Rep. **4**, (2014).

172. S. K. Vashist, P. B. Luppa, L. Y. Yeo, A. Ozcan, and J. H. T. Luong, "Emerging Technologies for Next-Generation Point-of-Care Testing," Trends Biotechnol. **33**, 692–705 (2015).

173. E. Hecht, *Optics*, 4th ed (Addison-Wesley, 2002).

174. A. V. Oppenheim, A. S. Willsky, and S. H. Nawab, *Signals & Systems*, 2nd ed, Prentice-Hall Signal Processing Series (Prentice Hall, 1997).

175. P. A. Dieppe, P. R. Crocker, C. F. Corke, D. V. Doyle, E. C. Huskisson, and D. A. Willoughby, "Synovial Fluid Crystals," QJM **48**, 533–553 (1979).

176. P. Phelps, "Compensated Polarized Light Microscopy: Identification of Crystals in Synovial Fluids From Gout and Pseudogout," JAMA **203**, 508 (1968).

177. "Research System Microscope BX51/BX61 BX2 series," http://www.olympuslatinoamerica.com/spanish/seg/img/Catalog/BX51_BX61_new_catalog.pdf.

178. "CDC - Parasites - Neglected Parasitic Infections (NPIs) in the United States," https://www.cdc.gov/parasites/npi/index.html.

179. D. N. Poole and R. S. McClelland, "Global epidemiology of *Trichomonas vaginalis*," Sex. Transm. Infect. **89**, 418–422 (2013).

180. J. A. Pérez-Molina and I. Molina, "Chagas disease," The Lancet **391**, 82–94 (2018).

181. P. Büscher, G. Cecchi, V. Jamonneau, and G. Priotto, "Human African trypanosomiasis," The Lancet **390**, 2397–2409 (2017).

182. T. Krüger and M. Engstler, "Flagellar motility in eukaryotic human parasites," Semin. Cell Dev. Biol. **46**, 113–127 (2015).

183. C. Josenhans and S. Suerbaum, "The role of motility as a virulence factor in bacteria," Int. J. Med. Microbiol. **291**, 605–614 (2002).

184. M. M. Shimogawa, S. S. Ray, N. Kisalu, Y. Zhang, Q. Geng, A. Ozcan, and K. L. Hill, "Parasite motility is critical for virulence of African trypanosomes," Sci. Rep. **8**, (2018).

185. M. C. Field, D. Horn, A. H. Fairlamb, M. A. J. Ferguson, D. W. Gray, K. D. Read, M. De Rycker, L. S. Torrie, P. G. Wyatt, S. Wyllie, and I. H. Gilbert, "Anti-trypanosomatid drug discovery: an ongoing challenge and a continuing need," Nat. Rev. Microbiol. **15**, 217–231 (2017).

186. G. Langousis and K. L. Hill, "Motility and more: the flagellum of Trypanosoma brucei," Nat. Rev. Microbiol. **12**, 505–518 (2014).

187. D. Malvy and F. Chappuis, "Sleeping sickness," Clin. Microbiol. Infect. **17**, 986–995 (2011).

188. S. Khare, A. S. Nagle, A. Biggart, Y. H. Lai, F. Liang, L. C. Davis, S. W. Barnes, C. J. N. Mathison, E. Myburgh, M.-Y. Gao, J. R. Gillespie, X. Liu, J. L. Tan, M. Stinson, I. C. Rivera, J. Ballard, V. Yeh, T. Groessl, G. Federe, H. X. Y. Koh, J. D. Venable, B. Bursulaya, M. Shapiro, P. K. Mishra, G. Spraggon, A. Brock, J. C. Mottram, F. S. Buckner, S. P. S. Rao, B. G. Wen, J. R. Walker, T. Tuntland, V. Molteni, R. J. Glynne, and F. Supek, "Proteasome inhibition for treatment of leishmaniasis, Chagas disease and sleeping sickness," Nature **537**, 229–233 (2016).

189. K. Stuart, R. Brun, S. Croft, A. Fairlamb, R. E. Gürtler, J. McKerrow, S. Reed, and R. Tarleton, "Kinetoplastids: related protozoan pathogens, different diseases," J. Clin. Invest. **118**, 1301–1310 (2008).

190. A. H. Fairlamb and D. Horn, "Melarsoprol Resistance in African Trypanosomiasis," Trends Parasitol. (2018).

191. M. C. Fernandes and N. W. Andrews, "Host cell invasion by *Trypanosoma cruzi* : a unique strategy that promotes persistence," FEMS Microbiol. Rev. **36**, 734–747 (2012).

192. P. L. Dorn, A. G. McClure, M. D. Gallaspy, E. Waleckx, A. S. Woods, M. C. Monroy, and L. Stevens, "The diversity of the Chagas parasite, Trypanosoma cruzi, infecting the main Central American vector, Triatoma dimidiata, from Mexico to Colombia," PLoS Negl. Trop. Dis. **11**, e0005878 (2017).

193. T. Vos, C. Allen, M. Arora, R. M. Barber, Z. A. Bhutta, A. Brown, A. Carter, D. C. Casey, F. J. Charlson, A. Z. Chen, M. Coggeshall, L. Cornaby, L. Dandona, D. J. Dicker, T. Dilegge, H. E. Erskine, A. J. Ferrari, C. Fitzmaurice, T. Fleming, M. H. Forouzanfar, N. Fullman, P. W. Gething, E. M. Goldberg, N. Graetz, J. A. Haagsma, S. I. Hay, C. O. Johnson, N. J. Kassebaum, T. Kawashima, L. Kemmer, I. A. Khalil, Y. Kinfu, H. H. Kyu, J. Leung, X. Liang, S. S. Lim, A. D. Lopez, R. Lozano, L. Marczak, G. A. Mensah, A. H. Mokdad, M. Naghavi, G. Nguyen, E. Nsoesie, H. Olsen, D. M. Pigott, C. Pinho, Z. Rankin, N. Reinig, J. A. Salomon, L. Sandar, A. Smith, J. Stanaway, C. Steiner, S. Teeple, B. A. Thomas, C. Troeger, J. A. Wagner, H. Wang, V. Wanga, H. A. Whiteford, L. Zoeckler, A. A. Abajobir, K. H. Abate, C. Abbafati, K. M. Abbas, F. Abd-Allah, B. Abraham, I. Abubakar, L. J. Abu-Raddad, N. M. E. Abu-Rmeileh, I. N. Ackerman, A. O. Adebiyi, Z. Ademi, A. K. Adou, K. A. Afanvi, E. E. Agardh, A. Agarwal, A. A. Kiadaliri, H. Ahmadieh, O. N. Ajala, R. O. Akinyemi, N. Akseer, Z. Al-Aly, K. Alam, N. K. M. Alam, S. F. Aldhahri, M. A. Alegretti, Z. A. Alemu, L. T. Alexander, S. Alhabib, R. Ali, A. 'a Alkerwi, F. Alla, P. Allebeck, R. Al-Raddadi, U. Alsharif, K. A. Altirkawi, N. Alvis-Guzman, A. T. Amare, A. Amberbir, H. Amini, W. Ammar, S. M. Amrock, H. H. Andersen, G. M. Anderson, B. O. Anderson, C. A. T. Antonio, A. F. Aregay, J. Ärnlöv, A. Artaman, H. Asayesh, R. Assadi, S. Atique, E. F. G. A. Avokpaho, A. Awasthi, B. P. A. Quintanilla, P. Azzopardi, U. Bacha, A. Badawi, K. Balakrishnan, A. Banerjee, A. Barac, S. L. Barker-Collo, T. Bärnighausen, L. Barregard, L. H. Barrero, A. Basu, S. Bazargan-Hejazi, E. Beghi, B. Bell, M. L. Bell, D. A. Bennett, I. M. Bensenor, H. Benzian, A. Berhane, E. Bernabé, B. D. Betsu, A. S. Beyene, N. Bhala, S. Bhatt, S. Biadgilign, K. Bienhoff, B. Bikbov, S. Biryukov, D. Bisanzio, E. Bjertness, J. Blore, R. Borschmann, S. Boufous, M. Brainin, A. Brazinova, N. J. K. Breitborde, J. Brown, R. Buchbinder, G. C. Buckle, Z. A. Butt, B. Calabria, I. R. Campos-Nonato, J. C. Campuzano, H. Carabin, R. Cárdenas, D. O. Carpenter, J. J. Carrero, C. A. Castañeda-Orjuela, J. C. Rivas, F. Catalá-López, J.-C. Chang, P. P.-C. Chiang, C. E. Chibueze, V. H. Chisumpa, J.-Y. J. Choi, R. Chowdhury, H. Christensen, D. J. Christopher, L. G. Ciobanu, M. Cirillo, M. M. Coates, S. M. Colquhoun, C. Cooper, M. Cortinovis, J. A. Crump, S. A. Damtew, R. Dandona, F. Daoud, P. I. Dargan, J. das Neves, G. Davey, A. C. Davis, D. D. Leo, L. Degenhardt, L. C. D. Gobbo, R. P. Dellavalle, K. Deribe, A. Deribew, S. Derrett, D. C. D. Jarlais, S. D. Dharmaratne, P. K. Dhillon, C. Diaz-Torné, E. L. Ding, T. R. Driscoll, L. Duan, M. Dubey, B. B. Duncan, H. Ebrahimi, R. G. Ellenbogen, I. Elyazar, M. Endres, A. Y. Endries, S. P. Ermakov, B. Eshrati, K. Estep, T. A. Farid, C. S. e S. Farinha, A. Faro, M. S. Farvid, F. Farzadfar, V. L. Feigin, D. T. Felson, S.-M. Fereshtehnejad, J. G. Fernandes, J. C. Fernandes, F. Fischer, J. R. A. Fitchett, K. Foreman, F. G. R. Fowkes, J. Fox, R. C. Franklin, J. Friedman, J. Frostad, T. Fürst, N. D. Futran, B. Gabbe, P. Ganguly, F. G. Gankpé, T. Gebre, T. T. Gebrehiwot, A. T. Gebremedhin, J. M. Geleijnse, B. D. Gessner, K. B. Gibney, I. A. M. Ginawi, A. Z. Giref, M. Giroud, M. D. Gishu, G. Giussani, E. Glaser, W.

W. Godwin, H. Gomez-Dantes, P. Gona, A. Goodridge, S. V. Gopalani, C. C. Gotay, A. Goto, H. N. Gouda, R. Grainger, F. Greaves, F. Guillemin, Y. Guo, R. Gupta, R. Gupta, V. Gupta, R. A. Gutiérrez, D. Haile, A. D. Hailu, G. B. Hailu, Y. A. Halasa, R. R. Hamadeh, S. Hamidi, M. Hammami, J. Hancock, A. J. Handal, G. J. Hankey, Y. Hao, H. L. Harb, S. Harikrishnan, J. M. Haro, R. Havmoeller, R. J. Hay, I. B. Heredia-Pi, P. Heydarpour, H. W. Hoek, M. Horino, N. Horita, H. D. Hosgood, D. G. Hoy, A. S. Htet, H. Huang, J. J. Huang, C. Huynh, M. Iannarone, K. M. Iburg, K. Innos, M. Inoue, V. J. Iyer, K. H. Jacobsen, N. Jahanmehr, M. B. Jakovljevic, M. Javanbakht, S. P. Jayaraman, A. U. Jayatilleke, S. H. Jee, P. Jeemon, P. N. Jensen, Y. Jiang, T. Jibat, A. Jimenez-Corona, Y. Jin, J. B. Jonas, Z. Kabir, Y. Kalkonde, R. Kamal, H. Kan, A. Karch, C. K. Karema, C. Karimkhani, A. Kasaeian, A. Kaul, N. Kawakami, P. N. Keiyoro, A. H. Kemp, A. Keren, C. N. Kesavachandran, Y. S. Khader, A. R. Khan, E. A. Khan, Y.-H. Khang, S. Khera, T. A. M. Khoja, J. Khubchandani, C. Kieling, P. Kim, C. Kim, D. Kim, Y. J. Kim, N. Kissoon, L. D. Knibbs, A. K. Knudsen, Y. Kokubo, D. Kolte, J. A. Kopec, S. Kosen, G. A. Kotsakis, P. A. Koul, A. Koyanagi, M. Kravchenko, B. K. Defo, B. K. Bicer, A. A. Kudom, E. J. Kuipers, G. A. Kumar, M. Kutz, G. F. Kwan, A. Lal, R. Lalloo, T. Lallukka, H. Lam, J. O. Lam, S. M. Langan, A. Larsson, P. M. Lavados, J. L. Leasher, J. Leigh, R. Leung, M. Levi, Y. Li, Y. Li, J. Liang, S. Liu, Y. Liu, B. K. Lloyd, W. D. Lo, G. Logroscino, K. J. Looker, P. A. Lotufo, R. Lunevicius, R. A. Lyons, M. T. Mackay, M. Magdy, A. E. Razek, M. Mahdavi, M. Majdan, A. Majeed, R. Malekzadeh, W. Marcenes, D. J. Margolis, J. Martinez-Raga, F. Masiye, J. Massano, S. T. McGarvey, J. J. McGrath, M. McKee, B. J. McMahon, P. A. Meaney, A. Mehari, F. Mejia-Rodriguez, A. B. Mekonnen, Y. A. Melaku, P. Memiah, Z. A. Memish, W. Mendoza, A. Meretoja, T. J. Meretoja, F. A. Mhimbira, A. Millear, T. R. Miller, E. J. Mills, M. Mirarefin, P. B. Mitchell, C. N. Mock, A. Mohammadi, S. Mohammed, L. Monasta, J. C. M. Hernandez, M. Montico, M. D. Mooney, M. Moradi-Lakeh, L. Morawska, U. O. Mueller, E. Mullany, J. E. Mumford, M. E. Murdoch, J. B. Nachega, G. Nagel, A. Naheed, L. Naldi, V. Nangia, J. N. Newton, M. Ng, F. N. Ngalesoni, Q. L. Nguyen, M. I. Nisar, P. M. N. Pete, J. M. Nolla, O. F. Norheim, R. E. Norman, B. Norrving, B. P. Nunes, F. A. Ogbo, I.-H. Oh, T. Ohkubo, P. R. Olivares, B. O. Olusanya, J. O. Olusanya, A. Ortiz, M. Osman, E. Ota, M. Pa, E.-K. Park, M. Parsaeian, V. M. de Azeredo Passos, A. J. P. Caicedo, S. B. Patten, G. C. Patton, D. M. Pereira, R. Perez-Padilla, N. Perico, K. Pesudovs, M. Petzold, M. R. Phillips, F. B. Piel, J. D. Pillay, F. Pishgar, D. Plass, J. A. Platts-Mills, S. Polinder, C. D. Pond, S. Popova, R. G. Poulton, F. Pourmalek, D. Prabhakaran, N. M. Prasad, M. Qorbani, R. H. S. Rabiee, A. Radfar, A. Rafay, K. Rahimi, V. Rahimi-Movaghar, M. Rahman, M. H. U. Rahman, S. U. Rahman, R. K. Rai, S. Rajsic, U. Ram, P. Rao, A. H. Refaat, M. B. Reitsma, G. Remuzzi, S. Resnikoff, A. Reynolds, A. L. Ribeiro, M. J. R. Blancas, H. S. Roba, D. Rojas-Rueda, L. Ronfani, G. Roshandel, G. A. Roth, D. Rothenbacher, A. Roy, R. Sagar, R. Sahathevan, J. R. Sanabria, M. D. Sanchez-Niño, I. S. Santos, J. V. Santos, R. Sarmiento-Suarez, B. Sartorius, M. Satpathy, M. Savic, M. Sawhney, M. P. Schaub, M. I. Schmidt, I. J. C. Schneider, B. Schöttker, D. C. Schwebel, J. G. Scott, S. Seedat, S. G. Sepanlou, E. E. Servan-Mori, K. A. Shackelford, A. Shaheen, M. A. Shaikh, R. Sharma, U. Sharma, J. Shen, D. S. Shepard, K. N. Sheth, K. Shibuya, M.-J. Shin, R. Shiri, I. Shiue, M. G. Shrime, I. D. Sigfusdottir, D. A. S. Silva, D. G. A. Silveira, A. Singh, J. A. Singh, O. P. Singh, P. K. Singh, A. Sivonda, V. Skirbekk, J. C. Skogen, A. Sligar, K. Sliwa, M. Soljak, K. Søreide, R. J. D. Sorensen, J. B. Soriano, L. A. Sposato, C. T. Sreeramareddy, V. Stathopoulou, N. Steel, D. J. Stein, T. J. Steiner, S. Steinke, L. Stovner, K. Stroumpoulis, B.

F. Sunguya, P. Sur, S. Swaminathan, B. L. Sykes, C. E. I. Szoeke, R. Tabarés-Seisdedos, J. S. Takala, N. Tandon, D. Tanne, M. Tavakkoli, B. Taye, H. R. Taylor, B. J. T. Ao, B. A. Tedla, A. S. Terkawi, A. J. Thomson, A. L. Thorne-Lyman, A. G. Thrift, G. D. Thurston, R. Tobe-Gai, M. Tonelli, R. Topor-Madry, F. Topouzis, B. X. Tran, T. Truelsen, Z. T. Dimbuene, M. Tsilimbaris, A. K. Tura, E. M. Tuzcu, S. Tyrovolas, K. N. Ukwaja, E. A. Undurraga, C. J. Uneke, O. A. Uthman, C. H. van Gool, Y. Y. Varakin, T. Vasankari, N. Venketasubramanian, R. K. Verma, F. S. Violante, S. K. Vladimirov, V. V. Vlassov, S. E. Vollset, G. R. Wagner, S. G. Waller, L. Wang, D. A. Watkins, S. Weichenthal, E. Weiderpass, R. G. Weintraub, A. Werdecker, R. Westerman, R. A. White, H. C. Williams, C. S. Wiysonge, C. D. A. Wolfe, S. Won, R. Woodbrook, M. Wubshet, D. Xavier, G. Xu, A. K. Yadav, L. L. Yan, Y. Yano, M. Yaseri, P. Ye, H. G. Yebyo, P. Yip, N. Yonemoto, S.-J. Yoon, M. Z. Younis, C. Yu, Z. Zaidi, M. E. S. Zaki, H. Zeeb, M. Zhou, S. Zodpey, L. J. Zuhlke, and C. J. L. Murray, "Global, regional, and national incidence, prevalence, and years lived with disability for 310 diseases and injuries, 1990–2015: a systematic analysis for the Global Burden of Disease Study 2015," The Lancet **388**, 1545–1602 (2016).

194. C.-C. for D. C. and Prevention, "CDC - Chagas Disease - Epidemiology & Risk Factors," https://www.cdc.gov/parasites/chagas/epi.html.

195. F. Chappuis, L. Loutan, P. Simarro, V. Lejon, and P. Buscher, "Options for Field Diagnosis of Human African Trypanosomiasis," Clin. Microbiol. Rev. **18**, 133–146 (2005).

196. J. L. Bargul, J. Jung, F. A. McOdimba, C. O. Omogo, V. O. Adung'a, T. Krüger, D. K. Masiga, and M. Engstler, "Species-Specific Adaptations of Trypanosome Morphology and Motility to the Mammalian Host," PLOS Pathog **12**, e1005448 (2016).

197. M. A. de Sousa, "Morphobiological characterization of Trypanosoma cruzi Chagas, 1909 and its distinction from other Trypanosomes," Mem. Inst. Oswaldo Cruz **94**, 205–210 (1999).

198. C. Lumbala, S. Biéler, S. Kayembe, J. Makabuza, S. Ongarello, and J. M. Ndung'u, "Prospective evaluation of a rapid diagnostic test for Trypanosoma brucei gambiense infection developed using recombinant antigens," PLoS Negl. Trop. Dis. **12**, e0006386 (2018).

199. W. V. de Souza, M. da S. Barros, M. Nakazawa, M. A. Krieger, Y. de M. Gomes, and F. L. N. Santos, "Chronic Chagas Disease Diagnosis: A Comparative Performance of Commercial Enzyme Immunoassay Tests," Am. J. Trop. Med. Hyg. **94**, 1034–1039 (2016).

200. A. M. Afonso, M. H. Ebell, and R. L. Tarleton, "A Systematic Review of High Quality Diagnostic Tests for Chagas Disease," PLOS Negl Trop Dis **6**, e1881 (2012).

201. C. Hernández, A. Teherán, C. Flórez, and J. D. Ramírez, "Comparison of parasite loads in serum and blood samples from patients in acute and chronic phases of Chagas disease," Parasitology 1–7 (2018).

202. P. Büscher, D. Mumba Ngoyi, J. Kaboré, V. Lejon, J. Robays, V. Jamonneau, N. Bebronne, W. Van der Veken, and S. Biéler, "Improved Models of Mini Anion Exchange Centrifugation Technique (mAECT) and Modified Single Centrifugation (MSC) for Sleeping Sickness Diagnosis and Staging," PLoS Negl. Trop. Dis. **3**, e471 (2009).

203. B. Storey, C. Marcellino, M. Miller, M. Maclean, E. Mostafa, S. Howell, J. Sakanari, A. Wolstenholme, and R. Kaplan, "Utilization of computer processed high definition video imaging for measuring motility of microscopic nematode stages on a quantitative scale: "The Worminator,"" Int. J. Parasitol. Drugs Drug Resist. **4**, 233–243 (2014).

204. P. G. E. Kennedy, "Human African trypanosomiasis of the CNS: current issues and challenges," J. Clin. Invest. **113**, 496–504 (2004).

205. "STD Facts - Trichomoniasis," https://www.cdc.gov/std/trichomonas/stdfact-trichomoniasis.htm.

206. G. Uilenberg and W. P. Boyt, *A Field Guide for the Diagnosis, Treatment and Prevention of African Animal Trypanosomosis*, New ed. (Food and Agriculture Organization of the United Nations, 1998).

207. "Artificial Cerebrospinal Fluid (ACSF) (10 ×)," Cold Spring Harb. Protoc. **2017**, pdb.rec094342 (2017).

208. M. Oberholzer, M. A. Lopez, K. S. Ralston, and K. L. Hill, "Approaches for Functional Analysis of Flagellar Proteins in African Trypanosomes," in *Methods in Cell Biology* (Elsevier, 2009), Vol. 93, pp. 21–57.

209. N. K. Kisalu, G. Langousis, L. A. Bentolila, K. S. Ralston, and K. L. Hill, "Mouse infection and pathogenesis by Trypanosoma brucei motility mutants," Cell. Microbiol. **16**, 912–924 (2014).

210. C. G. Clark and L. S. Diamond, "Methods for Cultivation of Luminal Parasitic Protists of Clinical Importance," Clin. Microbiol. Rev. **15**, 329–341 (2002).

211. G. E. Garber, "The Laboratory Diagnosis of *Trichomonas vaginalis*," Can. J. Infect. Dis. Med. Microbiol. **16**, 35–38 (2005).

212. O. Twu, D. Dessi, A. Vu, F. Mercer, G. C. Stevens, N. de Miguel, P. Rappelli, A. R. Cocco, R. T. Clubb, P. L. Fiori, and P. J. Johnson, "Trichomonas vaginalis homolog of macrophage migration inhibitory factor induces prostate cell growth, invasiveness, and inflammatory responses," Proc. Natl. Acad. Sci. **111**, 8179–8184 (2014).

213. M. Patil, J. Nagamoti, and S. Metgud, "Diagnosis of Trichomonas vaginalis from vaginal specimens by wet mount microscopy, in pouch TV culture system, and PCR," J. Glob. Infect. Dis. **4**, 22 (2012).

214. "Trichomoniasis - 2015 STD Treatment Guidelines," https://www.cdc.gov/std/tg2015/trichomoniasis.htm.

215. S. Deborggraeve, V. Lejon, R. A. Ekangu, D. Mumba Ngoyi, P. Pati Pyana, M. Ilunga, J. P. Mulunda, and P. Büscher, "Diagnostic Accuracy of PCR in gambiense Sleeping Sickness Diagnosis, Staging and Post-Treatment Follow-Up: A 2-year Longitudinal Study," PLoS Negl. Trop. Dis. **5**, e972 (2011).

216. J. C. K. Enyaru, E. Matovu, B. Nerima, M. Akol, and C. Sebikali, "Detection of *T.b. rhodesiense* Trypanosomes in Humans and Domestic Animals in South East Uganda by Amplification of Serum Resistance-Associated Gene," Ann. N. Y. Acad. Sci. **1081**, 311–319 (2006).

217. E. C. Sabino, A. L. Ribeiro, T. H. Lee, C. L. Oliveira, A. B. Carneiro-Proietti, A. P. Antunes, M. M. Menezes, B. M. Ianni, V. M. Salemi, L. Nastari, F. Fernandes, V. Sachdev, D. M. Carrick, X. Deng, D. Wright, T. T. Gonçalez, E. L. Murphy, B. Custer, M. P. Busch, and for the Chagas Study Group of the NHLBI Retrovirus Epidemiology Donor Study-II (REDS-II), International Component, "Detection of *Trypanosoma cruzi* DNA in blood by PCR is associated with Chagas cardiomyopathy and disease severity: *T. cruzi* PCR status correlates with clinical disease," Eur. J. Heart Fail. **17**, 416–423 (2015).

218. J. E. Rosenblatt, "Laboratory Diagnosis of Infections Due to Blood and Tissue Parasites," Clin. Infect. Dis. **49**, 1103–1108 (2009).

219. H. Feilij, L. Muller, and S. M. Gonzalez Cappa, "Direct micromethod for diagnosis of acute and congenital Chagas' disease," J. Clin. Microbiol. **18**, 327–330 (1983).

220. M. Cheesbrough, *District Laboratory Practice in Tropical Countries* (Cambridge University Press, 2005).

221. S. Bisser, C. Lumbala, E. Nguertoum, V. Kande, L. Flevaud, G. Vatunga, M. Boelaert, P. Büscher, T. Josenando, P. R. Bessell, S. Biéler, and J. M. Ndung'u, "Sensitivity and Specificity of a Prototype Rapid Diagnostic Test for the Detection of Trypanosoma brucei

gambiense Infection: A Multi-centric Prospective Study," PLoS Negl. Trop. Dis. **10**, e0004608 (2016).

222. C. L. Sanchez-Camargo, P. Albajar-Vinas, P. P. Wilkins, J. Nieto, D. A. Leiby, L. Paris, K. Scollo, C. Florez, C. Guzman-Bracho, A. O. Luquetti, N. Calvo, K. Tadokoro, A. Saez-Alquezar, P. P. Palma, M. Martin, and L. Flevaud, "Comparative Evaluation of 11 Commercialized Rapid Diagnostic Tests for Detecting Trypanosoma cruzi Antibodies in Serum Banks in Areas of Endemicity and Nonendemicity," J. Clin. Microbiol. **52**, 2506–2512 (2014).

223. P. Büscher, P. Mertens, T. Leclipteux, Q. Gilleman, D. Jacquet, D. Mumba-Ngoyi, P. P. Pyana, M. Boelaert, and V. Lejon, "Sensitivity and specificity of HAT Sero-K-SeT, a rapid diagnostic test for serodiagnosis of sleeping sickness caused by Trypanosoma brucei gambiense: a case-control study," Lancet Glob. Health **2**, e359–e363 (2014).

224. M. Camara, O. Camara, H. Ilboudo, H. Sakande, J. Kaboré, L. N'Dri, V. Jamonneau, and B. Bucheton, "Sleeping sickness diagnosis: use of buffy coats improves the sensitivity of the mini anion exchange centrifugation test," Trop. Med. Int. Health **15**, 796–799 (2010).

225. D. Muhanguzi, W. O. Okello, J. D. Kabasa, C. Waiswa, S. C. Welburn, and A. P. M. Shaw, "Cost analysis of options for management of African Animal Trypanosomiasis using interventions targeted at cattle in Tororo District; south-eastern Uganda," Parasit. Vectors **8**, (2015).

226. J. A. Rodriguez, M. A. Lopez, M. C. Thayer, Y. Zhao, M. Oberholzer, D. D. Chang, N. K. Kisalu, M. L. Penichet, G. Helguera, R. Bruinsma, K. L. Hill, and J. Miao, "Propulsion of African trypanosomes is driven by bihelical waves with alternating chirality separated by kinks," Proc. Natl. Acad. Sci. **106**, 19322–19327 (2009).

227. N. Heddergott, T. Krüger, S. B. Babu, A. Wei, E. Stellamanns, S. Uppaluri, T. Pfohl, H. Stark, and M. Engstler, "Trypanosome Motion Represents an Adaptation to the Crowded Environment of the Vertebrate Bloodstream," PLOS Pathog **8**, e1003023 (2012).

228. P. J. Hotez, P. J. Brindley, J. M. Bethony, C. H. King, E. J. Pearce, and J. Jacobson, "Helminth infections: the great neglected tropical diseases," J. Clin. Invest. **118**, 1311–1321 (2008).

229. M. V. D'Ambrosio, M. Bakalar, S. Bennuru, C. Reber, A. Skandarajah, L. Nilsson, N. Switz, J. Kamgno, S. Pion, M. Boussinesq, T. B. Nutman, and D. A. Fletcher, "Point-of-care quantification of blood-borne filarial parasites with a mobile phone microscope," Sci. Transl. Med. **7**, 286re4-286re4 (2015).

230. X. Glorot and Y. Bengio, "Understanding the difficulty of training deep feedforward neural networks," in *Proceedings of the Thirteenth International Conference on Artificial Intelligence and Statistics* (2010), pp. 249–256.

231. D. P. Kingma and J. Ba, "Adam: A Method for Stochastic Optimization," ArXiv14126980 Cs (2014).

232. B. J. Kirby, *Micro- and Nanoscale Fluid Mechanics: Transport in Microfluidic Devices* (Cambridge University Press, 2010).